



A COTUTELLE THESIS PRESENTED FOR THE DEGREE OF

DOCTOR OF PHILOSOPHY FROM

UNIVERSITÉ DE BORDEAUX

ÉCOLE DOCTORALE SCIENCES PHYSIQUES ET DE L'INGÉNIEUR
SPÉCIALITÉ MÉCANIQUE

AND

OXFORD BROOKES UNIVERSITY

SCHOOL OF ENGINEERING, COMPUTING AND MATHEMATICS

by **Timothée GENTIEU**

**DEVELOPMENT OF FILLED POLYMERS FOR
THE REPLACEMENT OF CERAMICS USED AS
BALLISTIC PROTECTION LAYER**

Under the supervision of:

Julien JUMEL

James BROUGHTON

Anita CATAPANO

Defended the 19th December 2018

Jury members:

| | | | |
|-------------------------|------------|----------------------------|------------|
| Mr Monerie Yann, | Professor, | Université de Montpellier, | Rapporteur |
| Mr Forquin Pascal, | Professor, | Université Grenoble Alpes, | Rapporteur |
| Ms Dartois Sophie, | Lecturer, | Université Paris Sorbonne, | Examiner |
| Mr Durodola John, | Professor, | Oxford Brookes University, | President |
| Mr Martin Eric, | Professor, | Université de Bordeaux, | Invited |
| Mr Barthélémy François, | Engineer, | DGA, | Invited |

Development of filled polymers for the replacement of ceramics used as ballistic protection layer

Abstract

Ceramics have extensively been used for ballistic protection in the last decades. The combination of their mechanical properties makes them very interesting for armouring. Indeed, they exhibit a high hardness, large compression strength, high stiffness and low density. Ceramic armouring plates are commonly manufactured through a sintering process, where ceramic powders are pressed at high temperatures. This manufacturing process tends to limit the size and shape of components and imparts high costs. On the other hand, moulding using a polymer matrix composite provides an alternative process for developing lower cost parts whilst accommodating increased complexity of geometry and size.

However, the mechanical behaviour of such a material is not completely known and depends on multiple design parameters: the mechanical properties of the phases, their volume fraction, the size and spatial distributions of the particles, and the adhesion between the components. The aim of this thesis is to evaluate the primary morphological parameters that affect the overall mechanical properties, emphasising the influence of the particle/matrix adhesion. To do so, both numerical and experimental multiscale analyses of the material under quasi-static and dynamic loadings were carried out.

More precisely, static and dynamic properties of the particle-reinforced composite have been determined for different constituent material combinations. In particular, attention has been dedicated to the particle/matrix debonding mechanism. Cohesive zone models (CZM) and Finite Fracture Mechanics (FFM) approaches were used to model this phenomenon and a strong effect of the particle size on decohesion was observed.

Keywords: Composite, Particle reinforced polymer, microstructure, homogenisation, micromechanics

Développement de polymères chargés pour le remplacement de plaques céramiques utilisées comme couche de protection balistique

Résumé

Les matériaux céramiques présentent généralement des propriétés mécaniques très intéressantes pour la réalisation de blindages. Ce sont des matériaux très durs et pourtant légers. Les plaques de blindages en céramique sont classiquement mises en forme par pressage à haute température de poudres, ce qui limite la taille et la forme des réalisations tout en impliquant un coût élevé. Une alternative pour produire ces pièces est le moulage d'un composite constitué de particules de céramiques dans une matrice époxy. Ce procédé permet de réduire le coût des pièces tout en autorisant des géométries plus complexes et des dimensions plus importantes.

Le comportement mécanique de ce type de matériau dépend de multiples paramètres de conception : propriétés mécaniques des constituants (matrice polymère et particules céramiques), proportion volumique des deux phases, taille et distribution spatiale des particules ou encore l'adhésion entre les constituants. L'objectif de la thèse est d'évaluer l'influence de ces paramètres sur les propriétés d'usage du matériau. Pour ce faire, une analyse multi-échelle du matériau sous sollicitations quasi-statique et dynamique est réalisée.

Plus précisément, les propriétés statiques et dynamiques du composite à renforts particuliers ont été déterminées pour différentes combinaisons de ces paramètres de conception. En particulier, le mécanisme de décohésion particule/matrice a été spécifiquement étudié. Les approches de Modèles de Zone Cohésive (CZM) et de Mécanique de la Rupture Finie (FFM) ont été utilisées pour modéliser ce phénomène et un fort effet de taille des particules a été observé.

Mots-clés: Composite, Polymère à renfort particulaire, Microstructure, Homogénéisation, Micromécanique

Résumé substantiel

Les matériaux céramiques présentent généralement des propriétés mécaniques très intéressantes pour la réalisation de blindages. Ce sont des matériaux très durs et pourtant légers. Les plaques de blindages en céramique sont classiquement mises en forme par pressage à haute température de poudres, ce qui limite la taille et la forme des réalisations tout en impliquant un coût élevé. Une alternative pour produire ces pièces est le moulage d'un composite constitué de particules de céramiques dans une matrice époxy. Ce procédé permet de réduire le coût des pièces tout en autorisant des géométries plus complexes et des dimensions plus importantes.

Le comportement mécanique de ce type de matériau dépend de multiples paramètres de conception : propriétés mécaniques des constituants (matrice polymère et particules céramiques), proportion volumique des deux phases, taille et distribution spatiale des particules ou encore l'adhésion entre les constituants. L'objectif de la thèse est d'évaluer l'influence de ces paramètres sur les propriétés d'usage du matériau. Pour ce faire, une analyse multi-échelle du matériau sous sollicitations quasi-statique et dynamique est réalisée.

Concernant le volet Matériau/procédé/propriétés, un travail important a été conduit à l'université d'Oxford Brookes qui a élaboré en premier ce nouveau matériau. Les conditions de mise en œuvre ont été optimisées en utilisant différentes fractions volumiques de particules, différentes tailles et types de particules ou encore en appliquant des étapes de dégazage ou de traitement de surface des particules. Différents types d'essais mécaniques ont été réalisés pour caractériser le matériau. Des essais de traction uniaxiale sur échantillons, type haltères, avec suivi par corrélation d'image ont permis de déterminer les modules d'élasticité du matériau en fonction de la fraction volumique de particules introduites. Des essais type Iosipescu ont été mis au point pour observer la rupture en traction du matériau caractéristique des matériaux fragiles. Ensuite, des essais Single Edge V-Notch Beam (SEVNB) ont permis de déterminer la ténacité du matériau. L'utilisation d'éprouvettes avec et sans silane a permis de démontrer que l'amélioration des propriétés d'interface entre les particules et la matrice augmente grandement la contrainte à rupture du matériau.

Une part importante du projet concerne la modélisation du comportement du matériau en fonction des paramètres microstructuraux (types, tailles et fractions volumiques des particules, utilisation de silane). Pour cela, une méthode d'homogénéisation numérique basée sur des analyses éléments finis a été mise en place. Tout d'abord, des algorithmes de génération de microstructures représentatives ont été développés. Les Volumes Élémentaires Représentatifs (VER) ainsi générés ont été corrélés à des observations mi-

crostructurales afin d'obtenir des structures plus proches de la réalité. Les algorithmes de génération de microstructures permettent ensuite de réaliser un travail d'homogénéisation numérique que ce soit pour les caractéristiques élastiques ou jusqu'à la rupture.

Une attention toute particulière est d'ailleurs dédiée à la modélisation de la décohésion particule/matrice. Pour cela, Modèle de Zones Cohésives (CZM) et Mécanique de la Rupture Finie (FFM) ont été employés. La FFM repose sur des critères en contrainte et en énergie couplés. L'ouverture d'une fissure de longueur finie est générée lorsque les deux critères sont simultanément respectés. Un fort effet de la taille des particules sur leur décohésion a été caractérisé à l'aide de ces deux modèles. En effet, les grosses particules tendent à se détacher de la matrice avant celles de dimension inférieure. Deux régimes asymptotiques sont observés : pour les particules de taille importante, la contrainte à appliquer pour l'activation de la décohésion tend vers une valeur plateau alors que celle-ci augmente plus le rayon de la particule est faible pour les petites particules.

En parallèle, des essais d'indentation statiques et dynamiques ont été mis en place afin de rendre compte de l'influence de la microstructure du matériau et du traitement de surface des particules sur la résistance à la perforation. Ces essais ont été développés afin de disposer d'une base de données exhaustive pour décrire l'intérêt de ce type de matériau pour la protection balistique. Pour la perforation à vitesses de sollicitations lentes, des essais d'indentation instrumentés monotones et cycliques ont été mis en place. Ceux-ci permettent de déterminer les propriétés élastiques et la dureté du matériau à renfort particulaire sous sollicitation de compression localisée. Les essais balistiques ont quant à eux été réalisés à l'aide d'un canon à air comprimé qui permet au projectile d'atteindre des vitesses de plusieurs mètres par seconde.

Funding

This thesis is funded by the Direction Générale de l'Armement (DGA) of France through "Allocation de Thèse" Grant (2015).

Acknowledgements

First, I would like to acknowledge my supervisors Anita Catapano and Julien Jumel from the University of Bordeaux and James Broughton from Oxford Brookes University. Thank you for having allowed me to participate to this fantastic project divided between France and United Kingdom. It has been a formidable experience for me either from a professional point of view or from a personal one. I learned a lot from this and, no doubt, it will help me a lot in my future life. For the three of you, thank you for all the advices, corrections and the time you have spent to help me.

I would like to thank all the jury members who used some of their time to read and evaluate my work: Yann Monerie and Pascal Forquin who kindly accepted to review this document and made some meaningful observations, Sophie Dartois, John Durodola, and Eric Martin for the examination.

Also, the DGA and DSTL are gratefully acknowledged for providing the financial support to the project with the UK-Fr PhD scheme that is a great opportunity do collaborative research. The scientific supervision has been carried out by François Barthélémy from DGA and Peter Brown from DSTL who both gave me very valuable information and shared their experience on the subject.

I am also very grateful to everyone who helped me in the lab, especially to set all the experiments up. Jérémy Guitard in Bordeaux and Nick Hooper at Oxford Brookes who both helped me a lot to carry out all the experiments and to make sure that everything works fine in the lab. Also, the people who spent some time to guide and then assist me for the impact tests: Jérémie Girardot for the conception and Simon Dousset who was king enough to help me to set everything up and carry out the experiments although he had his own PhD to finish. During this project, I also benefited from the assistance of two interns, Matt Manger and Alexandre Le Fur who both patiently carried out so much experimental work, even when the tasks were repetitive and time consuming.

Then, a big thank you to all the students who worked with me in the lab and participate everyday to create a great atmosphere: the French and English ones, the old school and new ones, Valentin, Mahfoudh, Aurore, Racine, Benoit, Alexis, Sarah, Léna, Justine, Joao, Miguel, Erasmo, Davide, just to name a few. Thank you also to all my friends in

France and abroad, especially (and they will recognize themselves) la Team Saucisson and le Motul for their everlasting friendship and the joy they bring me. A thought also goes to my flatmates and my judo partners from both France and UK.

Finally, my warmest thoughts go to my family who supported from the beginning, my parents for their love, my brother Odelin for all the time we spend together and his technical assistance, my grandparents, and all the others. And to the love of my life, H el ene, yes we will be together soon.

Contents

| | |
|---|-----------|
| Introduction | 5 |
| 1 Literature review | 6 |
| 1.1 Monolithic ceramics applied for ballistic protection | 6 |
| 1.2 Particulate reinforced materials applied for ballistic protection | 8 |
| 1.3 Experimental determination of ballistic efficiency of ceramics | 10 |
| 1.4 Relationship between quasi-static behaviour and ballistic efficiency of ce- ramics and particle reinforced materials | 13 |
| 1.4.1 Monolithic ceramics | 13 |
| 1.4.2 Particle reinforced materials | 15 |
| 1.5 Properties of particulate reinforced polymers | 17 |
| 1.5.1 Effect of particle volume fraction | 17 |
| 1.5.2 Effect of particle size | 19 |
| 1.5.3 Effect of particle shape | 20 |
| 1.5.4 Effect of particle/matrix adhesion | 20 |
| 1.5.5 Effect of epoxy resin material | 21 |
| 1.5.6 Summary on the effect of microstructure and constituents properties on particle reinforced polymers | 22 |
| 1.6 Tools to study the behaviour of a particle reinforced composite | 23 |
| 1.6.1 Phenomenological models | 24 |
| 1.6.2 Analytical models | 25 |
| 1.6.3 Numerical simulations | 30 |
| 1.7 Conclusions | 35 |
| 2 Highly filled polymers: Microstructure and elastic behaviour | 37 |
| 2.1 Material description at the microscale level | 37 |
| 2.1.1 Components properties | 38 |
| 2.1.2 Manufacturing of the composite | 41 |
| 2.1.3 Description of the microstructure | 46 |
| 2.1.4 Semi-realistic artificial microstructure generation | 47 |

| | | |
|----------|--|------------|
| 2.2 | Elastic properties and homogenisation | 53 |
| 2.2.1 | Experimental determination of elastic properties | 53 |
| 2.2.2 | Numerical elastic homogenisation | 59 |
| 2.2.3 | Comparisons of numerical and analytical homogenisation results . . | 66 |
| 2.2.4 | Comparison between numerical and experimental elastic modulus . | 74 |
| 2.3 | Conclusions | 75 |
| 3 | Static failure of the ceramic particle reinforced material | 77 |
| 3.1 | Experimental observation of tensile quasi-static failure | 77 |
| 3.1.1 | Tensile strength and limitations of tensile tests for brittle materials | 78 |
| 3.1.2 | Iosipescu shear tests | 78 |
| 3.1.3 | Single Edge V-Notch Beam tests (SEVNB) | 86 |
| 3.2 | Modelling of the debonding phenomenon at the micro and meso-scale levels | 89 |
| 3.2.1 | Semi-analytical homogenisation model | 90 |
| 3.2.2 | FE model | 96 |
| 3.2.3 | Results of the numerical simulations | 98 |
| 3.2.4 | Calibration of the semi-analytical model and results | 104 |
| 3.2.5 | Generalisation of the model | 106 |
| 3.3 | Conclusions | 107 |
| 4 | Particle size effect on the particle/matrix debonding | 109 |
| 4.1 | Numerical and analytical approaches to tackle particle debonding | 110 |
| 4.1.1 | Particle debonding in the literature | 110 |
| 4.1.2 | Presentation of the case study | 111 |
| 4.1.3 | Cohesive Zone Model (CZM) approach | 112 |
| 4.1.4 | Finite Fracture Mechanics (FFM) approach | 114 |
| 4.2 | Case studies of particle debonding | 117 |
| 4.2.1 | Hydrostatic debond of a single spherical particle: FFM / CZM comparison | 117 |
| 4.2.2 | Uniaxial debond of a single spherical particle: FFM / CZM com- parison | 119 |
| 4.2.3 | Discussion on the physical interpretations for both models | 123 |
| 4.2.4 | Uniaxial debond of a single angular particle: FFM / CZM comparison | 127 |
| 4.3 | Conclusions | 131 |
| 5 | Perforation at slow loading rate: Indentation tests | 133 |
| 5.1 | Instrumented indentation tests setup | 133 |
| 5.1.1 | Specimen manufacturing and geometry | 134 |
| 5.1.2 | Experiment protocol | 135 |

| | | |
|----------|---|------------|
| 5.2 | Monotonic loading until failure | 136 |
| 5.2.1 | Failure of the particle reinforced composite under indentation loading | 136 |
| 5.2.2 | Effect of the design parameters on the indentation behaviour | 137 |
| 5.3 | Cyclic loading | 140 |
| 5.3.1 | Penetration of a spherical indenter during cyclic indentation | 141 |
| 5.3.2 | Evaluation of hardness and elastic properties with cyclic indentation | 145 |
| 5.3.3 | Description of cyclic indentation test protocol | 147 |
| 5.3.4 | Effect material parameters on composite hardness and indentation stiffness | 148 |
| 5.4 | Conclusions | 153 |
| 6 | Perforation at high loading rate: Development of impact tests | 155 |
| 6.1 | Ballistic impact test set up | 156 |
| 6.1.1 | Compressed gas gun | 156 |
| 6.1.2 | Sabot design | 157 |
| 6.1.3 | Samples/Targets | 158 |
| 6.1.4 | Instrumentation of the impact test | 159 |
| 6.2 | Validation of the test setup and preliminary results | 160 |
| 6.3 | Conclusions | 165 |
| | General conclusion and outlook | 169 |
| A | Density measurements for volume fraction determination | 185 |
| B | Study on the size of the process zone for particle debonding | 187 |
| C | Parametric study for particle debonding with CZM | 190 |
| D | Fracture surfaces after monotonic indentation tests | 196 |
| E | Publications and communications | 198 |

List of Figures

- 1 Advanced Combat Helmet design. 2
- 2 Different scales introduced for this study. 4
- 1.1 Radical weight reduction for future ground vehicles. 7
- 1.2 Successive loading conditions during impact 8
- 1.3 Concepts of armour systems with ceramics/polymer assemblies 10
- 1.4 Depth Of Impact test setup 11
- 1.5 Spherical expansion test setup. 12
- 1.6 Plate impact tests 12
- 1.7 Representation of the damage during a ballistic impact test and Edge On
Impact test. 13
- 1.8 Typical trend in armour ceramics. 14
- 1.9 Mean-field homogenisation schemes 26
- 1.10 Differential scheme 26
- 1.11 Comparisons between the homogenisation schemes 27
- 1.12 Debonding in high explosive materials 29
- 1.13 Two neighboring grains with an interconnecting material layer according
to Christoffersen. 29
- 1.14 Crack propagations using CZM, XFEM, and phase field 32
- 1.15 DEM modelling 33
- 1.16 Communication of forces in sand impacted by a sphere, at two different
packing configurations. 34
- 1.17 Lattice representation of a granular aggregate composed of particles, solid
matrix connecting the particles and voids. 35
- 2.1 Boron carbide particles, Grit sizes F60, F360, F1200, observed with SEM. . 39
- 2.2 Alumina particles, Grit sizes F20, F60, observed with OM. 40
- 2.3 Manufacturing process of the ceramic reinforced material. 42
- 2.4 Some steps of the manufacturing process of the ceramic reinforced material. 42

| | | |
|------|--|----|
| 2.5 | γ -Glycidyloxypropyl-trimethoxysilane (GPS) molecule structure before hydrolysis. | 43 |
| 2.6 | Silane treatment of the particles. | 43 |
| 2.7 | Particle packing effects | 44 |
| 2.8 | Particle packings | 45 |
| 2.9 | Polishing process of the ceramic particle reinforced polymer for microscopy. | 46 |
| 2.10 | Microstructure with alumina particles | 46 |
| 2.11 | Flowchart of the dropping and rolling algorithm. | 49 |
| 2.12 | Flowcharts for the Voronoi and dropping and rolling with polygonal particles algorithms | 51 |
| 2.13 | Algorithm generated microstructures | 52 |
| 2.14 | Stress-strain curves for tensile tests | 55 |
| 2.15 | Elastic moduli against particle volume fraction for monodisperse particle sizes | 56 |
| 2.16 | Estimated volume fraction and open porosities from density measurements | 56 |
| 2.17 | Elastic moduli against estimated particle volume fraction for monodisperse particle sizes | 57 |
| 2.18 | Young's modulus against particle volume fraction for polydisperse particle sizes | 58 |
| 2.19 | Numerical homogenisation scheme. | 60 |
| 2.20 | Displacement fields of the RVE | 61 |
| 2.21 | Evolution of the C_{1111} component of the stiffness tensor with standard deviation against the size of the RVE | 62 |
| 2.22 | Evolution of the C_{1111} component of the stiffness tensor with standard deviation against the size of the RVE | 63 |
| 2.23 | Evolution of the ratio C_{2222}/C_{1111} with standard deviation against the size of the RVE | 63 |
| 2.24 | Evolution of the ratio C_{2222}/C_{1111} with standard deviation against the size of the RVE | 64 |
| 2.25 | Evolution of the ratio C_{2212}/C_{1111} with standard deviation against the size of the RVE | 64 |
| 2.26 | Evolution of the ratio $C_{1212}/((C_{1111} - C_{1122})/2)$ with standard deviation against the size of the RVE | 65 |
| 2.27 | Eshelby equivalent problems | 67 |
| 2.28 | Two-steps Lielens homogenisation scheme for multiphasic material | 69 |
| 2.29 | Homogenised C_{1111} component of the stiffness tensor against volume fraction ϕ for analytical homogenisation schemes. | 70 |
| 2.30 | Local stress field σ_{11} in the the matrix of the RVE | 70 |

| | | |
|------|--|----|
| 2.31 | Histograms of stress distribution in the different types of microstructures. | 71 |
| 2.32 | Comparisons of histograms of σ_{11} distribution in the matrices of different types of microstructures. | 72 |
| 2.33 | Stress σ_{11} distribution in the different RVE. | 72 |
| 2.34 | Comparisons of histograms of σ_{eq}^{vm} distribution in the matrices of different types of microstructures. | 73 |
| 2.35 | Homogenised C_{1212} component of the stiffness tensor against volume fraction ϕ for analytical homogenisation schemes. | 74 |
| 2.36 | Local stress field σ_{12} in the the matrix of the RVE | 75 |
| 2.37 | Comparison between Young's moduli obtained numerically and experimentally against particle volume fraction. | 75 |
| 3.1 | 3-part Iosipescu mould. | 79 |
| 3.2 | Iosipescu test setup and loading | 79 |
| 3.3 | Contours of maximum principal stress field between the notches. | 80 |
| 3.4 | Types of failure Iosipescu test | 81 |
| 3.5 | Average strength and standard deviation of the material with and without silane treatment. | 82 |
| 3.6 | Iosipescu samples without silane treatment after failure. | 82 |
| 3.7 | Iosipescu samples with silane treatment after failure. | 83 |
| 3.8 | Weibull statistics of the strength of the material without (a) and with (b) silane treatment. | 83 |
| 3.9 | Comparison of Weibull statistics for the material without and with silane treatment. | 84 |
| 3.10 | Fracture surfaces with and without silane | 85 |
| 3.11 | Evolution of the material strength against particle volume fraction. | 85 |
| 3.12 | Evolution of the material strength against particle size. | 86 |
| 3.13 | Dimensions of the SEVNB sample from standard ISO 23146. | 87 |
| 3.14 | SEVNB test setup and notch dimensions | 88 |
| 3.15 | Toughness average and standard deviation for the material without and with silane treatment. | 89 |
| 3.16 | Imperfect interface modelled by a linear spring | 90 |
| 3.17 | Strain concentration in the inclusion. | 93 |
| 3.18 | Microstructure of the composite: the different phases | 95 |
| 3.19 | Traction-separation laws | 97 |
| 3.20 | Displacement fields of the RVE with particle debonding | 99 |

| | | |
|------|---|-----|
| 3.21 | Typical tress-strain curve for RVE with particle debonding (1) particles are perfectly bonded, (2) particles start to debond, (3) particles are completely debonded. | 99 |
| 3.22 | Displacement field of the RVE with particle debonding | 100 |
| 3.23 | Displacement field of the RVE with particle debonding | 100 |
| 3.24 | Stress-strain curves for RVE with particle debonding generated with different algorithms | 101 |
| 3.25 | Stress-strain curves for RVE with particle debonding (Dropping and Rolling soft walls, monodisperse particles $R=80\mu\text{m}$) - Particle volume fraction effect. 101 | |
| 3.26 | Stress-strain curves for RVE with particle debonding (Dropping and Rolling soft walls, particle volume fraction $\phi=0.3$) - Particle size effect. | 102 |
| 3.27 | Stress-strain curves for RVE with particle debonding generated with different algorithms | 103 |
| 3.28 | Stress-strain curves for RVE with particle debonding (Dropping and Rolling soft walls, particle volume fraction $\phi=0.3$, $R=80\mu\text{m}$) - Effect of interface parameters | 104 |
| 3.29 | Stress-strain curves for numerical simulations (circles) and for the homogenisation model (continuous lines) for different volume fractions ($R = 40\mu\text{m}$). | 105 |
| 3.30 | Stress-strain curves for numerical simulations (circles) and for the homogenisation model (continuous lines) for different particle sizes ($\phi = 0.3$). 106 | |
| 3.31 | Stress-strain curves for the homogenisation model for different volume fractions ($R = 40\mu\text{m}$) with matrix damage introduced. | 107 |
| 4.1 | Spherical particle embedded in a cylindrical matrix; geometric reduction of the problem using symmetries. | 112 |
| 4.2 | Bilinear Cohesive Zone Model. | 112 |
| 4.3 | Geometry, mesh and loading conditions of the spherical particle debonding study with the CZM. | 113 |
| 4.4 | Load-displacement and pressure-dilatation curves of an elastic body before and after crack propagation | 117 |
| 4.5 | Debonding of a particle under hydrostatic loading before and after crack propagation | 118 |
| 4.6 | Critical remote stress responsible for first debond against particle radius under hydrostatic tension | 119 |
| 4.7 | Debonding of the particle under uniaxial tensile loading | 120 |
| 4.8 | Normalised energy release rate against debonding angle for different particle sizes | 121 |

| | | |
|------|---|-----|
| 4.9 | Local stress fields around the particle (for an arbitrary remote stress of 90 MPa). | 122 |
| 4.10 | Remote critical stress against debonding angle for the energy and the stress criteria for different particle sizes. | 122 |
| 4.11 | Critical remote stress responsible for first debond against particle radius under uniaxial tension | 123 |
| 4.12 | Critical remote stress against particle radius for different CZM parametric analysis | 125 |
| 4.13 | Equivalent stress concentration around the particle and size of the process zone, the time step before debonding onset. | 126 |
| 4.14 | Boron Carbide (B_4C) particle embedded in the epoxy matrix observed with SEM. | 127 |
| 4.15 | Rotations of the angular particle from 0° to 90° | 128 |
| 4.16 | Geometries of embedded particle (circular and angular). | 128 |
| 4.17 | Geometry, mesh and loading conditions of the angular particle debonding study with the CZM. | 129 |
| 4.18 | Critical remote stress against particle (equivalent) radius for the circular and angular (0° rotation) particles. | 129 |
| 4.19 | Critical remote stress against particle (equivalent) radius for the circular and all the angular (0° to 90° rotation) particles. | 130 |
| 4.20 | Critical remote stress against rotation angle for angular particles | 130 |
| 5.1 | Indentation sample (Al_2O_3 F20 $\phi = 50\%$). | 134 |
| 5.2 | 3-part mould for indentation samples. | 135 |
| 5.3 | Digital Image Correlation for the indentation tests. | 136 |
| 5.4 | Fractured samples under monotonic indentation | 137 |
| 5.5 | Monotonic indentation - Effect of particle volume fraction | 138 |
| 5.6 | Monotonic indentation - Effect of particle size | 139 |
| 5.7 | Monotonic indentation - Effect of matrix material | 140 |
| 5.8 | Monotonic indentation - Effect of particle material | 141 |
| 5.9 | Monotonic indentation - Effect of silane treatment | 142 |
| 5.10 | One cycle of indentation, complete load and unload. | 142 |
| 5.11 | Schematic representation of the cyclic indentation with a spherical indenter. | 143 |
| 5.12 | Cyclic indentation with unloading fit - Contact radius determination | 143 |
| 5.13 | Cyclic indentation force-displacement curve. | 147 |
| 5.14 | Fitting parameters of the unloading phases | 148 |
| 5.15 | Indentation Young's modulus and Brinell hardness against cycle number | 149 |

| | | |
|------|---|-----|
| 5.16 | Effect of particle volume fraction on indentation Young's modulus, Meyer's hardness, and Brinell hardness. | 149 |
| 5.17 | Effect of particle volume fraction on Brinell hardness for samples with polydisperse alumina particles. | 150 |
| 5.18 | Effect of particle size on indentation Young's modulus, Meyer's hardness, and Brinell hardness for alumina particles. | 151 |
| 5.19 | Effect of particle size on indentation Young's modulus, Meyer's hardness, and Brinell hardness for boron carbide particles. | 151 |
| 5.20 | Effect of matrix material on indentation Young's modulus, Meyer's hardness, and Brinell hardness | 152 |
| 5.21 | Effect of particle material on indentation Young's modulus, Meyer's hardness, and Brinell hardness | 152 |
| 5.22 | Effect of particle silane treatment on indentation Young's modulus, Meyer's hardness, and Brinell hardness | 153 |
| 6.1 | Section view of the impact test setup. | 157 |
| 6.2 | Sabot drawing. | 157 |
| 6.3 | Sabots made from PVC, PMMA, and PC. | 158 |
| 6.4 | Sabots after impact. | 158 |
| 6.5 | Impact sample (Al_2O_3 mix $\phi = 60\%$). | 159 |
| 6.6 | Tension signal given by the gauge bridge during impact. | 160 |
| 6.7 | Impact force-time curves. | 161 |
| 6.8 | Force and energy transmitted to the bar against time. | 162 |
| 6.9 | Pictures of the penetration process for shot 1. | 162 |
| 6.10 | Pictures of the penetration process for shot 2. | 163 |
| 6.11 | Pictures of the penetration process for shot 3. | 163 |
| 6.12 | Post failure pictures of sample (Al_2O_3 mix $\phi = 60\%$) shot 1. | 164 |
| 6.13 | Post failure pictures of sample (Al_2O_3 mix $\phi = 50\%$) shot 2. | 164 |
| 6.14 | Post failure pictures of sample (Al_2O_3 mix $\phi = 30\%$) shot 3. | 165 |
| A.1 | Forces acting on the sample for density measurement | 185 |
| A.2 | Mass determination of the immersed sample. | 186 |
| B.1 | Equivalent stress concentration around the particle and size of the process zone, the time step before debonding onset. | 187 |
| B.2 | Equivalent stress concentration around the particle and size of the process zone, the time step before debonding onset. | 188 |
| B.3 | Size of the process and damaged zones for different particle sizes. | 189 |

| | | |
|-----|---|-----|
| C.1 | Critical remote stress against particle radius for different CZM parametric analysis | 191 |
| C.2 | Traction-separation laws for different interface stiffness | 192 |
| C.3 | Effect of the interface stiffness on the debonding onset of a spherical particle. | 192 |
| C.4 | Effect of interface strength and fracture energy on debonding | 193 |
| C.5 | Effect of elastic moduli of the phases on debonding | 194 |
| D.1 | Fracture surfaces of specimens with Al_2O_3 particles (camera). | 196 |
| D.2 | Fracture surfaces of specimens with Al_2O_3 particles (optical microscope). . | 197 |
| D.3 | Fracture surfaces of specimens with $\phi = 60\%$ of mixed B_4C particles (camera). | 197 |
| D.4 | Fracture surfaces of specimens with $\phi = 60\%$ of mixed B_4C particles (optical microscope). | 197 |

List of Tables

| | | |
|-----|---|-----|
| 1.1 | Mechanical properties of materials used for armouring | 8 |
| 1.2 | Effect of microstructural parameters on the mechanical parameters of particle reinforced polymers | 23 |
| 2.1 | Mechanical properties of Al_2O_3 and B_4C | 38 |
| 2.2 | Grit sizes of ceramic particles. | 38 |
| 2.3 | Composition and cure of the epoxy resins. | 40 |
| 2.4 | Properties of the epoxy resins. | 41 |
| 2.5 | Geometrical capacities of the microstructure generation algorithms. | 52 |
| 2.6 | Imposed displacements for the PBC, 3 different loading cases. | 60 |
| 3.1 | Mechanical properties of materials used for armouring | 105 |
| 4.1 | Mechanical properties of the materials | 112 |
| 4.2 | CZM properties | 125 |
| 6.1 | Summary of impact tests | 161 |
| C.1 | CZM properties | 190 |

Introduction

Background of the project

The present work focuses on polymers reinforced with a high content of ceramic particles that may represent an interesting alternative to the classical design of ceramic layers used as front-face armours for ballistic protection. In this framework the main purpose of this thesis is to evaluate the performance of this type of material and the influence of various microstructural parameters on its overall mechanical behaviour. A particular emphasis is placed on the role of particle/matrix adhesion as it can drastically alter the mechanical performances of such a material.

The idea of using particle reinforced polymers for ballistic protection was initiated in Oxford Brookes University at the Joining Technology Research Centre, where a reliable manufacturing process has especially been developed in order to obtain composites reinforced with a high volume fraction of hard particles. Previous studies on the material revealed the importance of particle/matrix interfaces and various particle surface treatments were tested to enhance the adhesion between the two phases. In particular, the silane treatment induced substantial improvements in the mechanical behaviour of the material. In order to deeply analyse the particle/matrix interface phenomena, a collaboration between Oxford Brookes University and the I2M (*Institut de Mécanique et d'Ingénierie*) of Université de Bordeaux was then developed to benefit from the I2M expertise on joining technologies and interface problems and especially on modelling.

This thesis is part of this international collaboration. It has then been conceived as a *cotutelle* between Oxford Brookes University and the Université de Bordeaux. Half of the project has been developed in England, where the manufacturing process of the material was studied and where various mechanical tests have been carried out. The other half of the thesis took place in France where analytical and numerical models were elaborated and empirical methods were developed to study the penetration of the materials at different loading rates.

The thesis benefited from the UK-France PhD scheme that aims to develop research in key areas of mutual interest to France and the UK. This programme is jointly managed

by Dstl (Defence Science and Technology Laboratory) and DGA (Direction Générale de l'Armement). The DGA has provided the totality of the funding for this project.

Context of the study

Ceramic materials exhibit very good mechanical properties for ballistic protection. They are both very hard (a property that gives them the ability to break and fragment different types of projectiles such as bullets, debris, fragments) and lightweight. Weight reduction has always been one of the main preoccupations for the armouring industry. Lighter armour gives soldiers and vehicles an increased mobility. Cost is also a very important parameter while manufacturing armour. Different types of ceramics, with varying mechanical properties, densities and costs, have been used ranging from alumina to boron carbide.

These ceramics are mainly used as front face layers backed with a more ductile material to absorb the kinetic energy of the impact and the fragments generated during this impact. The tiles used for front face layers are commonly manufactured using a sintering process. High pressure and temperature are applied to ceramic powders to agglomerate them. This manufacturing process exhibits several drawbacks such as high costs and limited geometries (shape and size), while some armouring parts have complex designs (see Fig. 1). Monolithic ceramics also show weak multi-hit resistance because of their inherent brittleness.

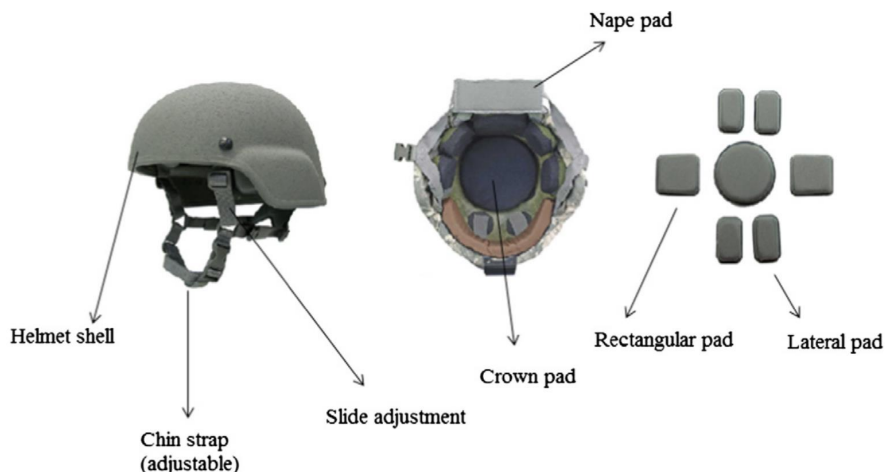


Figure 1: Advanced Combat Helmet design (from [83]).

A possible way to overcome these issues might be to develop a new material based on a moulding manufacturing process, in which ceramic particles are mixed with an epoxy resin. The resulting material can be moulded polymerised to obtain structural elements

of this new composite material. In order to obtain a material with interesting mechanical properties for ballistic protection, as much ceramic particles must be introduced into the material. Varying types of ceramic particles (alumina or boron carbide), varying contents of particles, or varying particle sizes can be used to create the material. Does this material still have interesting mechanical properties for ballistic applications? Are we able to evaluate the effect of the different microstructural parameters evoked previously on the mechanical behaviour of the material? These are the questions we have tried to answer with the present study.

Definition of the problem

As the material developed for this study is quite innovative, an important lack of knowledge was observed. First, this kind of materials has rarely been used for ballistic protection and only few published studies provide insights on its mechanical performances under ballistic impact. Secondly, even at the quasi-static loading regime, the bibliographic resources on the behaviour of such a material are quite scarce. Indeed, even though the reinforcement of polymer materials with hard particles is quite a common practice (e.g. for stiffness or toughness enhancement, or abrasion capacities), a majority of the studies are limited to low to moderate particle volume fractions.

The consequence of such an observation is that, in order to understand the very complex mechanisms occurring during a ballistic impact, the behaviour of the material under much simpler and uncoupled loadings must first be evaluated. For this reason, a large part of the study is devoted to the observations and the modelling of the particle reinforced composite under quasi-static loadings. Even at this regime, complex phenomena deserve attention and must be analysed.

Furthermore, the study takes into account the different working-scales of the material and attempts to create transitions between them through homogenisation techniques. The different scales considered for this study are (Fig. 2):

- the micro-scale, where the effects of the whole microstructure are taken into account. This scale shows strong heterogeneities due to high mechanical contrast between the phases. The adhesion between the components also plays a preponderant role;
- the macro-scale, where the material is considered to be homogeneous and only the overall mechanical properties are evaluated. The local properties of the material components however have an influence on the behaviour of the material and can for example induce anisotropy;
- the meso-scale, where the different phases are taken into account but no field (stress,

strain, etc.) fluctuations are considered. This can be introduced as a link between the micro and the macro-scales.

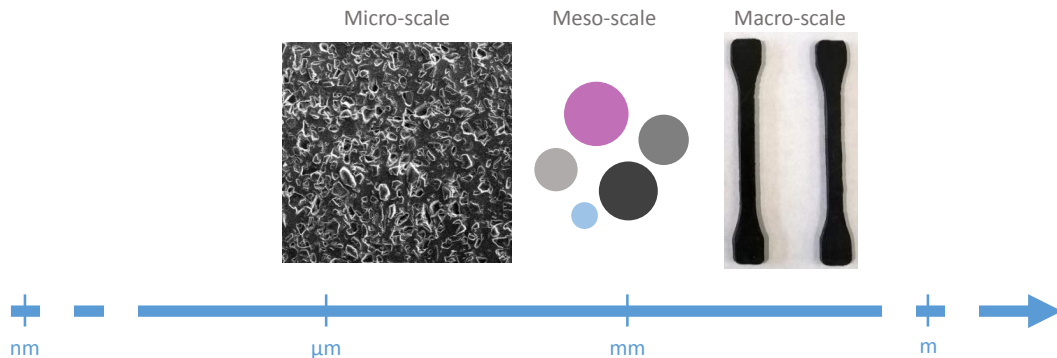


Figure 2: Different scales introduced for this study.

The main scientific difficulties pinpointed for this study consist in the modelling of interface phenomena between the particles and the matrix, the description of a significant scale effect, especially for particle/matrix debonding and the development of experimental methods adapted to evaluate the resistance to penetration of the particle reinforced composite under quasi-static and ballistic loading conditions.

Content of the thesis

To overcome the scientific obstacles observed, multiple actions were undertaken to evaluate the mechanical properties of such a material and the influence of morphological parameters. In the first Chapter of the thesis, a bibliographic review is conducted on the materials used for armouring and the material properties associated to ballistic efficiency. The different stress states observed during a ballistic impact are analysed. A particular emphasis is given to particle reinforced materials and the relationships between their microstructures and their mechanical properties.

The second Chapter of the thesis focuses on two aspects. First, the ceramic particle reinforced polymer developed for this study is described based on its components properties, its manufacturing process, and its microstructure. Then, the elastic properties of the material are determined in three different ways: experimentally using tensile tests, analytically with homogenisation models, and numerically by developing a specific homogenisation procedure based on the generation of random synthetic microstructures and using the strain energy resolution of the problem.

The third Chapter is devoted to the description of the material failure under quasi-static loading. First, appropriate experimental means are developed. The effect of particle/matrix enhancement with a silane coupling agent is also studied. Then, analytical

homogenisation schemes are enriched and numerical models are implemented in order to describe one of the main failure mechanisms observed: particle debonding.

The fourth Chapter focuses on the particle size effect on debonding. This aspect is precisely described by studying a single isolated particle and its debonding under a remote loading. Two approaches are developed: an analytical derivation using Finite Fracture Mechanics and a numerical simulation with Cohesive Zone Models. This study is first conducted on a spherical particle. The effect of the geometry of the particle is then taken into account by introducing an angular particle.

The fifth Chapter describes the resistance of the particle reinforced material to quasi-static penetration. To do this, monotonic and cyclic indentation tests were developed. Adequate post-processing methods are implemented to extract multiple mechanical properties (resistance to penetration, hardness, stiffness). The effect of various morphological parameters (such as particle volume fraction and size, type of reinforcement, or particle/matrix interface enhancement) are estimated.

Finally, the sixth Chapter presents the last developments made to experimentally observe the impact resistance of the particle reinforced material. The setup consisting of a gas canon is described in detail. The test is specially designed to carry out impact tests at a very high loading rate (up to several hundreds of meters per second). A Hopkinson bar instrumented with strain gauges is used as a dynamic load sensor to evaluate the energy dissipated by the material during the impact.

Chapter 1

Literature review: Ballistic performance of ceramics and particle reinforced materials

1.1 Monolithic ceramics applied for ballistic protection

Over the years, many different techniques have been developed to ensure individual protection of soldiers or vehicles. Since the beginning of the XXe century, steel plates have been employed, but the only way to improve protection was to increase the thickness of the metal layers. The consequence was a significant weight increase, which was detrimental for the mobility of both individuals and vehicles. Such a solution was employed up to World War I, where rolled steel thick plates were mainly employed for vehicle protection [2]. Subsequently, during World War II, different alloys had been developed in order to attain greater levels of hardness: manganese was added to the steel and lighter aluminium alloys were used too [2].

Since the 50's and the 60's, ceramic materials have been introduced in ballistic protection plates for a multiple of reasons: they are very hard and stiff, they show incredible compressive strengths, they are very lightweight and, due to this combination, they are able to erode or to fragment the projectiles [122]. However, there are severe drawbacks including relatively low tensile strength and low toughness. Because of their brittle nature, ceramics are rarely used alone [2]. Dual-hardness armours was a big step in improving ballistic efficiency and reducing weight of armours (see Fig. 1.1). The front face, a tile made of very hard material (e.g. ceramics), is backed with a ductile material layer. The latter is called “backing” and is commonly made of fibrous composites or metallic ma-

materials such as aluminium. The ceramic front face aims to blunt or break the tip of the projectile and to spread out the energy of impact over a larger area of backing material by forming a cone shaped cracking zone. The role of the backing is then to absorb the remaining kinetic energy that has not been dissipated by the ceramic and to decelerate the fragments of projectile. On ballistic impact, the resulting angle of the fracture conoid relies on many factors, such as dynamic loading and mechanical properties of the target, but is in general close to 65° [75].

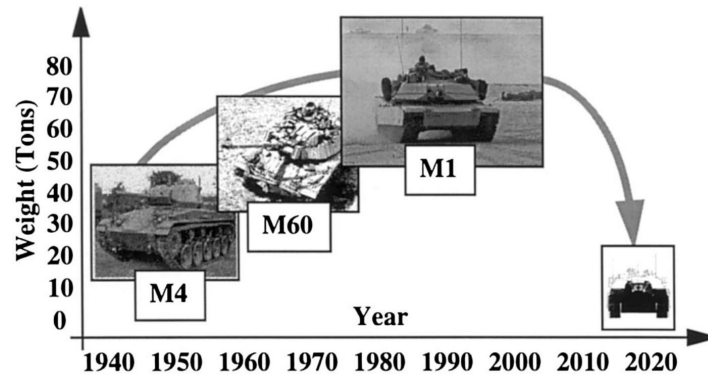


Figure 1.1: Radical weight reduction for future ground vehicles (from [20]).

The impact between a projectile and a ceramic armouring plate can be divided into three distinct phases [163], that are schematised in Fig. 1.2:

- (a) Immediately after the impact, a divergent hydrostatic compressive wave propagates through the ceramic. The loading rate and level are extremely high and they can trigger local damage mechanisms (micro-plasticity or micro-cracking). This phase results in an intense fragmentation of the ceramics.
- (b) In the wake of the passage of the compressive wave, the material is radially dilated, and a new compression/bi-tension wave propagates. It is responsible of orthoradial tensile stress fields that causes the onset of numerous and oriented cracks.
- (c) Finally, the projectile (or its fragments) penetrates in the fragmented ceramic. The penetration of the projectile depends on the properties of the fragmented ceramic such as the size and the mobility of the fragments. When only a layer of ceramic is employed, the compressive waves can be reflected on the back-face of the ceramic as tensile waves and spalling of the material eventually occurs.

It is then clear that multiple loading conditions are responsible for the failure on the front-face layers under impact. All of them induce different damage mechanisms and they are to be accounted for in order to understand the performances of such materials.

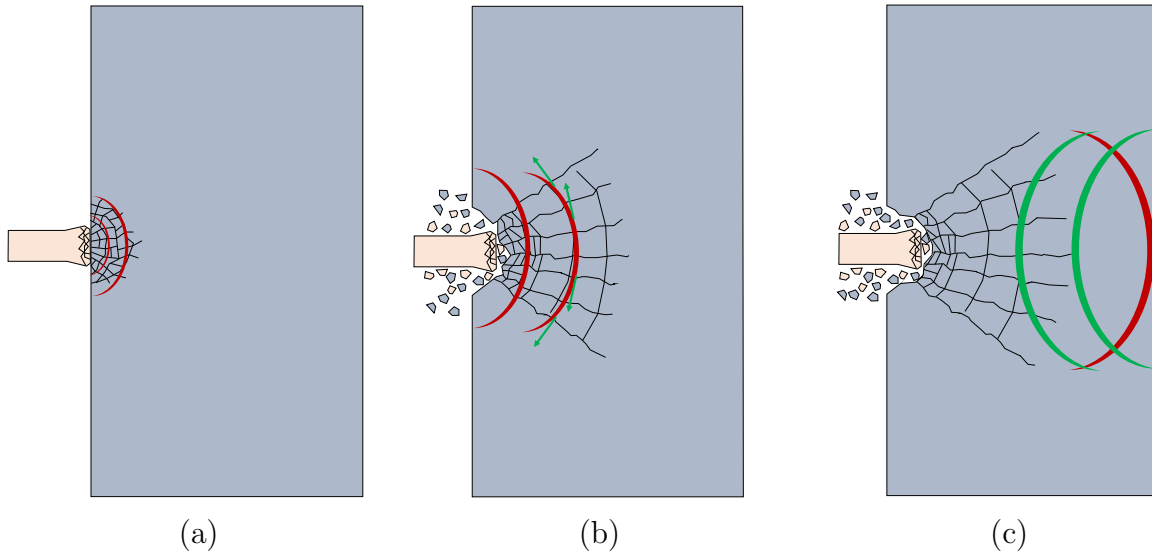


Figure 1.2: Successive loading conditions during an impact, due to hydrostatic compression (a), compression/bi-tension (b), penetration of the projectile and fragments and eventual spalling (c).

Today, the the most common materials used as ceramic armouring plates are Alumina (Al_2O_3), Silicon Carbide (SiC) and Boron Carbide (B_4C) [163]. Sometimes, Aluminium nitride (AlN) or titanium diboride (TiB_2) are also employed. All of them show increased stiffness and hardness compared to steel. The mechanical properties of multiple types of ceramics compared to steel are shown in Table. 1.1 [11].

| Mechanical properties | Steel | Al_2O_3 | SiC | B_4C |
|--|-------|-----------|-------|--------|
| Density ρ [g/cm^3] | 7.82 | 3.9 | 3.0 | 2.52 |
| Young's modulus E [GPa] | 206 | 407 | 350 | 450 |
| Tensile strength σ_{maxt} [MPa] | 1500 | 220 | 440 | 350 |
| Compressive strength σ_{maxc} [MPa] | 1500 | 2500 | 2500 | 2900 |
| Hardness HV [GPa] | 5.38 | 18 | 20 | 28 |

Table 1.1: Mechanical properties of materials used for armouring

1.2 Particulate reinforced materials applied for ballistic protection

Ceramics faced armours have proved their efficiency against the impact of low and medium calibre projectiles [122]. However, this technology also exhibits several drawbacks and there is still need for the development of a new material able to replace ceramic front tiles

[10].

First, structural ceramics used for these applications often impart higher costs that might be prohibitive for certain applications [10]. The sintering process used to manufacture ceramic tiles is also not completely satisfactory, not least because the geometries obtained with this manufacturing process are limited in terms of shapes and of size [123]. An assembly of multiple tiles is commonly employed to overcome this issue. It is also a way to increase the multi-hit capability of such materials, which is one the greatest drawbacks of ceramics [2]. The traditional method to create a ceramic armour able to withstand multiple impacts is to use multi-tile configurations with hexagons or squares of different sizes [2]. Reducing the size of the tiles also affects the damage spread, resulting in a decreased capacity to absorb energy [61].

Several authors have attempted to create new materials as a replacement for monolithic ceramics as front-face layers. Some of them proposed to use composite materials that combine ceramics with more ductile materials, especially to increase the multi-hit capacity of the armour [2]. The first development was proposed by [82]. They developed a gradient design armour with alumina spheres embedded in an epoxy matrix. Spheres of different sizes were employed in order to increase the ceramic content of the composite. The ceramic spheres, that are very hard compared to the matrix, have the capability of defeating the projectile, with a reduced fragmentation after impact. [70] developed a model able to estimate the behaviour of this class of materials under impact.

Arias et al [10] developed a low-cost manufacturing process of ceramic/polymer composites. They introduced angular alumina particles, that are cheap and readily obtainable as an abrasive product. Different sizes of alumina particles were also employed to reach higher volume fraction. Once the ceramic particles and the epoxy resin are blended together, the mixture is moulded under pressure, and the resin is cured. They used depth of impact (DOP) tests to estimate the efficiency for ballistic protection of such a material. A behaviour halfway between metals used for ballistic applications and monolithic ceramics was found. The efficiency was also increased when large ceramics particles with dimensions comparable to the ones of the impactor were used.

Naebe et al [106] also studied the behaviour of composite armours reinforced with ceramic particles. The manufacturing was also compression moulding. They observed the effect of the different components introduced into the composite materials: two types of resins (phenolic and epoxy) and two types of ceramic particles (cubic boron nitride - cBN and boron carbide - B_4C). The ballistic limit of the materials was used to test the efficiency of the materials. They observed that cBN and the phenolic resin showed slightly better results compared to B_4C and epoxy, in accordance with the fact that they individually have higher mechanical properties. The composite material was also observed to have a similar ballistic limit as standard aramid composites when normalised with their

areal densities. It also had a favourable multi-hit capability.

[123] developed a composite material made of angular boron carbide particles embedded in an epoxy matrix. They mechanically tested the behaviour of such a material and stated that one of its main limitations was the lack of adhesion between the particles and the matrix. They found that a proper particle surface treatment with silane was able to considerably enhance the adhesion between the two components.

Some patents have been filed for armour systems incorporating ceramics/polymer assemblies.

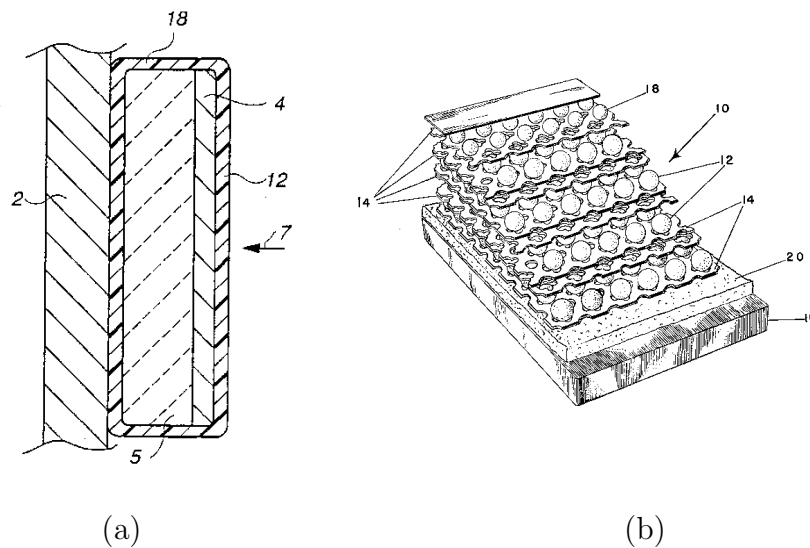


Figure 1.3: (a) Constraint cell of ceramic particles mixed an epoxy resin (from [127]); (b) Armour design with ceramic spheres restrained by interwoven layers (from [25]).

1.3 Experimental determination of ballistic efficiency of ceramics

The design of armour was traditionally carried out experimentally [2], based on the testing of the armour with real threats. This method is very reliable but also very expensive because the tests must be repeated for all the types of service conditions, impactors velocities and armour types. Another major inconvenience is the lack of understanding of damage mechanisms occurring during high velocity impacts. To obtain meaningful information as target deformation or position of the impactor during penetration, specific data acquisition systems and test methods have been developed.

The fundamental task to be conducted for correct armour design consists in the determination of the coating thickness and the material employed to stop the projectile.

The ballistic limit might then be defined as the “minimum velocity at which a particular projectile is expected to completely penetrate an armour” or the “maximum velocity at which the projectile is expected to fail to penetrate an armour” [2]. This ballistic limit is often determined as the impactor velocity with an associated probability of penetration equal to 50%. This limit is generally denoted V_{50} .

The ballistic efficiency of a ceramic material is commonly determined using DOP (Depth Of Penetration) tests [124]. The DOP test is characterised by two steps: first the impactor is shot onto a thick reference backing material (usually aluminium or clay), then the impactor is shot into the same backing but covered with a ceramic front layer (see Fig. 1.4). The relative penetration varies with the efficiency of the ceramic front face. However, this type of test only allows for a qualitative comparison of ceramics, and no material property can be determined [163].

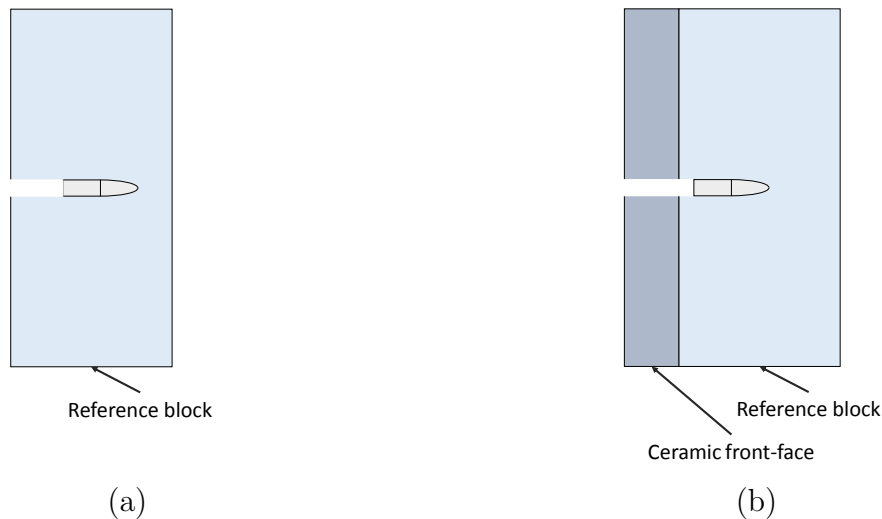


Figure 1.4: Depth Of Impact test setup with the reference configuration (a) and the test with ceramic target (b).

Other experimental means have then been used to dynamically characterise ceramic materials. The Hopkinson bars technique has been developed to determine the dynamic uniaxial compression limit of a material. A cylindrical bar is projected to impact the sample to be tested. The loading wave is transmitted to the sample and then to a transmission bar. Both bars need to be long enough to eliminate any reflections. For materials with very high elastic limits such as ceramics, the dimensions of the sample must be very small to reach the elastic limit. This is one of the main limitation of this technique [163].

The spherical expansion tests were developed to obtain a triaxial compression state in the material followed by a compression/bi-tension as the compression wave propagates, a loading close to the one observed around the impact location (see Fig. 1.5). An intense

fragmentation is observed around the centrally located explosive whereas long oriented cracks are observed away from it. To obtain such a loading, an explosive material is detonated at the center of a face of the material to be tested. The main issues with this test are that the loading conditions are not precisely controlled and that large dimensions for the block of ceramics are required.

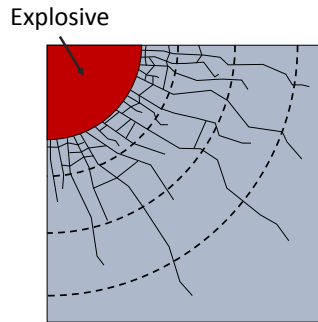


Figure 1.5: Spherical expansion test setup.

Plate impact tests are used to characterise the confined compressive behaviour of a material. An impactor plate is projected onto a target plate (see Fig. 1.6). A uniaxial deformation state is generated at the impact and propagates through the plates. The loading is controlled as the intensity of the loading depends on the kinetic energy of the impactor plate and duration of the impact depends on the thickness of the impactor plate. It is also possible to determine the tensile performances of the material if the back of the target plate is free, which causes reflection of the compressive waves into tensile ones and spalling of the target plate is then observed.

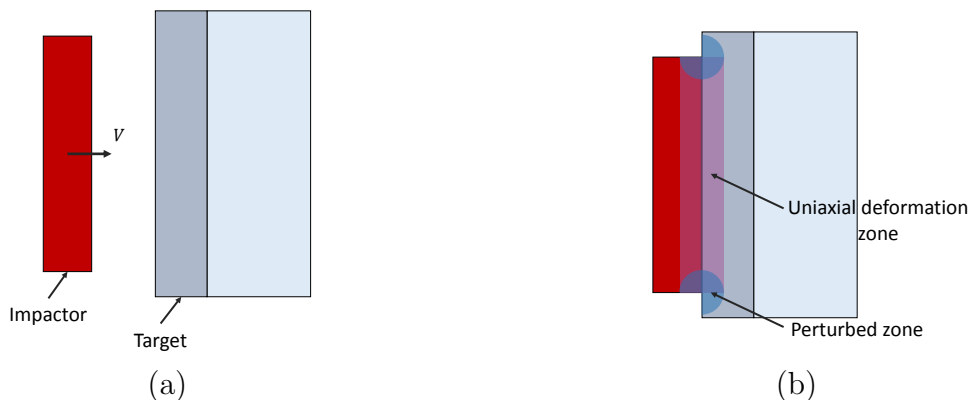


Figure 1.6: Plate impact test setup represented before (a) and during impact (b).

Edge-on impact tests have been developed to determine the fracture mechanisms and to visualise the fragmentation process of brittle materials during an impact [32]. A cylindrical projectile hits a ceramic tile on its edge. The compressive wave propagating within the target induces a radial motion of the matter generating an intense damage of the

ceramics 1.7. The damage mechanisms observed during these types of tests are very similar to the one observed during real impacts [33]. An open or close configuration with a confinement have been developed, the second one allowing to keep all the fragments together.

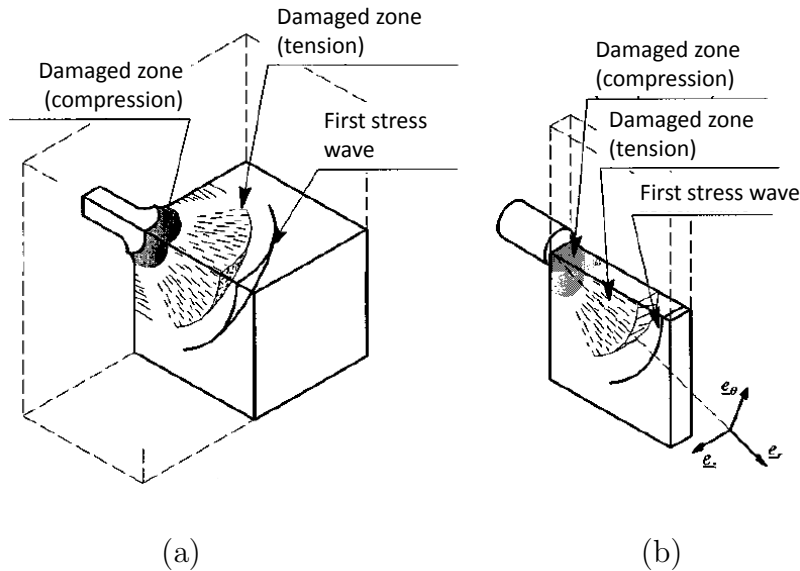


Figure 1.7: Representation of the damage during a ballistic impact test (a) and Edge On Impact test (b) (adapted from [31]).

1.4 Relationship between quasi-static behaviour and ballistic efficiency of ceramics and particle reinforced materials

The ability of a material to be efficient for ballistic protection depends on its mechanical properties. However, the relationship between individual material property and its protection capability is far from straightforward, especially because ballistic impacts involve many different damage mechanisms at all scales, from the localised triaxial compression around the impact point to spalling due to stress waves reflections.

1.4.1 Monolithic ceramics

Multiple mechanical parameters have an influence on the ballistic efficiency of a material. Only material properties and not structural ones will be considered here. Concerning ceramics used for personal body armour, the effects of the following mechanical parameters have been observed in the literature.

Hardness

Numerous studies tend to show that hardness of the ceramic is the predominant parameter governing its resistance under impact [163]. For each ceramic grade, there is a strong experimental correlation between its hardness and its ballistic efficiency (see Fig. 1.8). The hardness of ceramics must be high enough compared to the impactor in order to blunt or destroy the impactor tip [122]. Indeed, blunted or fragmented impactors have a greatly reduced capacity to penetrate into armours.

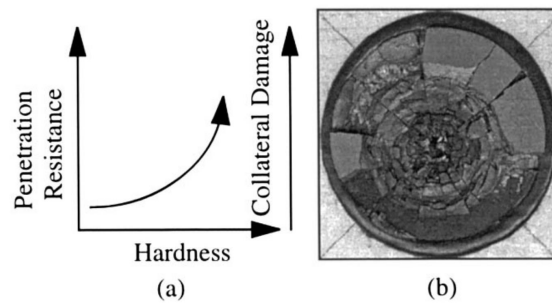


Figure 1.8: (a) Typical trend in armour ceramics. (b) Typical collateral damage on armour ceramics suffered from a ballistic impact (from [20]).

Compressive and shear strength

Shockey et al [133] have stated that the compressive strength of ceramics is related to their initial resistance to penetration. Indeed, the compressive strength helps defeating the projectiles, by fracturing, deforming or deflecting them [75].

Also, large stress gradients exist between the area directly underneath the projectile loaded in compression and in tension around the contact area. Therefore, a high yield stress helps the material to resist the failure caused by the large shear stresses generated near the impact site [155].

Elastic moduli

According to [155], the elastic moduli of the ceramic material such as Young's, bulk or shear moduli are important to defeat a projectile. Indeed, these properties help to resist the deformations induced by the projectile.

Hugoniot elastic limit

The Hugoniot Elastic Limit (HEL) is the uniaxial yield stress when the material undergoes high rate loadings. When the dynamic stress exceeds the HEL, several compressive

damage mechanisms can be triggered such as micro-plasticity or micro-cracking. This limit is typically exceeded during the initial moments near the impact location, where high triaxial compressive states are observed [163]. Materials loaded above the HEL may exhibit a significant loss of yield strength.

Toughness

The toughness of a material is defined as its ability to resist crack propagation. Because of the inherent brittleness, ceramics commonly show very low toughness values and long radial cracks are observed away from the impact location. A higher toughness will increase the multi-hit resistance capacity of an armour [11].

Weibull parameters

The fragmentation behaviour of ceramics is highly dependent on its Weibull modulus. A high Weibull modulus leads to a deterministic failure of the material while a low one coincides with a probabilistic failure. A low Weibull modulus is then detrimental for the quasi-static failure of the material. However, for high velocity impacts, a low Weibull modulus provides a good sensitivity of the strength to loading rate and to generate a lower crack density, creating larger fragments [163].

1.4.2 Particle reinforced materials

As seen previously, several authors tried to reinforce materials with ceramics particles in order to obtain more efficient materials against ballistic threats. As explained beforehand, multiple mechanical parameters are involved in the ballistic efficiency of a material. They have been described for monolithic ceramics and can be extrapolated to particle reinforced materials. However, for ceramic particle reinforced polymers, very few studies were carried out on the relationship between mechanical properties and ballistic efficiency. Specific relationships between the quasi-static and impact behaviour, with a strong focus on the effect of confinement, have been developed for other particle reinforced materials as concrete or ceramic particle reinforced mortars. The complex loadings observed for monolithic ceramics under impact are still valid for these types of materials, however the damage mechanisms observed are very different.

Confined and unconfined behaviour

According to [8], the behaviour under confined compression cannot be deduced a priori from the results of simple compression or bending tests, nor can the ballistic performance of materials.

Triaxial compression tests, called quasi-oedometric tests [45], were developed to observe the mechanical behaviour of such material under confined compressive loadings that are more representative of the loading observed under ballistic impact. The quasi-oedometric test consists of a uniaxial compression of a cylindrical sample confined in a metal vessel. The radial extension is not eliminated but is considerably reduced. The lateral confinement pressure is registered by means of gauges attached to the outer surface of the vessel.

First, the behaviour of cement under unconfined, confined and ballistic loading was observed in [46] and quasi-oedometric results correlated better with impact tests than unconfined loadings. The same study was carried out with cements reinforced with spherical and angular alumina particles in [8]. Both angular and spherical particles have a beneficial effect on the strength under confined compression and act more as reinforcement, whereas the opposite effect is observed in bending and simple compression tests. As for monolithic ceramics, the particle reinforced materials experience high compression loadings under the impact point. The confined compressive behaviour of a material is then important to estimate its ballistic efficiency.

Relationship between microstructure and quasi-static behaviour - confined and unconfined compression

The presence of hard particles has a significant effect on material behaviour. As a first approach, [9] observed correlations between bending and uniaxial compressive loading for spherical and angular alumina particle reinforced cements. They observed a noticeable correlation between the strengths obtained with 3-point bending tests and uniaxial compression for both spherical and angular particles. They also observed that for both types of loading, the cracks originated either from porosities or from particles acting as stress raisers. They concluded that the addition of particles hinder crack propagation (especially angular ones), which increases ballistic efficiency. However with low particle/matrix adhesion many cracks develop from particles that act like defects. For this reason, strength is increased with particle content only when the particle/matrix cohesion is good [8].

For confined compression, with oedometric tests, [47] were able to separate the hydrostatic and the deviatoric behaviour of the particle reinforced cement. For the hydrostatic behaviour, the presence of particles is beneficial because there is less volume reduction observed. For the deviatoric one, they observed noticeable differences with the types of particles employed. In particular, angular particles led to higher strength than spherical particles, and medium-size particles were preferable to small particles. The particle/matrix adhesion enhancement with silica fumes was also beneficial, especially with angular particles. From analysis of the failure mode, it was concluded that spherical

particles acted as crack initiators and higher crack density was observed with spherical particles. Spherical particles were also intact whereas intra-granular cracks were observed with angular particles. This is why angular particles offer enhanced shear performance, but their efficiency is greatly diminished when fractured and/or debonded.

Dynamic and impact loading

For impacts, multiple types of cracks occur. The material is severely fragmented just under the impact location due to triaxial compression, then long radial cracks are observed away from the impact location due to tensile loadings. Both appear at high loading rates. It is then important to test the mechanical properties of particle reinforced material under multiple types of loadings within the dynamic loading range.

For spalling tests representing the tensile waves propagating after impact, [40] observed the effect of aggregate size on the dynamic tensile failure of concrete. They observed a cracking pattern that was mainly inter-granular. The failure was then predominantly governed by the matrix and consequently, the maximum aggregate size appears to play a limited role on the cracking pattern.

Finally, good correlation is seen between confined compression and ballistic efficiency. Bending and uniaxial compression tests however give a good representation of damage mechanisms. So ballistic efficiency seems to be a combination of the results from both confined compression and bending tests [8].

1.5 Properties of particulate reinforced polymers

The use of rigid particles (glass, ceramics, carbon nano-tubes, etc.) to reinforce a polymer is quite common practice now. The effects of rigid fillers on the mechanical properties of the composite material have been extensively studied in the literature from an experimental point of view [50], [110], [53]. The effect of the microstructural parameters such as particle volume fraction, size, shape, or the adhesion between the particles and the matrix on the material behaviour are observed thereafter.

1.5.1 Effect of particle volume fraction

First, the effect of rigid reinforcements on the elastic behaviour of the material is studied. Fu et al [50] wrote a very complete review on the mechanical properties of polymers reinforced with inorganic particles. The effect of particle volume fraction introduced in the material is first studied. As the particles are very stiff compared to the polymeric matrices employed, the more particles are introduced into the material, the higher Young's

modulus is obtained as their load-bearing capability is higher than the one of neat matrix. The composite Young's modulus can be estimated using simple or more complex rules of mixtures based on the individual mechanical properties of the components.

The failure of particle reinforced polymers is characterised by the maximum load that the material can withstand under uniaxial tensile loading, i.e. its strength. The effect of particle volume fraction on strength is still quite unclear as the failure of particle reinforced material is driven by many damage mechanisms depending on loading conditions [50]. The introduction of rigid particles in the material can affect its strength in two ways: either a strengthening effect as the particles have an improved load-bearing capability compared to the polymer or a weakening effect as it induces a reduction of the effective volume of matrix. The strengthening effect is observed when the stresses are effectively transmitted from the matrix to the particles, i.e. when the adhesion between the particles and the matrix is strong. The strength reduction is particularly visible when the adhesion between the particles and the matrix is weak, a situation where the particles act more like defects inside the matrix than reinforcements. The particles might lead to other conflicting effects: for example they can form barriers to crack propagation through microcracking mechanisms but also create significant stress concentrations responsible of the nucleation of new cracks. The strength of a particulate reinforced composite depends on the load-bearing capability of the weakest path throughout the microstructure, rather than the statistically averaged values of the microstructure parameters [50], making it difficult to give universal trends.

Sapnoudakis and Young [140] determined the strength of an epoxy resin filled with glass beads. They treated the particles to increase or lower the adhesion with the matrix. For particles with enhanced interface properties, they obtained a small decrease in strength with increasing particle volume fraction (compared to unfilled epoxy) until a limit value. Above this value, the strength increased and they reached strength values above the one of the unfilled epoxy. However, for particles with weak interface properties, they observed a clear drop in strength and the addition of more particles only had a detrimental effect. For poorly bonded particles, the stress-transfer capacity of interfaces is inefficient (i.e. the particles are unloaded) and the strength of the reinforced polymer decreases with particle content [50].

The toughness of particulate composites is commonly measured using pre-notched specimens where either the stress concentration factor K_c or critical energy release rate G_c is determined. The toughness corresponds to the ability of a material to resist crack propagation. Toughness is observed to increase with particle volume fraction [100], as particles tend to hinder the propagation of a crack by perturbing its path. Generally speaking, toughness is higher for particle reinforced polymers compared to the bulk material because of crack deflection around particles [50]. The following toughening mechanisms have been

observed: crack front pinning [136] where the surface of the crack front is altered by the presence of impenetrable particles and it requires more energy to propagate if the crack front is lengthened by bowing, [139], crack tip blunting through localised shear yielding [139] causing the crack propagation to become unstable rather than continuous, [140] or crack tip twisting and tilting [79] where more energy is consumed for crack propagation as the crack tip geometry is modified. However, several studies found that above a critical value (usually around 30%), the toughness starts to decrease [139] and [77]. This peak value of toughness was explained by [139], where they observed that with high particle volume fractions, there were a lot of particle/matrix interface breakdown, making the crack pinning more difficult and hence reducing the composite toughness.

The toughness of filled epoxy can also be studied under dynamic conditions by using a gas canon to impact a notched specimen [78]. The introduction of rigid inclusions into neat epoxy led to an increase in dynamic toughness and the higher the inclusion volume fraction is, the higher the toughness increases [68]. Higher loading rates also leads to higher toughness values.

The effect of particle volume fraction in the literature is however limited to quite low values of volume fractions as most of the studies consider that particles volume fractions between 10% to 30% are high contents [50], which is considered as very loose granular media.

1.5.2 Effect of particle size

On the elastic properties, [50] first concluded that particle size does not seem to have any effect on the composite Young's modulus as long as the particles are above the nanometric size. This observation is corroborated by many studies such as [67], [68] and [109].

However, the particle size has a significant effect on the strength of the particle reinforced polymer. There is a large improvement in tensile strength with decreasing particle size as demonstrated by [109] for spherical silica particles in an epoxy matrix and by [108] for angular ones. [87] used binary mixes of spherical silica particles of two different sizes to show that the strength increases with increasing surface area of the filler particles. Indeed, for a given particle content, smaller particles have a higher total surface area and provide a more efficient stress transfer mechanism [50].

The toughness increases with increasing particle size as observed with angular silica particles in [107] or with aluminium particles in [136]. The fracture surfaces were observed to be rough for large particles and smooth with small ones. This means that large crack deflections occur with large particles inducing the toughness increase with particle size. Spanoudakis and Young [139] concluded that the highest toughness values were found with the highest volume fractions of the largest particles but that particle size was only

a secondary effect compared to volume fraction.

These observations hold true with micro-scale reinforcements. Under quasi-static loading rate conditions, nano-scale particulate composites show a considerably higher toughness than micro-scale ones, whereas in a dynamic loading rate, they show a slightly lower value than micro-scale ones [68]. This was corroborated by fracture surface observations, where the roughness was higher for nano-scale reinforced materials in the case of quasi-static loading and higher for micro-scale ones in the case of dynamic loadings.

1.5.3 Effect of particle shape

The elastic properties of particulate composites can be affected by the shape of the reinforcements. This is especially true when large particles with high aspect ratios are oriented. The deformation behaviour of the composite material is influenced by this orientation and the material becomes anisotropic. The angularity however does not seem to have an influence on the elastic properties as long as the material is isotropic.

Concerning the strength of composites containing irregularly shaped-particles, it is reduced because of high stress concentrations. This effect is stronger in the presence of sharp corners than for rounded cracks or inclusions [5].

The use of angular particles instead of spherical ones increases the toughness of the particulate composite. This was observed by Moloney and Kausch [100] who determined the toughness of epoxy reinforced with angular alumina and silica particles and compared the values to the one of spherical glass beads. They also stated that the aspect ratio of the reinforcements is an important parameter for the determination of fracture properties. For reinforcements with higher aspect ratios, such as short glass fibres, other toughening mechanisms appear such as fibre pull-out, deformation, and breakage. However, [97] observed no effect of particle shape (between angular and spherical ones) when studying the toughness of alumina filled epoxies.

In the dynamic range, [84] observed the toughness of epoxies reinforced with glass spheres, flakes and rods and concluded that the highest toughness values were obtained with rods followed by flakes and finally spheres. This corresponds to an increase of toughness with reinforcement aspect ratio.

1.5.4 Effect of particle/matrix adhesion

The particle/matrix adhesion can be enhanced with the use of coupling agents. Most of the studies conclude that this enhancement has only a marginal effect on the elastic properties of particle reinforced materials [50]. This is explained by the fact that in the elastic regime, no debonding of particles is observed. However Sapnoudakis and Young

[140] determined the flexural modulus of a glass bead filled epoxy with particles treated with release agent to reduce the interface adhesion on one hand, and with particles treated with a coupling agent to increase the interface adhesion on the other hand. They obtained a noticeable, nevertheless, small increase for the flexural modulus when the adhesion between the particles and the matrix is enhanced.

As in fibre reinforced composites, the quality of adhesion at the interfaces has a crucial impact on the behaviour of particle reinforced composites. The adhesion strength at the interface determines the load transfer between the particles and the matrix [50]. The composite strength is observed to be increased with particle/matrix adhesion. This was observed in Sapnoudakis and Young [140] where for any glass beads volume fraction considered, the strength of the reinforced polymer with enhanced interfaces was above the one with untreated particles that was also above the one of particles treated to have very poor adhesion. Moloney and Kausch [100] made the same observation and explained it by the fact that weakly bonded particles act as sources of inherent flaws provoking crack initiation. As observed previously, the adhesion between the particles and the matrix can change the effect of particle volume fraction or size [50].

Only a marginal effect of the particle/matrix adhesion has been observed for toughness [76]. Moloney and Kausch [100] confirmed that no effect of particle/matrix adhesion is visible on the toughness of epoxies reinforced with alumina particles treated or not with silane.

However, in the dynamic range of loadings, [78] observed that the toughness was strongly affected by particle size when the adhesion between the particles and the matrix is weak, and that it was almost unaffected by particle size when the adhesion is strong. The dynamic toughness is always lower for strong interfaces than weak ones [78] as the toughening mechanisms are modified [79].

1.5.5 Effect of epoxy resin material

The polymer matrix also plays a significant role in the mechanical behaviour of the particulate composite. One property of polymer materials such as epoxy that is irrelevant to ceramic materials is the effect of temperature, especially glass transition temperature T_g . The effect of temperature on the mechanical behaviour of epoxy resins can be determined by Dynamical Mechanical Analysis (DMA) or even Molecular Dynamics Simulations [137], where an equivalence between the viscous effect (time) and the temperature effect is observed (principle of time-temperature superposition). Hence, the temperature and loading rate have a significant effect on the behaviour of polymers.

[81] studied the ultra high strain rate performance of epoxy resins as a function of T_g (or more specifically, the difference between the T_g and the temperature at which a ballistic

impact occurs). The T_g of the epoxy resin was varied using different diamine curing agents. Ballistic impact tests on polymer tiles were carried out at room temperature to determine the V_{50} as a function of T_g . the conclusions were the following:

- When $T - T_g > 0$, the epoxy is in a rubbery state and a constant decrease of V_{50} with decreasing T_g was measured. The material was observed to fail by shearing a plug of polymer resin, and no fracture lines were observed. The fracture being very localised explains the poor resistance to impact of the material in the rubbery state.
- When $T - T_g \approx 0$, a peak of V_{50} is detected. This peak is slightly offset from the exact value of T_g because of heating during impact (by around -25°C). A large cone of failure is observed dissipating a large amount of energy.
- When $T - T_g < 0$, the epoxy is in a glassy state, and the V_{50} is observed to decrease as the temperature differs from T_g before reaching a plateau value. The number of radial cracks increases the more different the temperature is from the T_g . However, a smaller cone of failure is observed compared to when the temperature is close to the T_g .

The modification of the glass temperature transition can then be an interesting feature to increase the impact properties of an epoxy resin, a peak of impact performance being determined around the glass temperature transition.

The addition of ceramic particles in the epoxy might however have an influence on the dynamic mechanical behaviour of the material. This was studied by [97] who conducted a DMA for alumina/epoxy composites. on the first hand, the storage modulus of the composite increased from the initial value of the pure epoxy with particle volume fraction in both the glassy and rubbery state of the polymer. The results were independent of particle size, shape, and size distribution. In the first instance, the composite T_g did not change with filler loading. However, the shear storage modulus-temperature profile exhibited a subtle broadening in the glass transition region and at temperatures slightly above the T_g , with increased filler loading. It was concluded that this effect was due to particle-particle contacts that increase with filler loading.

1.5.6 Summary on the effect of microstructure and constituents properties on particle reinforced polymers

Finally, the particle volume fraction introduced in the material is the key parameter to improve the elastic properties of such a material. The other parameters (particle size, particle shape, and particle/matrix adhesion) only produce low to non-existent effects concerning the elastic response of the material.

The strength, however, relies on many different factors. A first clear effect is the particle size, as the strength significantly decreases with increasing particle size. The effect of particle volume fraction is unclear as it can lead to contrasting variations depending on the properties of the reinforcements employed, i.e. their shape, or the adhesion between them and the matrix. Also, the better the adhesion between the particles and the matrix, the higher the strength.

Multiple phenomena have been introduced to explain the toughness increase with the use of particles as reinforcements (crack deflection, bowing, crack tip blunting). Increasing particle volume fraction and particle size seem to have a beneficial effect on toughness while particle/matrix adhesion does not. However, the toughening mechanisms observed depend on the characteristics of the components, crack front interactions, and the filler/matrix adhesion. The mechanisms responsible for the toughness increase are often triggered by the presence of numerous crack initiators in the material. It is then also clear that high strength and high toughness particle reinforced polymers are mutually exclusive [53].

Finally, the microstructural effects on the mechanical behaviour of particle reinforced polymers are summed up in Table 1.2.

| Effect of / on | Elastic modulus | Strength | Toughness |
|--------------------------------------|-----------------------|-------------------------------|------------------------|
| Increase particle volume fraction | ↗ | Depending on other parameters | ↗ (then possible ↘) |
| Increase particle size | No effect | ↘ | ↗ |
| Angularity | No effect | ↘ | ↗ |
| Aspect ratio | Orientation dependent | Orientation dependent | ↗ |
| Particle/matrix adhesion enhancement | No effect | ↗ | Low effect |

Table 1.2: Effect of microstructural parameters on the mechanical parameters of particle reinforced polymers

1.6 Tools to study the behaviour of a particle reinforced composite

The effect of rigid particles introduction into polymer materials was first experimentally observed. It was possible to determine the effect of multiple material parameters (particle

volume fraction, size, particle/matrix adhesion) on the mechanical properties of a particle reinforced composite. However, the experimental techniques employed are generally time consuming and costly to carry out. Therefore, a large variety of models have been developed in order to predict the behaviour of a composite material based only on the individual properties of its components. The homogenisation techniques of the mechanical properties of composite materials are divided in three categories: phenomenological ones where empirical rules are developed and fitted on experimental results, numerical ones where Finite Elements (FE) computations are employed, and analytical ones based on physical approaches.

1.6.1 Phenomenological models

Based on experimental evidence observed previously, some researchers tried to predict the elastic moduli of particle reinforced materials based on their microstructural parameters. For Young's modulus, it has been previously assessed that the main parameter is the particle volume fraction. Based on this observation, researchers tried to fit experimental moduli. Einstein's equation that is originally derived for the effective shear viscosity for dilute suspensions of rigid spheres, is expressed as follows:

$$E_c = E_m(1 + 2.5\phi) \quad (1.1)$$

This gives a linear relationship between the composite Young's modulus and the volume fraction of particles. This is only valid for very diluted particle volume fractions. Hence Guth added a particle interaction term in Einstein's equation now expressed as a second order polynomial:

$$E_c = E_m(1 + 2.5\phi + 14.1\phi^2) \quad (1.2)$$

Halpin-Tsai developed a semi-empirical relationship that was extensively used in the literature to estimate the elastic properties of particle reinforced composites:

$$E_c = E_m \frac{1 + AB\phi}{1 - B\phi} \quad (1.3)$$

Where A and B are constants that need to be experimentally determined for each type of composite and depend on particle shape and matrix Poission's ratio for A and Young's moduli of particles and matrix for B. Other, more refined, estimates exist in the literature [50], but their main limitation consists in their phenomenological nature, which require the calibration of parameters based on experimental data.

1.6.2 Analytical models

Other estimates have been developed in order to determine the homogenised behaviour of materials based on the mechanical properties of the phases and microstructural information such as reinforcements morphology and distribution. Several levels of complexity could be introduced depending on the types of mechanical behaviours introduced (elastic, nonlinearities, damage) or the microstructural information taken into account. The main advantage of such analytical models consist in their low computational cost compared to numerical approaches presented later.

Elastic behaviour

The first approaches proposed in the literature to determine the elastic properties of heterogeneous materials are mixture laws. In the Voigt model, the phases are supposed to be stacked in series showing the same stress. With this model, the macroscopic homogenised stiffness moduli is equal to the arithmetic average of the modulus of the phases. In Reuss model, the phases are considered stacked in parallel, and sustain the same strain. This model gives an homogenised stiffness equal to the harmonic average of the phases stiffness. Voigt model is an upper bound for the global behaviour of a composite material while Reuss one is a lower bound. These two models are known as first-order bounds of the elastic moduli.

Hashin and Shtrikman [60] established, thanks to the variational principle, that tighter bounds can be obtained. These bounds are well-known especially because it was demonstrated that they are the tightest bounds one can get for composite materials when no additional information on the distribution or orientations of the phases is available. They are second-order bounds of the elastic moduli. Finally, by taking into account morphological information on the constituents such as spatial distribution of the phases, Torquato in [149], developed third-order bounds of the elastic moduli.

Various mean-field homogenisation schemes have been developed based on the classical Eshelby inclusion problem [41], where the stress and strain fields of a single inclusion embedded in an infinite matrix subjected to a remote loading is determined. From this model, homogenisation schemes have been developed (see Fig. 1.9). The simplest model is applicable to low particle volume fraction materials so that no interactions inbetween particles are considered. This is the High-Dilute scheme and is only valid up to very low particle volume fractions. In order to take into account particle interactions and hence be representative of higher particle volume fractions, Mori-Tanaka [101], [13] considered that the remote load applied can be replaced by the load experienced by the matrix phase itself.

For the self-consistent scheme [64], [14] considers the inclusion directly into the ho-

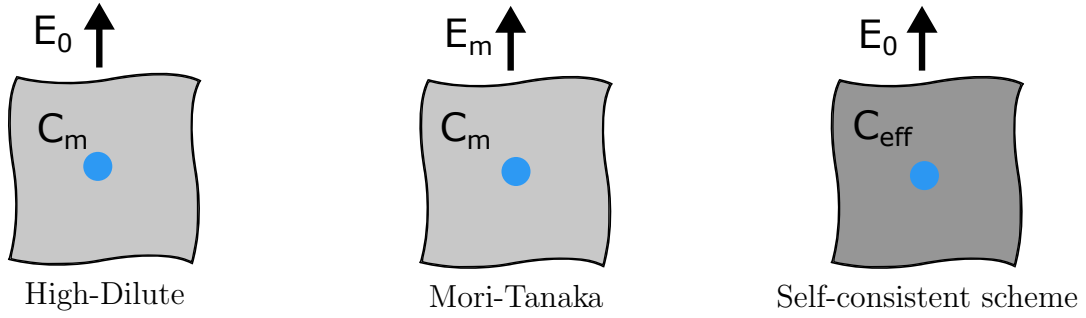


Figure 1.9: Mean-field homogenisation schemes

mogenised material, and this process is repeated for all phases in the material. The equation to obtain the effective stiffness tensor is implicit and is solved with an iterative process. This scheme is particularly efficient when no clear matrix phase is present inside the material, such as polycrystalline materials for example.

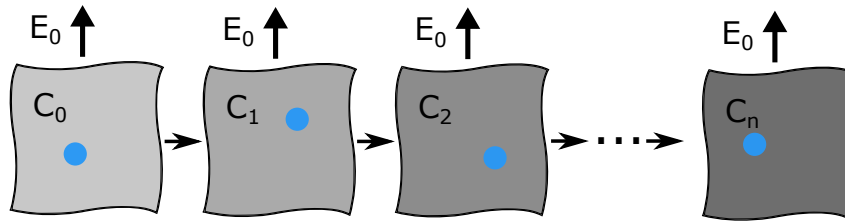


Figure 1.10: Differential scheme

In the differential scheme [112], inclusions are incrementally introduced into the matrix. First an amount of inclusions with a volume fraction $d\phi$ is introduced into the material. The effective stiffness tensor for this composite is calculated with Eshelby's high dilute scheme. Then a new increment of volume fraction $d\phi$ is introduced in the previously homogenised material. This procedure is then repeated until the final volume fraction of inclusions is reached.

Lielens [93] then developed a model where a non-trivial interpolation of Mori-Tanaka and inverse Mori-Tanaka (the materials used as particles and matrix are switched) applicable to higher volume fractions of particles. According to Lielens, very high volume fractions of particles percolate and can be considered as a continuous phase. These homogenisation schemes will be developed more in detail in the next chapter.

Comparisons between the various homogenisation schemes reported have been carried out in this work, and were then compared to results obtained with a numerical homogenisation procedure on a Representative Volume Element (RVE) based on the Finite Elements (FE) method. In Fig. 1.11, results of different homogenisation models are depicted with the evolution of the effective Young's modulus of the composite normalised with the matrix Young's modulus against the volume fraction of inclusions. Here, only spherical particles of same elastic moduli are considered. The numerical homogenisation

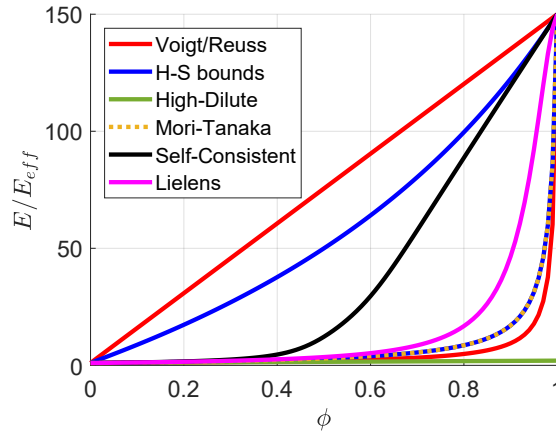


Figure 1.11: Comparisons between the homogenisation schemes - Evaluation of the normalised effective Young's modulus against the volume fraction of particles (H-S = Hashin-Shtrikman).

procedure gives, for now, results only up to 0.35 volume fraction of particles. Thanks to those results, it is clear that Mori-Tanaka gives good predictions of the elastic moduli for low to moderate volume fractions ($\phi < 0.3$), as commonly stated in the literature. According to [56] and [80], Lielens model is the one which gives the best results for high volume fractions. They also establish that Lielens model gives good predictions for high contrasts between the elastic moduli of the phases.

Nonlinear homogenisation

It is possible to include nonlinear behaviours for the phases (such as plasticity, or viscoelasticity for example) using mean-field homogenisation schemes. To solve this problem, the behaviour of the composite can be locally linearised using the incremental form of the constitutive behaviour (relationship between $\dot{\sigma}$ and $\dot{\epsilon}$) [73]. Several possibilities exist in the literature to linearise the incremental constitutive behaviour, such as the determination of secant, tangent, or affine moduli.

Some authors also introduced the effect of particle/matrix interface behaviour on the global properties of the composite. The first approach is to introduce a third layer between the reinforcement and the matrix called interphase. This interphase layer has a given thickness and distinct elastic modulus from the inclusions and matrix. Perfect bonding is usually assumed between 1) matrix and the interphase, 2) the inclusion and the interphase. This kind of homogenisation models considers at least three distinct phases in the medium. The first model to deal with multi-coated spheres or cylinders is Hervé and Zaoui's model [63] which is an extension to a N-layer coated inclusion of Christensen & Lo's three-phase model [22], also known as the Generalised Self Consistent Scheme (GSCM). A direct computation of the composite effective bulk modulus is possible, whereas, a sequence

of second-order polynomial equations must be solved in order to get the effective shear modulus.

Instead of introducing an interphase, the expression of the Eshelby tensor has been modified to introduce zero-thickness compliant interfaces inbetween the matrix and the particles. The particle/matrix interfaces are modelled with normal and tangential linear springs. Expression of the Eshelby tensor for compliant interfaces were developed in [120], [119], or [117]. The expressions were limited to continuously compliant interfaces and cannot account for partial debonding.

The partial debonding of particles in the matrix involves a partial loss of load transfer capacity of these particles. This causes a reduction of elastic stiffness in the loading direction. That is the reason why Liu, Sun & Ju [94] tried to model the damaged isotropic particles like orthotropic equivalent inclusions. Inspired from the work of Zhao & Weng [162], this employed the volume of inclusion directly beneath the interfacial cracks as a measure of damage, which can easily be obtained in two-dimensional cases. In general three-dimensional cases, however, it is difficult to proceed in a similar way to obtain simple expressions. For this reason, they used the ratio of the projected debonded area over the original interface area. This ratio is calculated in every principal directions of the inclusion (3 in the case of ellipsoidal particles). Three damage parameters $D_i (i = 1, 2, 3)$ are defined thanks to this ratio and they are used to calculate the loss of stiffness in the different directions.

Some authors tried to tackle the problem of the debonding of particles from the matrix within the framework of homogenisation schemes. This was especially developed for high explosive materials to predict the decohesion between energetic particles in a polymeric binder matrix (see Fig. 1.12 (a)). They first determined the mechanical properties of particles/matrix interfaces based on a bilinear Cohesive Zone Model approach [145]. Then, the cohesive behaviour of interfaces was introduced into High-Dilute and Mori-Tanaka homogenisation scheme under hydrostatic loading conditions [143] (see Fig. 1.12 (a)) and then under uniaxial loading [144]. Comparisons with numerical results gave good correlations between numerical and homogenisation and were especially able to take into account the particle volume fraction and size effect on particle debonding [66]. However, it is unable to catch particle interactions leading to heterogeneous stress and strain fields. This is especially the case for material reinforced with high volume fractions of particles ($\phi > 0.5$), where high stress concentrations are visible and responsible for localisation of failure, an effect that the homogenisation fails to capture.

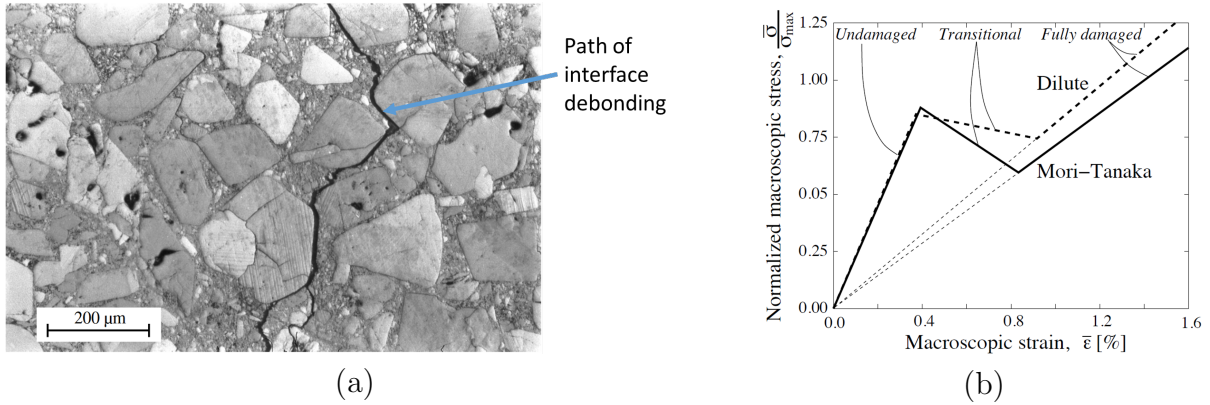


Figure 1.12: (a) Optical micrograph of the post failure route in the high explosive PBX 9501 (from [121]);
 (b) The stress-strain curves (under hydrostatic tension) predicted by the High-Dilute and Mori-Tanaka method with cohesive interfaces (from [65]).

Morphological Approach

Another approach that was developed to model the behaviour of highly filled particulate composites, such as energetic materials used as propellants, is the Morphological Approach (MA) [29]. This model is based on the work of Christoffersen [23] for linear elastic highly filled composites, where localisation/homogenisation problems have been resolved within a geometrical and kinematical framework. This was developed as an alternative to Eshelby-based methodologies for this specific composite class. Successive modifications have been added to the original model to introduce various types of nonlinearities. The model was extended to the viscoelastic regime in [105], to account for finite deformations in [59], for applications concerning particulate composites with hyperelastic and viscohyper-elastic matrix [104]. The damage by particle/matrix debonding was introduced with [103].

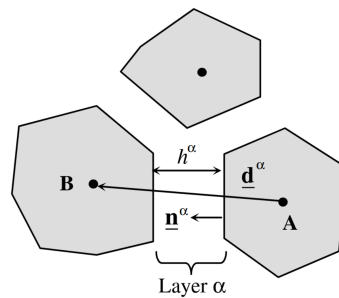


Figure 1.13: Two neighboring grains with an interconnecting material layer according to Christoffersen (from [29]).

In the MA, the geometry of the microstructure is explicitly represented. It is however limited to polyhedrons, any two of them interconnected by a thin layer of constant thickness of matrix (Fig. 1.13). The model is then controlled by the multiple kinematical

assumption such as ([29]):

- The kinematics of grains centroids is controlled by the global (macroscopic) displacement gradient;
- The particles are supposed to be homogeneously deformed and the corresponding displacement gradient assumed to be common to all grains within the representative volume element (RVE);
- Each interconnecting layer is subjected to a homogeneous deformation;
- Local disturbances at grain edges and corners are neglected on the basis of thinness of the layers.

The advantages of such a method [28] are that the MA is adapted to highly filled particulate composites as it has been developed especially for this class of materials. The microstructure of the material is directly and explicitly taken into account. Local fields are partially obtained in the matrix, and can incorporate multiple nonlinear behaviours. It however relies on limiting geometrical and kinematical assumptions. Moreover, it does not take into account the local fields in the reinforcements, it does not have appropriate kinematics for the overlapping areas between particle corners, and the continuity of stress vectors are not satisfied at the particle/matrix interfaces. For the special case of particle debonding, the MA cannot account for partial decohesion of interfaces.

1.6.3 Numerical simulations

The main limitation of the analytical models developed previously is that they rely on simplistic assumptions that allow the problem to be solved. It is, for example, important to note that stress and strain heterogeneities are not taken into account in mean field homogenisation schemes. Full-field models solved with various numerical methods have been developed to catch local effects such as local stress and strain fields in the materials. For particle reinforced materials, they are often based on Representative Volume Elements (RVE) where the whole geometry of the microstructure is explicitly represented (particles positions, sizes, shapes, etc.).

Elastic full-field calculations on Representative Volume Elements

Several authors have developed a numerical tool where they consider the evolution of simple pattern like a single inclusion in a matrix. This unit cell approach is based on the assumption that the material microstructure is fully periodic. However, observing the

microstructure of particle reinforced composite materials, such an assumption seems to be very unrealistic because most of these materials show highly random microstructures.

This microstructural randomness can be represented in a better way with RVE approach, where a synthetic random microstructure is generated. The definition and the size of the RVE is a complicated question, as discussed in [72]. Once the size of the RVE is defined (it has to be sufficiently large to be representative of the macroscopic behaviour of the real material) and the microstructure randomly generated, three types of boundary conditions can be imposed: Kinematic Uniform Boundary Conditions (KUBC, where a uniform displacement is applied to the boundaries of the RVE), Static Uniform Boundary Conditions (SUBC, where a uniform traction is applied on the boundaries of the RVE), and Periodic Boundary Conditions (PBC, where a relative displacement between all the points on opposing sides of the RVE is imposed). Then the problem is solved numerically, using methods such as Finite Elements (FE) or Fast Fourier Transformation (FFT). As explained in [72], the KUBC tends to overestimate the homogenised elastic moduli whilst the SUBC tends to underestimate it. The results of the PBC lie somewhere between these two bounds and the periodic boundary conditions seem to be the best compromise.

Multiples studies based on a numerical approach have already been carried out to obtain numerically the homogenised elastic moduli of particle reinforced composites. Synthetic microstructures with spherical or ellipsoidal particles are created and then the mechanical problem is resolved with a FE analysis in [128, 74, 135] or with FFT method in [55]. These works show that they are able to evaluate the elastic moduli up to a maximum 60% of particles volume fraction.

Crack propagation within numerical context

To numerically tackle the problem of interface debonding or crack nucleation and propagation, various techniques have been set up. The Cohesive Zone Model (CZM) was first introduced by [12] to handle discrete crack propagation in brittle materials and by [38] in plastic materials by postulating the existence of a process zone at the crack tip. Traction-separation laws are introduced at interfaces to represent the process zone ahead of the crack tip replacing the stress singularity. Different shapes of traction-separation laws have been developed to represent different mechanical behaviours depending on the type of materials and crack to be described. Cohesive laws have been introduced in FE simulations by [15] or [157]. More detailed description of the CZM will be presented in Chapter 3.

However the description of crack propagation with CZM induces well known issues such as mesh dependency. To overcome the crack path mesh dependency, eXtended Finite Element Method (XFEM) has been introduced. The usual FE are enriched with

additional nodal variables that allow displacement jumps over surfaces not matching the mesh. However, this technique has shown difficulties to describe crack nucleation and requires level-set function construction to describe the crack, which can be cumbersome when multiple cracks interact.

The Phase Field Method has been developed based on the pioneering work of Marigo and Francfort [49]. The discontinuities are regularised using an additional phase field variable. The problem is solved by minimising an energetic problem. This allows the description of cracks with a regular mesh and considerably reduces the mesh dependency of brittle crack description. The implementation of such a method in a numerical framework was carried out by [98] and was for example applied to microstructured composites by [111].

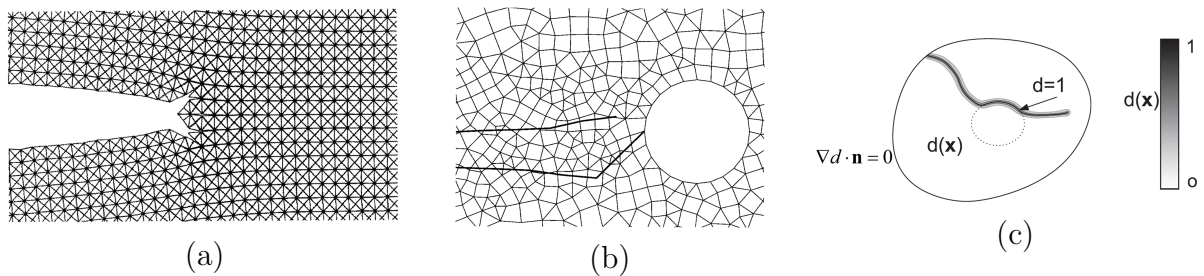


Figure 1.14: Crack propagations using (a) CZM (from [157]), (b) XFEM (from [99]), and (c) phase field (from [111]).

Penetration in granular media

The ballistic impacts on highly filled particulate composites can also be compared to the penetration of a projectile in granular media. This kind of study has predominantly been carried out for materials such as soils and geomaterials. The impact on granular media can be described as a sequence of distinct phases: a first transient stage of penetration characterised by significant energy loss and resistance to penetration, a compaction of the medium in a denser arrangement, and the creation of cavities in the wake of the projectile [115].

The modelling of penetration into granular media was tackled using various methods in the literature: the phenomenology of the impact was studied based on different variations on Newton's second law of motion, empirical formulae were developed to fit experimental data and rely on parameters controlling the soil and projectile behaviour, analytical formulations were written based on cavity expansion solutions (e.g. [48]), or numerical simulations. The latter can be divided in two main categories: continuum or discrete methods. On the first hand, the continuum methods can be solved using classical FE simulations or finite differences. On the other hand, using the Discrete Elements

Method (DEM), the granular media is treated as an assemblage of discrete interacting particles (see Fig. 1.15 (a)). Various rheological laws can be implemented to represent the interactions between all the discrete elements. A combination of FE methods and DEM can also be employed (see Fig. 1.15 (b)).

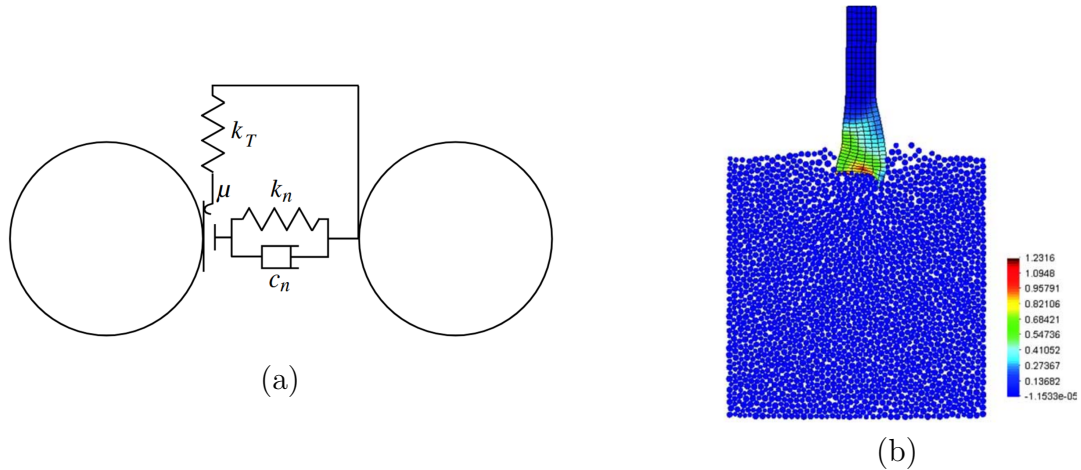


Figure 1.15: (a) Model of the contact interface;
 (b) Impact of projectile using DEM-FEM simulation - effective plastic strain distribution (from [116]).

It is noteworthy that the DEM has already been used to solve impact problems on continuous materials instead of granular ones by introducing different types of interaction laws (for example in [132]), because it is particularly convenient to represent fragmentation within this framework.

From both experimental and numerical points of view, various observations were drawn on the effects of the granular media morphologies on projectile penetration [115]:

- When grains collide and crush, strain energy is dissipated through the creation of new surfaces as well as friction and release of elastic energy.
- Size effect: here two competing mechanisms are experienced due to the fact that large particles tend to show more inherent flaws, which makes them prone to crushing, whilst they also show a higher number of contacts per grain when surrounded by small particles, thus redistributing the stresses and reducing the likelihood of tensile failure.
- Packing density: Increasing the packing density reduces penetration depth and increases projectile deceleration. The size distribution also has an effect as quasi-static penetration of long rods has confirmed that the resistance to penetration of well graded particles is higher than that of uniform distribution. A polydisperse

distribution generates a random force chain distribution (network of granular contacts), whilst a monodisperse one produces a concentrated response in a lattice-type formation (see Fig. 1.16).

- Grain shape: increase the angularity of grains increases strength and dilatant behaviour. The mineralogy also affects the strength of grains.

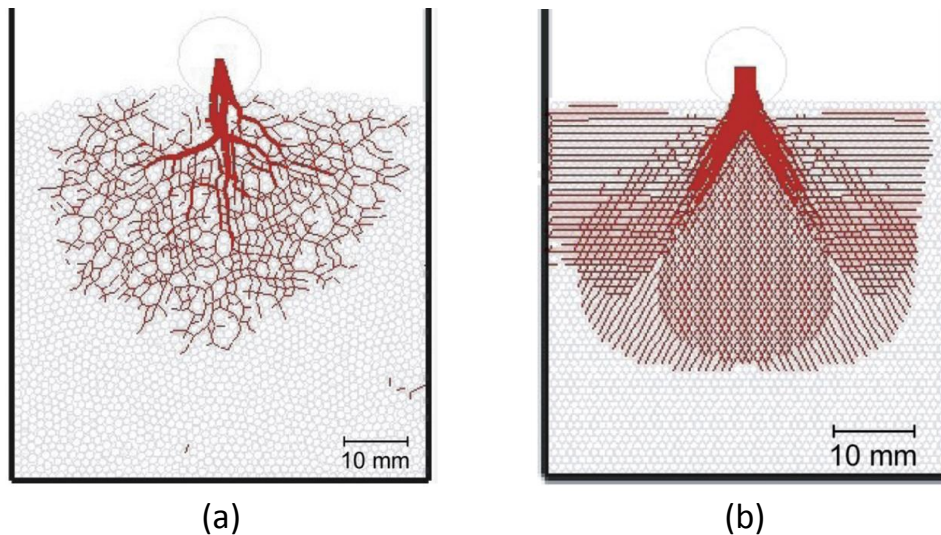


Figure 1.16: Communication of forces in sand impacted by a sphere, at two different packing configurations; monodisperse (a), polydisperse (b) (from [24]).

Lattice Elements Model

Discrete Element Modelling (DEM) is a powerful approach for the simulation of granular materials composed of rigid particles. However, in DEM, cohesive behaviours can only be introduced by using force laws at the contact points or by connecting the particles by rigid beams. In such models, the bulk effect of a cementing matrix cannot be taken into account [3].

The lattice element method (LEM) is based on the discretisation of different phases of a solid on a regular or irregular lattice [3]. Lattice-type discretisation has extensively been used for the statistical mechanics of fracture in disordered media, and applied to study the fracture properties of concrete and ceramics [148]. The space is represented by a regular or disordered grid of points (nodes) interconnected by one-dimensional elements (bonds) [148]. Each bond can transfer various types of forces (normal, shear and bending moment) up to a threshold in force or energy, representing the cohesion of the phase or its interface with another phase. In its simplest version, the elements are linear springs characterized by an elastic modulus and a breaking threshold. Each bulk phase (particle,

matrix, pores) or surface phase (interface between two bulk phases) is materialised by the bonds carrying the properties of that phase (see Fig. 1.17).

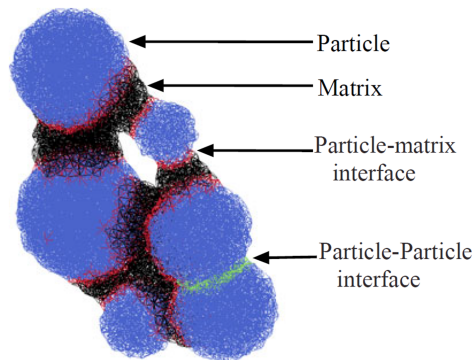


Figure 1.17: Lattice representation of a granular aggregate composed of particles, solid matrix connecting the particles and voids (from [3]).

This model allows to simulate the behaviour of large granular aggregates, composed of a dense packing of particles at a reduced computational cost [3]. The stiffness and tensile strength of each bulk phase and the interface zones between different phases may be adjusted, and cracks are generated naturally as a result of breaking bonds [3].

For granular aggregates linked elements of matrix, depending on the matrix volume fraction and on the resistance of the interfaces, different fracture regimes can be observed: deflection around particles, abrasion of particles, or even particle fragmentation [4].

1.7 Conclusions

Ceramics are employed for front-face ballistic protection because of their advantageous mechanical properties. During an impact, complex loadings are observed and different damage mechanisms are triggered. The resistance to penetration of a material then depends on multiple mechanical properties. Through this first chapter, it has been seen that:

- Ceramic particle reinforced materials have been proposed in order to advantageously replace monolithic ceramics. Indeed, polymers filled with a high content of ceramic particles can be moulded to obtain armour with complex geometries and might even improve their multi-hit capabilities. However, very few studies have been carried out on the subject and the performance under impact of such a material is quite unknown.
- The resistance to penetration of ceramic materials relies on multiple quasi-static mechanical properties. Similar complex loadings are observed for particle reinforced

polymers. To understand the performance under impact of such a material, various mechanical properties must be determined. The latter depend on multiple design parameters such as the individual properties of the components, the particle volume fraction introduced in the material, the particle size and shape, or the adhesion between the particles and the matrix.

- Homogenisation techniques allow to determine the equivalent properties of heterogeneous materials and have been developed in the literature. Analytical and numerical methods have been reviewed in order to determine the mechanical properties of particle reinforced materials. However, for both the experimental determination of mechanical properties or homogenisation models for stiff particles reinforced polymers, most of the studies developed in the literature focus on low to moderate volume fractions (below 30% of particles).

Through the next chapters, a particular attention will be given to the extension and the development of models of polymers filled with high particle content. An experimental campaign will also be carried out in order to characterise the mechanical behaviour of such a material.

Chapter 2

Highly filled polymers: Microstructure and elastic behaviour

The objective of this chapter is to experimentally and numerically evaluate the linear elastic properties of the polymer resin reinforced with a high particle volume fraction. Both an empirical and a numerical analyses were employed to determine the elastic moduli of such a material. Concerning the experimental evaluation process, we first developed a manufacturing protocol to build specimens with a reduced porosity, then we observed the obtained microstructure using microscopy and finally we performed uniaxial traction tests to determine the elastic properties of the composite. On the other hand, from a numerical point of view, representative random microstructures of the composite have been developed and a finite element based homogenisation procedure was implemented to determine the elastic properties of the composite. The influence of constituents morphology, distribution, volume fraction, and mechanical properties will be analysed through this chapter. All of these aspects will be detailed in the next sections.

2.1 Material description at the microscale level

The particle-reinforced composite analysed in this work is composed of ceramic embedded in a polymeric resin. According to [10], in order to obtain interesting mechanical properties for armouring, the amount of ceramic particles introduced in the material needs to be as high as possible to erode the projectile and distribute the load over a wide area of the backing plate without loss of the necessary cohesion. To determine the linear elastic properties of the material, the components are first described.

2.1.1 Components properties

Inclusions: ceramic particles

Two types of ceramics have been used as reinforcements in this study. The boron carbide (B_4C) and the alumina (Al_2O_3), whose mechanical properties are listed in Table 2.1. The boron carbide shows outstanding mechanical properties: it is very hard and lightweight at the same time. The alumina shows inferior properties (lower stiffness and hardness and weighs 1.5 times more than boron carbide). However, the boron carbide is extremely expensive, that is why alumina can be an interesting substitution for armouring at lower cost.

| Mechanical properties | Al_2O_3 | B_4C |
|-------------------------------|-----------|--------|
| Density ρ [g/cm^3] | 3.90 | 2.52 |
| Young's modulus E [GPa] | 407 | 450 |
| Poisson's ratio ν [] | 0.25 | 0.20 |

Table 2.1: Mechanical properties of Al_2O_3 and B_4C .

| Grit sizes | $F20$ | $F60$ | $F360$ | $F1200$ |
|------------|----------------------|---------------------|-------------------|-----------------|
| Size | $850\mu m-1180\mu m$ | $212\mu m-300\mu m$ | $12\mu m-40\mu m$ | $1\mu m-7\mu m$ |

Table 2.2: Grit sizes of ceramic particles.

Four sizes of particles, see Table 2.2, are used for two reasons: to study the particle size effect on the mechanical performances of the material and to reach higher volume fractions with mixed particle sizes (as it will be seen in the paragraph dedicated to particle packing).

The morphology of the particles has been observed using Optical Microscopy (OS) and Scanning Electron Microscopy (SEM), see Figs. 2.1 and 2.2. Fig. 2.1 shows three types of boron carbide particles observed with SEM: $F60$, $F360$, and $F1200$. They all present faceted geometries. In particular, larger particles ($F60$) show very sharp angles and some of the facets present a rippling and concentric geometry characteristic of the conchoidal fracture of brittle materials. The smaller the particles, the more rounded and polygonal they seem to be, exhibiting less sharp edges as a result of faceted fractures. These geometries can be explained by the fabrication process of the boron carbide particles, as the material is milled to obtain powders of different grit sizes [7].

Two types of alumina particles are then observed with OM (Fig. 2.2). They are also very angular particles with thin edges, however they show a less faceted geometry. Their

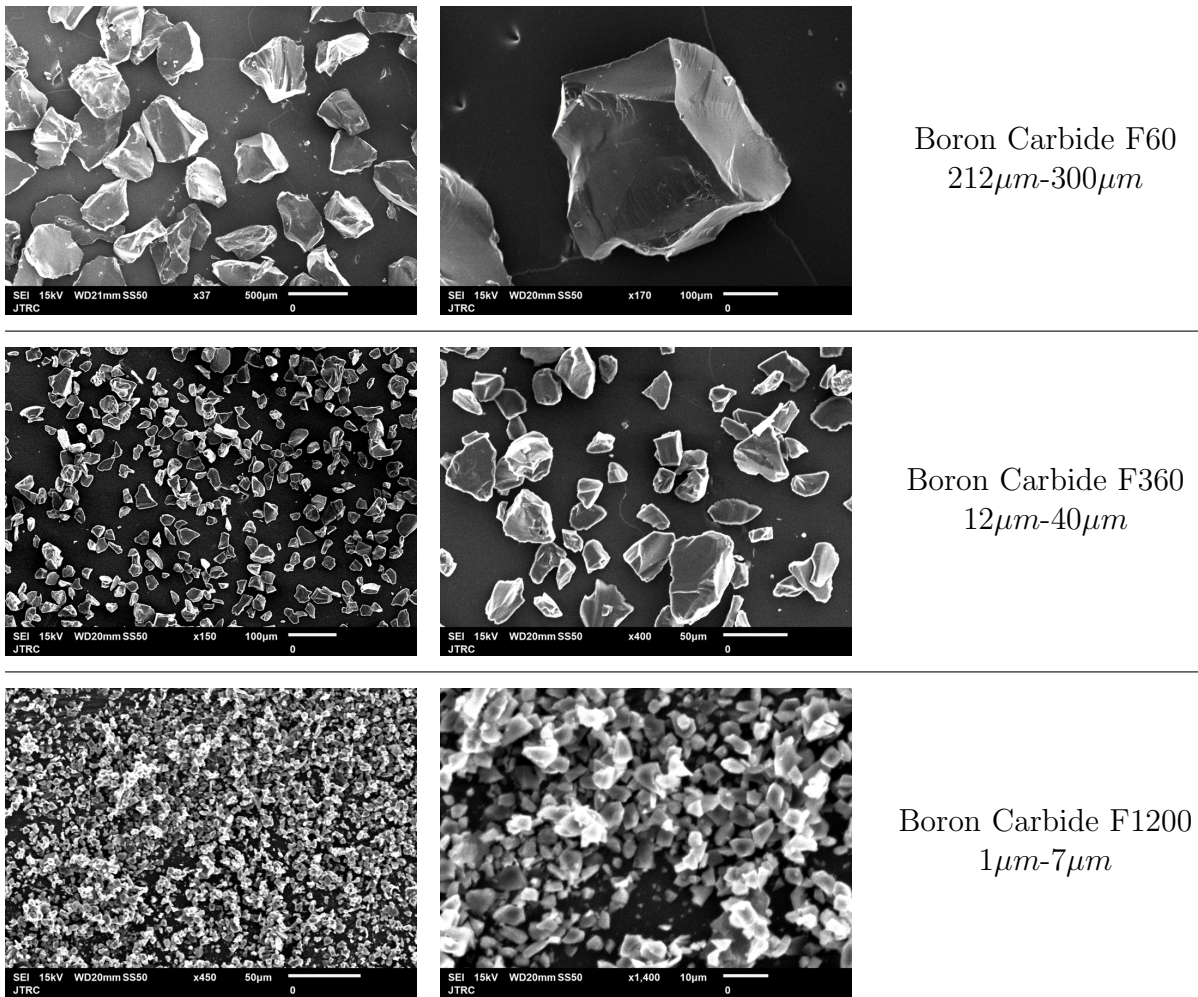


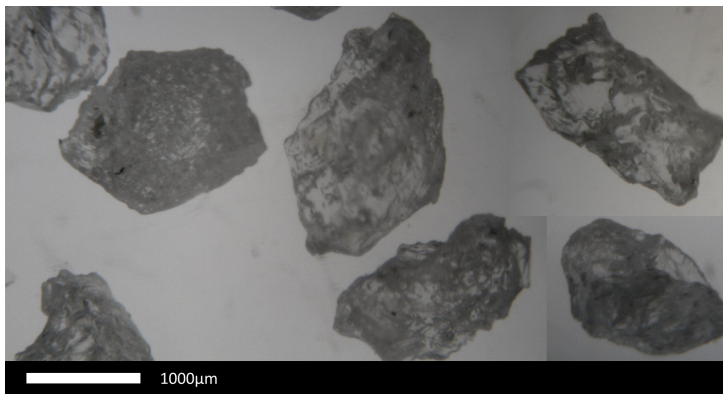
Figure 2.1: Boron carbide particles, Grit sizes F60, F360, F1200, observed with SEM.

surfaces are rougher than the ones of boron carbide particles facets. They can still be characterised as angular particles.

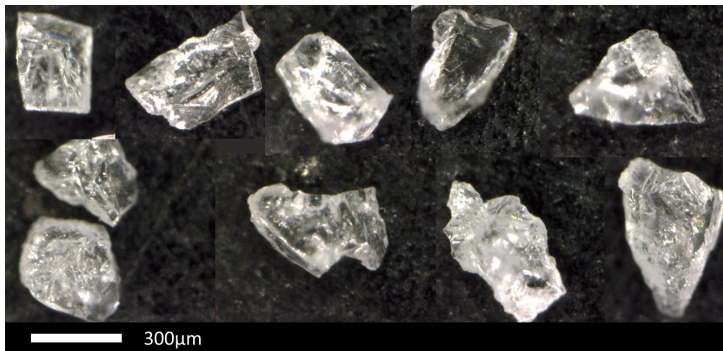
Matrix: Epoxy resin

Three types of resins have been used for this study. All these resins are two-components epoxy adhesives, made of a base (modified epoxy) and a hardener. Both components are mixed according to weight ratios defined by the manufacturers. The epoxy resin then needs to be polymerised with an appropriate cure cycle. The manufacturers recommendations for the preparation of the epoxy resins are listed in Table 2.3.

The mechanical properties of the three epoxy resins are listed in Table 2.4. The two first resins (Arapox and RenLam) show very similar properties. They have a low viscosity before curing that helps reaching high volume fractions of particles for the fabrication of particle reinforced materials. They both exhibit a brittle behaviour. The Arapox resin was



Alumina F20
850µm-1180µm



Alumina F60
212µm-300µm

Figure 2.2: Alumina particles, Grit sizes F20, F60, observed with OM.

employed in Oxford Brookes University for all the tensile, Iosipescu and beams samples, whereas the RenLam was employed in the University of Bordeaux for indentation samples.

The SW 2216 resin shows a very compliant and ductile behaviour. The glass transition temperature is also very low compared to the two former resins. This resin will only be used as a comparison to test the effect of the matrix material on the composite behaviour.

| Epoxy resins | Arapox | Renlam | SW 2216 |
|--------------------------|-------------|-------------------------------|---------|
| Base parts by weight | 100 | 100 | 5 |
| Hardener parts by weight | 54 | 30 | 7 |
| Viscosity before curing | fluid | fluid | viscous |
| Typical cure cycles | 8 hrs, 40°C | 24 h, 25°C + 4 h, 120°C | 7 days |

Table 2.3: Composition and cure of the epoxy resins.

| Epoxy resins | Arapox | Renlam | SW 2216 |
|---------------------------------------|---------|---------|---------|
| Young's modulus E [GPa] | 2.0 | 3.0 | 0.5 |
| Poisson's ratio ν [] | 0.38 | 0.35 | 0.40 |
| Tensile strength σ_{max} [MPa] | 47.4 | 78.0 | 26.6 |
| Glass transition temp. T_g [°C] | 120 | 120 | 40 |
| Behaviour | Brittle | Brittle | Ductile |
| Colour | Amber | Blue | Gray |




Table 2.4: Properties of the epoxy resins.

2.1.2 Manufacturing of the composite

The composite material is fabricated according to a precise procedure outlined in Fig.2.3. The weight ratios of all the components are determined depending on the target particle volume fraction. Then, the different types of particles are introduced (Figs. 2.3 and 2.4, step 1). The epoxy resin, the hardener, and the wetting agent are respectively added according to the mix ratios previously defined. The mechanical blending was conducted to ensure a uniform mixture and effective dispersion of the particles (Figs. 2.3 and 2.4, step 4). To reach low or intermediate volume fractions (20 – 40 % Vf), the material can be left for three hours at ambient temperature so that the viscosity of the resin increases, as the curing process starts. Thanks to a higher matrix viscosity we can avoid the sedimentation of the particles at the bottom of the mould. Moreover, due to the introduction of a large amount of particles, air is trapped in the material. To get rid of this, the mixture is degassed under vacuum for 10 minutes. The material can then be moulded in metallic or plastic moulds (Figs. 2.3 and 2.4, step 6). The moulds are sealed with a top and a bottom metallic plates and pressure is applied to ensure a good compaction. After the resin is cured, the samples can then be demoulded (Figs. 2.3 and 2.4, step 8) to perform the mechanical tests.

To enhance adhesion between the particles and the resin, a chemical surface treatment can be applied to the particles. In this work, a silane coupling agent is used to modify the particle surface and the bonding process at the interface. The silane creates a chemical

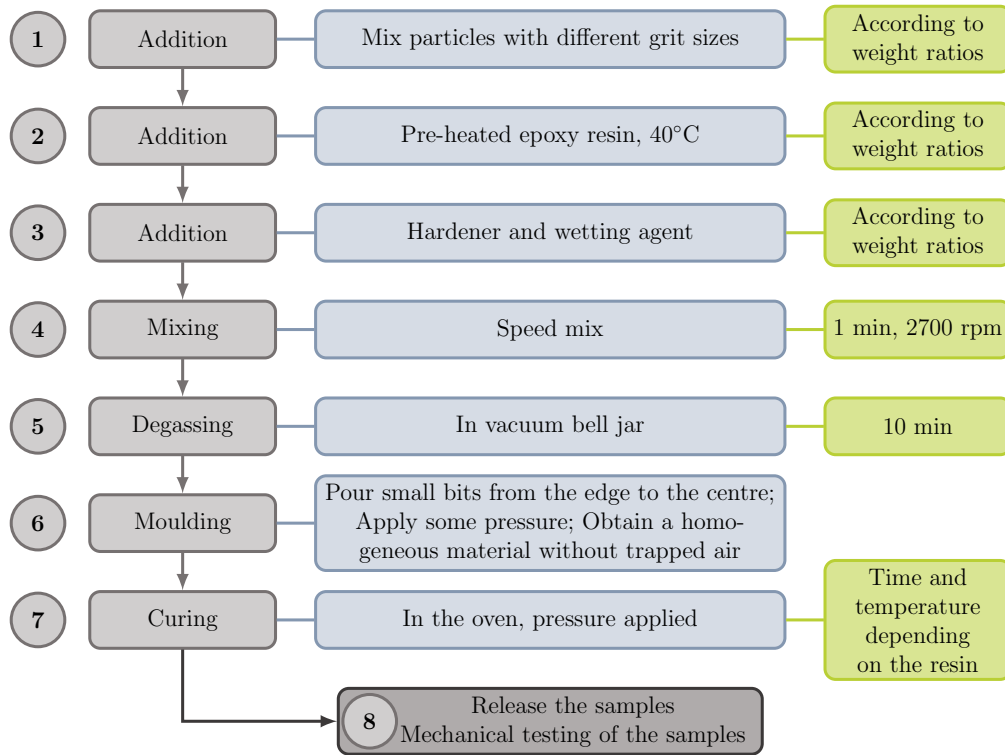


Figure 2.3: Manufacturing process of the ceramic reinforced material.

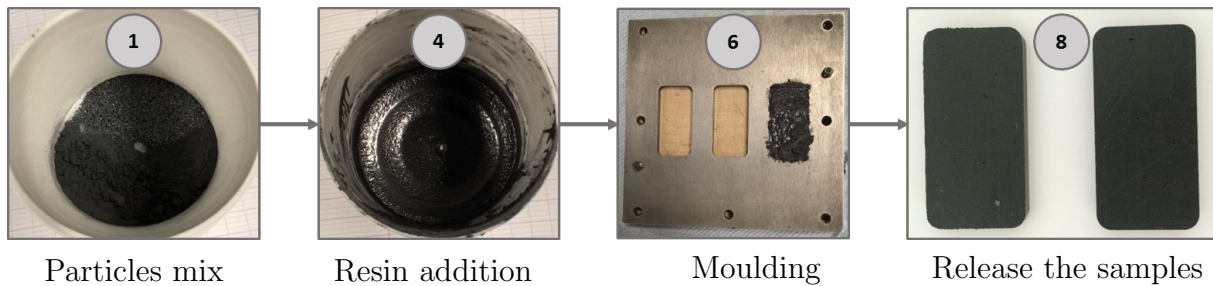


Figure 2.4: Some steps of the manufacturing process of the ceramic reinforced material.

bridge between the inorganic particles and the resin, resulting in a better stress transfer from the matrix to the fillers [123]. Additional effects can be a higher hydrophobicity to prevent moisture penetration, more efficient dispersion of the reinforcements and a reduction of the apparent viscosity of the mix before curing [123]. A γ -glycidyoxypropyl-trimethoxysilane (GPS) in an aqueous solution was used in this study (Fig.2.5). The silane treatment of the particles is highly dependent on multiple preparation parameters and is generally determined empirically [1]. The process used for the present study is summarised in Fig. 2.6.

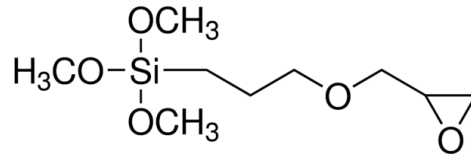


Figure 2.5: γ -Glycidyloxypropyl-trimethoxysilane (GPS) molecule structure before hydrolysis.

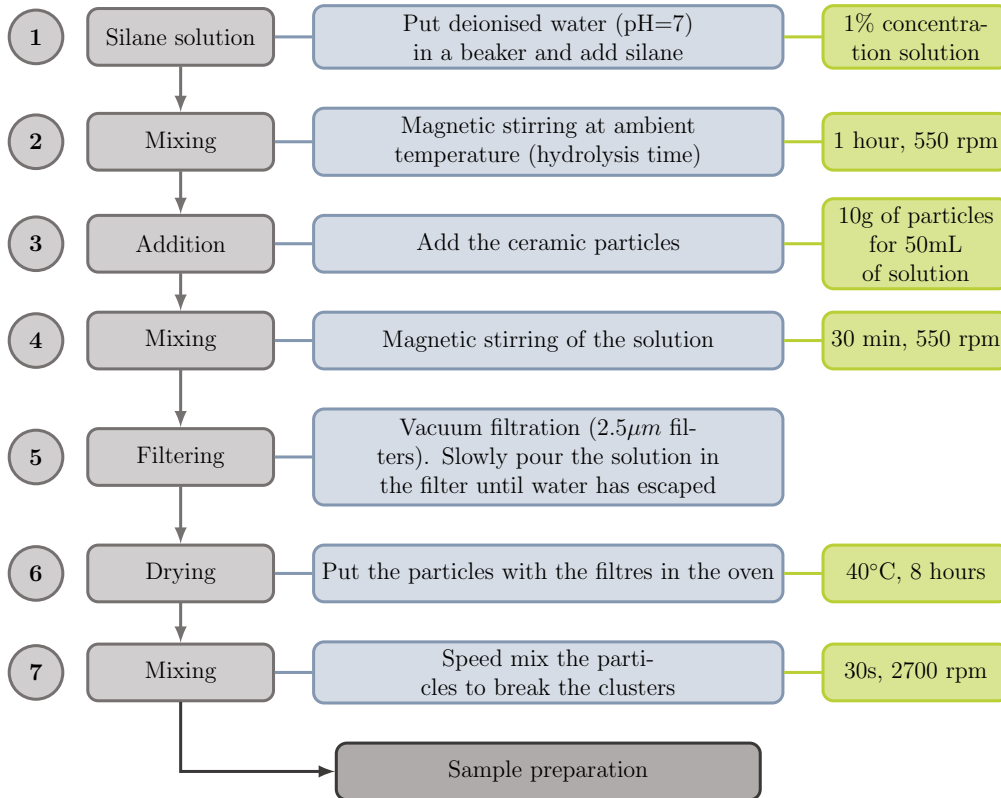


Figure 2.6: Silane treatment of the particles.

Particle packing

In order to increase the particle volume fraction introduced into the composite material, one can use binary or polydisperse mixes of particles. Indeed, a proper repartition of the of volume occupied by big and small particles can increase the particle volume fraction (filling effect of the fine particles filling into the voids of the coarse particles, and occupying effect of the coarse particles occupying solid volumes in place of porous bulk volumes of the fine particles [17]). Two regimes are observed for particle packing: when coarse particles are dominant and when fine particles are dominant. With dominant coarse particles, the free space between large particles tends to be increased by the loosening effect (see Fig. 2.7 (a)): it consists in a small particle inclusion between large ones, that loosens the particle packing. With dominant fine particles, the packing density is reduced by the wall

effect (see Fig. 2.7 (b)), that consists in coarse particles disrupting the packing of the fine particles at the wall-like boundaries of the coarse particles.

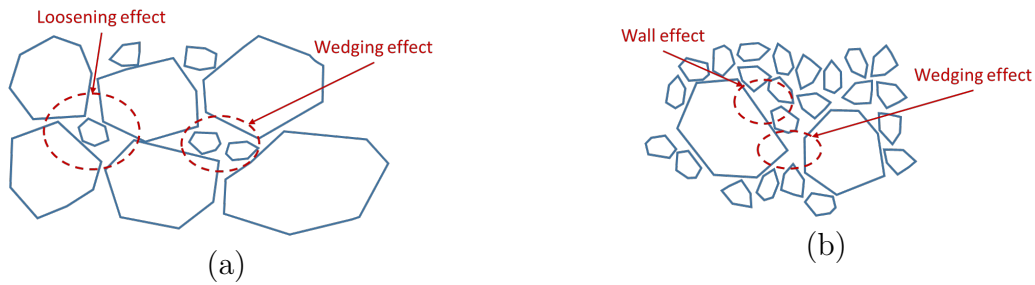


Figure 2.7: (a) Loosening and wedging effect (coarse particles dominant);
(b) Wall and wedging effects (fine particles dominant).

The packing density of binary mix has been evaluated in the literature. Three main types of models have been developed: the 2-parameter model [158], the 3-parameter model [85], and the compressible model [30]. All models are first designed for spherical particles and then extended to angular ones [86]. They are all based on three basic inputs: the monodisperse packing densities of coarse and fine particles respectively and the size ratio between fine and coarse particles. All the models also take into account the loosening and wall effect (corresponding to the first two parameters). The 3-parameter model takes into account the wedging effect that happens at both regimes and that is maximal at the intersection of the two regimes. It consists in interactions between particles with the same size. The compressible model also introduces a third parameter, but this time, it corresponds to the effect of a pressure applied on the packing. The parameters introduced are fitted on experimental data.

The 2 and 3-parameter models have been compared to experimental results with binary mixes of spherical ceramic beads. The diameter of the smallest type of particles ranges between 0 and $63\mu m$, whereas the largest one is between 250 and $425\mu m$. The mean of the extreme values are taken as the particle size for the models. To determine the packing density, a cylinder with known volume is filled and then weighed: the density of different mixes of particle sizes are measured (r_1 is the ratio of small particles over the total particle population). The packing density is plotted against the fraction of small particles in Fig. 2.8 (a) for the experimental values and the ones predicted by the models. It can be seen the models give a good estimation of the packing densities: the packing densities for mixed particle sizes is higher than the ones of monodisperse particles. The maximal value is reached for a small particle fraction between 0.3 and 0.4 for both the experimental and analytical models. This maximal value is better described by the 3-parameter model as the 2-parameter one overestimates the packing densities at the intersection between the two regimes.

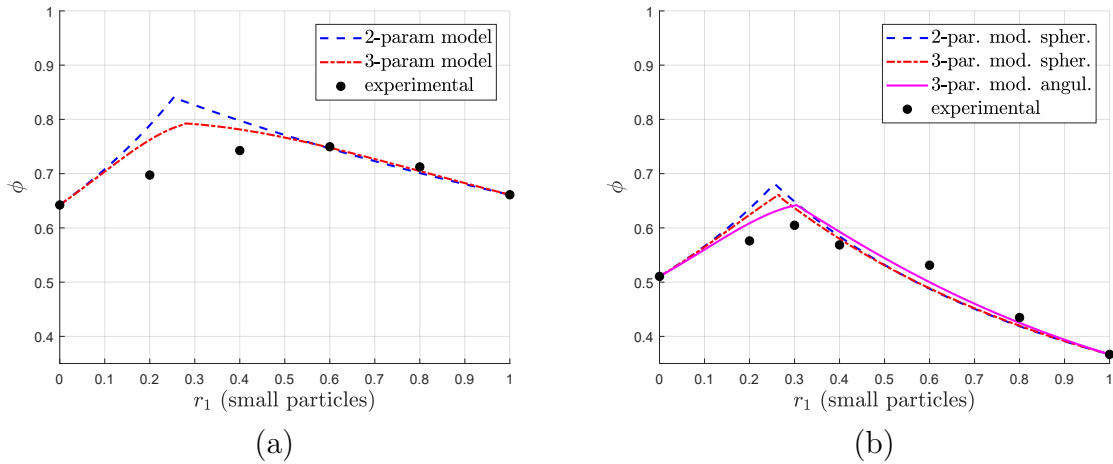


Figure 2.8: (a) Particle packing of spherical beads;
 (b) Particle packing of angular particles.

The same experiment was carried out for the angular ceramic particles of alumina described previously. More precisely, the F360 alumina particles are used as small particles and the F20 as the large ones. The results are plotted in Fig. 2.8 (b). It is first to be noted that the packing density of small particles is lower than the one of larger ones (for large particles $\phi = 0.51$ and for small ones $\phi = 0.37$). This phenomenon has been observed also in [86] and the authors also observed this phenomenon and explained it by inter-particles cohesive forces that causes agglomeration and tend to be higher than the weight of small particles. The experimental data are once more compared to the 2-parameter model and the 3-parameter model for spherical beads but also to the 3-parameter model adapted to angular particles. The evolution of the packing density against the fraction of small particles is quite well described by the models. The model adapted for the angular particles is the one that gives the best predictions especially for the location and the value of the maximal packing. A maximum of $\phi = 0.60$ is obtained for a small particle fraction equal to 0.3.

Finally, the packing density of spherical and angular particles can be estimated by models. The packing densities of spherical particles are higher than the one of angular particles. The packing density of large particles is higher than the one of smaller particles. Higher packing densities can be reached with binary mixes of particles. The maximum packing density for the angular particles used for this study is reached with a fraction of small particles of 0.3 and is around 0.6, that corresponds to the maximal volume fraction of particles that can be introduced into the composite material.

2.1.3 Description of the microstructure

The desired composite is characterised by a high filler content which is supposed to confer optimum behaviour under ballistic impact. Therefore, after manufacturing, the microstructure of the material was observed. First, the samples were polished as a flat surface is required to get quality images for the two different types of microscopy used: SEM and OM. Particular care was given to the polishing process as the high hardness contrast between the two phases leads to uneven surfaces: the soft material (the resin) is easily removed whereas the hard one (the particles) is much more resistant (see Fig. 2.9).

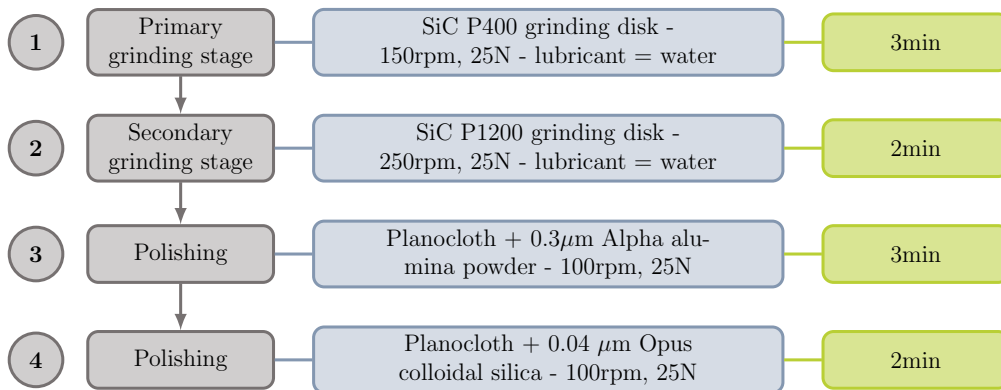


Figure 2.9: Polishing process of the ceramic particle reinforced polymer for microscopy.

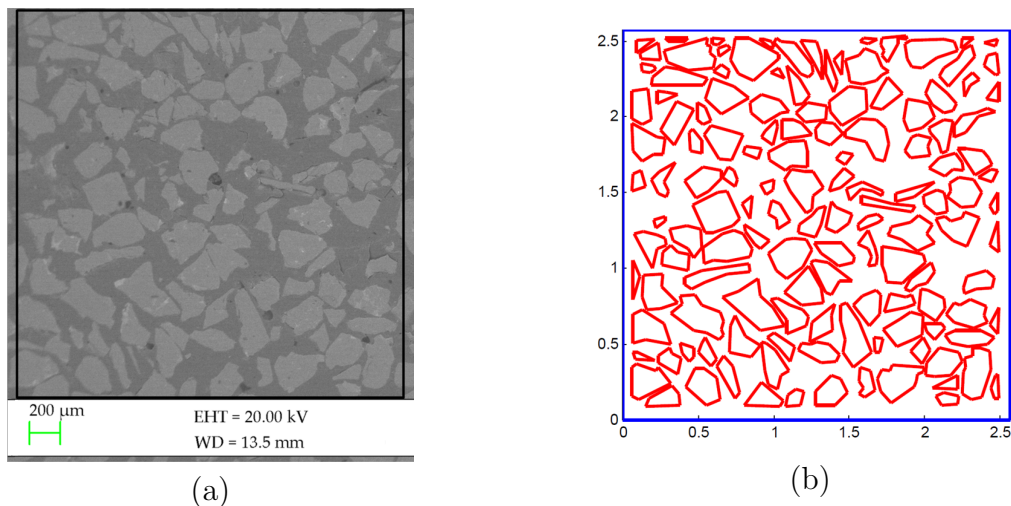


Figure 2.10: (a) Microstructure of the material with alumina particles (with SEM); (b) Extracted geometry of the microstructure.

Fig. 2.10 (a) represents the microstructure of the composite with alumina particles observed with SEM. The particles seem to be “uniformly” dispersed in the material. The particles boundaries have manually been drawn as automatic image analysis procedure lead to unreliable results due to poor contrast between phases (Fig. 2.10 (b)). This image

can be used as a RVE for FE analysis. In order to carry out a parametric analysis of the material, it is interesting to get multiple RVE with different particle volume fractions, sizes, distributions, and shapes. Since the process of manufacturing, polishing, observing and drawing multiple samples take a lot of time, an “ad hoc” algorithm for random microstructures generation has been developed. The microstructure depicted in Fig. 2.10 (b) can then be used only as a reference RVE to be compared to the random artificial microstructures.

2.1.4 Semi-realistic artificial microstructure generation

To randomly generate the RVE for a particulate reinforced composite, multiple strategies can be used. The first characteristic to take into account is the shape of the particles. For this study, carried out in 2D, two shapes of particles are used: circular and polygonal particles. We also remind that the objective of this work is to evaluate the response of highly filled composite materials, therefore the microstructure of the RVE has to reach high volume fraction of particles. Two families of circular packing algorithms can be distinguished: the dynamic and the constructive ones. Concerning the dynamic algorithms, the positions and/or sizes of particles as well as the interactions between them are updated continuously during the iterations of the algorithms. For this reason, they are usually time-consuming. For example, moving and shrinking or growing algorithms ([95, 96]) are well known dynamic algorithms. On the other hand, for the constructive algorithms, the position and the size of each particle is defined sequentially and, when a particle is placed, its position is recorded and will not be updated. The most intuitive algorithm to generate a microstructure is the Random Sequential Adsorption (RSA) algorithm, where the location of each particle is randomly defined [149]. However, this algorithm can't achieve high volume fraction (up to a maximal value of 0.3). That is the reason why several studies ([128, 135, 74, 55]) use a an improved version of the RSA algorithm, where the particle positioning sequence is controlled. In any case, even when using an improved version of the RSA algorithm, it is not possible to achieve volume fractions higher than about 0.6 and requires many iterations.

Dropping and Rolling algorithm

For this study, a dropping and rolling algorithm based on the work of [151] and [131] has been chosen. This method is able to generate denser microstructures than the previously cited constructive algorithms. The steps characterising the algorithm (see Fig. 2.11) developed in the framework of the present study are described thereafter:

1. A first disk is dropped from a random position on the upper side of the frame;

2. the disk falls (incremental vertical displacement) until it touches the floor (bottom of the RVE) and its final position is recorded;
3. a new disk is dropped from another random position;
4. during the fall, two possibilities appears:
 - (a) no previous disk is under the falling one and the latter goes straight to the floor;
 - (b) there is a contact between the falling disk and already placed ones \Rightarrow the new disk rolls on the previous ones until it reaches an equilibrium position: either hitting the floor or on two existing disks;
5. repeat the process from step 3 item until the box is filled with disks.

Roughly speaking, this procedure is very similar to grains of sand flowing into a box. The advantage of such an algorithm is that the microstructure generated can reach high volume fraction of inclusions in a reasonable time. Moreover, a radii distribution can be defined (either discrete or continuous), unlike most dynamic methods. The final volume fraction attained is controlled via a parameter representing the inter-inclusion minimal distance. Two boundaries were developed for the dropping and rolling algorithm. The first one is called “rigid wall” where the disks cannot bypass those walls (see Fig. 2.13 (a)). The second one is called “soft wall”: the disks are allow to bypass the walls and they reappear on the opposite side of the frame to ensure periodicity of the microstructure (see Fig. 2.13 (b)). The soft wall conditions also avoid non homogeneous particles distribution near the boundaries of the RVE and reach higher volume fractions.

Voronoi tessellation microstructure algorithm

The circular shape of the inclusions in a particulate reinforced composite is not always a realistic assumption. As seen previously, ceramic particles show multiple facets and sharp angles. To deal with this kind of microstructure, an algorithm based on a Voronoi tessellation has been implemented, see Fig. 2.12 (a). The steps characterising such an algorithm are described hereafter:

1. N seeds (points) are randomly generated in the frame delimited by RVE sides. A loop can be implemented to recreate seeds that are to close to other ones;
2. this frame (with seeds) is duplicated 8 times and translated all around the frame (top, bottom, right, left and in diagonals). This step ensures that when the growth step of the grains occurs, the periodicity of the boundaries is respected;

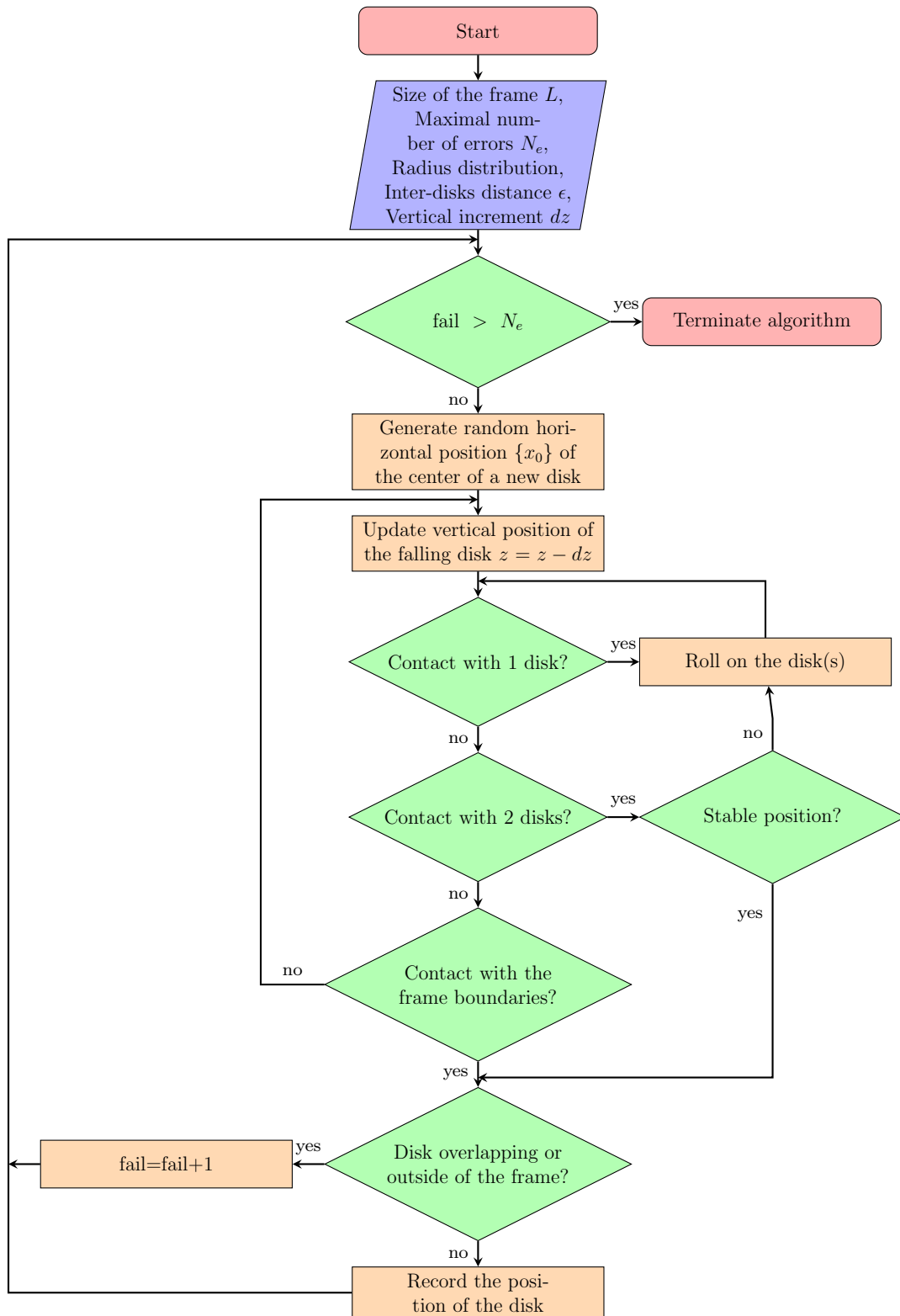


Figure 2.11: Flowchart of the dropping and rolling algorithm.

3. the edges of all the cells are created using a Delaunay triangulation (the Voronoi diagram being the dual graph of this triangulation); the Matlab functions *delau-
nayTriangulation* and *voronoiDiagram* are used here. In fact, this process gives the same results as circles growing from each seed. The boundaries are created when two points from two circles are in contact;
4. a reduction factor is applied to all the cells so that their edges are no longer in contact to create the matrix phase. The advantage of such a reduction is that the volume fraction of particles is exactly determined by this factor.

A typical microstructure obtained with this algorithm is depicted in Fig. 2.13 (c).

Polygonal microstructure from Dropping and Rolling algorithm

The dropping and rolling algorithm was modified to include polygonal particles, which may be more representative of the microstructure. The steps charactering such an algorithm (see Fig. 2.12 (b)) are described thereafter:

1. A microstructure is created using the dropping and rolling algorithm;
2. each circular particle is transformed into a polygonal inscribed in the circle:
 - (a) the number of vertices of each polygon N_{angles} is randomly generated between 5 and 8;
 - (b) for each vertex n (from 1 to N_{angles}), a number θ_n between $(2\pi)/(n-1)$ and $(2\pi)/(n)$ is randomly generated. The use of intervals is included to avoid obtaining polygons that are too distorted;
 - (c) the coordinates of each vertex of the polygon is the intersection of a line going from the center of the circular particle and forming an angle θ_n from horizontal and the circle:

$$\begin{cases} x_n = x_0 + R \cos(\theta_n) \\ y_n = y_0 + R \sin(\theta_n) \end{cases} \quad (2.1)$$

where $\{x_0; y_0\}$ are the coordinates of the circular particle's center and R is its radius.

This algorithm has been implemented using either rigid or soft wall boundary conditions. In order to avoid boundary effects, only soft wall boundary types will be used in the present study. The resulting microstructure is represented in Fig. 2.13 (d).

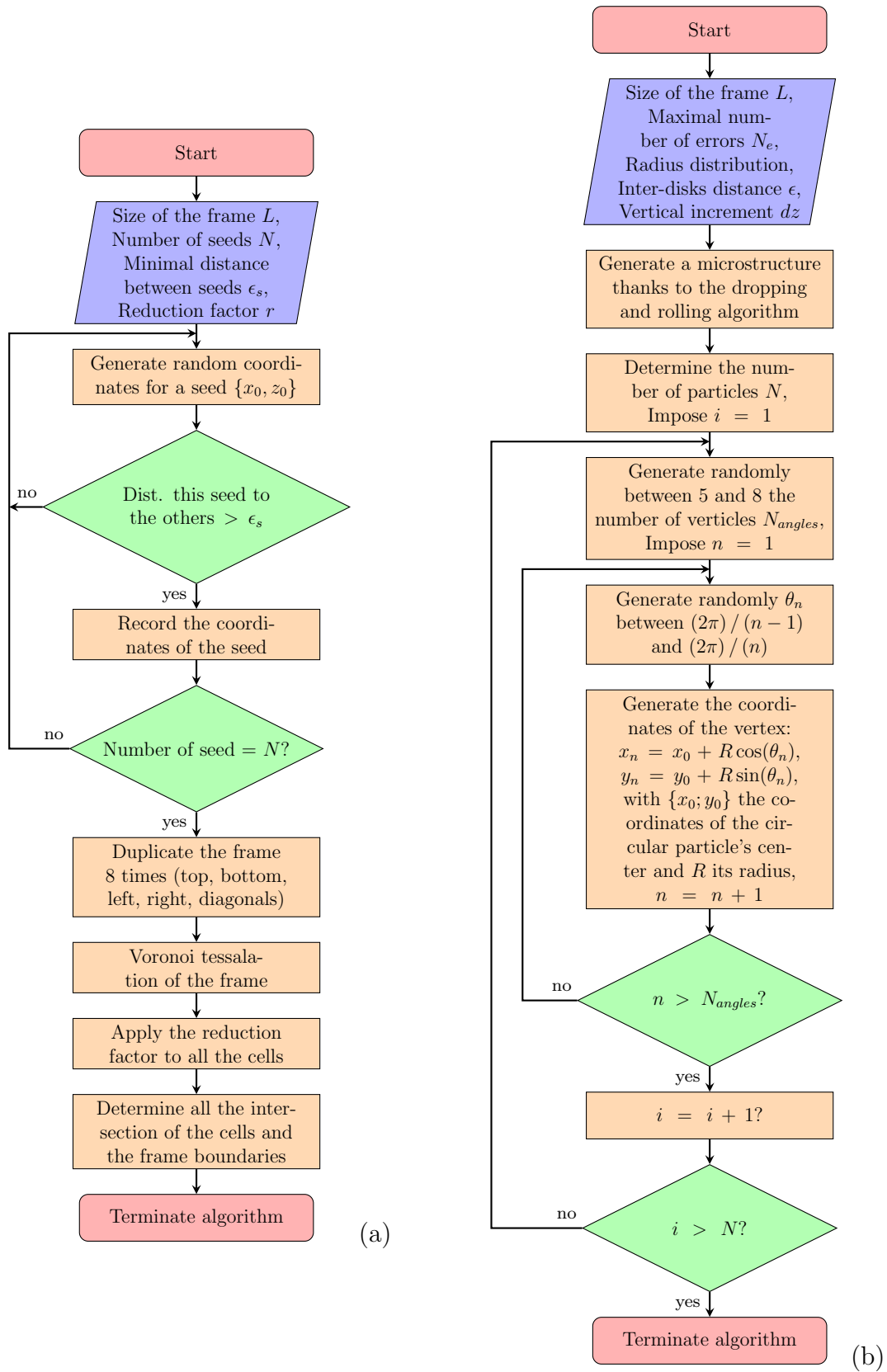


Figure 2.12: (a) Flowchart of the Voronoi tessellation-based algorithm; (b) Flowchart of the D&R algorithm with polygonal particles.

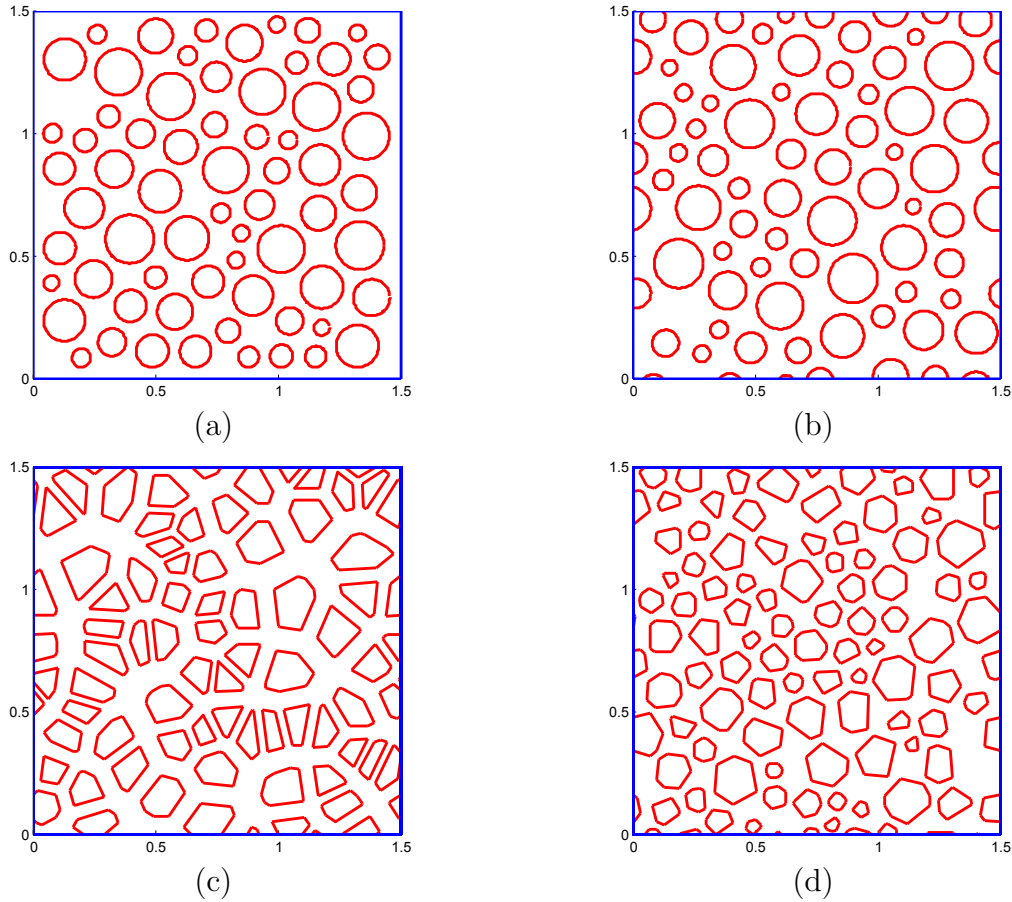


Figure 2.13: Microstructures obtained with the dropping and rolling algorithm with rigid walls (a), with soft walls (b), with Voronoi tessellation algorithm (c), with the dropping and rolling algorithm with polygonal particles (d). Volume fraction of particles for each microstructure $\phi = 0.4$.

Geometrical capacities of these algorithms

Finally, three different models were generated based on the algorithms described beforehand: Dropping and Rolling algorithm with rigid walls or soft walls, the Voronoi tessellation-based algorithm, and Dropping and Rolling with polygonal particles. The geometrical capacities of these algorithms are shown in Table 2.5.

| Algorithm | Particle shape | Particles size distribution | Volume fraction | Max Volume fraction |
|-----------------|----------------|-----------------------------|--------------------|---------------------|
| D&R Rigid walls | circular | defined | calculated | 0.68 |
| D&R Soft walls | circular | defined | calculated | 0.75 |
| Voronoi | polygonal | undefined | input of the model | 1 |
| D&R Polygons | polygonal | defined | calculated | 0.60 |

Table 2.5: Geometrical capacities of the microstructure generation algorithms.

The first algorithm generates microstructures with circular particles whereas the latter two generate polygonal particles. A parameter ϵ , representing the inter-particle minimal

distance, is used in the Dropping and Rolling algorithms to set up the volume fraction. However, the volume fraction is for this reason unknown a priori and calculated once the microstructure has been generated. One can clearly see that the soft wall boundary condition allows higher volume fractions of particles than the rigid wall conditions. Also, the creation of inscribed polygons reduces the maximum volume fraction. One of the strengths of the Voronoi tessellation-based algorithm is that the number of particles and their volume fraction are inputs to the model. Unlike the Dropping and Rolling algorithms, the particles size distribution cannot be employed with this algorithm.

2.2 Elastic properties and homogenisation

The elastic properties of the material are estimated using three different techniques. First, they are experimentally determined by performing tensile tests. Then, two types of models are employed: analytical ones based on *mean fields homogenisation* that are based only on the volume fraction of the components and numerical ones that are full field analyses. The latter takes into account the whole geometry of the material and gives access to more local results as the stress distributions inside the phases.

2.2.1 Experimental determination of elastic properties

In this section the elastic properties of the ceramic-based composite will be determined experimentally through standard tests. The material is considered as isotropic, therefore a set of only two parameters is required to fully describe its elastic behaviour. Such parameters can be either Young's modulus E and Poisson's ratio ν , the Lamé coefficient λ and μ , or the the bulk and shear moduli κ and μ , used to describe the spherical and deviatoric behaviour of the material. The first set of coefficients E and ν are very convenient to evaluate from an experimental point of view and therefore, in the following study, only those two coefficients will be considered. The most common way to determine Young's modulus and Poisson's ratio is to perform a tensile test on the material. E is calculated as the ratio of the stress and the longitudinal strain and ν is calculated as the ratio of the transversal strain and the longitudinal strain. Different methods are commonly employed to have access to the different stresses and strains during tensile testing.

The samples are dogbone-shaped specimens, whose geometry is extracted from the British standard BS EN ISO 527-2:1996. The width of the useful part of the sample is $5mm$ and its thickness $2mm$. The strains (both longitudinal and transverse) are evaluated using video monitoring coupled with Digital Image Correlation algorithm. A camera is synchronised to record the displacement of the sample. The movements of 4 white dots

are tracked during the tensile testing for the first series of experiments and with a speckle pattern for the second one. The load is determined with the $5kN$ load cell installed on the Instron tensile machine.

The effect of particle volume fraction and particle size on the elastic moduli of the material is analysed.

Tensile tests on samples with monodisperse particle sizes

For the first series of experiments, each sample is manufactured using only one particle grit size. The following samples have been tested:

- 7 bulk epoxy samples;
- 9 samples with 40% volume fraction of particles (3 samples with F1200 particles, 3 samples with F360 particles, 3 samples with F60 particles);
- 9 samples with 50% volume fraction (3 samples with F1200 particles, 3 samples with F360 particles, 3 samples with F60 particles);
- 9 samples with 60% volume fraction (3 samples with F1200 particles, 3 samples with F360 particles, 3 samples with F60 particles).

The samples were tested at room temperature (approximately $23^{\circ}C$) and with a loading rate of 0.5 mm/min .

The stress-strain curves of samples having the same volume fractions are plotted in Fig. 2.14. In Fig. 2.14 (a), the stress-strain curves for the bulk adhesive samples are plotted. We can observe that the elastic parts overlap quite well, providing confidence in the determined Young's modulus for the epoxy. The average Young's modulus value for bulk adhesive is $E = 2.357GPa$. The average Poisson's ratio is also calculated, $\nu = 0.38$. Samples 2 and 7 break prematurely. Therefore, their strength values are not taken into account for the determination of the epoxy strength. The average strength for the epoxy resin is $\sigma_{max} = 51.6MPa$.

Fig. 2.14 (b) depicts the stress-strain curves for samples with a 40% volume fraction of B_4C particles. The scatter between the values for the elastic modulus is very high. Several factors could explain this: the effective volume fraction is not the expected one (some resin might have escaped during compaction process), the samples are not homogeneous, there are more or less air bubbles within the samples, etc. However, the strength seems to be relatively steady except for sample 18.

Fig. 2.14 (c) represents the stress-strain curves for samples with a 50% volume fraction of particles. This time, all the curves have more or less the same elastic behaviour. However, the scatter for the strength is quite high.

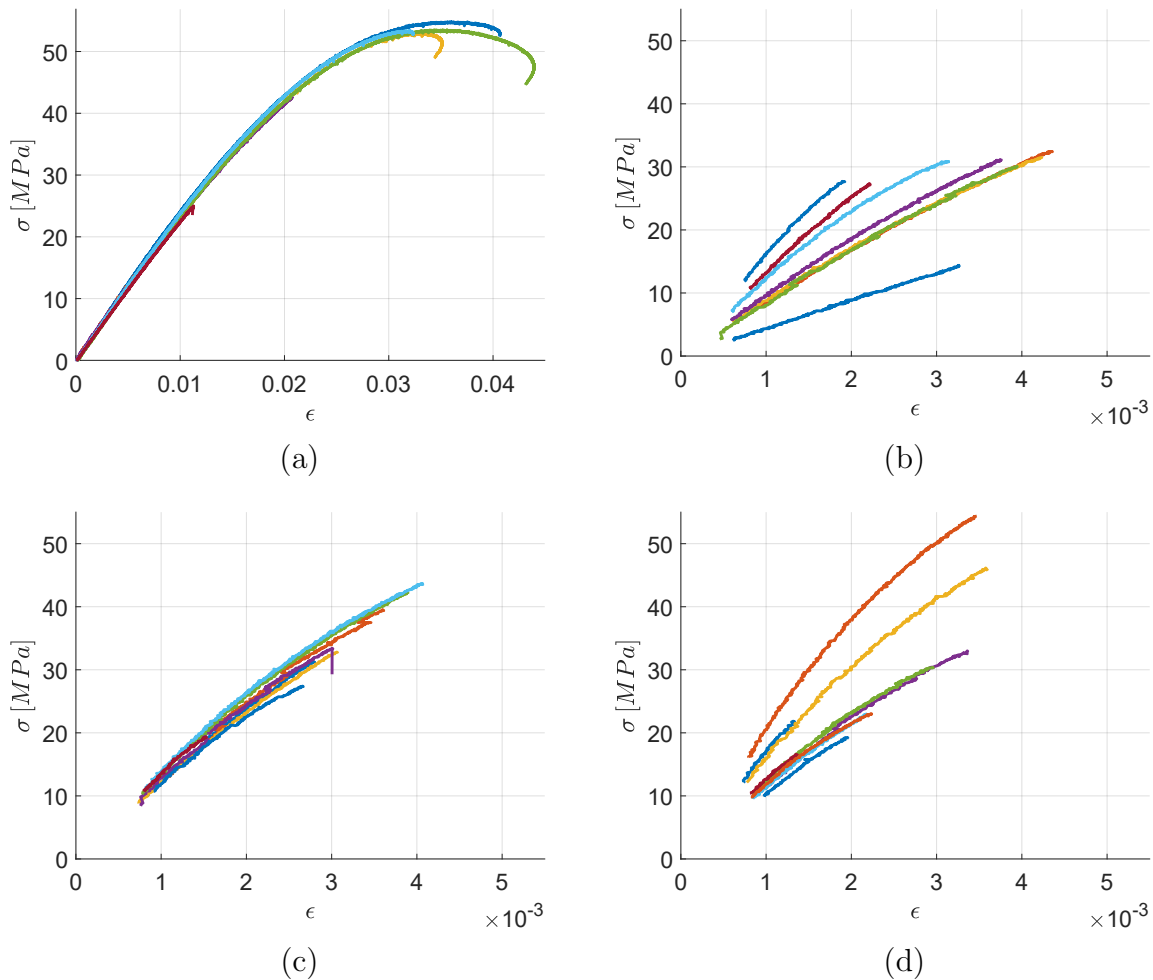


Figure 2.14: (a) Stress-strain curves for bulk adhesive samples;
 (b) Stress-strain curves for 40% volume fraction samples;
 (c) Stress-strain curves for 50% volume fraction samples;
 (d) Stress-strain curves for 60% volume fraction samples.

Fig. 2.14 (d) shows the stress-strain curves for samples with a 60% volume fraction and, once more, the scatter for elastic modulus and strength is very high. Some samples might have been saturated in particles as some of them look quite porous.

Concerning the failure, all the samples (from low to high particle volume fraction) exhibit a brittle behaviour. The first part of the loading is linear and is used to determine the elastic behaviour of the material. Then, a small non-linear behaviour is detected. It can be explained by particles debonding or matrix entering plastic regime. However, no softening behaviour is observed at all and the material catastrophically fails when a critical strength is reached.

From all these stress-strain curves, Young's modulus is determined with a linear regression of the elastic part of the curves. Young's moduli of all the samples are plotted against particle volume fraction in Fig. 2.15 (a). The scatter between the samples is very

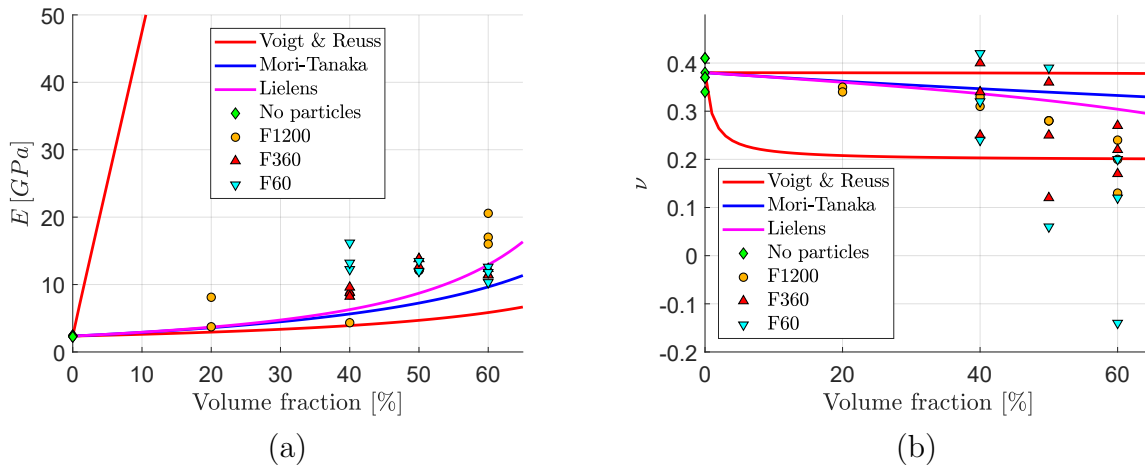


Figure 2.15: (a) Experimental Young's modulus for monodisperse particle sizes; (b) Experimental Poisson's ratio for monodisperse particle sizes.

high. Therefore, an a posteriori evaluation of the effective volume fraction of particles is presented here below in order to understand the scatter between the obtained results.

Poisson's ratio is also plotted in Fig. 2.15 (b) but the experimental measurements give unreliable values. This might be explained by the very low deformations observed during tensile testing and that the image correlation was not precise enough to accurately capture these small deformations.

Density measurements for effective volume fraction determination

As the scatter for Young's modulus is very high, it is interesting to determine the effective volume fractions of the samples. To do so, a precise protocol to measure the density is employed. This protocol is described in Appendix A.

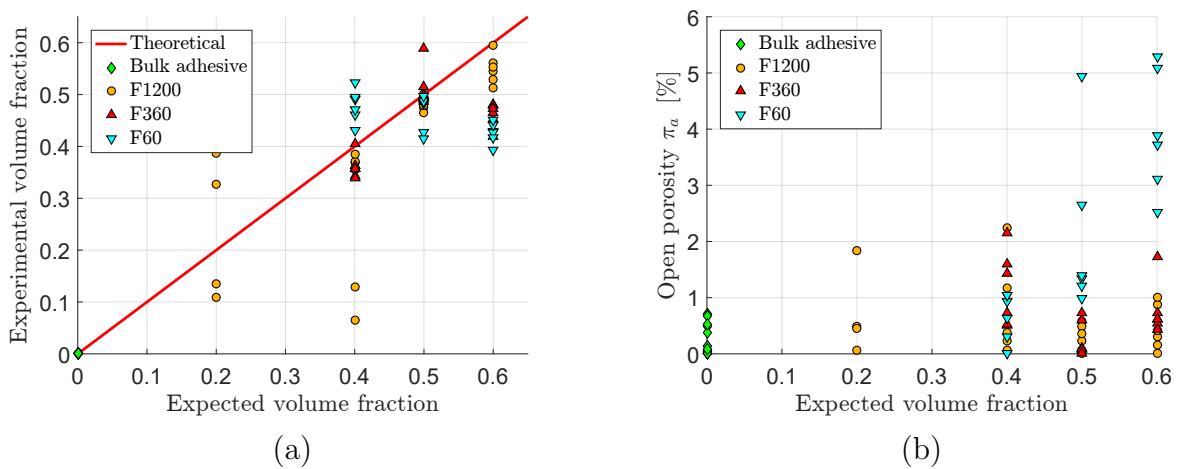


Figure 2.16: (a) Experimental volume fraction against expected volume fraction; (b) Experimental open porosity against expected volume fraction.

Fig. 2.16 (a) represents the volume fraction calculated from the density measured if we make the (strong) assumption that all our samples are not porous. We can see that for the expected volume fractions of 0.5, the real volume fractions are very close to the expected ones. That is not very surprising as for most particles, the packing density is close to this value. For volume fractions above 0.5, the density is clearly below the expected one. This suggests that the samples are quite porous. Then Fig. 2.16 (b) shows the open porosity of the samples against the expected volume fraction. The open porosity values rely on very small mass variations, and only a small water droplet can greatly influence the measurements. That is why these values are not of a great significance. However, they can give interesting trends. Notably, we see that at high volume fractions (0.5 and 0.6) and for the largest particles (F60), the open porosity values increase significantly (up to around 5%). This consolidates the observation that the porosities content increases with particle volume fraction.

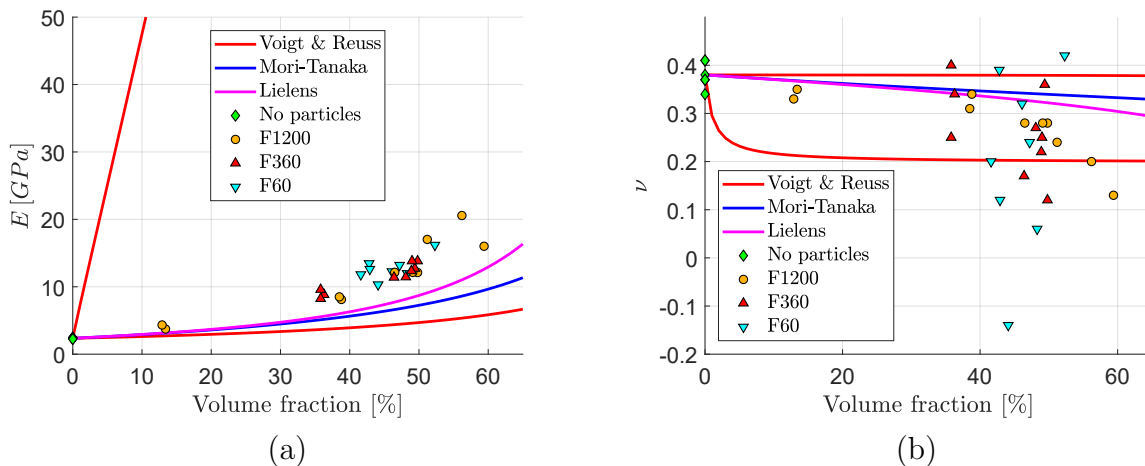


Figure 2.17: (a) Young's modulus against estimated volume fraction; (b) Poisson's ratio against estimated volume fraction.

Young's modulus of the composite is plotted against the estimated particle volume fraction in Fig. 2.17 (a). The scatter is significantly reduced, meaning that the expected volume fractions is indeed quite far from the real values. Two analytical homogenisation schemes are also represented on this figure (Mori-Tanaka and Lielens). The experimental values follow well the evolution predicted from both analytical models. However, they are slightly higher than both models. No particle size effect on material Young's modulus is detected. The analytical homogenisation models don't take into account particle size either. The values for Poisson's ratio (plotted in Fig. 2.17 (b)) are still very unreliable, and these tensile tests failed to give us the evolution of Poisson's ratio.

Tensile tests on samples with polydisperse particle sizes

The same tensile tests were carried out to determine the elastic properties of the composite with polydisperse particle sizes. It is interesting to study this material category as the differences in particle sizes allow to introduce higher volume fractions of particles (as seen in paragraph 2.1.2). The proportion of particle sizes is kept constant and is directly taken from [123] : 50% F1200, 25% F360, 25% F60.

Different total volume fractions of particles are used, and the following samples have been tested:

- 6 samples with 40% particle volume fraction;
- 6 samples with 50% particle volume fraction;
- 6 samples with 60% particle volume fraction;
- 6 samples with 65% particle volume fraction.

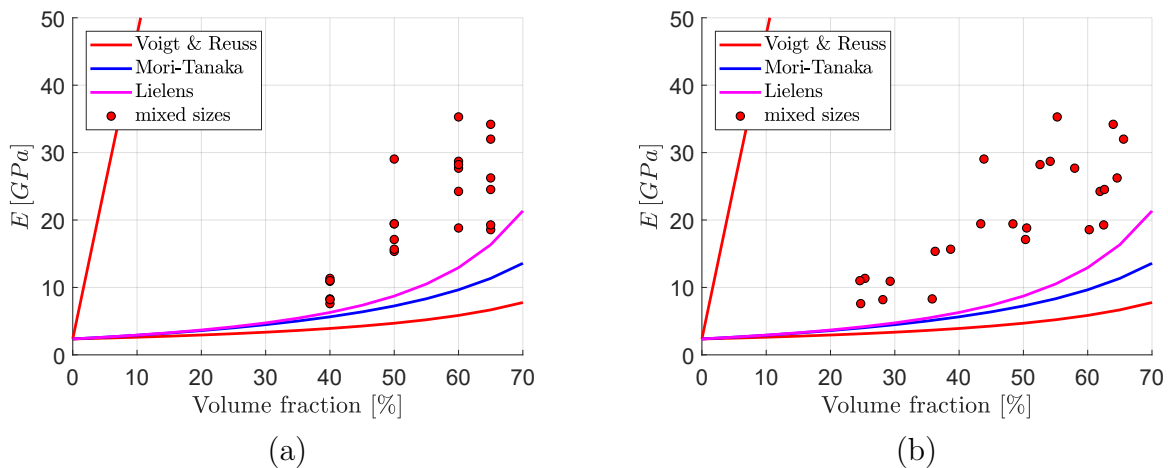


Figure 2.18: (a) Young's modulus for polydisperse particle sizes;
(b) Young's modulus with volume fraction from density.

Fig. 2.18 (a) depicts the evolution of the measured Young's moduli against particle volume fraction. Once more the scatter is quite high and the real particle volume fraction of the samples is estimated from density measurements. Contrary to what has been obtained with monodisperse particles, the scatter is still significant with the estimated volume fraction (Fig. 2.18 (b)). The values are still consistent with the previous ones obtained for monodisperse particles. This confirms the absence of influence of particle size on elastic properties on the material. Also, the introduction of particles with different sizes allows higher filler content (up to 65%) to be attained.

2.2.2 Numerical elastic homogenisation

Several analytical, numerical and experimental techniques have been developed in order to determine the effective properties of composite materials as a function of geometric and material properties of both the inclusions and the matrix. Each method presents a certain level of sophistication. Contrary to analytical theories, numerical-based techniques such as FE methods, do not make use of simplifying assumptions and are not as expensive as the experimental tests. In addition, depending on the level of refinement of the model, they can lead to realistic solutions in terms of the elastic response of the structure.

Unlike periodic structures, such as cellular solids, particle-filled composites do not show a repetitive unit that neatly reproduces the microstructure of the composite. In these materials the particles are in fact more or less randomly distributed and the resulting microstructure is a matrix containing a certain volume fraction of inclusions inordinately distributed. Therefore, the homogenisation method is applied at the micro-scale (the scale of the particles) not, as usually done, on a repetitive volume element but on a RVE able to take into account within the elastic response of the structure also the random distribution of the inclusions and their shape. No assumptions are made on the degree of symmetry of the homogenised structure, and all of the components of stiffness tensors are calculated. Thus, only in a second stage, through the analysis of the stiffness tensor components, the type and degree of elastic symmetry of the equivalent homogeneous medium is determined. Only after this second analysis, we are able to state that the equivalent medium is actually isotropic, orthotropic, etc.

Overview of the numerical homogenisation procedure

The basic assumptions made to evaluate the elastic response of the model and, hence, to determine the effective properties are:

1. linear, elastic behaviour for the materials of the matrix and particles;
2. perfect bonding for the wall-to-wall contact between matrix and particles.

An outline of the numerical homogenisation procedure developed in the framework of this study is presented in Fig. 2.19. The first step concerns the generation of the microstructure of the a RVE (characterised by imposed shapes, sizes and volume fraction of the particles). During the second step of the strategy, the FE-based homogenisation is performed on the RVE. Finally, a homogenised stiffness tensor is extracted, that gives the effective elastic moduli of a particles reinforced composite considered as an equivalent homogeneous material.

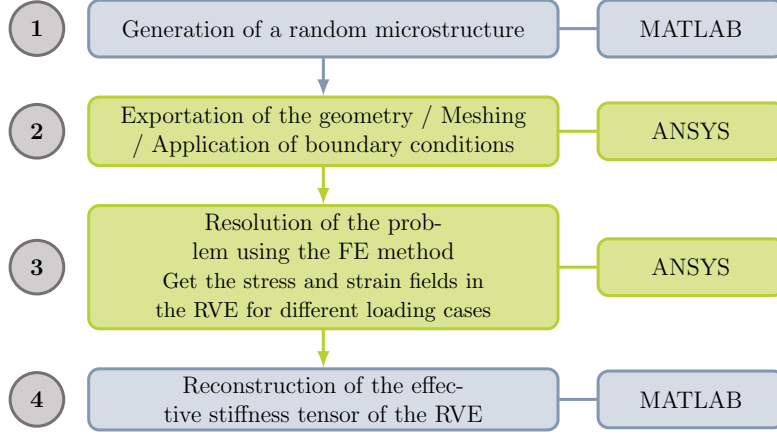


Figure 2.19: Numerical homogenisation scheme.

Periodic Boundary Conditions (PBC)

Periodic boundary conditions are applied to the square cell faces in order to ensure continuity of the displacement, stress and strain fields. The displacement of corresponding nodes on opposite faces are coupled. Let us denote the two directions of the plane as 1 and 2. The periodic boundary conditions can be expressed as a function of the displacement vector \underline{u} as:

$$\begin{cases} \underline{u}(0, y) - \underline{u}(L, y) = \underline{u}_1, \\ \underline{u}(x, 0) - \underline{u}(x, L) = \underline{u}_2, \end{cases} \quad (2.2)$$

where L is the length of both sides of the RVE. Then, to obtain three different loading cases in the plane (tensile loading along 1-direction, tensile loading along 2-direction, and shear in the 12-plane), three displacement combinations are imposed as presented in Tab. 2.6.

| Tensile 1-direction | Tensile 2-direction | Shear 12-direction |
|--|--|--|
| $\underline{u}_1 = \underline{U}_1$ $\underline{u}_2 = 0$ | $\underline{u}_1 = 0$ $\underline{u}_2 = \underline{U}_2$ | $\underline{u}_1 = \underline{U}_1/2$ $\underline{u}_2 = \underline{U}_2/2$ |

Table 2.6: Imposed displacements for the PBC, 3 different loading cases.

The global strain in the RVE is then calculated using the following equation:

$$\bar{\epsilon}_{11} = \frac{u_1}{L}, \quad \bar{\epsilon}_{22} = \frac{u_2}{L}, \quad \bar{\epsilon}_{12} = \frac{u_1 + u_2}{L}. \quad (2.3)$$

Once the linear elastic problem is solved, we can have access to the global averaged

stress, which corresponds to an area average on the RVE surface, computed as follows:

$$\bar{\sigma}_\alpha = \frac{1}{S_{RVE}} \int_{S_{RVE}} \sigma_\alpha dS, \quad \alpha = 11, 22, 12. \quad (2.4)$$

Reconstruction of the stiffness tensor

Under plane strain assumption, Hooke's law is written as follows:

$$\begin{Bmatrix} \bar{\sigma}_{11} \\ \bar{\sigma}_{22} \\ \bar{\sigma}_{12} \end{Bmatrix} = \begin{bmatrix} C_{1111} & C_{1122} & C_{1112} \\ C_{1122} & C_{2222} & C_{2212} \\ C_{1112} & C_{2212} & C_{1212} \end{bmatrix} \begin{Bmatrix} \bar{\epsilon}_{11} \\ \bar{\epsilon}_{22} \\ 2\bar{\epsilon}_{12} \end{Bmatrix}. \quad (2.5)$$

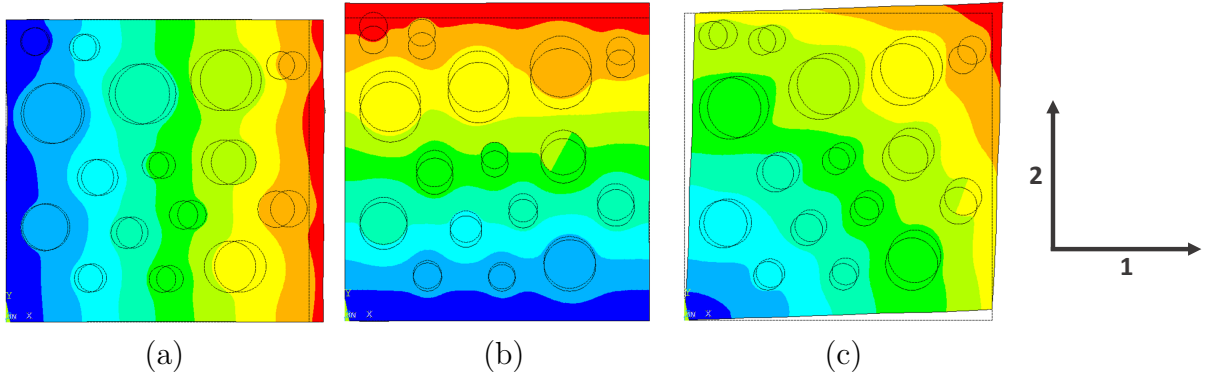


Figure 2.20: (a) Displacement field U_{11} of the RVE under tensile loading (1-axis);
 (b) Displacement field U_{22} of the RVE under tensile loading (2-axis);
 (c) Displacement field U_{12} of the RVE under shear loading (12-plane).

Three loading cases are necessary to determine all the components of the effective stiffness tensor in 2D (6 loading cases are required in 3D): uniaxial tension along the 1-axis and 2-axis and shear in the 12-plane. To reconstruct directly the columns of the effective stiffness tensor, we want to obtain a single non-zero value in the strain tensor (ϵ_{11} in the case of tension along 1-axis, ϵ_{22} in the case of tension along 2-axis, ϵ_{12} in the case of the shear in 12-plane). Fig. 2.20 represents the displacement field of each loading case. From each loading case, the strain and stress fields are determined thanks to eqs. 2.2.2 and 2.2.2, and then a column of the stiffness tensor is then calculated using the following relationships (eqs. 2.6, 2.7, 2.8):

$$\begin{Bmatrix} \bar{\sigma}_{11} \\ \bar{\sigma}_{22} \\ \bar{\sigma}_{12} \end{Bmatrix} = \begin{bmatrix} C_{1111} & * & * \\ C_{1122} & * & * \\ C_{1112} & * & * \end{bmatrix} \begin{Bmatrix} \bar{\epsilon}_{11} \\ 0 \\ 0 \end{Bmatrix}, \quad (2.6)$$

$$\begin{Bmatrix} \bar{\sigma}_{11} \\ \bar{\sigma}_{22} \\ \bar{\sigma}_{12} \end{Bmatrix} = \begin{bmatrix} * & C_{1122} & * \\ * & C_{2222} & * \\ * & C_{2212} & * \end{bmatrix} \begin{Bmatrix} 0 \\ \bar{\epsilon}_{22} \\ 0 \end{Bmatrix}, \quad (2.7)$$

$$\begin{Bmatrix} \bar{\sigma}_{11} \\ \bar{\sigma}_{22} \\ \bar{\sigma}_{12} \end{Bmatrix} = \begin{bmatrix} * & * & C_{1112} \\ * & * & C_{2212} \\ * & * & C_{1212} \end{bmatrix} \begin{Bmatrix} 0 \\ 0 \\ 2\bar{\epsilon}_{12} \end{Bmatrix}. \quad (2.8)$$

The 2D FE model

The finite element analysis is carried out using the commercial FE code ANSYS[®]. The geometry of the RVE, imported in ANSYS[®], is meshed with plane quadratic triangular elements (PLANE183, 6 nodes triangular elements) having two Degrees Of Freedom (DOFs) per node, i.e. the translations in the nodal 1 and 2 directions. The plain strain option is activated for these elements. A preliminary study allows to ensure that the results are mesh-independent with a mean elements size 100 times smaller than the length of the RVE.

Size of the RVE and its mechanical symmetries

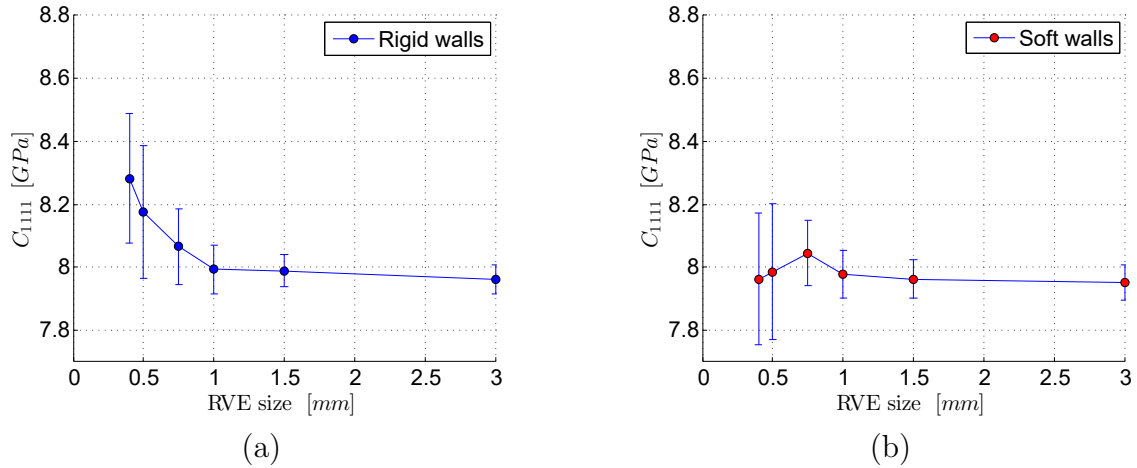


Figure 2.21: Evolution of the C_{1111} component of the stiffness tensor with standard deviation against the size of the RVE for the dropping and rolling algorithm with rigid walls (a) and with soft walls (b) for a fixed volume fraction $\phi = 0.4$.

The numerical tool described beforehand is used to evaluate the homogenised elastic behaviour of a particle reinforced composite, as a function of the elastic moduli of the phases and the volume fraction, the size, and shape of inclusions.

Three different RVE generation algorithms have been utilised and the results obtained from these types of microstructures will now be compared. The average size of particles

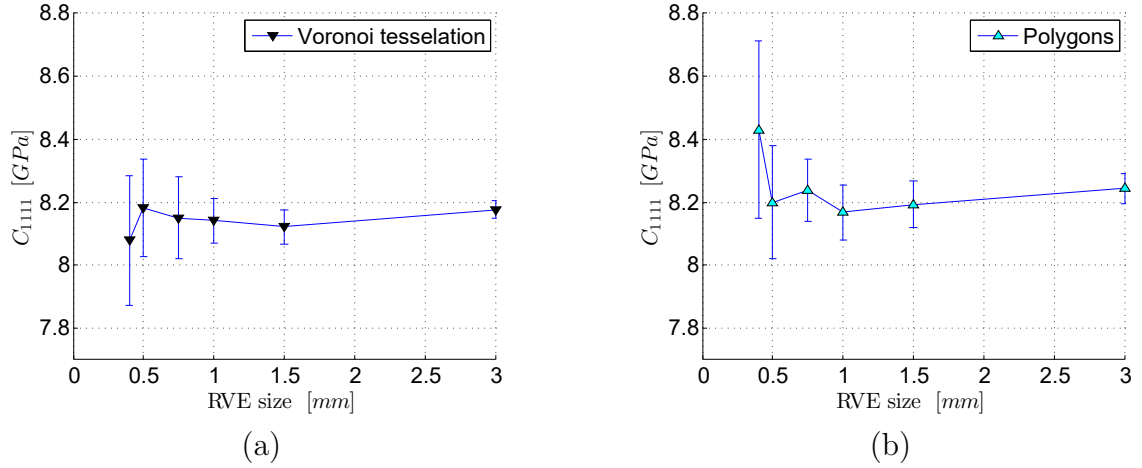


Figure 2.22: Evolution of the C_{1111} component of the stiffness tensor with standard deviation against the size of the RVE for Voronoi tessellation algorithm (a) and for the dropping and rolling algorithm with polygonal particles (b) for a fixed volume fraction $\phi = 0.4$.

obtained using the algorithms detailed beforehand ranges from $30\mu\text{m}$ to $100\mu\text{m}$. It is important to note that the calculation is fully elastic so that no scale effect appears.

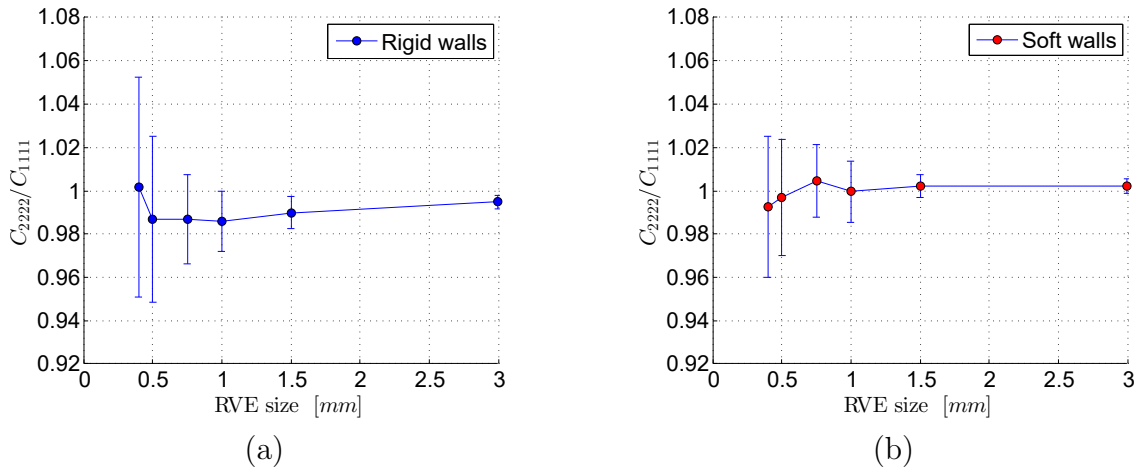


Figure 2.23: Evolution of the ratio C_{2222}/C_{1111} with standard deviation against the size of the RVE for the dropping and rolling algorithm with rigid walls (a) and with soft walls (b) for a fixed volume fraction $\phi = 0.4$.

Before performing the homogenisation, the first task is to determine the minimum size of the RVE able to give a proper representation of the macroscopic response of the composite material. This study is based on both the evolution of the elastic properties scatter and the one of mechanical symmetries as function of the size of the RVE. This is done for a fixed volume fraction of $0.40 (\pm 0.005)$.

For each algorithm, 20 microstructures are generated for different sizes of RVE (the

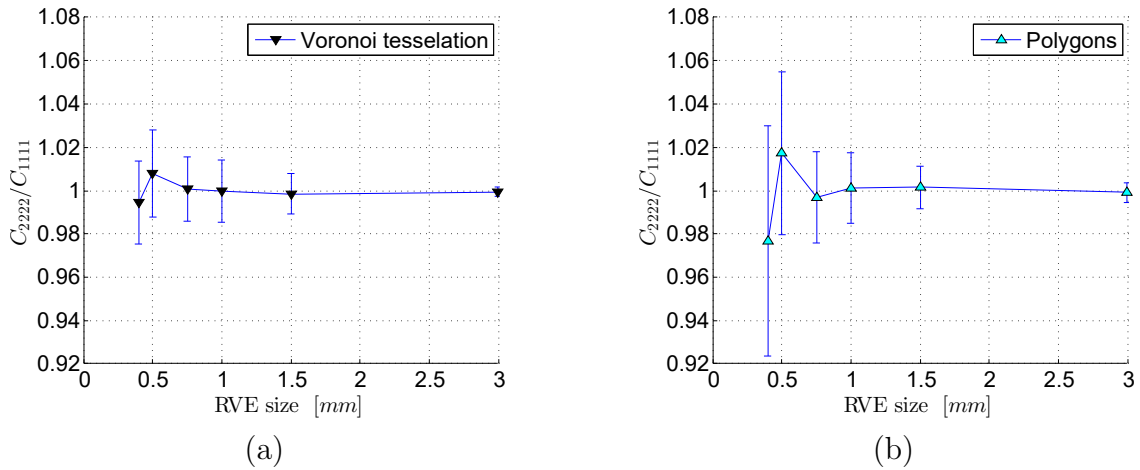


Figure 2.24: Evolution of the ratio C_{2222}/C_{1111} with standard deviation against the size of the RVE for Voronoi tessellation algorithm (a), for the dropping and rolling algorithm with polygonal particles (b) for a fixed volume fraction $\phi = 0.4$.

length of the square side ranging from 0.4 mm to 3 mm). The average for each 20 microstructures and the corresponding standard deviation are represented in Figs. 2.21 and 2.22. One can observe that under a 1 mm-size RVE, the average values and the standard deviation are not acceptable (the deviation is higher than a maximum tolerance value equal to 1%). A size of 1.5 mm seems to be the best compromise between accuracy and computational time. This size corresponds to approximately 60 particles.

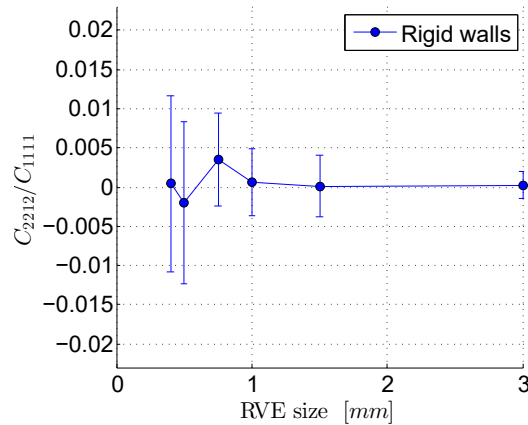


Figure 2.25: Evolution of the ratio C_{2212}/C_{1111} with standard deviation against the size of the RVE for the dropping and rolling algorithm with rigid walls for a fixed volume fraction $\phi = 0.4$.

The different algorithms will now be compared according to the mechanical symmetries of the RVE they generate. As well, in these analyses, the dependency of the RVE size is highlighted. This type of study has been carried out in [16], also for particulate reinforced

adhesives. The orthotropy of the RVE is first evaluated. Figs. 2.23 and 2.24 represent the ratio of the tensile elastic moduli in the 2-direction over the 1-direction. The average and the standard deviation are depicted for 20 microstructures and for different volume fractions. As for the size of the RVE study, the variation in results seems to be steady for a RVE size of 1.5 mm. All the algorithms converge to a ratio of 1, except the dropping and rolling with rigid wall boundaries. In this case, a slight orthotropy between the vertical and horizontal directions is evidenced due to oriented microstructure generation process.

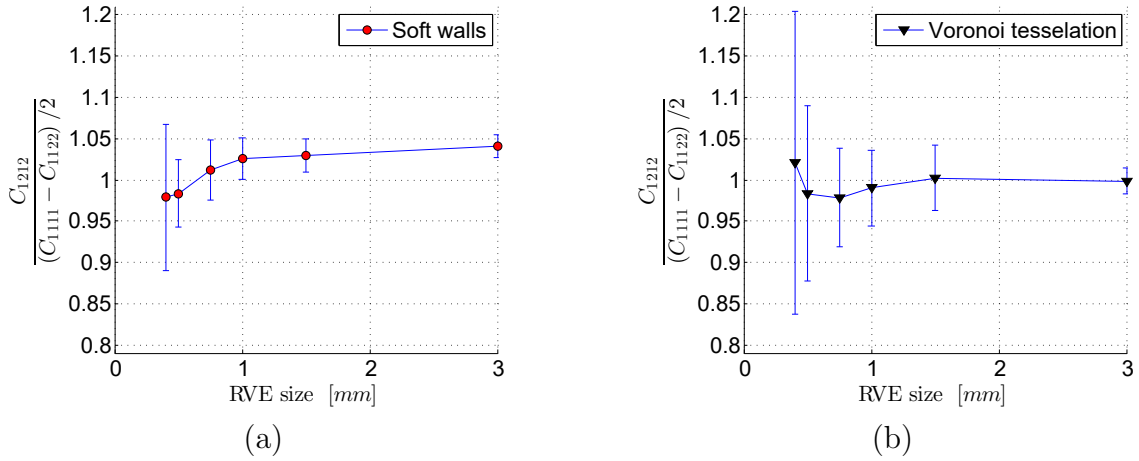


Figure 2.26: Evolution of the ratio $C_{1212}/((C_{1111} - C_{1122})/2)$ with standard deviation against the size of the RVE for the dropping and rolling algorithm with soft walls (a) and for Voronoi tessellation algorithm (b) for a fixed volume fraction $\phi = 0.4$.

The component C_{2212} of the stiffness tensor should be equal to 0 for isotropic materials (as for most of the materials with lower symmetries). Fig. 2.25 represents the ratio of C_{2212} over C_{1111} for the dropping and rolling algorithm. We see that for a RVE size of 1.5 mm, the variation of the component C_{2212} is lower than 0.5% of C_{1111} , which falls within the fixed tolerance. Same results are observed for all the other algorithms.

The isotropy of the microstructures is validated using the shear component C_{1212} of the stiffness tensor. In this case, C_{1212} is equal to $(C_{1111} - C_{1122})/2$ for isotropic materials. The evolution of the ratio of these components is depicted in Fig. 2.26. For isotropic microstructures, the ratio should tend to 1. For the three microstructures based on the dropping and rolling algorithm, this ratio tends to a value ranging between 1.03 and 1.05. Although the difference is very low (less than a 5% difference between C_{1212} and $(C_{1111} - C_{1122})/2$), this means that the microstructures generated from dropping and rolling are slightly cubic and not completely isotropic. The Voronoi tessellation algorithm gives fully isotropic microstructures as the ratio tends to 1.

2.2.3 Comparisons of numerical and analytical homogenisation results

In the framework of analytical homogenisation models existing in literature, one can also find the mean-field homogenisation schemes. These schemes attempt to describe the behaviour of a homogeneous medium equivalent to that of the heterogeneous one. All the mean-field homogenisation schemes described thereafter are derived from the pioneering work of Eshelby [41].

Eshelby's inclusion problem

In this section we will give a brief description of Eshelby's inclusion problem in order to give the mathematical and mechanical basis of the proposed model of this thesis. Then homogenisation schemes, derived from Eshelby's work will be explained.

A single ellipsoidal inclusion characterised by a stiffness tensor $\underset{\approx}{\mathbf{C}}_i$ is embedded in an infinite homogeneous matrix, with a stiffness matrix $\underset{\approx}{\mathbf{C}}_m$, submitted to a remote loading. Eshelby established that, for this so-called Eshelby's inclusion problem, the stress and strain field inside this ellipsoidal inclusion are homogeneous. To solve this problem, he uses an equivalent problem to the inclusion problem: one can consider a fictitious inclusion, whose stiffness tensor is equivalent to the one of the matrix, but submitted to a residual strain field called eigenstrain $\underset{\approx}{\boldsymbol{\epsilon}}^*$ (Fig. 2.27). Perturbation stress and strain fields ($\underset{\approx}{\boldsymbol{\epsilon}}^d$ and $\underset{\approx}{\boldsymbol{\sigma}}^d$) also appear due to the presence of the inclusion. Eshelby relates this perturbation strain field to the eigenstrain with a fourth-order tensor $\underset{\approx}{\mathbf{S}}^{Esh}$ called Eshelby tensor:

$$\underset{\approx}{\boldsymbol{\epsilon}}^d = \underset{\approx}{\mathbf{S}}^{Esh} : \underset{\approx}{\boldsymbol{\epsilon}}^* \quad (2.9)$$

Mura in [102] explained that this Eshelby tensor $\underset{\approx}{\mathbf{S}}^{Esh}$ only depends on the material properties of the matrix and on the inclusion shape. The expressions of the tensor are developed in [102] as a function of the different inclusions shape and the matrix symmetries. Explicit analytical formulations are obtained for special symmetries of the matrix (isotropic or transversely isotropic matrix for example).

Thanks to this fictitious equivalent problem, one can establish a relationship between the global stress $\underset{\approx}{\boldsymbol{\Sigma}}$ and strain fields $\underset{\approx}{\mathbf{E}}$ and the ones inside the inclusion ($\underset{\approx}{\boldsymbol{\sigma}}$ and $\underset{\approx}{\boldsymbol{\epsilon}}$). This relation between the micro and macro scale fields is called Kröner scale transition rule:

$$\underset{\approx}{\boldsymbol{\sigma}} = \underset{\approx}{\boldsymbol{\Sigma}} + \underset{\approx}{\mathbf{C}}_m : \left(\underset{\approx}{\mathbf{S}}^{Esh^{-1}} - \underset{\approx}{\mathbf{I}} \right) : \left(\underset{\approx}{\mathbf{E}} - \underset{\approx}{\boldsymbol{\epsilon}} \right) \quad (2.10)$$

With this relationship one can get a link between the strain inside the inclusion and the remote one, a fourth-order tensor called strain localisation tensor:

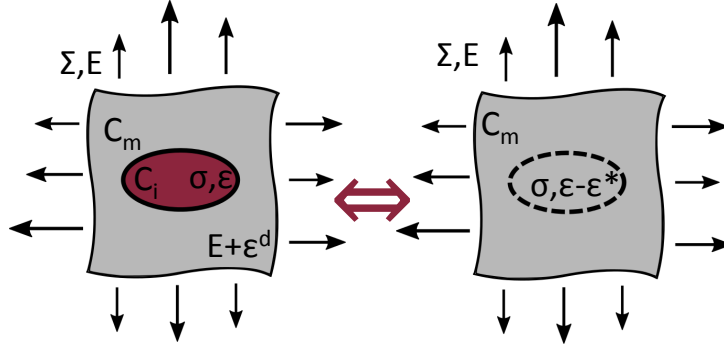


Figure 2.27: Eshelby equivalent problems

$$\underline{\underline{\mathbf{A}}}_i = \left(\underline{\underline{\mathbf{I}}} - \underline{\underline{\mathbf{S}}}^{Esh} : \left(\underline{\underline{\mathbf{I}}} - \underline{\underline{\mathbf{C}}}_m^{-1} : \underline{\underline{\mathbf{C}}}_i \right) \right)^{-1} \quad (2.11)$$

It is important to notice that one can obtain the strain localisation tensor for the matrix phase by replacing the subscript i of the inclusions by m and $\underline{\underline{\mathbf{A}}}_m$ becomes equal to the identity tensor $\underline{\underline{\mathbf{I}}}$. A similar relationship can be obtained with the micro and macro stress fields linked by the stress localisation tensor.

Directly derived from this theory, a single inclusion is considered in an infinite matrix (so that the interactions between the inclusions are completely neglected). The typical relationship of the mean-field homogenisation scheme to get the effective stiffness tensor is (for $(n + 1)$ -phase material with $r = 0$ being the matrix material):

$$\underline{\underline{\mathbf{C}}}_{eff} = \sum_{r=0}^n \phi_r \underline{\underline{\mathbf{A}}}_r : \underline{\underline{\mathbf{C}}}_r \quad (2.12)$$

This model allows to determine a homogenised stiffness tensor for composite materials. A drawback of this model relies on the fact that its results are relevant only when very low volume fraction of inclusions (< 0.1) are considered. That is the reason why this model is called High-Dilute model (HD) and localisation tensors related to the high-dilute model will now be written with the superscript HD.

Mori-Tanaka homogenisation scheme

Mori and Tanaka [101] tried to take into account the effect of the inclusions interactions. Their mean-field homogenisation was revisited by Benveniste [13]. According to [13], the effect of the interaction between the particles can be modelled by replacing the remote loading by the strain inside the matrix phase. The strain localisation tensor of an inclusion

becomes:

$$\mathbf{A}_{\approx i}^{MT} = \mathbf{A}_{\approx i}^{HD} : \left((1 - \phi) : \mathbf{A}_{\approx m}^{HD} + \phi \mathbf{A}_{\approx i}^{HD} \right)^{-1} \quad (2.13)$$

For multiphasic materials, the Mori-Tanaka scheme becomes:

$$\mathbf{A}_{\approx r}^{MT} = \mathbf{A}_{\approx r}^{HD} : \left(\sum_{r=0}^n \phi_r \mathbf{A}_{\approx r}^{HD} \right)^{-1} \quad (2.14)$$

$$\mathbf{C}_{\approx eff} = \sum_{r=0}^n \phi_r \mathbf{A}_{\approx r}^{MT} : \mathbf{C}_{\approx r} \quad (2.15)$$

Benveniste [13] demonstrates that the symmetry of the stiffness tensor is no longer certified when more than two phases are taken into account in the Mori-Tanka scheme (or non-aligned inclusions in the case of ellipsoidal inclusions).

The Mori-Tanaka scheme must be used for low to moderate volume fraction of inclusions because interactions between particles are not explicitly introduced in the formulae. However, thanks to its explicit formulation, this model can be easily and quickly implemented and its use is widely spread.

Lielens model

Lielens [93] explained that at low to moderate volume fractions of inclusions ($\phi < 0.4$), one can consider that the inclusions are clearly embedded in a matrix material. However, for high volume fractions of inclusions ($\phi > 0.6$), we can consider that the inclusions percolate and they can be therefore considered as the matrix material. To summarise, Mori-Tanaka scheme (which is, in the case of biphasic composite, equivalent to Hashin-Shtrikman lower bound) seems to be appropriate to determine the effective elastic moduli of composite materials for low to moderate volume fraction and inverse Mori-Tanaka (where we consider the particles as the matrix and the resin as inclusions, and which is equivalent to Hashin-Shtrikman upper bound) gives good results for high volume fraction.

To deal with these considerations, Lielens proposed to do a non-trivial interpolation between the Mori-Tanaka and the inverse Mori-Tanaka schemes. A mixture function F_{mix} is introduced to do the interpolation between the dilute strain localisation tensors of both models:

$$\mathbf{A}_{\approx i}^{Li HD} = \left((1 - F_{mix}(\phi)) \mathbf{A}_{\approx i}^{HD Low^{-1}} + F_{mix}(\phi) \mathbf{A}_{\approx i}^{HD Up^{-1}} \right)^{-1} \quad (2.16)$$

This mixture rule only depends on the volume fraction of inclusions ϕ . It must be monotonously increasing and must satisfy $F_{mix}(0) = 0$ and $F_{mix}(1) = 1$. Lielens proposed a simple relation:

$$F_{mix}(\phi) = \frac{\phi + \phi^2}{2} \quad (2.17)$$

Then, the strain localisation tensor of an inclusion is calculated:

$$\underline{\underline{A}}_i^{Li} = \underline{\underline{A}}_i^{Li HD} : \left((1 - \phi) : \underline{\underline{A}}_m^{Li HD} + \phi \underline{\underline{A}}_i^{Li HD} \right)^{-1} \quad (2.18)$$

It is important to notice that Lielens model cannot be applied to the case of porous media because the inverse Mori-Tanaka scheme gives an incoherent result for a medium with voids. Indeed, in this scheme, the voids are considered as the matrix, and the cohesion of the medium is no longer guaranteed.

To apply this model for multiphasic composites, Lielens in [93], recommends to use a two-steps homogenisation. He developed this procedure to homogenise composite with non-aligned ellipsoidal inclusions. First, the RVE is divided in multiple aggregates of similar inclusions embedded in the matrix. These aggregates are created so that they all have the same volume fraction, which is equal to the global volume fraction of the composite. Then, a first homogenisation step is carried out on each aggregate. Finally, a second homogenisation step is done between the homogenised aggregates. This procedure is depicted in Fig 2.28. Lielens recommends to use Lielens scheme for the first step of the homogenisation to obtain good results for the whole range of volume fraction, then to use Voigt model for the second step of the homogenisation in order to avoid non-symmetrical effective stiffness tensors.

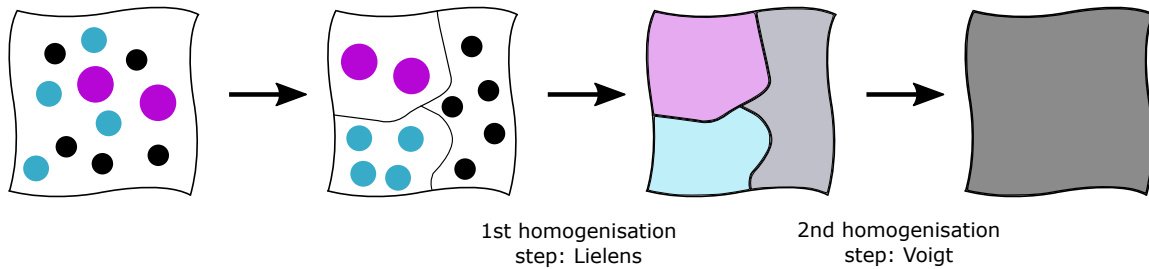


Figure 2.28: Two-steps Lielens homogenisation scheme for multiphasic material

Results of analytical and numerical models

The results obtained with this numerical procedure can be compared to those obtained using the analytical homogenisation schemes. To fit with the numerical results obtained under plane strain assumption, the homogenisation schemes presented hereafter are expressed with transversely isotropic structures, a matrix with infinite circular cylinders.

The Fig. 2.29 represents the evolution of the component C_{1111} of the stiffness tensor against the volume fraction of particles for all the analytical homogenisation schemes used in this study: Voigt and Reuss bounds, Hashin-Shtrikman bounds, Mori-Tanaka scheme, Self Consistent Scheme and Lielen's model. The computational results are compared to

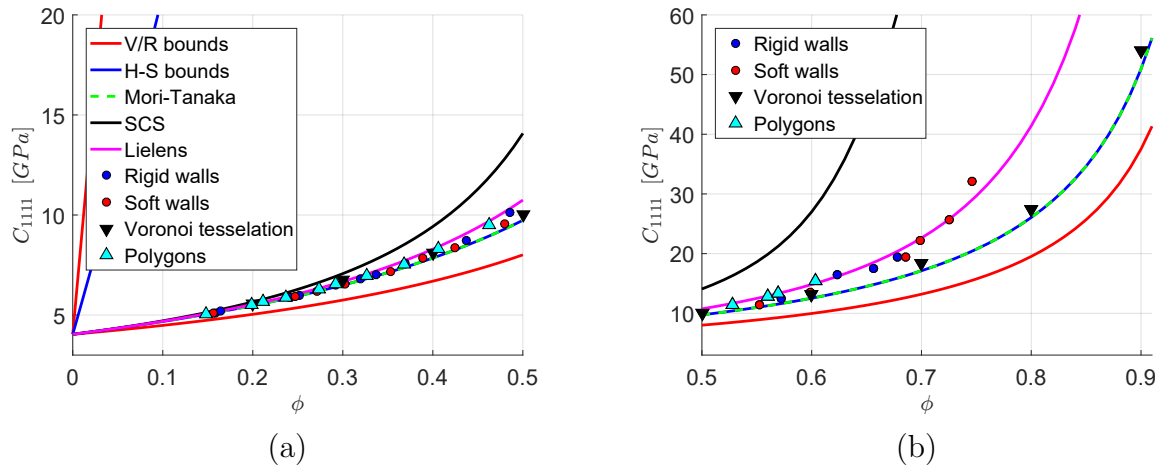


Figure 2.29: Homogenised C_{1111} component of the stiffness tensor against volume fraction ϕ for analytical homogenisation schemes; V/R bounds = Voigt and Reuss bounds, H-S bounds = Hashin-Shtrikman bounds, Mori-Tanaka scheme, SCS = Self-Consistent Scheme, Lielens' model; and for numerical simulations on RVE for (a) low volume fractions (b) high volume fractions.

these analytical models (Fig. 2.29 (a) for low volume fractions ranging from 0 to 0.5 and (b) for high volume fraction ranging from 0.5 to 0.9). The comparison is carried out on a volume fraction range between 0 and 0.9, even if the dropping and rolling algorithm is not able of producing volume fractions higher than 0.75. Over the whole range of volume fractions, the results lie between the Hashin-Shtrikman bounds.

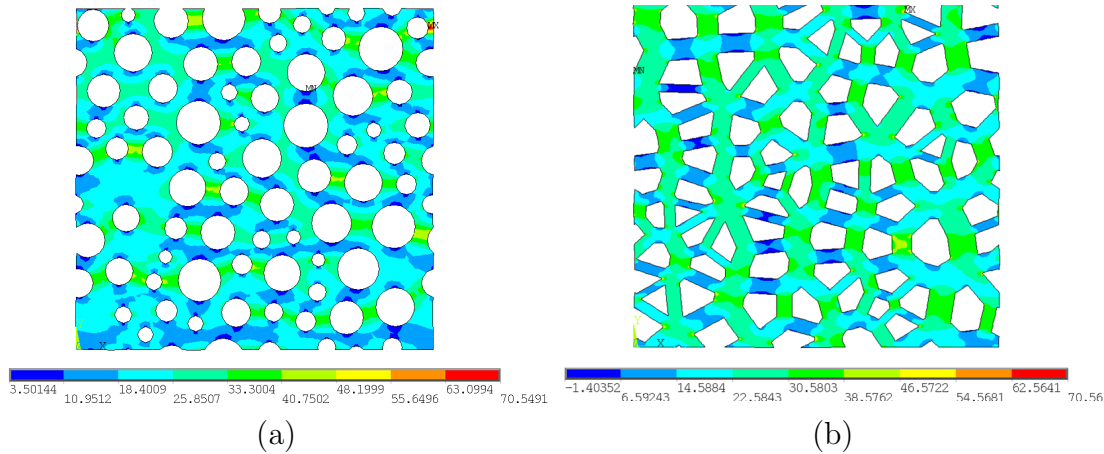


Figure 2.30: Local stress field σ_{11} in the the matrix of the RVE for the dropping and rolling algorithm (a) and the Voronoi tessellation algorithm (b).

For low to moderate volume fraction (0 to 0.4), the elastic moduli given by all the microstructures are very similar and are very close to the lower Hashin-Shtrikman bounds. Below a volume fraction around 0.5, the results start to differ for the different microstructure types. Similar trends are observed for most of the analytical homogenisation models.

The two boundary types (rigid wall and soft wall) give similar homogenised elastic moduli. A difference might appear when nonlinearities are taken into account, because the distribution of particles is less homogeneous due, to boundary effects in the case of rigid wall condition. The dropping and rolling algorithm with polygonal particles also seems to provide similar trends (differences lower than 10%). In the case of polygonal particles, we observe slightly stiffer equivalent homogeneous properties.

The best analytical homogenisation model to fit these data is Lielen's model, as cited by [80] and [55]. The microstructures given by the Voronoi tessellation algorithm give lower homogenised elastic moduli, close to Hashin-Shtrikman lower bounds. This could be due to the fact that, with this algorithm, the edges of the polygons are aligned with respect to that of its neighbours. To picture this difference with the other algorithms, Fig. 2.30 represents the local stress σ_{11} in the matrix of the RVE for a dropping and rolling microstructure and that of the Voronoi models. We can observe that some paths are completely unloaded in the case of the Voronoi microstructure.

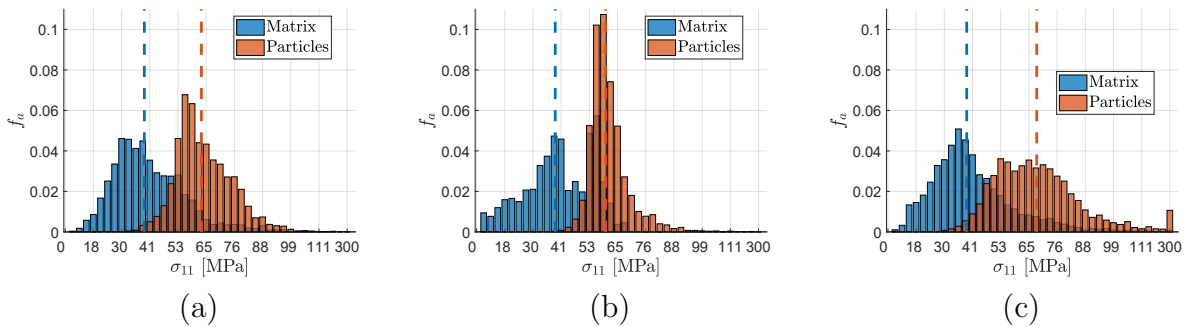


Figure 2.31: Histograms of stress distribution (area fraction) in the different types of microstructures with mean stress value (a) D&R with circular particles, (b) Voronoi tessellation, (c) D&R with polygonal particles ($\phi = 50\%$).

To have a better understanding of the stress distribution in the RVE, histograms of area fractions loaded are plotted in Fig. 2.31. The stress σ_{11} distributions in the two phases (matrix and particles) are represented for the three types of RVE generated (Dropping & Rolling with circular particles, Voronoi tessellation, and Dropping & Rolling with angular particles for a volume fraction $\phi = 50\%$ of monodisperse particles). The first observation is that particles support most of the load applied compared to the matrix and this for all the types of RVE. The mean stresses in the matrix are also very similar for each type of RVE meaning that the differences between the RVE lie in the stress field heterogeneities, hence the shape of the stress distribution histograms represented here. As an example, the stress field in the particles generated with the Voronoi algorithm shows a high peak and a small distribution around this peak meaning that the stress field is almost homogeneous in the particles generated using this algorithm.

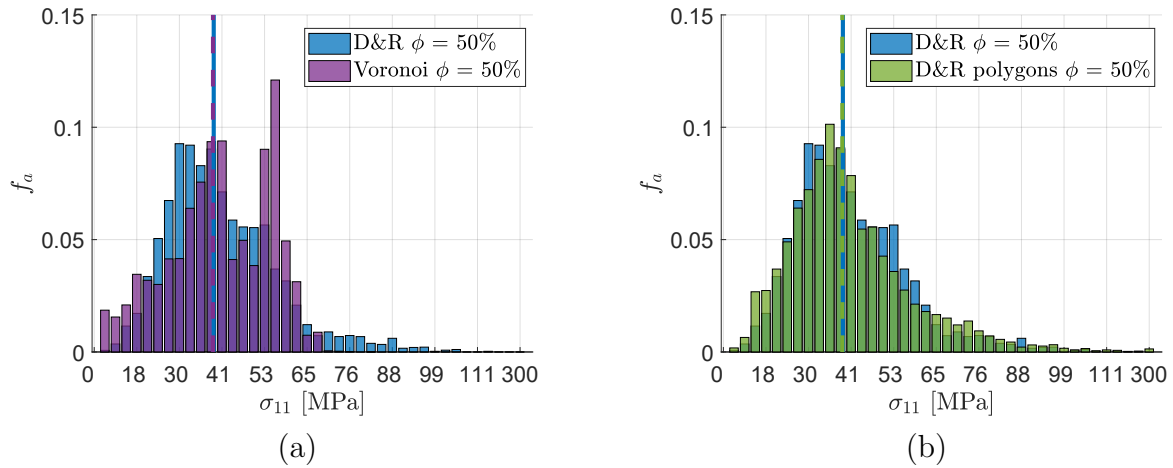


Figure 2.32: Comparisons of histograms of σ_{11} distribution (area fraction) in the matrices of different types of microstructures with mean stress value.

Comparisons between the stress σ_{11} distributions in the matrix using the Dropping & Rolling algorithm with circular particles and using the Voronoi tessellation (Fig. 2.32 (a)) and using the Dropping & Rolling algorithm with polygonal particles (Fig. 2.32 (b)) are made. The D& R algorithms with both circular and polygonal particles show bell-shaped-like curves centred on their mean values. However, with the Voronoi algorithm, two peaks are visible (around 40 MPa and 55 MPa). Also a large area fraction of the RVE is completely unloaded in tension contrary to the D& R algorithms.

These observations are correlated to observations of the stress fields in the matrix of the RVE represented in Fig. 2.33. Different stress zones are visible in the Voronoi RVE. The areas located between two particles which relative positions are perpendicular to the loading direction (vertical here) are all almost unloaded in tension. On the contrary, areas between two particles aligned with the loading direction are severely loaded.

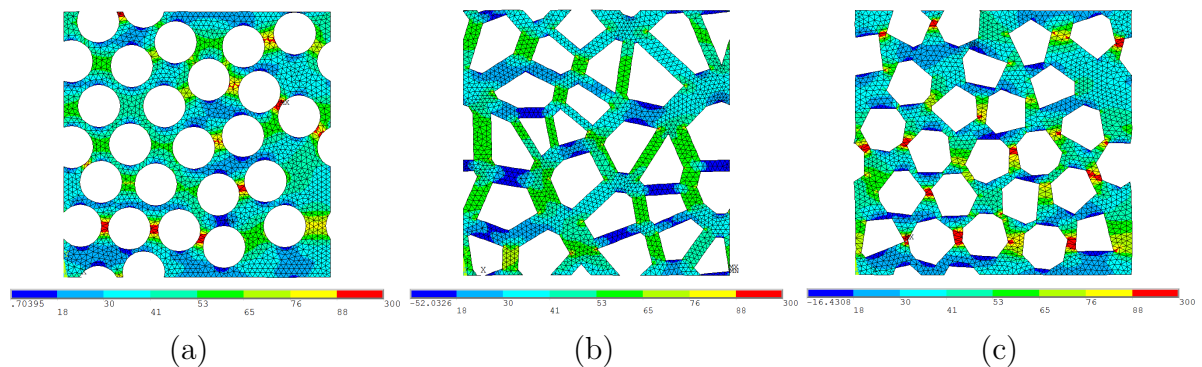


Figure 2.33: Stress σ_{11} distribution in the different RVE (a) D&R with circular particles, (b) Voronoi tessellation, (c) D&R with polygonal particles ($\phi = 50\%$) .

Very high stress concentrations are visible in the histograms of stress distribution with

polygonal D& R algorithm, which are not present with circular particles or Voronoi based microstructure. With the Fig. 2.33, one can remark that these very high stress concentrations are located at corners of polygons close to corners or edges of other polygons in the loading direction. It is also worthy to note that even if the Voronoi RVE contain particles with sharp angles, it shows the lowest stress concentrations due to the peculiar arrangements of particle edges.

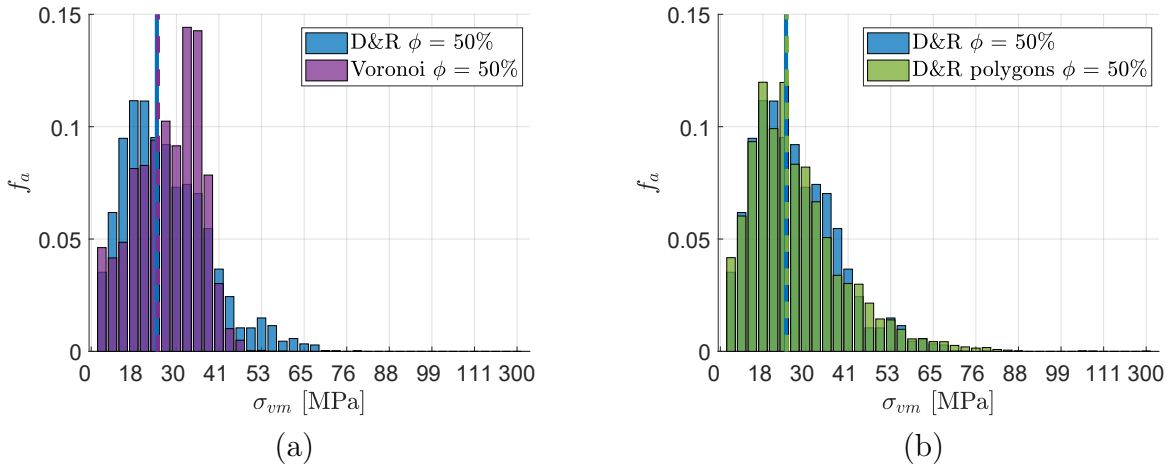


Figure 2.34: Comparisons of histograms of σ_{eq}^{vm} distribution (area fraction) in the matrices of different types of microstructures with mean stress value.

The same stress distribution analysis was carried out for von Mises stresses (σ_{eq}^{vm}) as this quantity is often used for plasticity or failure criteria and can represent the multi-axiality of the stress field. Histograms of area fraction loaded with von Mises stress are represented on Figs. 2.34. The stress distributions for the D& R algorithms with circular and polygonal particles are once more very similar. However, the Voronoi RVE show a more uniform distribution with a high peak around 35 MPa. Moreover, larger areas have very low von Mises stresses and the lowest stress concentrations of the three algorithms are determined.

The same analysis is made for the component C_{1212} of the stiffness tensor. This component represents the behaviour of the material under shear loading. A comparison between analytical models and numerical results is depicted in Fig. 2.35 (a) for low volume fractions and in Fig. 2.35 (b) for higher volume fractions. The numerical results also lie between the Hasin-Shtrikman bounds. The scatter between the different models seems to be a little bit higher than for the C_{1111} component. The same comparisons between analytical models and numerical results can be made, i.e. the results are very similar from low to moderate fractions and they start to differ for higher volume fraction (from $\phi = 0.5$).

Lielens model estimation seems to depict more accurately the results obtained with

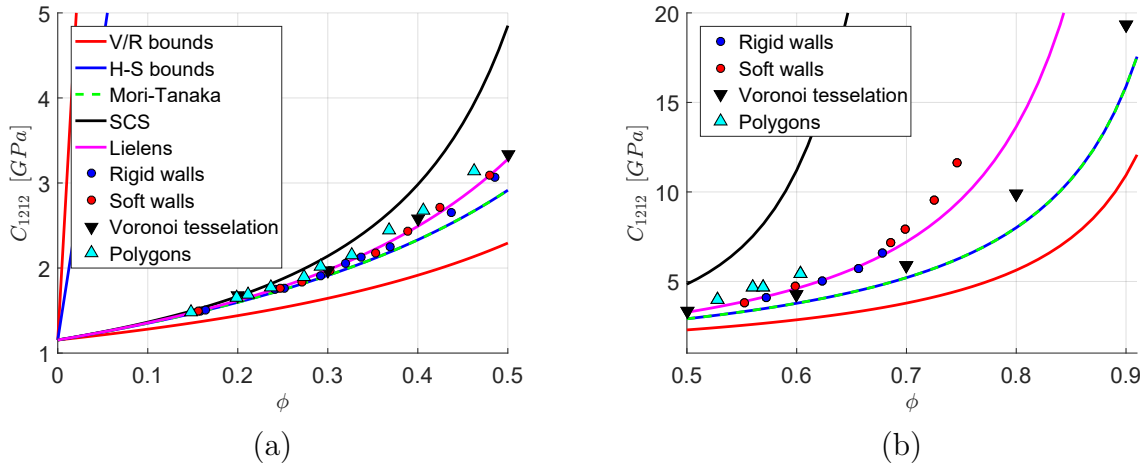


Figure 2.35: Homogenised C_{1212} component of the stiffness tensor against volume fraction ϕ for analytical homogenisation schemes; V/R bounds = Voigt and Reuss bounds, H-S bounds = Hashin-Shtrikman bounds, Mori-Tanaka scheme, SCS = Self-Consistent Scheme, Lielens' model; and for numerical simulations on RVE for (a) low volume fractions (b) high volume fractions.

the dropping and rolling RVE whilst the Voronoi tessellation RVE are closer to the lower Hashin-Shtrikman bound. The Voronoi tessellation microstructure shows this time a behaviour above the Hashin-Shtrikman lower bound. Similarly, the dropping and rolling RVE are slightly above Lielens model for this component, especially with polygonal particles. For the dropping and rolling models, this may be explained by the slightly cubicle behaviour that has been observed. Fig. 2.36 shows the local stress fields σ_{12} in the case of dropping and rolling microstructure type with circular particles Fig. 2.36 (a) and in the case of Voronoi type microstructure Fig. 2.36 (b). Multiples almost circular unloaded regions are visible between particles in the case of the dropping and rolling RVE, a phenomenon less important on the Voronoi RVE.

2.2.4 Comparison between numerical and experimental elastic modulus

The elastic properties obtained experimentally are now compared to the numerical models. Young's modulus is plotted against particle volume fraction in Fig. 2.37. The numerical results plotted here are obtained with the dropping and rolling algorithms (whether circular or polygonal inclusions are considered). As observed from the previous comparisons, experimental Young's modulus increase is well described by the numerical models. However, experimental values are still above the simulated ones.

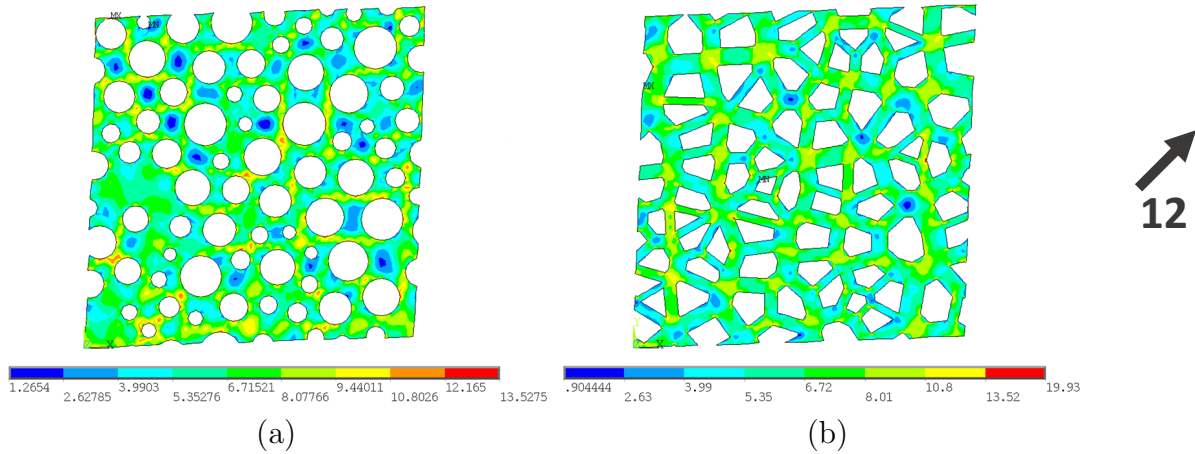


Figure 2.36: Local stress field σ_{12} in the the matrix of the RVE for the dropping and rolling algorithm (a) and the Voronoi tessellation algorithm (b).

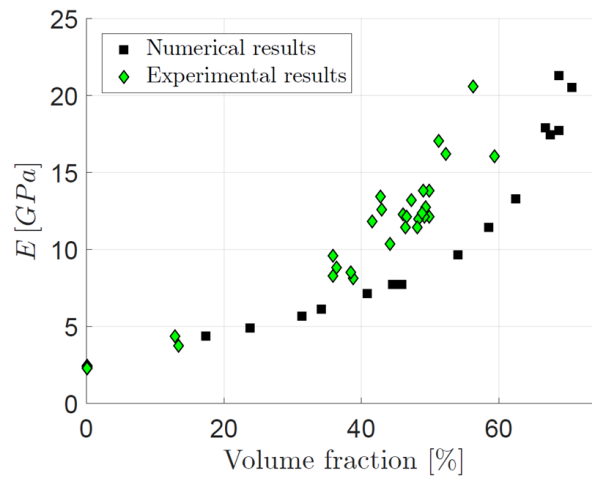


Figure 2.37: Comparison between Young's moduli obtained numerically and experimentally against particle volume fraction.

2.3 Conclusions

The first part of the chapter was dedicated to the observation of the components properties of a polymer reinforced with a high volume fraction of ceramic particles. The manufacturing process has been described and the elastic properties determined with three different analyses: experimental, analytical, and numerical ones. Finally, the following conclusions can be drawn from this study:

- The material is composed of angular particles embedded in a matrix. It is possible to reproduce representative microstructures with random generation algorithms. Higher volume fractions can be reached with the use of polydisperse particle sizes and their packing density can be estimated with simple models and experimental densities of monodisperse particles.

- The elastic properties of such a material have been determined from experiments and numerical models. Two types of homogenisation models can be employed to determine the effective elastic moduli of the material: analytical and numerical ones. The two types of models rely on different assumptions. The analytical models only depend on the components properties and their volume fractions. They only give access to averaged fields. Numerical ones are based on FE analyses of the complete microstructure. They give access to full fields.
- Young's modulus increases with particle volume fraction is similar to the one predicted by the different types of models. However, the experimental results are slightly above due to possible porosities that could lead to real particle volume fraction underestimation.
- No particle size effect on Young's modulus has been observed experimentally and none of the models predict an influence of the particle sizes. The shape of the particles do not seem to play a role in the elastic response of the material as long as the microstructure is not very specific (as with the Voronoi tessellation, where all the edges are parallel to each other). However, the angular geometry of the particles might play a significant role when damage occurs as there are strong stress concentrations at the sharp angles.
- Even for high particle volume fraction ($\phi = 0.6$), the composite stiffness is very low (around $15GPa$ against $450GPa$ for sintered B4C).

Chapter 3

Static failure of the ceramic particle reinforced material

In the previous chapter, the elastic properties of the particle reinforced material have been evaluated from a theoretical and experimental standpoint. However, for potential ballistic applications, not only the elastic properties but the failure conditions are of much importance. Then, the damage mechanisms and material properties such as strength and toughness should be studied. Impacts on ceramic tiles often lead to spalling failure due to the propagation of tensile acoustic waves produced by the reflection of the initial compression shock wave on the free surfaces of the tile. Long radial cracks are also observed away from the impact location because of tensile stress states developing along with the propagation of the incident compressive waves. For particle reinforced materials, multiple possible damage mechanisms can occur under tensile loading conditions: matrix failure and plasticity, particle failure, matrix/particle debonding. In this chapter, the material tensile failure is first studied experimentally using standard tensile test but also Iosipescu tests to determine the strength of the material. Bending tests on Single Edge V-Notch Beams (SEVNB) are then used to evaluate the material toughness. Then the numerical and analytical micromechanical models presented in the previous chapter are extended to take into account the material's nonlinear behaviour at the microstructure scale.

3.1 Experimental observation of tensile quasi-static failure

At first, series of experiments have been carried out to observe the failure of the material under tensile loading. Material properties such as tensile strength and toughness have been determined. Fracture surfaces are also observed with SEM to observe the damage

mechanisms at the microstructure scale. The effect of particle/matrix adhesion enhancement through the use of silane is also determined and observed.

3.1.1 Tensile strength and limitations of tensile tests for brittle materials

In the previous chapter, the tensile tests have been proposed for measuring the elastic moduli of the material. Exploiting these tests, the strength of the material is also determined. Except for the neat epoxy, the particle reinforced polymer exhibit a brittle-like behaviour similar to the one of a ceramic material. In this case, the overall failure of the specimen is attributed to the propagation of a single macro-crack initiating from the weakest point of the specimen where defects like a porosity or an inclusion could be observed. Such occurrence and consequently the specimen strength exhibit highly statistical behaviour. Also, large specimens may contain larger defect and tend to have lower strength. For such class of materials, not only the average strength should be evaluated but also the overall statistical failure behaviour.

Standard tensile tests on dogbone specimens are not recommended. Indeed, mastering such tests on brittle specimens is very delicate since early failure could occur if any misalignment of the specimen in the testing machine is introduced. Additional variability would then be introduced which is not due to the material behaviour. Alternative strength evaluation is proposed through the use of Iosipescu shear tests.

3.1.2 Iosipescu shear tests

Iosipescu shear tests were employed as an alternative to tensile tests to determine the strength of the material. Indeed, even if a shear loading is applied on the sample, the particular geometry of the Iosipescu sample leads to tensile failure in the notch region which induces the onset of a single crack in mode I condition in the case of brittle materials. The main advantages of this test configuration are localisation of tensile stresses in the specimen and better control of loading conditions limiting the variability on the test conditions [27].

Samples and setup

The geometry of the Iosipescu specimens is depicted in Fig. 3.2 (b). It consists in a straight beam where two V-notches of 90° angle are introduced in the middle. The tip of the notch is not sharp but curved, the radius of curvature is equal to $R = 1.5$ mm, to introduce a stress concentration rather than a stress singularity. To obtain such a geometry, the samples are manufactured in a three parts metallic mould, as presented in

Fig. 3.1. The three parts are screwed together once the mixture has been deposited in the mould. This division in three parts ensures a simple release of the samples after curing. The same manufacturing protocol as the one described in chapter 2 is used here, including mixture preparation, degasing and autoclave curing.

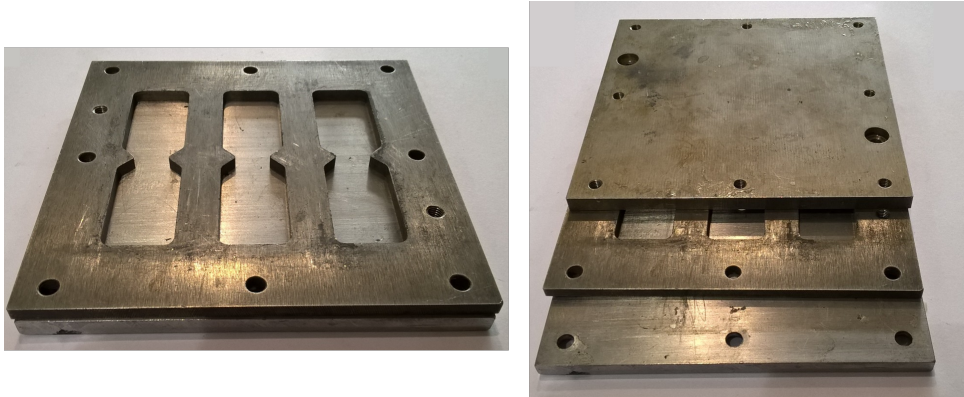
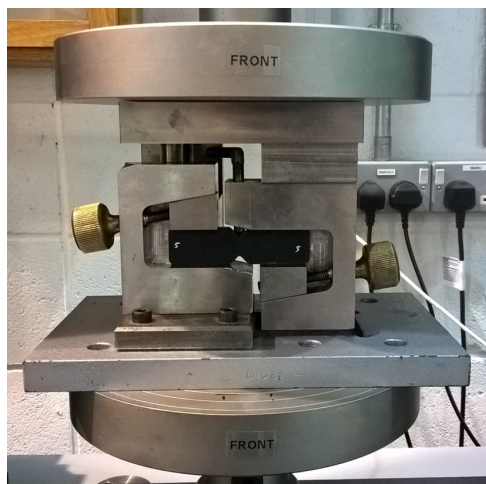
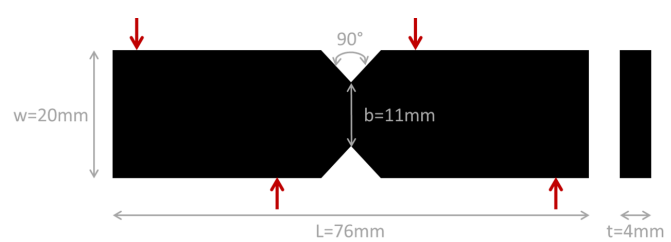


Figure 3.1: 3-part Iosipescu mould.

The Iosipescu shear tests are performed by placing the specimen in the fixture presented in Fig. 3.2 (a). The left part of the fixture is tightened to the fixed part of the tensile testing machine, while the right part of the fixture is loaded with a compression plate attached to the mobile crossbar.



(a)



(b)

Figure 3.2: (a) Iosipescu test setup;
(b) Iosipescu sample geometry and loading conditions (red arrows).

This test protocol was primarily designed to evaluate the shear behaviour of ductile materials. In that case, failure occurs when a vertical crack has developed in between the tips of the two notches. However, the evaluation of stress distribution in the notch region indicate peak tensile loading condition at the tip of the notches which could be used to

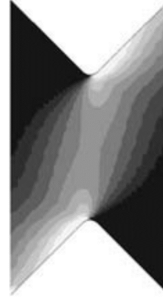


Figure 3.3: Contours of maximum principal stress field between the notches (from [129]).

evaluate tensile strength of brittle materials (see Fig. 3.3). Indeed, for brittle materials, because their tensile strength is low compared to their shear strength, two parallel cracks propagate orthogonally from the two notch surfaces. In the Iosipescu configuration, the principal normal stresses observed lay on a plane forming a 45° angle with the vertical plane between the notches. The failure observed in this direction is then due to a pure tensile stress state and this tensile stress state is equal to the shear one between the notches. The shear stress calculated with the formula 3.1, can therefore be used to evaluate the tensile strength of the material.

$$\tau_{xy} = \frac{P}{bt}, \quad (3.1)$$

where τ_{xy} is the shear stress between the notches, P is the load applied, b is the width between the notch tips, and t is the thickness of the sample.

Fracture observation

Although we previously stated that two parallel cracks perpendicular to the notch surfaces should develop for brittle material, four different types of failure are effectively observed during the tests:

- a single crack with an angle of 45° from the vertical direction (Fig 3.4 (a));
- a single crack with an angle of 0° from the vertical direction (Fig 3.4 (b));
- two cracks propagating, one at 45° and one at 0° (Fig 3.4 (c));
- two cracks propagating with a 45° angle (Fig 3.4 (d)), which is the nominal situation described previously for brittle materials.



Figure 3.4: (a) Single 45° crack;
(b) Single 0° crack;
(c) Double 0° and 45° cracks;
(d) Double 45° cracks.

Effect of silane treatment

The effect of the particle/matrix adhesion enhancement with silane on the fracture behaviour of the composite is first studied using the Iosipescu method. In order to reach high volume fraction (60% volume fraction) of particles, three different grit sizes were mixed with the following proportions:

- 50% of F1200 particles (small particles);
- 25% of F360 particles (medium particles);
- 25% of F60 particles (large particles).

Two series of specimens were tested: no silane treatment was applied to the particles of the first batch, whereas for the second batch, enhanced adhesion is expected due silane application.

The average values and the standard deviations of the measured strength of each specimen with and without silane treatment are reported in Fig. 3.5. The strength of the material treated with silane is almost twice as high as the one of the material without silane (38 MPa compared to 20 MPa). Also, the standard deviation is visibly lowered when silane is applied on the surface of particles (4 MPa against 6 MPa). The silane is expected to ensure the formation of strong covalent chemical bonds between the boron carbide particles and the matrix which might not be the case by direct bonding of the epoxy network to the particles. The enhanced strength of the material is a clear evidence that silane application was efficient. Apart from the mean strength increase, the strong

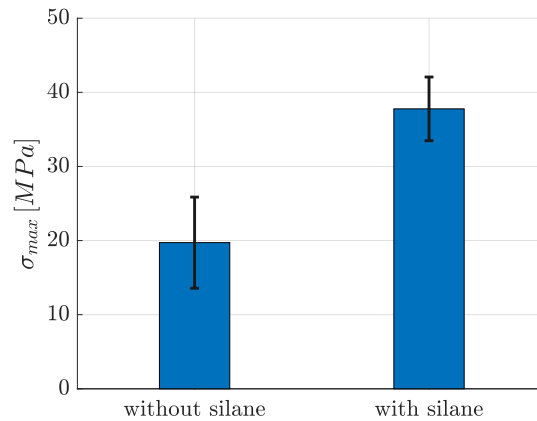


Figure 3.5: Average strength and standard deviation of the material with and without silane treatment.

reduction of the strength variability is also to be noticed. In relative value, the dispersion value is divided by a factor 3 leading to a more deterministic behaviour of the material.

The expected effect of the silane is to create chemical bonds between the boron carbide particles and the matrix. It is therefore clear that the silane plays its role and enhances the transfer of the stress from the resin to the very stiff particles, reason why the strength of the material is greatly increased. It also seems that the silane gives a more deterministic behaviour to the material as the standard deviation has been reduced by addition of silane.

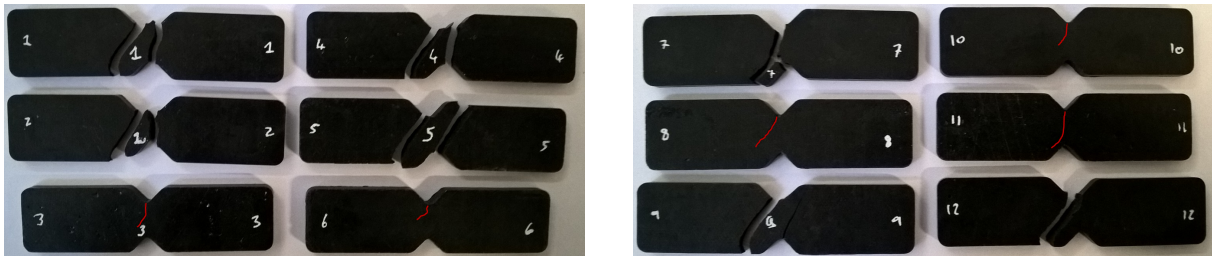


Figure 3.6: Iosipescu samples without silane treatment after failure.

Apart from the sole evaluation of the material strength, the observation of the failure mode is also of interest. All the Iosipescu specimens after failure are represented in Fig. 3.6 (no silane treatment) and Fig. 3.7 (with silane treatment). Multiple types of failure were observed for the specimens prepared without silane treatment, whereas only 45 cracks were observed when silane was applied to the particles.

For this experimental campaign, a sufficiently large number of samples have been tested to perform statistical analyses and identify a Weibull distribution parameter which is generally used for describing brittle failure statistic [153]. To determine the Weibull parameters, the N measured strength are first ranked in an ascending order $I = 1, \dots, N$

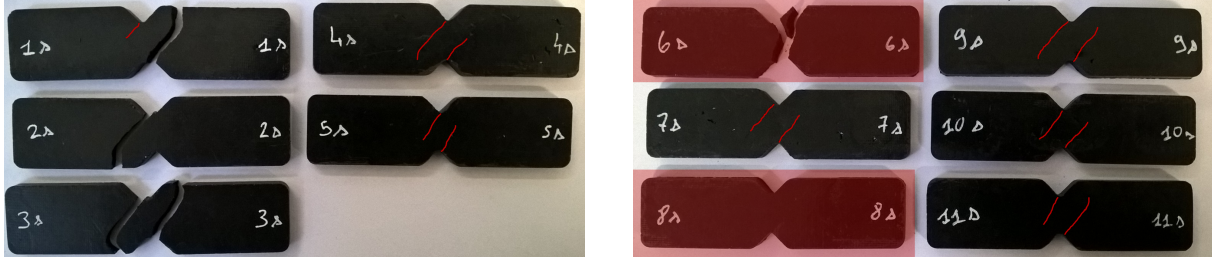


Figure 3.7: Iosipescu samples with silane treatment after failure.

and the associated failure probability is derived:

$$P_F = \frac{i - 0.5}{N}, \quad (3.2)$$

i and N being respectively the rank and total number of tested specimens. The probability of fracture is plotted as a function of measured strength in a $\ln(-\ln(1-P_F))$ against $\ln(\sigma_F)$ graph. Then, if the material failure is described with a Weibull distribution, the dots are aligned and a simple linear regression using least squares minimisation could be used to evaluate Weibull modulus and “average” material strength (see Fig. 3.8).

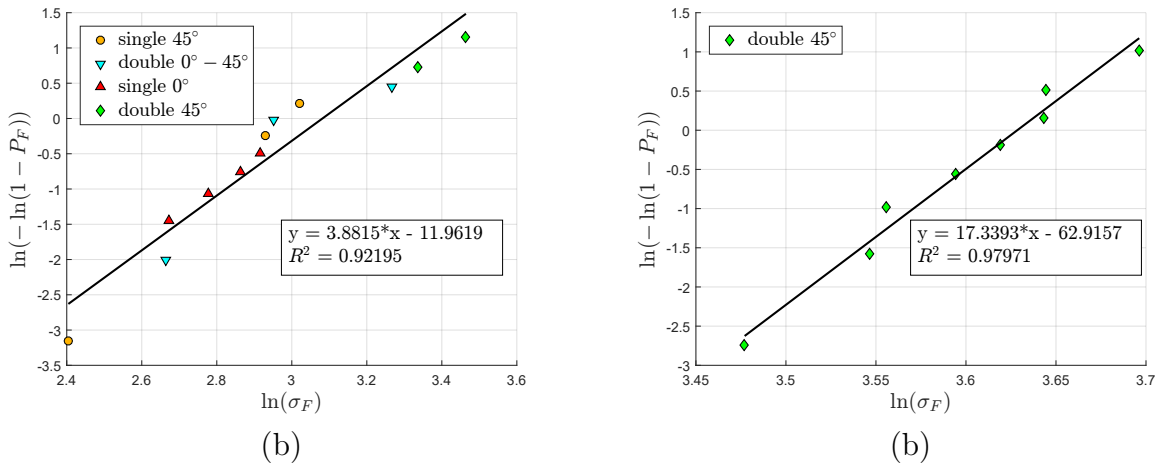


Figure 3.8: Weibull statistics of the strength of the material without (a) and with (b) silane treatment.

In Fig. 3.8 (a), the Weibull statistics of the material without silane is depicted. The different failure modes are also outlined using different dot shapes and colors. From this graph, we can effectively observe that the material follows a Weibull statistical behaviour. However, the double 45° cracks failure mode is only observed for the largest strength values and also correspond to the failure mode when silane treatment is applied to the particles (Fig. 3.8 (b)). This clearly indicates that the particle/matrix debonding mechanism is of most importance to trigger the root causes of the whole failure process which might be initiated by this initial damage.

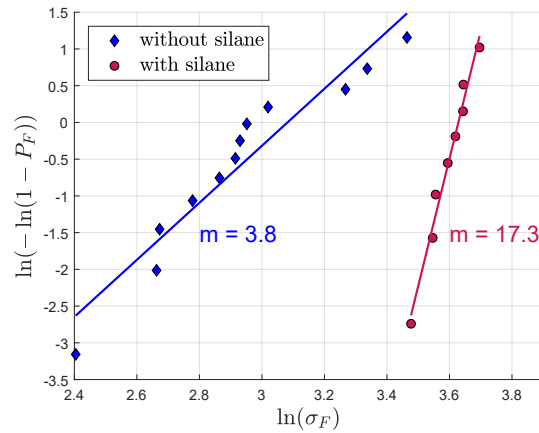


Figure 3.9: Comparison of Weibull statistics for the material without and with silane treatment.

Finally, both Weibull plots are reported on the same graph (Fig. 3.9). The slope of the line for the material with silane treatment is higher than the one for the material without silane which is consistent with larger strength dispersion associated to lower Weibull modulus value. A larger variability of the whole failure process in the case of non-treated particles indicates a larger variability on the strength of the particle/matrix interface or a larger sensitivity damage initiation to particle size.

Observation of silane effect

The composite material is obtained by adding boron carbide particles to a brittle epoxy resin matrix. This material exhibits a brittle behaviour so that the Iosipescu shear test is adequate to evaluate the tensile strength of the material because the crack initiate under uniaxial tensile stress condition, forming a 45° angle with the vertical plane between the notch tips. The addition of silane to enhance the cohesion between the boron carbide particles and the epoxy matrix is responsible for a considerable increase of strength. It also seems that the size of voids/porosities observed on the fracture surfaces has been reduced and can be one of the factors explaining such an improvement.

Fracture surfaces of the failed samples are depicted in Fig. 3.10. The effect of silane treatment is visible on the surface of the large particles (F60). Indeed, no residual resin is observed on the surface of such particles indicating adhesive failure (see Fig. 3.10 (a)) and poor adhesion. On the contrary, the fracture surface feature when silane treatment is applied is rather different since residual resin on the surface of these particles is observed (see Fig. 3.10 (b)) indicating particle/matrix might not be the root cause but a consequence of the whole process. It is more likely that the presence of particles strongly bonded to the resin activate plastic deformations in the resin prior to decohesion, that

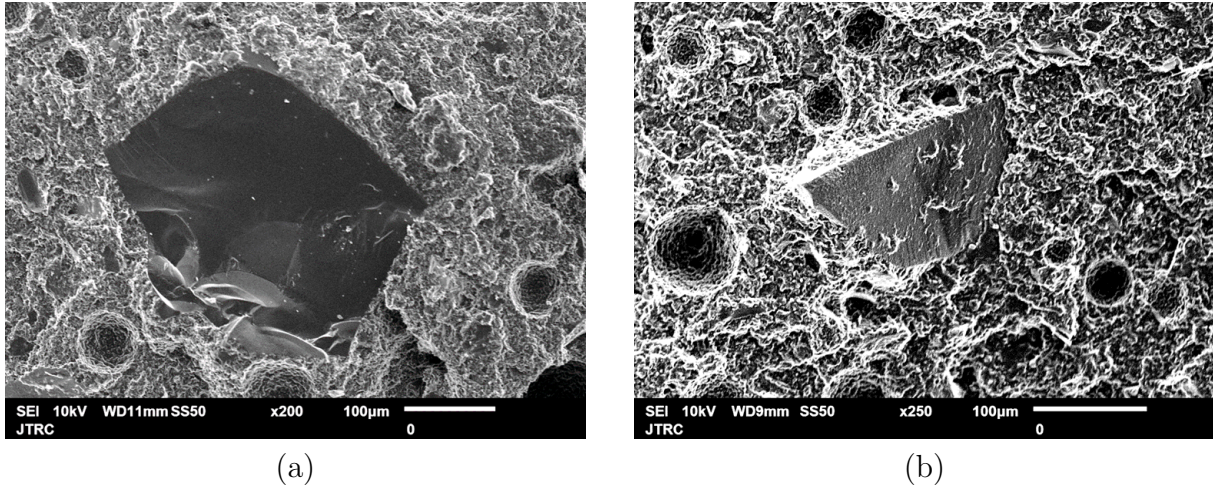


Figure 3.10: Fracture surfaces without (a) and with (b) particle silane treatment

can be observed in the material either in the resin alone or at the interfaces between the matrix and the particles.

Effect of particle volume fraction

Samples containing distinct volume fractions of particles were manufactured in order to observe the effect of particle volume fraction on the strength of the composite. Samples with mixed particle sizes (50% F1200, 25% F360, 25% F360) were manufactured. The considered particle volume fractions were 30%, 40%, 50% and 60%. Three samples for each volume fraction considered were tested. No silane treatment was used for these samples.

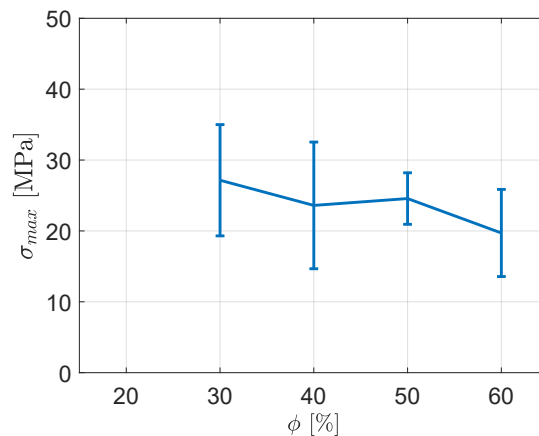


Figure 3.11: Evolution of the material strength against particle volume fraction.

The results of the Iosipescu tests on these samples are represented in Fig. 3.11. The strength seems to slightly decrease with particle volume fraction. Unfortunately, the dispersions on the strength measured for each configuration is the same order than the

overall variation so that no clear conclusion can be drawn. For particle weakly bonded to the resin, early interface failure is supposed to occur so that in the worst case the load is sustained by the resin only, so that the effective surface of the damaged material is smaller for composite having higher particle volume fraction, then leading to lower strength. Again, to maximise the material strength, it is important to optimise particle/matrix adhesion so that the resin enters plastic regime before particles separate from the matrix.

Effect of particle size

The effect of particle size has also been studied by measuring the material strength using the Iosipescu test and considering specimens made with distinct monodispersed particle sizes (i.e. F60, F360, and F1200 grades). 3 specimens were tested for each particle size. For all specimen the particle volume fraction is 50%.

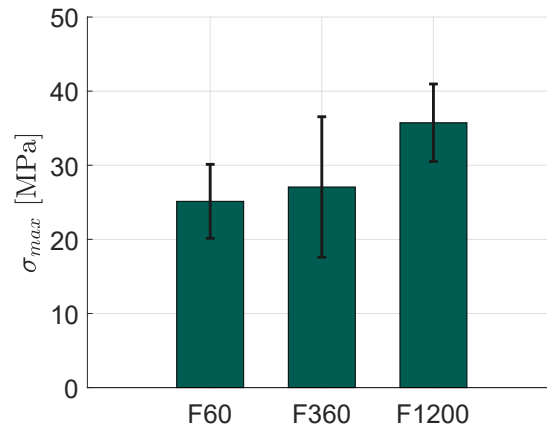


Figure 3.12: Evolution of the material strength against particle size.

The results are reported in Fig. 3.12. The strength visibly increases with decreasing particles sizes as the samples with F60 particles showed the lowest strength and the ones with F1200 particles the highest strength. This observation is in good accordance with the literature as seen in Chapter 1. Other theoretical evidences of the particle size effect will be discussed more in details in the next chapter.

3.1.3 Single Edge V-Notch Beam tests (SEVNB)

The influence of particle/matrix adhesion on the particle reinforced composite was also studied using four point bending tests on Single Edge V-Notch Beam (SEVNB) protocol. The test specimen consists in a slender beam having rectangular cross section ($B \times W$) where a sharp notch is introduced in the middle with a saw cut. The beam is loaded using 4-point bending fixture. A linear elastic response should be observed before the a

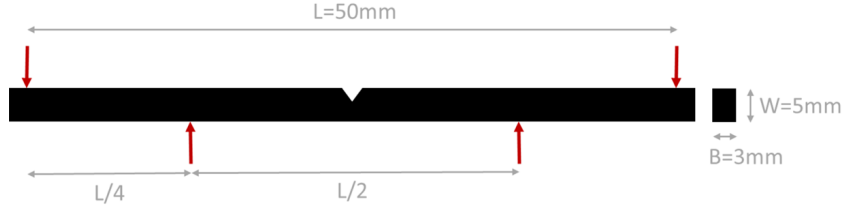


Figure 3.13: Dimensions of the SEVNB sample from standard ISO 23146.

critical load is reached where a single crack develops from the notch leading to brittle failure of the beam. The toughness of the material is then calculated from the critical load value and a stress concentration factor depending on the geometry of the notch and the specimen.

Samples and setup

The dimensions of the beam are adapted from the standard ISO 23146 in order to be compatible with the dimensions of the 4-point bending fixture available in the lab. Overall specimen dimensions are reported in Fig. 3.13, where L , B , and W respectively are the length of the beam, its thickness, and its width. The four-point bending configuration has been chosen to perform the tests for the same reasons as for the Iosipescu configuration. Such configuration is recommended for brittle specimens for which early failure could occur in case any tools misalignment would introduce spurious loads. The four point configuration introduces identical load condition whatever the crack position and facilitated handling of the specimen and its setup in the machine.

The dimensions of the notch are also determined according to standard recommendation. They are represented in Fig. 3.14 (b), where a is the depth of the V-notch, b is the depth of the pre-notch, c is the width of the pre-notch, and β is the angle of the V-notch.

The standard gives the following requirements for the notch dimensions:

$$\left\{ \begin{array}{l} 0.8mm < a < 1.2mm, \\ b \approx 0.5mm, \\ c < a - b, \\ (a_{max} - a_{min}) / a \leq 0.1, \\ \beta \text{ as small as possible.} \end{array} \right. \quad (3.3)$$

Pictures of all the pre-notches and notches have been taken during manufacturing process to ensure reproducible notch geometry and evaluate notch sharpness. The dimensions of the measured notches are also important because, they are required for material

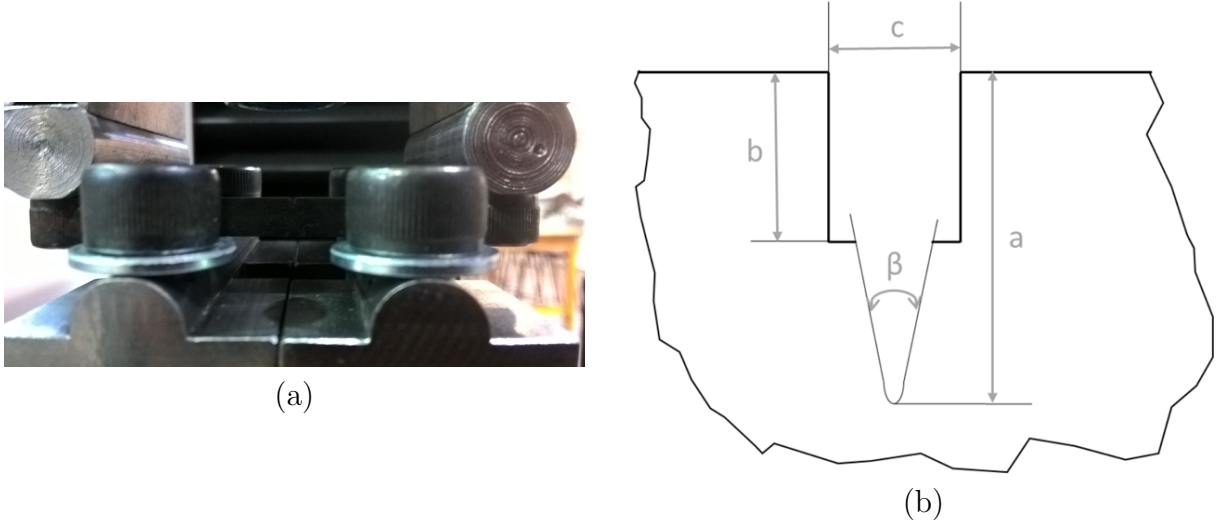


Figure 3.14: (a) SEVNB test setup;
 (b) Dimensions of the notch from standard ISO 23146.

toughness determination. The width of the notch c and the depth of the pre-notch b are measured from the pre-notch. Then two measurements are made for the notch depth, one from each side of the specimens (named a_1 and a_2). The depth of the notch used for the toughness calculation is the average value of the notch depth measured on both sides of the specimen $a = (a_1 + a_2)/2$.

The samples were obtained using the same manufacturing protocol as the one used for the Iosipescu specimen preparation half of the specimens were prepared using B_4C particles treated with silane, while no silane treatment was applied for the other half.

Results

A calculation of the toughness based on stress concentration at the notch tip is given in the standard. The stress concentration factor relies on the notch depth and a non-dimensional parameter α representative of the notch geometry is first calculated:

$$\alpha = \frac{a}{W}. \quad (3.4)$$

Then the toughness of the material is calculated thanks to eqs. 3.5 and 3.6.

$$K_{IC} = \frac{F}{B\sqrt{W}} \cdot \frac{S_1 - S_2}{W} \cdot \frac{3\sqrt{\alpha}}{2(1-\alpha)^{\frac{3}{2}}} \cdot Y^* \quad (3.5)$$

$$Y^* = 1.9887 - 1.326\alpha - \frac{(3.49 - 0.68\alpha + 1.35\alpha^2) \alpha (1 - \alpha)}{(1 + \alpha)^2} \quad (3.6)$$

The obtained average value for the toughness of the material without silane is 1.78

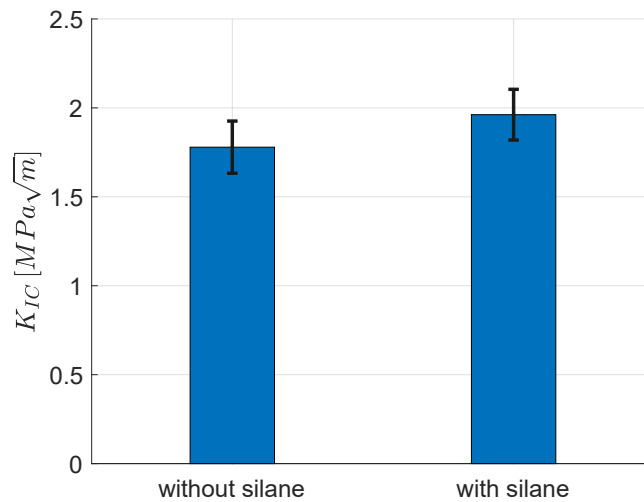


Figure 3.15: Toughness average and standard deviation for the material without and with silane treatment.

$MPa\sqrt{m}$ and for the material with silane $1.96 MPa\sqrt{m}$ (see Fig. 3.15). This means that a 10.11% improvement with the addition of silane can be obtained. The standard deviation of the samples with and without silane treatment are very similar ($0.1468 MPa\sqrt{m}$ against $0.1426 MPa\sqrt{m}$). A marginal increase of the toughness with the silane treatment was hence noticeable, but it doesn't seem to have any noticeable effect on the scatter of the results.

3.2 Modelling of the debonding phenomenon at the micro and meso-scale levels

The failure of the particle reinforced composite has been observed experimentally. The effect of several design parameters such as particle volume fraction, particle size, and the adhesion between the particles and the matrix on the fracture properties has been tested. It was determined that the debonding of particles from the matrix plays a significant role in the failure of the composite. Indeed, rigid particles stiffen the polymer material as long as the efforts are transmitted to them. After a given load is applied, the particles start to debond from the matrix and this represents the first damage mechanism in the composite. The matrix then fails and the fracture of the composite is observed. The initiation of interface debonding is then considered as the most critical phenomenon since it might trigger the overall failure process. This chapter is then dedicated to the modelling of particle debonding and two approaches will be described: a semi-analytical one and numerical simulations.

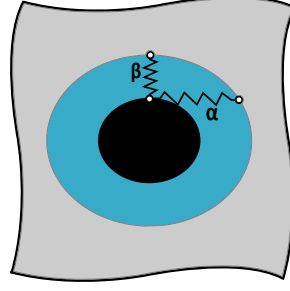


Figure 3.16: Imperfect interface modelled by a linear spring

3.2.1 Semi-analytical homogenisation model

Isotropic damage of the interface - Linear springs interfaces

In order to develop more realistic analytical models some researchers attempted to take into account the imperfect bonding between matrix and inclusions. Following the concept developed by Qu in [120] and [119], the imperfect interfaces between two phases can be modelled by introducing an infinitely thin layer in which tractions remain continuous and displacements become discontinuous (see Fig 3.16). S is used to denote the surface of the interface and n its outward normal vector. S^+ represent the interface when approaching it from outside the inclusion and S^- when approaching it from inside the inclusion. The stress at the interface being continuous, the stress jump between the phases $\Delta\sigma$ is null:

$$\Delta\sigma_{ij}n_j = [\sigma_{ij}(S^+) - \sigma_{ij}(S^-)]n_j = 0 \quad (3.7)$$

The displacement jump Δu is here modelled with a linear spring:

$$\Delta u_i = [u_i(S^+) - u_i(S^-)] = \eta_{ij}\sigma_{jk}n_k \quad (3.8)$$

The second order tensor η_{ij} represents the compliance of the spring-layer interface. It is assumed to be symmetric and definite positive. One can recognise perfect interface when η_{ij} is set to zero whereas $\eta_{ij} \rightarrow \infty$ implies complete debond. Two parameters α and β are introduced to model the interface compliance respectively in the tangential and normal direction of the interface (see Fig 3.16). The interface compliance tensor is given by the relationship:

$$\eta_{ij} = \alpha\delta_{ij} + (\beta - \alpha)n_in_j \quad (3.9)$$

where α and β represent the tangential and normal compliances of the interface:

$$\Delta u_i (\delta_{ik} - n_i n_k) = \alpha \sigma_{ij} n_j (\delta_{ik} - n_i n_k) \quad (3.10)$$

$$\Delta u_i n_i = \beta \sigma_{ij} n_j n_i \quad (3.11)$$

Considering this displacement jump at the interface, a new relationship between the perturbation strain field $\underline{\underline{\epsilon}}^d$ in the inclusion and the eigenstrain $\underline{\underline{\epsilon}}^*$ can be established:

$$\epsilon_{ij}^d(\underline{x}) = S_{ijkl} \epsilon_{kl}^* - C_{klmn} \int_S \Delta u_k(\underline{\xi}) G_{ijmn}(\underline{\xi} - \underline{x}) n_l dS(\underline{\xi}) \quad (3.12)$$

where $\underline{\underline{G}}$ is the Green function

It is possible to obtain a fourth-order tensor which relates the perturbation strain and the eigenstrain: the modified Eshelby tensor $\underline{\underline{S}}^{EshM}$. With the introduction of a compliant interface, the eigenstrain is not homogeneous in the inclusion any more. To overcome, this difficulty [119] calculated the volume averaged modified Eshelby tensor by performing the integration of the modified Eshelby tensor over the particle volume. [119] determined an exact solution of the problem by permuting the derivation and first integral operations and then permuting the surface and volume integrals. However, Othmani et al [117] noticed that this is not a valid operation as, according to Fubini's theorem, such permutations are only allowed when the integration volume is free from any singularity (that is not the case here as Green's function is singular along the imperfect interface).

To perform the calculation of this (volume averaged - but for convenience it will now be omitted) modified Eshelby tensor, [117] got rid of Green's function singularity by translating the calculations in Fourier space. Othmani obtained the following expression of the modified Eshelby tensor:

$$\underline{\underline{S}}^{EshM} = \left[\underline{\underline{I}} + \langle \underline{\underline{G}} \rangle_{\Omega} \right]^{-1} : \left[\underline{\underline{S}}^{Esh} + \langle \underline{\underline{G}} \rangle_{\Omega} \right], \quad (3.13)$$

while Qu got this expression that is different:

$$\underline{\underline{S}}^{EshM} = \underline{\underline{S}}^{Esh} + \langle \underline{\underline{G}} \rangle_{\Omega} : \left(\underline{\underline{I}} - \underline{\underline{S}}^{Esh} \right). \quad (3.14)$$

For both expressions of the modified Eshelby tensor, the tensor $\langle \underline{\underline{G}} \rangle_{\Omega}$ is expressed as:

$$\langle \underline{\underline{G}} \rangle_{\Omega} = \left(\underline{\underline{I}} - \underline{\underline{S}}^{Esh} \right) : \underline{\underline{H}} : \underline{\underline{C}}_m, \quad (3.15)$$

$$\text{with } H_{ijkl} = \frac{1}{\Omega} \int_S (\eta_{ik} n_j n_l + \eta_{jk} n_i n_l + \eta_{il} n_j n_k + \eta_{jl} n_i n_k) dS, \quad (3.16)$$

where $\underline{\underline{H}}$ fourth-order tensor represents the influence of both the interface compliance and the morphology of the inclusion in the modified Eshelby tensor expression. Analytical expressions of this tensor are given by Qu for specific cases where the shape of the inclusions allow to perform the integrals analytically. Othmani [117] claimed that the derivation of this tensor was also wrong in [119], however a comparison of the expressions given by both in the case of a spherical particle reveals that they give the same result. $\underline{\underline{H}}$ can always be decomposed as follows:

$$\underline{\underline{H}} = \alpha \underline{\underline{P}} + (\beta - \alpha) \underline{\underline{Q}} \quad (3.17)$$

For specific inclusion geometries, the expressions of $\underline{\underline{P}}$ and $\underline{\underline{Q}}$ can be analytically determined. For a spherical particle of radius a , one gets:

$$\text{with } P_{ijkl} = \frac{1}{a} I_{ijkl} \quad (3.18)$$

$$\text{and } Q_{ijkl} = \frac{1}{5a} (2I_{ijkl} + \delta_{ij}\delta_{kl}) \quad (3.19)$$

For the case of a cylindrical inclusion of radius a , (based on [36]) one can obtain the following expressions:

$$P_{1111} = P_{2222} = 4P_{2323} = 4P_{1313} = 2P_{1212} = \frac{1}{a}, \quad (3.20)$$

$$Q_{1111} = Q_{2222} = 3Q_{1122} = 3Q_{2211} = 3Q_{1212} = \frac{3}{4a}, \quad (3.21)$$

$$\text{others} = 0. \quad (3.22)$$

The strain localisation tensors obtained by Qu and Othmani are also different. Othmani obtained (and was confirmed by [36]):

$$\underline{\underline{A}}_i^{HD} = \left[\underline{\underline{I}} - \underline{\underline{S}}^{EshM} : \left(\underline{\underline{I}} - \underline{\underline{C}}_m^{-1} : \underline{\underline{C}}_i \right) \right]^{-1} : \left[\underline{\underline{I}} + \langle \underline{\underline{\Gamma}} \rangle_{\Omega} \right]^{-1}, \quad (3.23)$$

while Qu obtains:

$$\underline{\underline{A}}_i^{HD} = \left[\underline{\underline{I}} - \underline{\underline{S}}^{EshM} : \left(\underline{\underline{I}} - \underline{\underline{C}}_m^{-1} : \underline{\underline{C}}_i \right) \right]^{-1}. \quad (3.24)$$

To check the correction applied to the modified Eshelby tensor and the strain localisation tensor, the strain in an inclusion subjected to a remote hydrostatic loading is numerically determined and compared to the analytical prediction from Qu and from the corrected expressions. A compliant interface is introduced between the inclusion and the matrix ($\alpha = \beta = 4e^{-5}$ mm/MPa). Two types of inclusions are used: a spherical particle of

radius $a = 100 \mu\text{m}$ and a cylinder of radius $a = 100 \mu\text{m}$. The size of the matrix is $L = 20a$ so that it can be considered as infinite. The calculations are made under axisymmetric and plane strain assumption respectively.

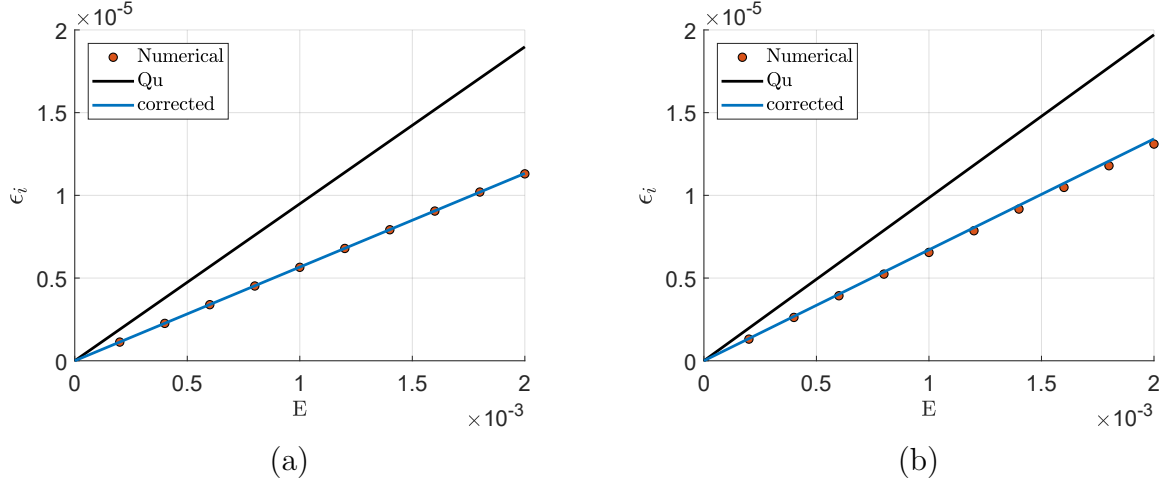


Figure 3.17: Strain concentration in the inclusion with (a) a spherical inclusion and (b) a cylindrical one.

Fig. 3.17 represents the strain in the inclusion (homogeneous because of the hydrostatic loading applied) against the global strain of the material. In both cases, the corrected expressions almost give a perfect match with the numerical simulations while the results obtained with the expressions of Qu diverge. This test validates the corrected expressions of the modified Eshelby tensor and the strain localisation tensor.

Mori-Tanaka with weakened interfaces

Using the modified Eshelby tensor, one can obtain the macroscopic behaviour of a composite material containing inclusions with imperfect interfaces. Esteva and Spanos [42] determined the effective elastic properties of nanotube reinforced composites with slightly weakened interfaces using a modified Mori-Tanaka scheme described thereafter. Lee and Pyo [89] used this approach to describe the evolution of the macroscopic behaviour with spherical particles considering that the progressive debonding could be represented with a reduction of interface stiffness.

Qu re-derived the Mori-Tanaka formulae with imperfect interfaces. According to this procedure, the imperfect interfaces contribute to the average strain in two ways [119]. First, the imperfect interfaces affect $\tilde{\epsilon}_i$, the average strain in each inhomogeneity. This effect can be taken into account by the use of the modified Eshelby tensor. Secondly, the imperfect interfaces introduce a displacement jump that induces another component $\tilde{\epsilon}^{inter}$ corresponding to the third term of the decomposition of the global strain (ϕ being

the volume fraction of inclusions i):

$$\underline{\underline{\mathbf{E}}} = (1 - \phi) \underline{\underline{\mathbf{\epsilon}}}_m + \phi \underline{\underline{\mathbf{\epsilon}}}_i + \phi \underline{\underline{\mathbf{H}}} : \underline{\underline{\mathbf{C}}}_i : \underline{\underline{\mathbf{\epsilon}}}_i. \quad (3.25)$$

The Mori-Tanaka strain localisation tensor for the phase i then becomes:

$$\underline{\underline{\mathbf{A}}}_i^{MT} = \underline{\underline{\mathbf{A}}}_i^{HD} : \left((1 - \phi) \underline{\underline{\mathbf{A}}}_m^{HD} + \phi \left(\underline{\underline{\mathbf{I}}} + \underline{\underline{\mathbf{H}}} : \underline{\underline{\mathbf{C}}}_i \right) : \underline{\underline{\mathbf{A}}}_i^{HD} \right)^{-1} \quad (3.26)$$

Thanks to this strain localisation tensor (3.26) and the typical mean-field homogenisation formula (2.12), an estimate of the effective stiffness tensor can be obtained:

$$\underline{\underline{\mathbf{C}}}_{eff} = (1 - \phi) \underline{\underline{\mathbf{A}}}_m^{MT} : \underline{\underline{\mathbf{C}}}_m + \phi \underline{\underline{\mathbf{A}}}_i^{MT} : \underline{\underline{\mathbf{C}}}_i \quad (3.27)$$

Transitions rules for progressive particle debonding

A homogenisation scheme is proposed to describe the progressive particle/matrix debonding. An equivalent material is considered containing two types of particles embedded in a matrix and voids. To represent the progressive failure due to an incrementally evolving strain the volume fraction of each phase is modified along with the loading. Initially, only matrix and inclusions compose the material. We then introduce imperfect interfaces between the inclusions and the matrix which represent partial particle/matrix debonding. The damage progressively increases until all inclusions are debonded from the matrix. As a consequence, at each load iteration, an equivalent material is considered represented with a mixture of 4 different phases (as depicted in Fig. 3.18) : 0) the matrix, 1) inclusions with imperfect interface, 2) inclusions with a damaged interface, 3) completely debonded inclusions that are replaced by voids. Initially, all the volume fractions are set to zero, except those of matrix ($\phi_0 = 1 - \phi$) and particles ($\phi_1 = \phi$), see Fig. 3.18. The volume fractions of the phases are modified according evolution rules developed thereafter. At each load increment, a homogenisation procedure, based on the modified Mori-Tanaka scheme, is performed to determine the global behaviour of the composite.

A probabilistic approach is proposed to describe the evolution of the volume fraction of each inclusion type based on a Weibull law. Such a phenomenological evolution rule it is defined by two parameters which must be calibrated: M the shape parameter and S_0 the scale parameter.

The evolution laws for the volume fractions given thereafter follow those given by Lee and Pyo [90]. The cumulative volume fraction of particles whose interface has been damaged (the inclusions going from state 1 to state 2 is denoted $\bar{\phi}_2$ and is given by the

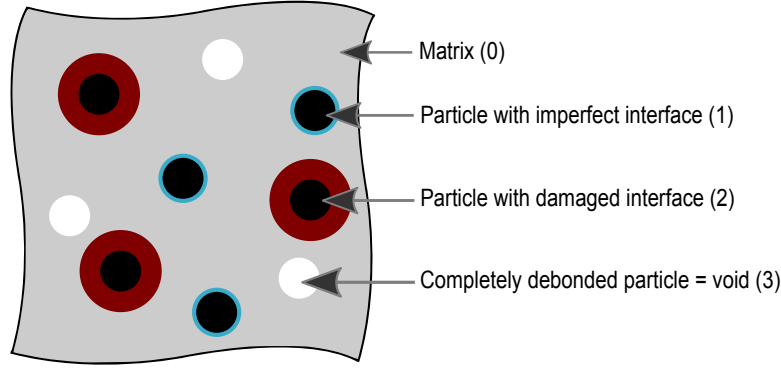


Figure 3.18: Microstructure of the composite: the different phases

following Weibull law:

$$\bar{\phi}_2 = \phi \left(1 - \exp \left[- \left(\frac{(\bar{\sigma}_{eq})_1}{S_0} \right)^M \right] \right) \quad (3.28)$$

The volume fraction of particles that have not been damaged is calculated from:

$$\phi_1 = \phi - \bar{\phi}_2 \quad (3.29)$$

Then, as driving load increases, some of the inclusions with damaged interfaces start to debond. The evolution rule from state 2 to state 3 is described by the same Weibull law, except that new moduli are introduced to simulate the fact that a higher load has to be applied to completely debond the inclusions than the one needed only to damage their interfaces.

$$\phi_3 = \bar{\phi}_2 \left(1 - \exp \left[- \left(\frac{(\bar{\sigma}_{eq})_1}{S_{01}} \right)^{M_1} \right] \right) \quad (3.30)$$

And the current volume fraction of inclusions with damaged interface becomes:

$$\phi_2 = \bar{\phi}_2 - \phi_3 \quad (3.31)$$

This Weibull laws are driven by the average stress in strongly bonded particles (phase 1) $(\bar{\sigma}_{eq})_1$ that is equal to $(\sigma_{11})_1$ in the case of uniaxial stress state and the quadratic mean of $(\sigma_{11})_1$ and $(\sigma_{22})_1$ in the case of biaxial stress state. Derived from the modified Mori-Tanaka homogenisation model, $\tilde{\sigma}_1$ can be obtained from the strain localisation tensor and the stiffness tensor of the inclusion:

$$\tilde{\sigma}_1 = \underline{\underline{C}}_1 : \underline{\underline{A}}_i^{MT} : \underline{\underline{E}} \quad (3.32)$$

The global behaviour of the damaged composite is then expressed with the calculation

of its effective stiffness tensor, once more thanks to the modified Mori-Tanaka mean-field estimate:

$$\underline{\underline{C}}_{eff} \approx \sum_{r=0}^3 \phi_r \underline{\underline{A}}_r^{MT} : \underline{\underline{C}}_r. \quad (3.33)$$

Once the effective stiffness tensor is evaluated, the macroscopic stress $\underline{\underline{\Sigma}}$ can be related to the macroscopic strain $\underline{\underline{E}}$ of the composite considering progressive debonding of the inclusions. The expressions of the Eshelby $\underline{\underline{S}}^{Esh}$ tensor following the shape of the inclusion and the symmetries of the matrix can be found in [102]. The modified Eshelby tensor $\underline{\underline{S}}^{EshM}$ and the compliance tensor of the interfaces $\underline{\underline{H}}$ are defined in a previous paragraph.

Two Weibull laws (i.e. 4 parameters) govern the transition rules for progressive particle debonding. These 4 parameters need to be calibrated. Instead of using experimental results that might show numerous other damage mechanisms such as matrix failure, reference results are generated using numerical simulations where particle debonding is the only damage mechanism represented. As the RVE considered are in 2D under plane strain assumption, the cylindrical inclusions are used for the homogenisation model.

3.2.2 FE model

The present subsection is dedicated to the numerical simulation of particle reinforced material taking into account particle debonding, by extending the numerical framework developed in Chapter 2. The numerical framework also allow to perform full-field simulations and hence obtaining local information such as stress and strain heterogeneities in the phases or partial debonding of the particles.

Cohesive Zone Models (CZM)

To describe the debonding mechanism between two surfaces or the delamination between two plies in a finite elements context, CZM are commonly used. A CZM is a zero thickness interface separation law where the stress vector at the interface is related to the displacement jump across the interface. Multiple traction-separation law shapes have been proposed such as the bilinear, trilinear, exponential ones (see Fig. 3.19) which are generally chosen according to the failure behaviour they describe (brittle, dissipative, etc.)

A bilinear law was used for this study (based on Alfano & Crisfield work [6] in the software Ansys). They are generally adequate to represent brittle failure processes taking into account the development of a finite size process zone ahead of the crack tip. The first part of the curve shows a linear elastic behaviour until ultimate stress is reached. Then, the cohesive stress at the interface linearly decreases as the interface stiffness is irreversibly decreasing describing damage mechanism. This cohesive law is governed by three main parameters viz. interface stiffness, strength and toughness. The initial slope

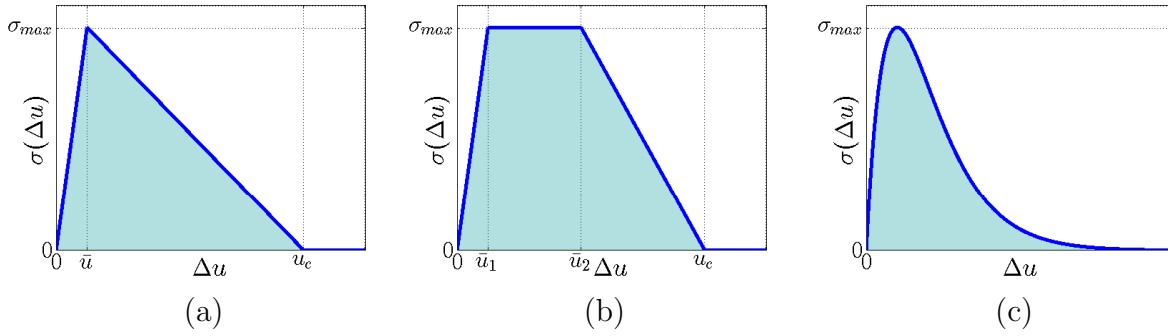


Figure 3.19: Bilinear (a), Trilinear (b), and Exponential (c) traction-separation laws.

is generally chosen according to numerical criteria. Indeed, the interface stiffness changes the one of the RVE itself despite it is commonly considered that interfaces should not significantly affect the overall material stiffness. Then, sufficiently high values are chosen so that the global elastic properties of the composite remain stable. The interface strength controls the damage initiation before a linear softening of the stress occurs until the stress completely vanishes and the interface is considered to be completely debonded. The whole elastic loading and damage process is governed by the interface fracture energy G_c which corresponds to the shaded area under the traction-separation curves. Such cohesive elements appear seducing since their properties could be easily determined or lead to parametric analyses. Indeed, the interface stiffness can be chosen for numerical reason, strength and toughness values are generally found in literature for numerous classical systems. Cohesive elements were then introduced at all the interfaces between the particles and the matrix to numerically simulate the debonding of these particles from the matrix.

Numerical setup and parameters

The RVE is meshed with quadratic quadrangular elements (PLANE183, 8 nodes quadrangles) in order to reach convergence with a limited number of elements. The RVE is still 2D, so plane strain option is activated. The element size must be small enough to reach convergence and to be also small enough to correctly discretise the process zone of the CZM. Indeed, when the cohesive zone is discretized using too few elements, the cohesive stress distribution in the process zone ahead of the crack tip is not represented accurately [150].

The size of the process zone of the CZM could be estimated from the characteristic length value. This length is an inverse evaluation of the brittleness of the interface failure (a small characteristic length corresponds to a brittle interface while a large one corresponds to a ductile one) [39]. This characteristic length has been expressed as a function

of interface parameters by several authors. In particular, [39], [134], [92] gave:

$$l_{ch} = \frac{G_c E}{\sigma_c}, \quad (3.34)$$

where G_c is the fracture energy, E Young's modulus of the material adjacent to the crack, and σ_c the strength of the interface. When the characteristic length is small compared the characteristic geometrical length, the assumption of Linear Fracture Mechanics (LEFM) is adequate and the failure of the interface is controlled by the surface fracture energy. When this characteristic length is larger than the characteristic geometrical length, non linear damage process can slowly develop and stable/slow crack initiation is observed which is controlled by the softening behaviour of the CZM [39].

Multiple authors have proposed some indication concerning the minimum number of cohesive elements to be used for proper simulation with CZM, but [150] observed that elements 5 times lower than the characteristic length is enough. The element size is chosen approximately equal to 1/50 of the RVE length. In all the following simulations, the elements sizes are then always lower than 1/5 of the characteristic length.

The fracture energy of the interface is chosen equal to 100 J.m⁻² and the strength to 50 MPa. The stiffness of the CZM is chosen high enough so that it does not visibly reduce the overall stiffness of the RVE. A small numerical viscosity is introduced by the software in order to improve the convergence. Again, the value of this viscosity parameter is chosen low enough so that it does not influence the overall results.

The material properties for the particles and the matrix are the same as the ones chosen in the previous chapter dealing with the evaluation of the material elastic properties. The same periodic boundary conditions as for the elastic homogenisation (presented in Chapter 2) are imposed.

Fig. 3.20 shows the displacement fields obtain for the three loading cases previously described, with the introduction of the CZM and the matrix failure.

3.2.3 Results of the numerical simulations

To investigate results experimentally observed previously, the effect of several material parameters are evaluated using numerical and analytical models. The three random microstructure generation algorithms are used to evaluate the influence of particle shapes, distributions, size so as the influence of particle/matrix adhesion strength and toughness.

Debonding of particles in a RVE

A typical stress-strain curve of a RVE loaded in uniaxial tension (lateral displacement prevented), as obtained with numerical simulations, is represented in Fig. 3.21. The first

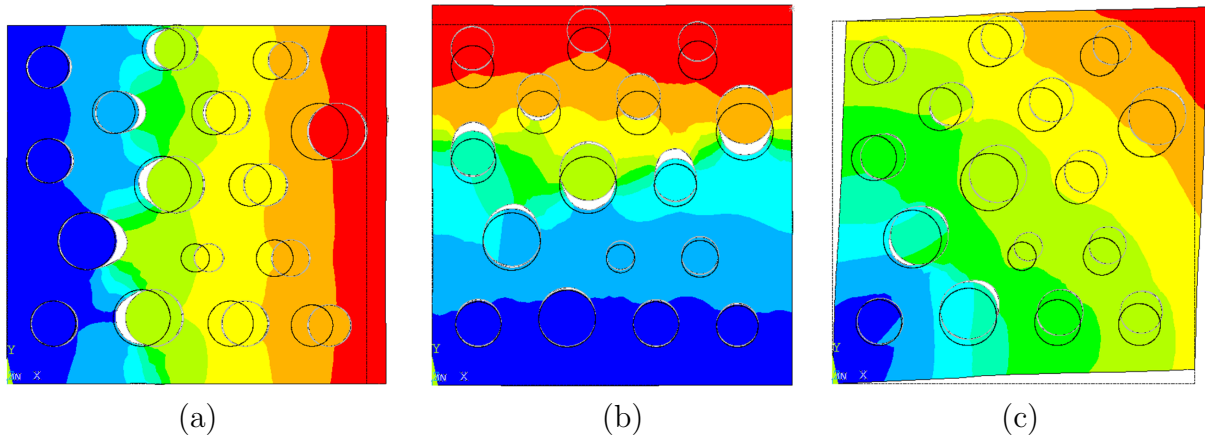


Figure 3.20: (a) Displacement fields (a) U_{11} under tensile loading (b) U_{22} under tensile loading, and (c) U_{12} under shear loading with particle debonding.

part of the curve is the elastic loading, where the particles are perfectly bonded to the matrix. An elastic simulation run with perfect interfaces confirm (black dashed line) that the stiffness of the CZM does not make the RVE artificially more compliant.

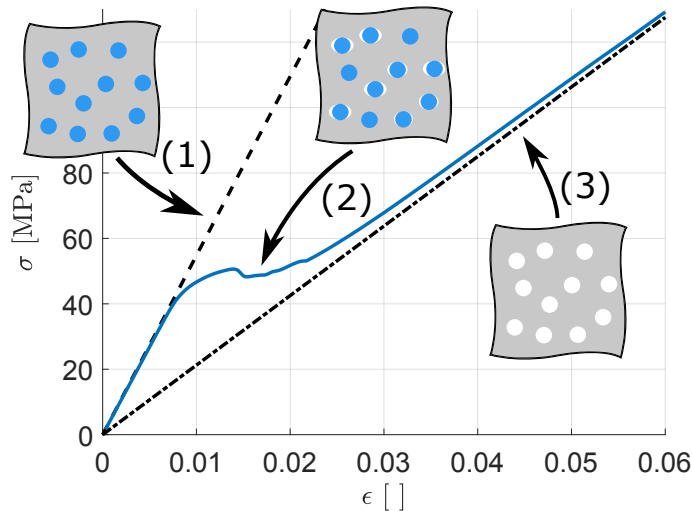


Figure 3.21: Typical stress-strain curve for RVE with particle debonding (1) particles are perfectly bonded, (2) particles start to debond, (3) particles are completely debonded.

During the second phase, particles start to debond sequentially and a softening of the behaviour is observed. As the applied displacement applied increases the debonded area increases. A third phase is finally observed, where a quasi linear stress/strain evolution is observed. A simulation run with voids instead of particles (represented with a black dashdotted line) show that during this third phase, most of the particles are debonded and their influence on the behaviour of the material is completely negligible. Indeed, the

behaviour of the material with debonded particles is almost equivalent to the one with voids instead of particles.

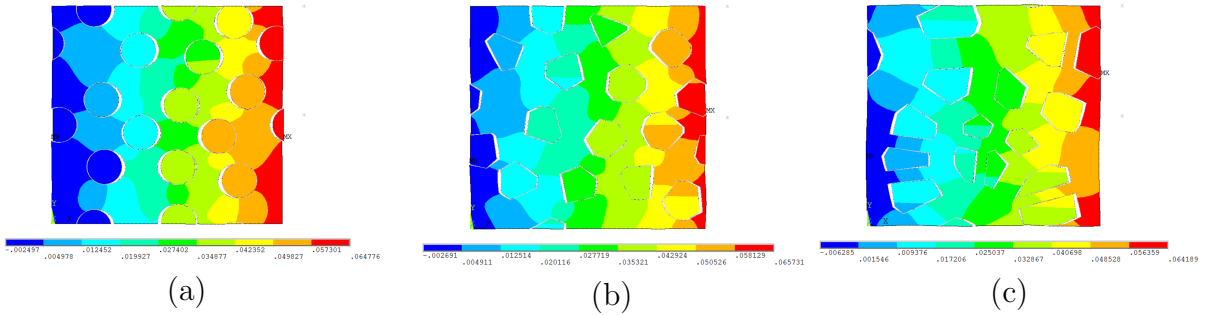


Figure 3.22: Displacement field in the RVE generated with (a) D & R with circular particles, (b) D & R with angular particles, (c) Voronoi tessellation algorithms ($\phi = 30\%$ of monodisperse particles).

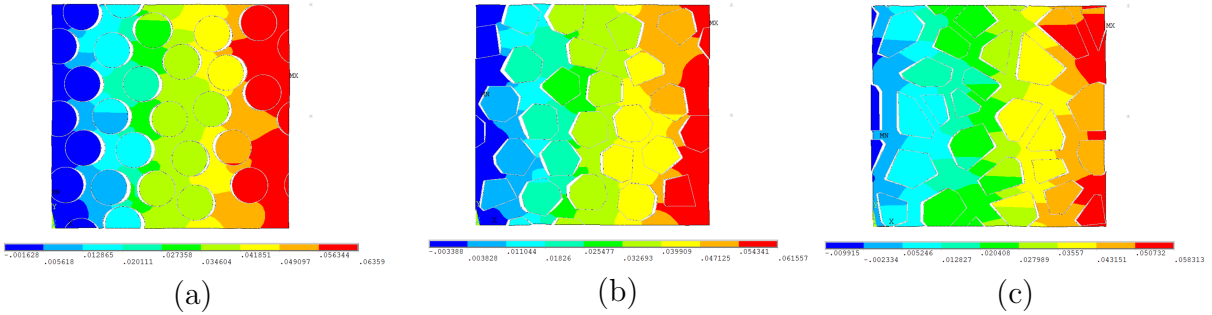


Figure 3.23: Displacement field in the RVE generated with (a) D & R with circular particles, (b) D & R with angular particles, (c) Voronoi tessellation algorithms ($\phi = 50\%$ of monodisperse particles).

To study the effect of various microstructural parameters, multiple RVE are generated using the three algorithms presented in Chapter 2. Different particle volume fractions are used (see Figs. 3.22 and 3.23).

Effect of the generated microstructure

Numerical simulations are then performed considering virtual RVE generated with the Dropping and Rolling algorithm with circular particles, angular particles, and with the Voronoi tessellation algorithm. For all configuration, the same particle volume fraction is generated with each algorithm. All the particles have the same “size” (as given by the equivalent particle radius $R = 80 \mu\text{m}$). The resulting stress-strain curves are plotted in Fig. 3.24 in case of (a) 30% and (b) 50% particle volume fractions.

For every configuration, a similar elastic behaviour is observed since all RVE have the same particle content. Then, a softening behaviour corresponding to the particle/matrix

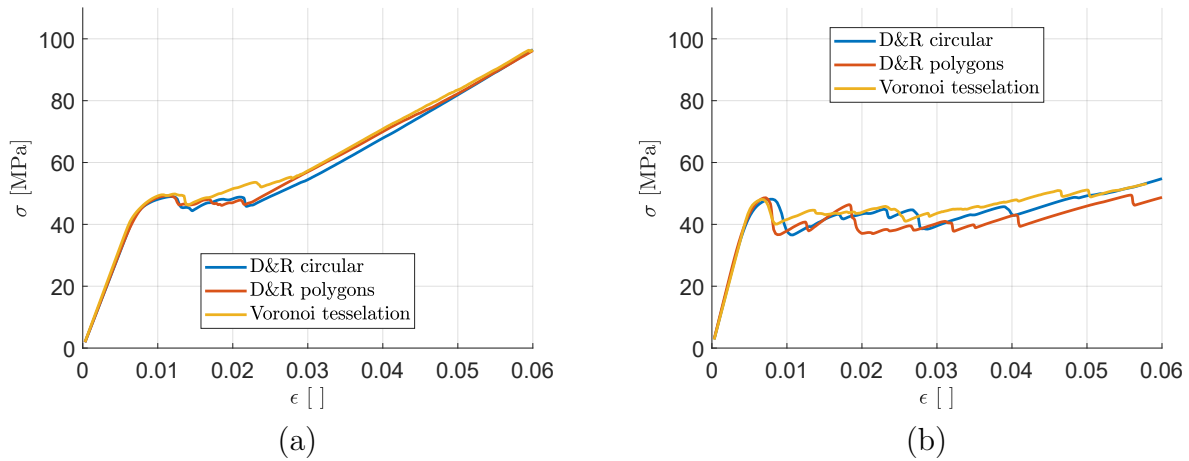


Figure 3.24: Stress-strain curves for RVE with particle debonding generated with different algorithms: (a) 30% and (b) 50% particle volume fractions of $80\mu\text{m}$ particles.

debonding phase. Even if larger stress concentrations are observed in the RVE with angular particles (polygons and Voronoi), the debonding phenomenon seems to start at the same level on stress applied on the RVE.

Effect of particle volume fraction

Different volume fractions of particles are then tested (20%, 30%, 40%, 50%, and 60%). The particle size is also monodisperse and kept constant through the simulations. The results are plotted in Fig. 3.25.

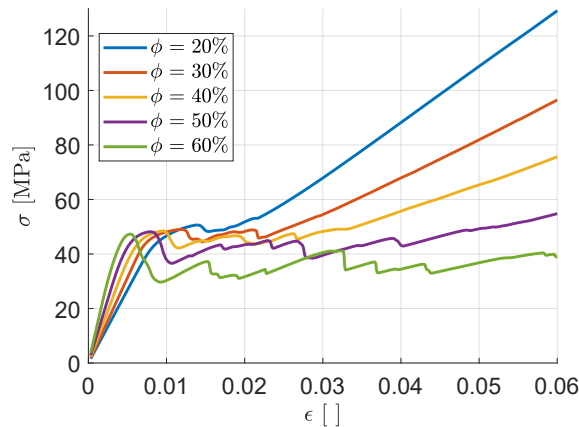


Figure 3.25: Stress-strain curves for RVE with particle debonding (Dropping and Rolling soft walls, monodisperse particles $R=80\mu\text{m}$) - Particle volume fraction effect.

During the elastic part of the loading, the higher the volume fraction of particles is, the higher the global stiffness is. Then, the onset of particle debonding stage seems

to start at similar levels of stresses applied to the RVE despite a very slight decrease could be observed with increasing particle volume fraction. For full particle debonding of all particles significantly higher displacement value must be reached for larger particle content.

Effect of particle size

The same RVE with monodisperse particles are homothetically replicated with larger and smaller particles. The particle sizes introduced in the material are $R = 20 \mu\text{m}$, $40 \mu\text{m}$, $80 \mu\text{m}$, $160 \mu\text{m}$, $240 \mu\text{m}$ and the volume fraction of particles is 30%. The results are plotted in Fig. 3.26. Two elastic simulations have also been carried out with particles perfectly bonded to the matrix and with voids instead of particles which are represented by a black dashed line and a black dashdotted line respectively.

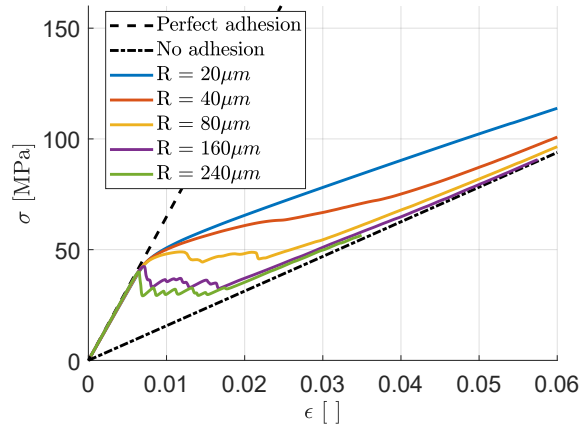


Figure 3.26: Stress-strain curves for RVE with particle debonding (Dropping and Rolling soft walls, particle volume fraction $\phi=0.3$) - Particle size effect.

For all particle sizes, the first elastic part of the loading is equivalent and match exactly with the behaviour of the RVE with perfect interfaces, indicating no influence of the CZM initial stiffness. Then the particles start to debond. For RVE with small particles, the debonding seems to be a very progressive phenomenon and a gradual softening of the behaviour is observed. For RVE with large particles, the debonding is faster and sudden load drops are visible when interfaces brutally fail. Finally, when the applied displacement is high enough, all the curves follow the same elastic asymptotic where all particles are replaced with voids.

To evidence such a size effect, a RVE containing a bimodal particle sizes distribution is generated (the particle sizes are $R = 120 \mu\text{m}$ and $R = 40 \mu\text{m}$ respectively) having a 50% particle volume fraction. The resulting stress-strain curve is plotted in Fig. 3.27 (a).

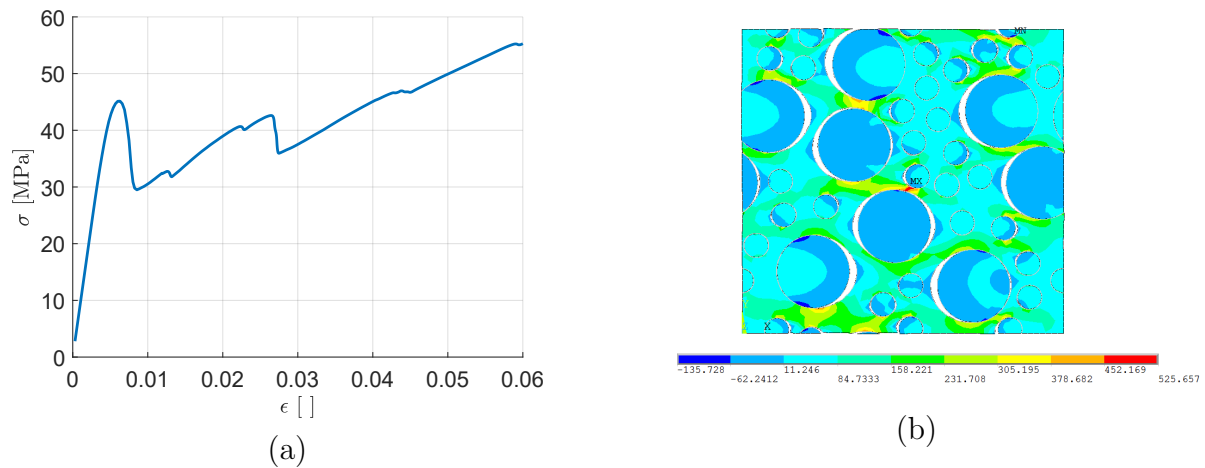


Figure 3.27: Bimodal particles ($R=120\mu\text{m}$ and $R=40\mu\text{m}$) with Dropping and Rolling soft walls, particle volume fraction $\phi=0.3$:
 (a) Stress-strain curves for RVE with particle debonding;
 (b) Stress field σ_{11} in the RVE.

A first sudden load drop is observed at c.a. 0.005 deformation value. A second one is observed at c.a. 0.0028. These two drops correspond to large particles being debonded from the matrix. Smaller particles debond more progressively and lead to more continuous evolution on the stress/strain curve.

Another conclusion is that large particles tend to debond before smaller ones, as observed in Fig. 3.27 (b). It represents the σ_{11} stress component distribution along the horizontal directions. The large particles are all visibly debonded, while for most of the small particles, the interface has not been damaged yet. This is in accordance with the experimental observations.

Effect of interface parameters

Once the interface stiffness is set, the triangular CZM is defined by only two parameters: the strength of the interface σ_{max} and the fracture energy G_c . The effect of both parameters has been tested on the same RVE with monodisperse particles. The results are plotted in Fig. 3.28. The RVE with the same interface strengths seems to debond at approximately the same level of stress and the debonding of particles with an interface strength of 50 MPa appears before the one of particles with an interface strength of 100 MPa. The fracture energy of the interface also plays a significant role and the higher it is, the later the end of the debonding process is, resulting in a larger overall dissipated energy density (as quantified by the area below the stress/strain curve).

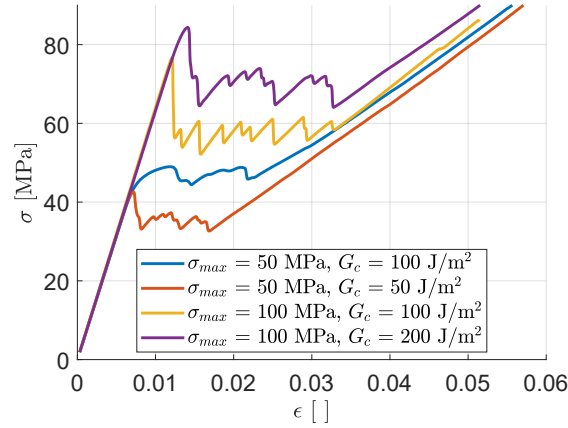


Figure 3.28: Stress-strain curves for RVE with particle debonding (Dropping and Rolling soft walls, particle volume fraction $\phi=0.3$, $R=80\mu\text{m}$) - Effect of interface parameters

3.2.4 Calibration of the semi-analytical model and results

This nonlinear homogenisation model taking into account particle debonding can now be calibrated. 4 parameters, from the two Weibull laws Eqs. 3.28 and 3.30, S_0 , M , S_{01} , M_1 are used. The calibration is made in order to fit the data from the RVE with CZM. The RVE with $40\ \mu\text{m}$ monodisperse particles are used as reference. Volume fractions ranging from 20% to 50% are considered. The same calibration is made for all the volume fractions and the following parameters are selected:

- $S_0 = 85\ \text{MPa}$,
- $M = 6$,
- $S_{01} = 136\ \text{MPa}$,
- $M_1 = 5.5$.

The results of both the numerical simulations and the nonlinear homogenisation model are plotted in Fig. 3.29. The first part of the curve, which represents the elastic regime, matches the results obtained with the homogenisation model. As no particle is debonded it therefore corresponds to Mori-Tanaka homogenisation scheme. Then, as the loading keeps increasing, particles start to debond. For the homogenisation model, particles start to go from stage 1 to stage 2, corresponding to particles with damaged interfaces. This softening in the global behaviour of the material is quite well described with the homogenisation model when compared to numerical simulations, and this for all particle volume fractions.

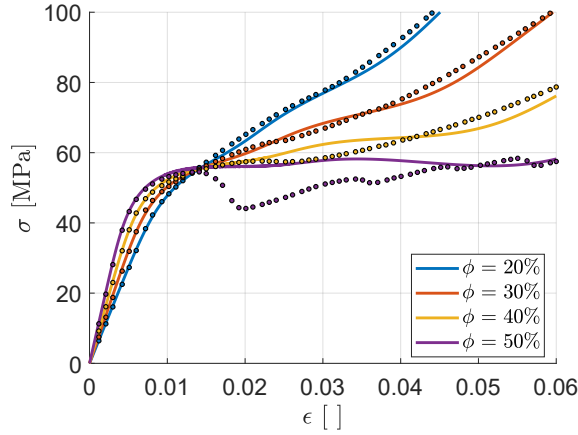


Figure 3.29: Stress-strain curves for numerical simulations (circles) and for the homogenisation model (continuous lines) for different volume fractions ($R = 40\mu\text{m}$).

Then, the full debonding of particles from the matrix starts to be observed. In the homogenisation model, some particles bonded to the matrix with finite stiffness interface are replaced with voids. During this phase, the homogenisation model and the numerical simulations match acceptably well for volume fractions between 20% to 40%. For higher volume fractions (50% here), a sudden stress drop is observed and the latter cannot be described by the nonlinear homogenisation model. The last part of the curve, where all the particles are debonded from the matrix is correctly described by the homogenisation model.

A major inconvenient of this approach is that the particle size effect on the debonding mechanism which has been observed with numerical simulations using CZM is not described here. The model has to be recalibrated every time a new particle size is used. To introduce a particle size effect, the parameters have to be calibrated again (see Table• 3.1).

| Particle size | S_0 | M | S_{01} | M_1 |
|-----------------------|-------|-----|----------|-------|
| $R = 20 \mu\text{m}$ | 92 | 5 | 184 | 4.6 |
| $R = 40 \mu\text{m}$ | 85 | 6 | 136 | 5.5 |
| $R = 80 \mu\text{m}$ | 80 | 8 | 96 | 7.3 |
| $R = 160 \mu\text{m}$ | 65 | 10 | 52 | 9.2 |

Table 3.1: Mechanical properties of materials used for armouring

It has been observed numerically that the debonding of particles is more brutal with increasing particle size. In order to reflect this effect, as the particle size is increased the Weibull moduli M and M_1 are also increased. As this parameter is increased, the scale parameter is decreased so that the debonding starts at the correct stress level. With these

new sets of parameters, the particles debond earlier than previously and go faster to the completely debonded stage. The stress-strain curves obtained are plotted in Fig. 3.30 and an acceptable fit was obtained for all the particle sizes.

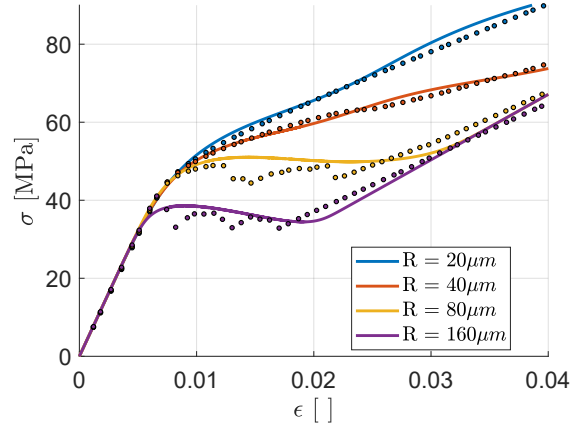


Figure 3.30: Stress-strain curves for numerical simulations (circles) and for the homogenisation model (continuous lines) for different particle sizes ($\phi = 0.3$).

As the semi-analytical homogenisation model has to be calibrated, an important step for the comprehension of the model would be to carry out a full parametric analysis to determine the dependence of the Weibull parameters on the morphological parameters (particle sizes, volume fractions, shapes, etc.). To do this, a large amount of numerical simulations would be required varying the morphological parameters to obtain abacuses for the Weibull parameters.

3.2.5 Generalisation of the model

A way to enrich the model can be the introduction of a fourth phase: voids. This new phase can embody two phenomena: the presence of initial porosity in the material and the failure of the matrix. The matrix failure would be characterised by the coalescence of voids in the matrix. As a new phase (referred to as phase 4) is introduced, a new Weibull law governing the transition of the matrix phase into voids (ϕ_4) is also introduced:

$$\phi_4 = (1 - \phi) \left(1 - \exp \left[- \left(\frac{(\bar{\sigma}_{11})_0}{S_{0v}} \right)^{M_v} \right] \right). \quad (3.35)$$

Two new Weibull parameters M_v and S_{0v} are introduced to represent the “cohesion failure within the matrix”. The equations from the previous subsections are still the same except that the volume fraction of voids is now $\phi_3 + \phi_4$. The effective stiffness tensor is then calculated at each iteration and gives the relationship between the macroscopic stress

$\tilde{\Sigma}$ and strain $\tilde{\mathbf{E}}$. The new Weibull law can be calibrated on FE simulations where the matrix failure is introduced by elastic-fragile elements, with a stiffness drop controlled by a maximum stress criterion.

Air bubbles can be trapped inside the material during the manufacturing process. To take into account, the presence of these porosities, we want to introduce an initial volume fraction of voids. To do so, the volume fraction parameter of voids ϕ_4 is initially set to the porosities volume fraction. Then the evolution of this ϕ_4 parameter is modified to take into account the presence of the porosities:

$$\phi_4 = (1 - \phi - \phi_4 \text{ ini}) \left(1 - \exp \left[- \left(\frac{(\bar{\sigma}_{11})_0}{S_{0v}} \right)^{M_v} \right] \right) + \phi_4 \text{ ini}. \quad (3.36)$$

This extension could give results like the ones depicted in Fig. 3.31.

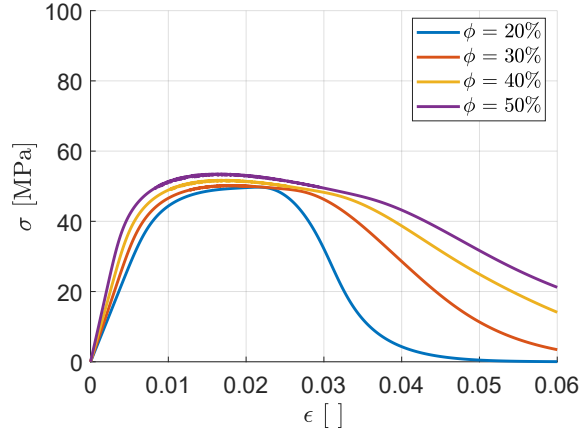


Figure 3.31: Stress-strain curves for the homogenisation model for different volume fractions ($R = 40\mu\text{m}$) with matrix damage introduced.

3.3 Conclusions

The conclusions of this chapter can be summarised through the following points:

- The ceramic particle reinforced polymer exhibits a brittle behaviour. Therefore, tensile tests are not suitable for tensile strength determination. Another option is to use the Iosipescu set up. Indeed, for brittle material, two parallel cracks appear perpendicular to the notch surfaces. This failure happens in tension, meaning this type of tests allow to determine the tensile strength of brittle materials.
- No particle fracture has been observed under tensile loading. The predominant failure in traction is particle/matrix debonding. In order to improve the strength

of the material, the interface strength must be increased. A solution is the silane treatment and its effectiveness has been demonstrated.

- There seems to be a slight decrease in strength with increasing particle content. As the adhesion between the particles and the matrix is quite low when no silane treatment is applied to the particles, the stress concentrations induced by the presence of particles make the composite fails at lower stress levels. A noticeable particle size effect is also visible as higher loads have to be applied in presence of small particles to break the material.
- It is possible to numerically simulate the particle debonding with Cohesive Zone Models (CZM) applied at all the interfaces between the particles and the matrix and numerical simulations were run to test the influence of multiple microstructural parameters. First, the volume fraction of particles stiffens the composite during the elastic loading but a higher load drop is observed as the particles start to debond. The effect of particle volume fraction on the debonding onset was not found as a first order phenomenon. An important size effect is also visible. Indeed, the debonding is facilitated for large particles. This is also confirmed by simulations of bimodal RVE, where large particles are debonded prior to smaller ones.
- Analytical models are also able to take into account the debonding between the particles and the matrix in homogenisation schemes by introducing a compliant interfaces between the particles and the matrix. The homogenisation scheme employed for this study is the Mori-Tanaka one. It is not the best for applications up to high particle volume fractions, however Lielens' model that was used previously and observed to be the most relevant one at high particle volume fraction is unable to take into account the apparition of voids inside the materials.
- This semi-analytical nonlinear homogenisation model requires the calibration of 4 parameters introduced by Weibull law describing the transition rules between three different particle states: bonded, damaged interfaces and completely debonded. A single calibration is able to fit data obtained numerically using a RVE and CZM for different volume fractions. New calibrations are however necessary to reproduce the particle size effect. The model is especially unable to reproduce severe load drops with particle debonding, a situation that appears for large particles or very high particle volume fractions.

Chapter 4

Particle size effect on the particle/matrix debonding

Three main types of fracture processes can be observed at the microstructural level in particle reinforced polymers at various stages of the damage development in the material: particle fracture, microcracks developing in the matrix from the particles and microvoids nucleation caused by cavitation, or particle/matrix debonding [19]. According to [19], the damage corresponding to the first two types is generally much less than that corresponding to the third type. The sequence and occurrence of these various failure mechanisms depend on the nature and mechanical behaviour of the constitutive phases but also strongly depends on the quality of matrix/particle bonding. Indeed, poor adhesion would lead to an overall reduced material strength, while too strong adhesion reduces the material toughness. Also, a particle size dependence has been observed in the previous chapter. Understanding the root causes of the particle/matrix debonding process is then fundamental for optimising particle reinforced polymer composition.

Through the present chapter, the influences of particle size and interface resistance (strength and toughness) on the particle/matrix debonding onset are evaluated considering a single isolated spherical particle in an infinite matrix. No particle interaction effect is considered here. Two methods are implemented in order to identify the scaling law which controls the debonding onset. On the one hand, the phenomenon is analytically described by the Finite Fracture Mechanics (FFM) and, on the other hand, a numerical simulation based on a Cohesive Zone Model (CZM) is employed to simulate the situation. The debonding of a particle that is no longer spherical but angular is then also studied to evaluate whether an equivalent particle radius parameter could be used for evaluating a scaling law.

4.1 Numerical and analytical approaches to tackle particle debonding

4.1.1 Particle debonding in the literature

The elastic field around a spherical particle embedded in an infinite matrix can be determined analytically assuming that the adhesion between the particle and the matrix is perfect (viz. rigid contact). When the particle is more rigid than the matrix, the peak interface stresses are located at the pole of the particle, parallel to the loading direction. An analytical expression of the maximal stress (σ_d) has been derived by Goodier [57] with respect to the remote stress applied to the material (σ_∞):

$$\frac{\sigma_d}{\sigma_\infty} = 1 - \frac{G_m - G_p}{(7 - 5\nu_m)G_m + (8 - 10\nu_m)G_p} \cdot \frac{(1 - 2\nu_p)(7 - 5\nu_m)G_m + (1 + 5\nu_p - 5\nu_m\nu_p)2G_p}{(1 - 2\nu_p)2G_m + (1 + \nu_p)G_p} + \frac{\left[(1 - \nu_m) \frac{1 - \nu_p}{1 + \nu_m} - \nu_p \right] G_p - (1 - 2\nu_p)G_m}{(1 - 2\nu_p)2G_m + (1 + \nu_p)G_p}. \quad (4.1)$$

with G_m and ν_m being the matrix shear modulus and Poisson's ratio, and G_p and ν_p the particle shear modulus and Poisson's ratio respectively. According to Eq. 4.1, it should be notice that peak stress value does not depend on the size of the particle. It is observed experimentally that the damage initiation stress depends on particle size [147] whereas the stress concentration does not. Lauke in [88] asks two crucial questions about the debonding parameters for a spherical particle: "First: Is the debonding stress, σ_{max} , dependent on the particle diameter? And second: Is the interface debonding energy, G_c , a material parameter, or is it dependent on geometrical conditions, such as different curvatures for different particle sizes, near the interface?".

Gent tried to analytically describe the debonding of a spherical particle [54]. He used Griffith's criterion on a sphere with a debonded patch at its pole (modelled as a zone of non-carrying load). He obtained the following debonding stress expression:

$$\sigma_{max}^2 = \frac{8\pi G_c E_m}{3kR \sin(2\theta)}, \quad (4.2)$$

E_m being matrix Young's modulus, k a numerical parameter, R the radius of the particle, and θ the angle of the debonded patch. The value of the applied stress becomes very high for debonding angles of θ around 0° and 90° . A minimum is reached for a debonding angle of 45° (Gent gives a value for the dimensionless numerical parameter $k = 2$ based

on a comparison with another case study):

$$\sigma_{max}^2 = \frac{4\pi G_c E_m}{3R}. \quad (4.3)$$

For a hydrostatic loading, it has been demonstrated by several authors [18], [88], [156], [159] [126] using the Linear Elastic Fracture Mechanics (LFEM) approach, that for a particle embedded in a much softer infinite matrix (viz. rigid spherical particle assumption), the critical stress at the interface needed to debond the particle from the matrix is given by the relationship:

$$\sigma_{dec} = \sqrt{\frac{G_c}{R} \frac{4E_m}{1 + \nu_m}}. \quad (4.4)$$

This expression indicated that the stress provoking particle decohesion, σ_{dec} , is proportional to the inverse of the square root of the radius of the particle R . Since only an energy-based criterion has been applied to describe crack propagation in this situation, the interface strength, σ_{max} , does not influence the decohesion process. The authors tried to describe the debonding of nanoparticles, but as stated by Salviato et al in [126], since no size limitations have been formulated in the model, the equations are valid both for nanosized and microsized particles. Chen et al in [18] tried to describe the energy dissipation by rigid particle debonding in a viscoelastic matrix. Williams in [156] tried to determine the toughness of a composite as function of the volume fraction of nano and micro particles with two different damage mechanisms, debonding and plastic voids growth. Salviato, Zappalorto and Quaresimin in [126], [160], [159], [161] determined the debonding stresses for nanoparticles coated with interphases under different loading conditions. Lauke in [88] tried to determine the toughness of a particle reinforced polymer and he cited Eq. 4.4 from all the previously cited works. Finally, it is noteworthy that considering the limit case of a rigid particle, in an infinite matrix, with no interphase nor surface stress, the crack onset criterion obtained always coincides to Eq. 4.4.

4.1.2 Presentation of the case study

The case study for the spherical particle debonding is one single particle embedded in a cylinder of matrix. The geometry of the Representative Volume Element (RVE) is the one presented in Fig. 4.1. The radius of the sphere is equal to one tenth of the diameter of the cylinder: $R = L/10$, which corresponds to a volume fraction $\phi = 0.0053$. The geometry is reduced to a 2D structure by axisymmetry, and then only half of the geometry is modelled by using a mirror symmetry along the horizontal axis. In any case the material properties associated to the particle are those of the boron carbide while the matrix is an epoxy

resin. The mechanical properties of the particle, the matrix and the interface are detailed in Table 4.1. The following assumptions always apply to the present study:

1. the material behaviour of both particles and matrix is linear elastic;
2. the interface is infinitely stiff.

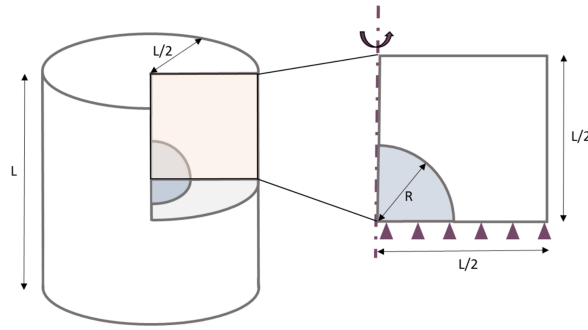


Figure 4.1: Spherical particle embedded in a cylindrical matrix; geometric reduction of the problem using symmetries.

| | E [GPa] | ν [] | σ_{max} [MPa] | G_c [J.m ⁻²] |
|-----------|-----------|-----------|----------------------|----------------------------|
| Particle | 450 | 0.2 | × | × |
| Matrix | 3 | 0.3 | × | × |
| Interface | ∞ | × | 50 | 100 |

Table 4.1: Mechanical properties of the materials

4.1.3 Cohesive Zone Model (CZM) approach

The CZM model has been introduced in Chapter 3 and was used to describe the debonding between particles and the matrix. A bilinear traction-separation law is chosen again for this study (Fig 4.2).

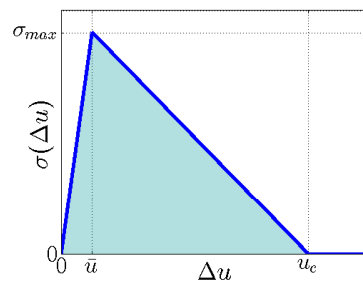


Figure 4.2: Bilinear Cohesive Zone Model.

It basically relies on two mechanical parameters: interface strength σ_{max} and interface fracture energy G_c (i.e. the shaded area under the traction-separation curve). The introduction of these two parameters induces the apparition of a critical displacement u_c which, according to Leguillon [91], is not a material parameter but a structural one. We can deduce the critical displacement u_c as a function of σ_{max} and G_c as follows:

$$u_c = \frac{2G_c}{\sigma_{max}} \quad (4.5)$$

The fracture energy of the traction-separation law is chosen to be 100 J.m^{-2} and its strength 50 MPa .

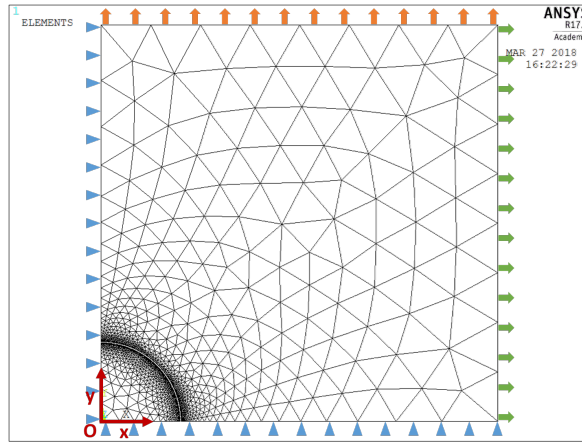


Figure 4.3: Geometry, mesh and loading conditions of the spherical particle debonding study with the CZM.

The mesh and boundary conditions are depicted in Fig. 4.3. The mesh is refined at the particle/matrix interface to suppress all mesh size effects. 180 interface elements are introduced so that each element represents 0.5° of angle. The following boundary conditions are applied to ensure mirror symmetries of the RVE:

$$\begin{cases} U_x(x = 0) = 0, \\ U_y(y = 0) = 0. \end{cases} \quad (4.6)$$

Uniform constant displacement conditions are imposed at the boundary of the mesh to reproduce either hydrostatic or uniaxial loading conditions. The reference stress applied to the RVE is obtained by summing all the nodal reaction forces where the displacement loading has been applied divided by the transverse surface area of the RVE.

4.1.4 Finite Fracture Mechanics (FFM) approach

For analysing crack onset and propagation with the FFM approach, the system elastic response is first evaluated considering several decohesion lengths along the particle contour. First considering a non-damaged situation (no decohesion), the FFM aims at determining the critical load responsible for crack onset over a finite length (or surface for the 3D case) ΔA . According to Leguillon [91], none of the traditional stress or energy criteria alone (i.e. LEFM, Griffith's theory) are sufficient to describe crack onset and propagation. Leguillon states that both criteria have to be simultaneously fulfilled for a crack to develop:

$$\begin{cases} \sigma_{eq} \geq \sigma_{max}, \\ \bar{G}(\Delta A) \geq G_c; \end{cases} \quad (4.7)$$

with σ_{eq} a scalar equivalent stress and \bar{G} the incremental energy release rate (IERR). More details related to the definition of these quantities are given below.

Stress criterion

Considering only an ultimate stress criterion, two surfaces are considered debonded when the interfacial stress reaches a critical value σ_{max} , which is a material parameter of the interface:

$$\sigma_{eq} \geq \sigma_{max}. \quad (4.8)$$

The cohesive stresses at the interface being a vector, one needs to define a scalar equivalent stress σ_{eq} to be compared to the interfacial strength. Several approaches exist in the literature, like the one of the maximal principal stress [154] or the quadratic average [52]. In the framework of this study, we will use a simple quadratic expression based on [52]:

$$\sigma_{eq} = f(\sigma_{ij}) = \sqrt{\langle \text{sgn}(\sigma) |\sigma|^2 + |\tau|^2 \rangle_+}, \quad (4.9)$$

which is a quadratic average of the normal and tangential stresses at the interface. The sign of the normal interfacial stress σ is introduced here so that a compressive stress state does not induce a favourable contribution to debonding. The use of the positive part implies that σ_{eq} is null when the compressive stress state is predominant, which is a rather severe condition. The stress criterion can then be applied using two different methods:

- the point method (PM) introduced by Leguillon [91], where the stress is evaluated at each position along the expected crack path, and then compared to the strength:

$$\sigma_{eq}(x) > \sigma_{max}, \quad \forall x \in \Omega_c; \quad (4.10)$$

- the line method (LM) introduced by Cornetti et al [26], where the stress is averaged along the crack propagation path, and then compared to the strength:

$$\frac{1}{\Delta A} \int_{\Omega_c} \sigma_{eq}(\tilde{x}) d\tilde{x} > \sigma_{max} \quad (4.11)$$

The PM will be employed for this study.

Energy criterion

An energy balance equation must be verified for a crack to propagate along the interface, considering the state of the system before and after crack propagation :

$$\Delta W_p + \Delta W_k + G_c \Delta A = 0, \quad (4.12)$$

where ΔW_p and ΔW_k are the variation of the potential energy and kinetic energy of the system respectively, G_c is the critical fracture energy per unit surface, and ΔA is the fractured surface created during the decohesion process. When a crack propagates in the system the kinetic energy increases so that $\Delta W_k \geq 0$. Then to satisfy the energy equilibrium, Eq. 4.12 becomes:

$$-\frac{\Delta W_p}{\Delta A} \geq G_c. \quad (4.13)$$

Now, according to Weißgraeber et al [154], one can introduce the concept of IERR \bar{G} . The crack propagates when \bar{G} reaches the fracture energy (per unit surface) G_c , also called surface toughness:

$$\bar{G} = -\frac{\Delta W_p}{\Delta A} \geq G_c. \quad (4.14)$$

This IERR clearly differs from the standard Griffith's criterion where the energy release rate $G = -\delta W_p / \delta A$ is compared to the fracture energy for each crack tip position. As defined by [154], the IERR is in fact the "average" of the energy release rate along the crack path so that the energy balance equation is evaluated over the whole crack propagation process:

$$\bar{G}(\Delta A) = \frac{1}{\Delta A} \int_{\Delta A} G(\tilde{A}) d\tilde{A}. \quad (4.15)$$

The energy release rate might be evaluated using the Virtual Closure Crack Technique (VCCT) [125]. This method is cited by Weißgraeber et al [154] as a way to determine the energy release rate for FFM. Cho et al [21] used this method in the case of a single spherical particle embedded in a polymer matrix to explain the size effect. Garcia et al [52] used it for a spherical particle in the FFM context. In the present study, another strategy is employed. The energy release rate is the change in potential energy of the system as the crack propagates. As schematically illustrated in Fig. 4.4 (a), the loss of

potential energy of a system loaded in uniaxial tension is equal to the shaded area between the load-displacement curves before (in blue) and after (in orange) crack propagation. From this consideration, it is possible to evaluate the energy release rate as a function of the evolution of the compliance of the structure. Indeed, deriving the expression of the potential energy in Eq. 4.14, and denoting P the load applied to the structure, U the associated displacement, and $C = U/P$ the compliance of the body, we are now able to calculate the energy release rate based on the compliance evolution of the body:

$$G = \frac{1}{2} P^2 \frac{dC}{dA} = P^2 G_{norm}, \quad (4.16)$$

where G_{norm} being the energy release rate normalised with the applied load. In the case of a spherical particle with a radius R embedded in a matrix, and θ the debonding angle, the normalised energy release rate becomes:

$$G_{norm} = \frac{1}{2} \frac{dC}{2\pi R^2 \sin(\theta) d\theta}. \quad (4.17)$$

To numerically determine G_{norm} , an elastic FE calculation is employed as the crack tip position is manually moved so that the evolution of the compliance provides the energy release rate.

The same method is employed for the hydrostatic loading case. The potential energy is this time the shaded area between the pressure-volume change curves before and after crack propagation (Fig. 4.4 (b)). To keep the same formalism as previously defined for uniaxial tension, a compliance c is defined as the ratio of the dilatation ΔV over the pressure p , and the energy release rate becomes:

$$G = \frac{1}{2} p^2 \frac{dc}{dA} = p^2 G_{norm}, \quad (4.18)$$

This procedure will be more precisely developed in the subsections 4.2.1 and 4.2.2 for the hydrostatic and uniaxial tensile loading cases.

Coupled criterion

The coupled criterion states that for a crack of a finite size ΔA , both the stress and energy criteria have to be simultaneously fulfilled along the crack path to allow the crack opening. Such a criterion leads to the following minimisation problem:

$$P_c = \min_{P, \Delta A} \{P \mid \sigma_{eq}(x) \geq \sigma_{max}, x \in \Omega_c \text{ and } \bar{G}(\Delta A) \geq G_c\} \quad (4.19)$$

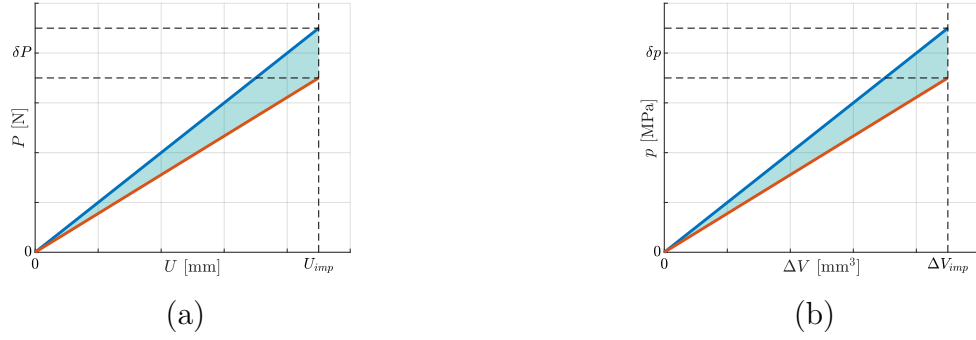


Figure 4.4: (a) Load-displacement curves of an elastic system before (blue) and after (orange) crack propagation;
 (b) Pressure-dilatation curves of an elastic system before (blue) and after (orange) crack propagation.

The solution to problem 4.19 indicates the minimum load that fulfills both criteria and the size of the crack ΔA . In the present work, the crack can only propagate along the interface between the spherical particle and the matrix. Therefore, for the sake of simplicity, the axisymmetry can be used to reduce the 3D problem to a 2D one. The problem 4.19 then becomes:

$$P_c = \min_{P, \theta} \left\{ P \mid \sigma_{eq}(\tilde{\theta}) \geq \sigma_{max}, \tilde{\theta} \in \Omega_c \text{ and } \bar{G}(\theta) \geq G_c \right\}. \quad (4.20)$$

4.2 Case studies of particle debonding

4.2.1 Hydrostatic debond of a single spherical particle: FFM / CZM comparison

The first reference case to be analysed is the debonding of a spherical particle from the matrix under hydrostatic tensile loading. Both the FFM approach and the CZM are employed. Concerning the boundary conditions (BCs), a displacement U is applied on every external surface on the structure (the imposed displacement is represented in Fig. 4.3 with the green and orange arrows):

$$\begin{cases} U_x(x = L) = U, \\ U_y(y = L) = U. \end{cases} \quad (4.21)$$

This particular loading case can lead to two different configurations: either the load is not sufficient to debond the particle from the matrix and the whole interface is still bonded (Fig. 4.5 (a)) or the load is sufficiently high to instantaneously trigger complete debonding of the particle (Fig. 4.5 (b)).

As stated previously, in the framework of FFM, the evaluation of the remote stress

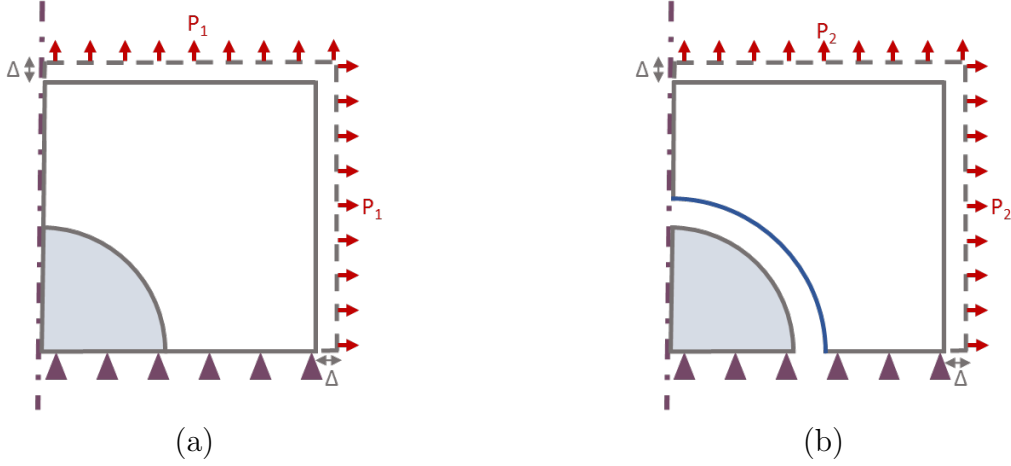


Figure 4.5: (a) Debonding of the particle under hydrostatic tensile loading before crack propagation: the interface is perfectly bonded; (b) Debonding of the particle under hydrostatic tensile loading after crack propagation: the particle is completely debonded.

responsible of debonding correspond to the minimum stress that fulfils both the stress and energy criteria, i.e. Eqs. 4.10 and 4.14 respectively.

An elastic FE calculation of the RVE considering perfect bonding (viz. rigid interface) between matrix and particle determines the relationship between the remote stress and the stress at the interface. The evaluation of the critical remote stress that fulfils the stress criterion is then straightforward (Eq. 4.10).

Concerning the energy criterion, the hydrostatic compliance c for both bonded and debonded situations is calculated with FE computation, and the normalised energy release rate is derived from the evolution of the compliance (Eq. 4.18). Then, the critical remote stress that fulfils the energy criterion (Eq. 4.14) is determined with the relation:

$$\sigma_{\infty c} = \sqrt{\frac{\Delta A G_c}{\Delta A G_{norm}}} = \sqrt{\frac{G_c}{G_{norm}}} \quad (4.22)$$

The same situation can then be described by introducing a cohesive zone along the particle/matrix interface.

This procedure is repeated for multiple particle radii (ranging from $10 \mu m$ to $2000 \mu m$). The R/L ratio being kept constant for all calculations. The results are plotted in Fig. 4.6 (a). The magenta dots represent the FFM predictions, the blue ones the CZM. The green solid line corresponds to that of the energy-based criterion Eq. 4.4. As a result, we observe that for small particles, the stress responsible for particle debonding increases when the particle size decreases. For larger particles, this stress reaches a plateau value. These observations hold for both FFM and CZM. The analytical expression derived in Eq. 4.4 matches very well with the results obtained from the FFM for small particles.

We can deduce that for particles whose radius is less than $400 \mu\text{m}$, according to both FFM and CZM approaches, the energy criterion controls the debonding onset. On the contrary, when particle radius is larger than this threshold value, the stress criterion is the predominant one.

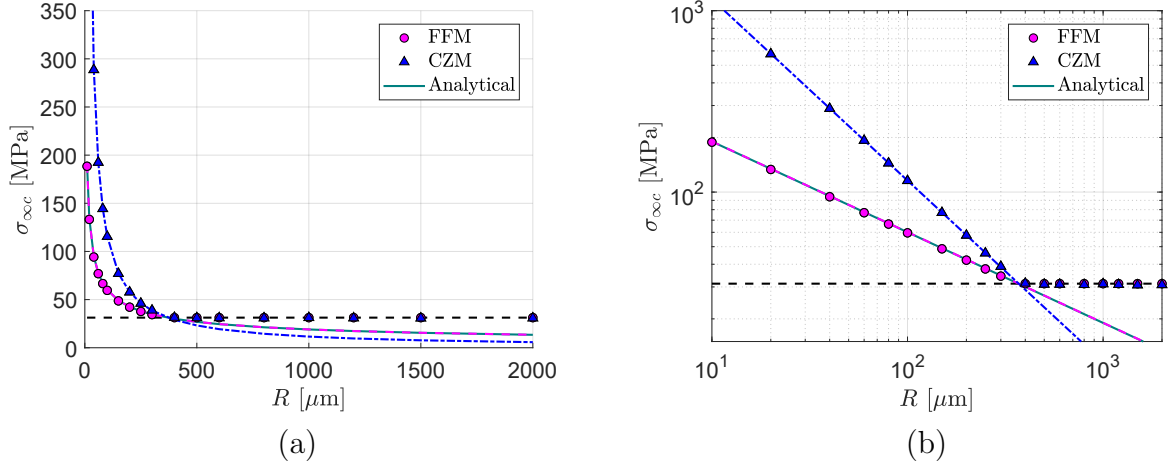


Figure 4.6: (a) Critical remote stress responsible for first debond against particle radius under hydrostatic tension;
 (b) Critical remote stress responsible for first debond against particle radius in logarithmic scale under hydrostatic tension.

The critical remote stress vs the particle radius can be represented on a log-log scale to help visualise the transition from $1/\sqrt{R}$ to stationary evolutions (Fig. 4.6 (b)) as predicted with the FFM approach. On the other hand, there is also a clear difference between the FFM and CZM approaches, since the remote stress for small particle sizes is proportional to $1/R$ in the (former) case. For larger particles, both models reach the same plateau value. The two regimes intersect at exactly the same particle radius for both models.

4.2.2 Uniaxial debond of a single spherical particle: FFM / CZM comparison

In this case, a vertical displacement U is imposed at the upper boundary of the RVE only in order to obtain a far field uniaxial stress state (the imposed displacement is represented in Fig. 4.3 with the orange arrows only). The right boundary ($x = L$) is left unconstrained so that the loading conditions can be summed up with:

$$U_y(y = L) = U. \quad (4.23)$$

For FFM analysis, the evolution of the system compliance is evaluated for several

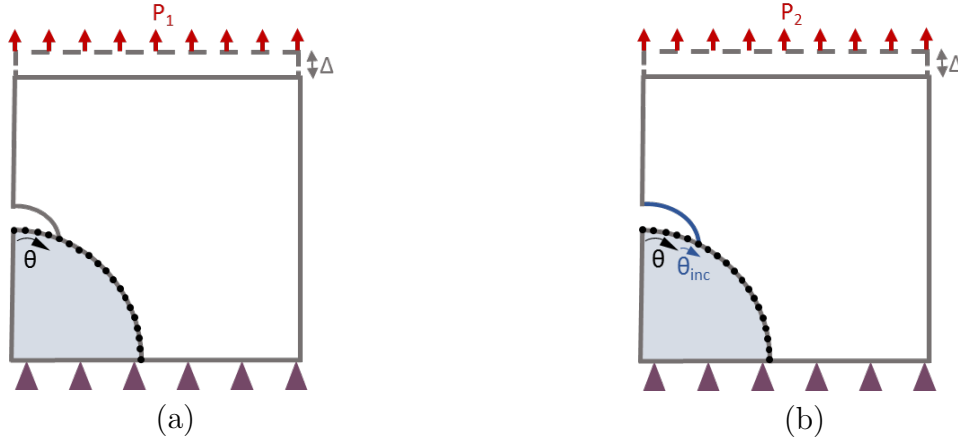


Figure 4.7: (a) Debonding of the particle under uniaxial tensile loading, the crack tip is at an angle θ ;
 (b) Debonding of the particle under uniaxial tensile loading, the crack tip is at an angle $\theta + \theta_{inc}$.

debonding angles with an increment θ_{inc} equal to 1° from fully bonded to fully debonded situation. The compliance is evaluated using the same methodology again: the imposed displacement, U , being known, the the reaction forces, P , on the top boundary is obtained by summing the nodal reaction forces (see Fig. 4.7 (a)). Then, the derivative of the compliance is calculated using finite difference scheme between the successive calculation steps: $dC/dA = \Delta C/\Delta A$ (see Fig. 4.7 (b)). Recalling Eq. 4.17, G_{norm} is calculated from the evolution of the compliance for every debonding angle, and for different particle sizes (see Fig. 4.8 (a)). The normalised energy release rate is found to be maximum for 45° for every particle size and the specific value of G_{norm} appears to be dependent on the particle radius. However, it is possible to find a quantity that is scale-independent if the normalised energy release rate is multiplied by R^3 , in which case all the curves are superimposed (see Fig. 4.8 (b)). The normalisation procedure allows the compliance evolution to be evaluated for only one particle size to determine the normalised energy release rate for all particle sizes (in accordance with [51]).

Using this energy criterion, it is possible to determine the remote stress which provokes the debond onset and the rapid decohesion of the particle over an angle θ , $\sigma_{\infty c}(\theta)$:

$$\bar{G}(\Delta A) = G_c, \quad (4.24)$$

$$\frac{1}{\Delta A} \int_{\Delta A} G(\tilde{A}) d\tilde{A} = G_c, \quad (4.25)$$

$$\frac{1}{\Delta A} \int_{\Delta A} P_c^2(\Delta A) G_{norm}(\tilde{A}) d\tilde{A} = G_c, \quad (4.26)$$

$$\frac{1}{\Delta A} P_c^2(\theta) \int_{\tilde{\theta}=0}^{\theta} G_{norm}(\tilde{\theta}) 2\pi R^2 \sin(\tilde{\theta}) d\tilde{\theta} = G_c, \quad (4.27)$$

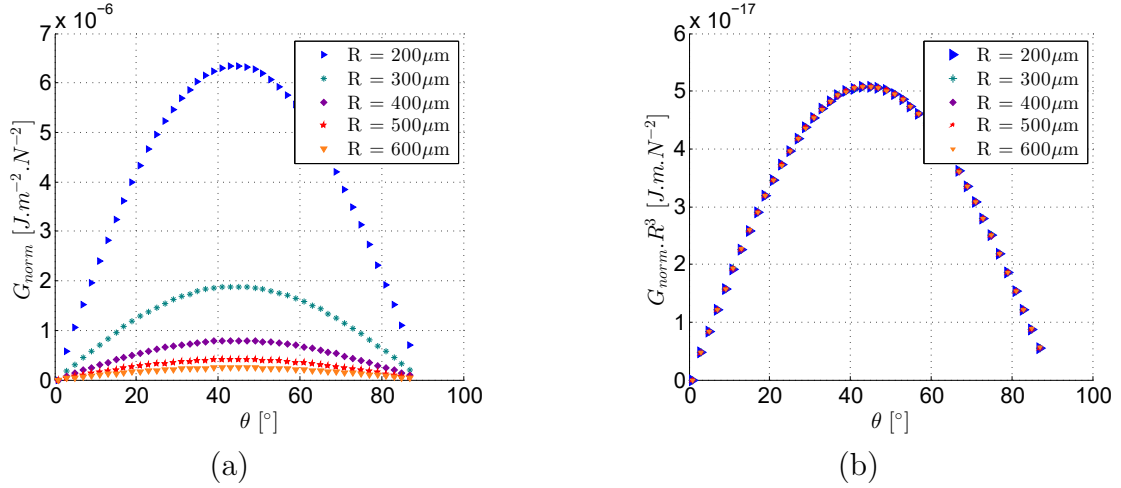


Figure 4.8: (a) Normalised energy release rate against debonding angle for different particle sizes;
 (b) Normalised energy release rates against debonding angle equalised for all the particle sizes.

$$P_c^2(\theta) = \frac{\Delta A G_c}{\int_{\tilde{\theta}=0}^{\theta} G_{norm}(\tilde{\theta}) 2\pi R^2 \sin(\tilde{\theta}) d\tilde{\theta}}, \quad (4.28)$$

$$\sigma_{\infty c}(\theta) = \frac{1}{S} \sqrt{\frac{\Delta A G_c}{2\pi R^2 \int_{\tilde{\theta}=0}^{\theta} G_{norm}(\tilde{\theta}) \sin(\tilde{\theta}) d\tilde{\theta}}}, \quad (4.29)$$

where $\Delta A = 2\pi R^2 (1 - \cos(\theta))$ is the crack surface, and $S = \pi(L/2)^2$ is the cross section of the representative element, under revolution symmetry assumption. The integral of G_{norm} only depends on one variable $\tilde{\theta}$ and is numerically evaluated using a trapezoidal rule.

Then, for FFM analysis, the stress criterion should be evaluated. The stress field along the particle/matrix interface, considered as rigid, is determined using linear elastic FE calculation. The stresses at the particle/matrix interface are obtained for every angular position along the interface and are plotted in Fig. 4.9. For spherical particles, the stress concentration only depends on the elastic contrast between the particle and the matrix and far field stress state. It is independent of the size of the particle. The evolution of the remote stress responsible for debonding according to the stress criterion is also reported in Fig. 4.10.

According to the FFM approach, both energy and stress criterion should be triggered for a crack to initiate. Then, the critical stress responsible for the debonding onset is the minimum stress that fulfils both criteria. This minimum value is also associated with a specific angle value, which actually corresponds to the debonding angle θ after onset. It

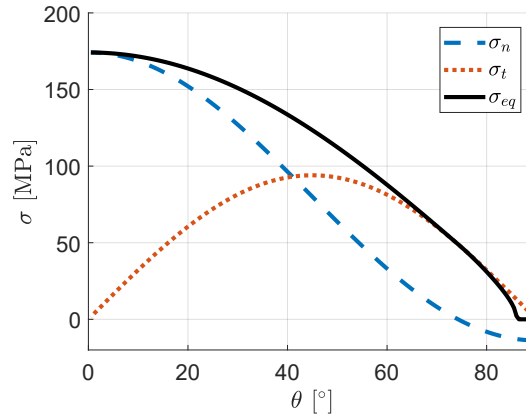


Figure 4.9: Local stress fields around the particle (for an arbitrary remote stress of 90 MPa).

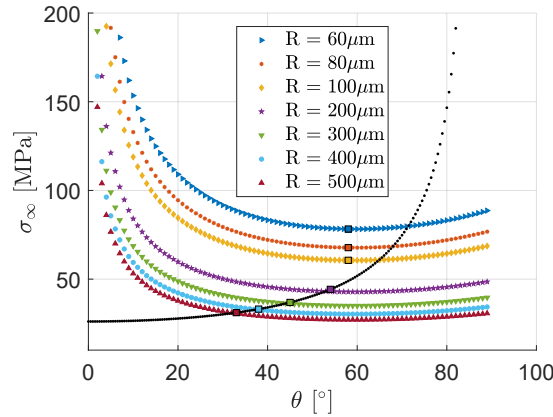


Figure 4.10: Remote critical stress against debonding angle for the energy and the stress criteria for different particle sizes.

is easy to observe from Fig. 4.10 that, with respect to the angular position, the stress criterion leads to a continuously increasing function, whilst, for all particle sizes, a local minimum is observed at ca 58° for all curves obtained with the energy criterion. Therefore, two different regimes can be observed. The first one is obtained when the curves of the stress and energy criteria intersect before the energy criterion minimum. For this regime, the minimum stress that fulfills both criteria is reached at the intersection of both curves. After this point (for smaller particles), the onset of decohesion is driven by the energy criterion rather than the stress one.

It is then possible to plot the remote stress responsible for debonding onset against the particle radius (Fig. 4.11 (a)). For small particles (R smaller than around $100\mu m$), the energy criterion is dominant and the critical remote stress increases with decreasing particle size. For particles whose radii are larger than $600\mu m$, the evolution of the critical remote stress reaches an asymptotic stationary evolution, as the stress criterion governs

the outcome. For intermediate particles size ($100\mu\text{m} \leq R \leq 600\mu\text{m}$) smooth transition between the two regimes is observed where both interface strength and fracture energy influence the debonding conditions.

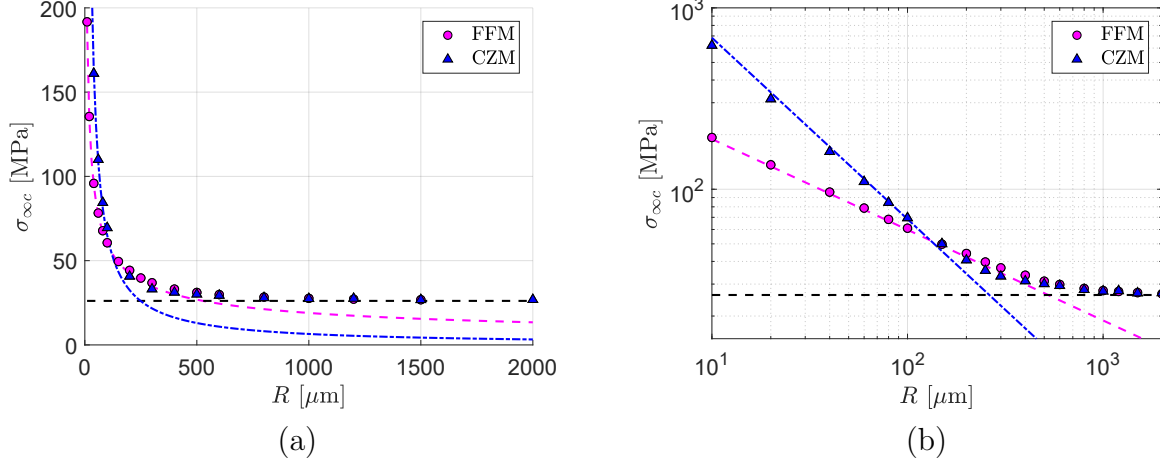


Figure 4.11: (a) Critical remote stress responsible for first debond against particle radius under uniaxial tension;
 (b) Critical remote stress responsible for first debond against particle radius in logarithmic scale under uniaxial tension.

Similar analysis is then carried out numerically using CZM to describe the particle/matrix interface separation behaviour. Very similar trends to the one obtained with the FFM approach are observed (see Fig. 4.11 (a)). For now, we focus on the dependence of the critical remote stress and decohesion angle as a function of the particle radius, R . This evolution has also been plotted in a log-log scale for comparison with the results obtained with the FFM method (Fig. 4.11 (b)). Again, two asymptotic regimes are observed. For the largest considered particle sizes, the critical remote stress obtained with both methods reaches the same plateau value corresponding to the situation when decohesion is driven by the interface strength. For the smallest particles, however, as previously observed under a hydrostatic loading condition, two different asymptotic regimes are observed. With the FFM, the critical stress is proportional to $1/\sqrt{R}$ while with the CZM, it is proportional to $1/R$.

4.2.3 Discussion on the physical interpretations for both models

Overall, both models (FFM and CZM based) provide the same outcomes: large particles tend to debond prior to smaller ones, which corroborates existing experimental findings. However, quantitatively, the results obtained by both numerical simulations and FFM method do not match. First, it is to be noted that for the hydrostatic loading, the results exactly match the trend lines, whereas for the uniaxial loading only asymptotic behaviours

are observed. Two different asymptotic behaviours are described, one for small particles and one for large particles.

For large particles, a plateau value is reached for the critical remote stress responsible for debonding onset $\sigma_{\infty c}$. This value is the exact one for which the stress at the particle/matrix boundary exceeds the interfacial strength. It is the same one for both the FFM and the CZM. It means, that for large particles, debonding is governed by the stress criterion.

For small particles, the critical stress $\sigma_{\infty c}$ is proportional to $1/\sqrt{R}$ in the framework of FFM and to $1/R$ when using the CZM approach. In the case of hydrostatic loading, asymptote matches that of the analytical approximation, based only upon the energy-based criterion from Eq. 4.4. This means that the debonding of small particles is governed by the energy criterion with the FFM. The evolution in $1/\sqrt{R}$ of $\sigma_{\infty c}$ is the one predicted by the energy criterion. However, with the CZM, the critical stress is proportional to $1/R$ which implies that the fracture process might not be properly captured by the simple linear fracture mechanics analysis. Indeed, from the numerical simulation with the CZM, not only the crack onset and propagation can be captured but also the development of the interface damage ahead of the crack tip. It should be remembered that with the FFM method, only infinitely small damage process zones are considered at the crack tip. For large particles, the size of the process zone is small compared to the particle dimension whatever the position of the crack tip is. In this case, the effect of interface behaviour nonlinearity is negligible in both stress and energy based analysis.

To the contrary, for small particles, a large process zone is observed ahead of the crack tip with the CZM. This means that the assumptions of the LEFM are not verified anymore and that the energy is dissipated not only at the crack tip but around the whole particle before full decohesion is reached at the pole of the particle. With the CZM, much higher critical stress is observed compared to the one predicted with the FFM approach, the difference being more pronounced as long as the particle reduces. This effect is simply attributed to the increase of the damage process zone observed with the CZM at the crack onset. For the smallest particle considered here, the process zone at damage onset is extended to almost the whole interface. These results question the capacity of both FFM method and CZM to properly capture the particle decohesion process since capturing the exact extent of process zone and/or shape of interface separation law seems difficult experimentally, despite the fact that they clearly control the critical stress scaling law for small particles.

In this preliminary analysis, only the far field stresses provoking the initial particle/matrix debonding as predicted with FFM and CZM were compared. Clearly, both approaches suggest that a different scaling law controls the evolution when the particle decohesion is governed by the fracture energy rather than the strength of the interface

(i.e. small particles). Additional simulations for parametric analysis were performed to evaluate the influence of CZM parameters on the master curve.

The influence of all three CZM law parameters (fracture energy G_c , strength of the interface σ_{max} , critical displacement u_c) on master curves is evaluated. Four CZM are employed and their properties are expressed in Table 4.2. The characteristic length, often used as a descriptor of the brittleness of interfaces, is defined as [51]:

$$l_{ch} = \frac{G_c E_{eff}}{\sigma_{max}^2}, \quad (4.30)$$

with G_c and σ_{max} being the interface fracture energy and strength respectively and E_{eff} being the harmonic mean of Young's moduli of the particle and the matrix.

| | G_c [$J.m^{-2}$] | σ_{max} [MPa] | u_c [mm] | l_{ch} [mm] |
|-------|----------------------|----------------------|------------|---------------|
| CZM 1 | 100 | 50 | 0.004 | 238.4 |
| CZM 2 | 50 | 50 | 0.002 | 119.2 |
| CZM 3 | 200 | 100 | 0.004 | 119.2 |
| CZM 4 | 100 | 100 | 0.002 | 59.6 |

Table 4.2: CZM properties

The CZM 1 and 2 share the same strengths σ_{max} . The CZM 1 and 3 share the same critical displacements u_c . The CZM 1 and 4 share the same critical energies G_c . The results for the critical remote stress against the particle radius are plotted in Fig. 4.12 a. for the 4 different CZM. Fig. 4.12 b. represents the same plot in a log-log scale.

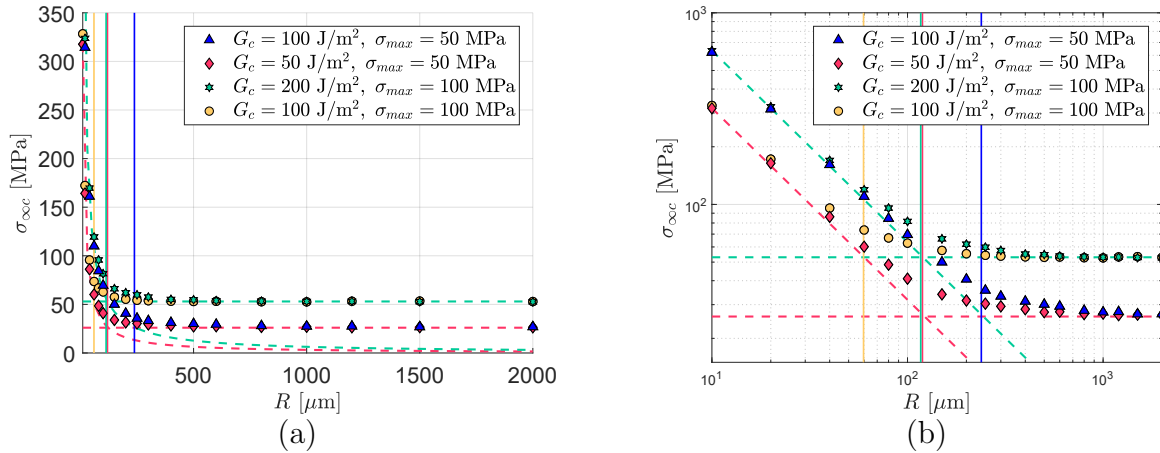


Figure 4.12: (a) Critical remote stress against particle radius for different CZM; (b) Same plot in log-log scale.

As previously observed, two asymptotic regimes are visible for small and large particles. The characteristic length l_{ch} seems to be a very good descriptor of the transition between

the two regimes as it corresponds to the intersection of the asymptotes for all the CZM. For small particles, the critical remote stresses obtained using the CZM 1 and 3 are the same. This result seems to imply that the predominant CZM parameter for small particle debonding is the critical length u_c . For large particles, the plateau values of $\sigma_{\infty c}$ when using CZM 1 and 2 are the same. This last result confirms that the strength σ_{max} of the CZM governs the debonding for large particle sizes. A final remark concerns the results related to the CZM 1 and 4 which share the same fracture energy: the respective remote stresses don't have any asymptote in common.

The same types of scaling laws are observed for all tested configurations, but in all cases it was not possible to match the results obtained from numerical simulations with the ones predicted with FFM. This suggests different physical phenomena drive the nucleation of the crack. The explanation is rather classical. Indeed, CZM are known to not only account for the dissipation of the energy required for crack propagation but also to describe the development of a process zone ahead of the crack tip having a finite length. This process zone size is an additional length scale to be taken into account in the dimensional analysis.

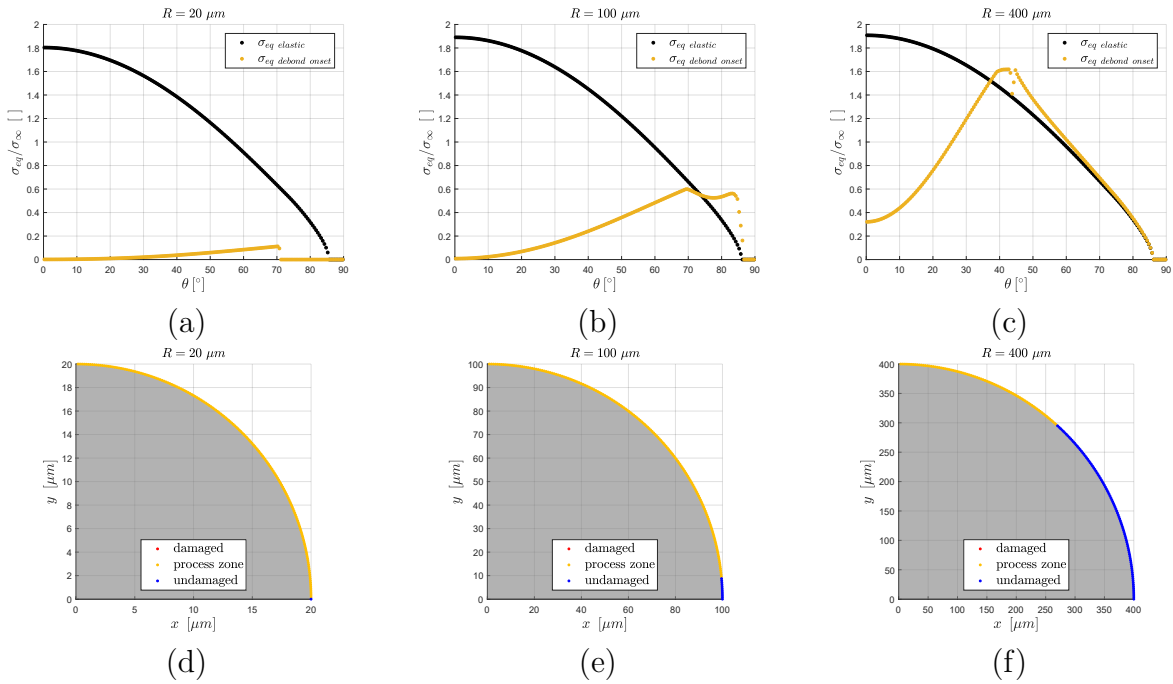


Figure 4.13: Equivalent stress concentration around the particle for (a) $R = 20 \mu\text{m}$, (b) $R = 100 \mu\text{m}$, and (c) $R = 400 \mu\text{m}$, and size of the process zone for (d) $R = 20 \mu\text{m}$, (e) $R = 100 \mu\text{m}$, and (f) $R = 400 \mu\text{m}$, the time step before debonding onset.

To investigate/illustrate the effect of process zone development during the debonding nucleation and onset process, the stress concentrations around the particle at the time step just before the debonding onset are represented in Fig. 4.13 together with the the size of the process zone obtained from the numerical simulation. Figs 4.13 (d), (e), and

(f) represent the quarter of the particle modelled (gray area) and the process zone is represented in yellow. Three particle sizes are considered ($R = 20 \mu\text{m}$, $R = 100 \mu\text{m}$, $R = 400 \mu\text{m}$). Clearly the situation appears different. For large particles, a small process zone is observed ahead of the crack tip prior to unstable crack propagation, whereas a large process zone is observed for small particles.

More complete analyses on the size of the process and on the effect of the CZM parameters are presented in Appendices B and C respectively.

4.2.4 Uniaxial debond of a single angular particle: FFM / CZM comparison

In the previous subsections, the debonding of perfectly spherical particles has been described with the FFM and the CZM. However, some applications of particle reinforced material require the use of angular particles rather than spherical ones. In order to analyse the debonding phenomenon of a more generic particle shape, the example of a boron carbide particle embedded in an epoxy matrix has been analysed. First, the angular particle has been observed with Scanning Electron Microscopy (SEM), see Fig. 4.14. This particle shows facets and sharp angles than can have a significant influence on the behaviour of the composite material, as this type of geometry can introduce significant stress concentrations. A typical 2D geometry of an angular particle has been extracted from Fig. 4.14. To avoid stress singularities, all the sharp angles of the particle have been rounded with small fillets. Maintaining sharp features would necessitate specific FFM treatment, which is out of the scope of the present study.

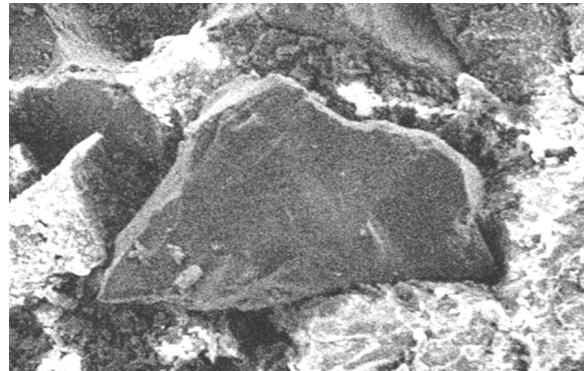


Figure 4.14: Boron Carbide (B_4C) particle embedded in the epoxy matrix observed with SEM.

The revolution symmetry condition cannot be applied to angular particles hence, to keep a 2D analysis framework, plane strain assumption is introduced. This situation is usually considered for cross sectional analysis of composite materials, but it will also give valuable physical insight into the debonding process of angular inclusions. More

quantitative analysis would necessitate full 3D calculations. Taking advantage of the 2D situation, we will now concentrate on the influence of both particle size and particle orientation on the critical stress leading to particle decohesion (see Fig. 4.15). To compare these results with a reference situation, the same calculation were performed considering circular (cylindrical) inclusion. The radius of the inclusion is denoted R again, for the RVE but the new volume fraction, $\phi = 0.0314$, is used for both the angular and circular inclusion (see Fig. 4.16). The equivalent radius of the angular inclusion R_{eq} is defined as the radius of the circular inclusion leading to the same volume fraction.

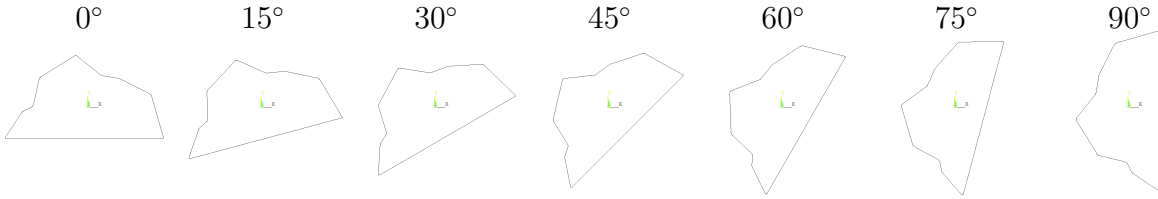


Figure 4.15: Rotations of the angular particle from 0° to 90° .

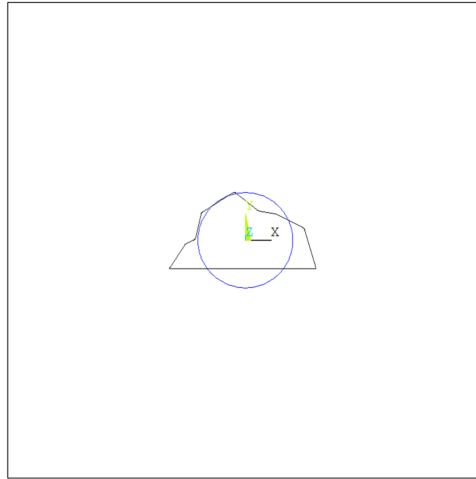


Figure 4.16: Geometries of embedded particle (circular and angular).

The CZM simulations are performed for various particle size and orientation to determine the critical remote stress responsible for the debond onset. The mesh and boundary conditions of the FE analysis are described in Fig. 4.17. A uniaxial tensile loading is applied to the RVE, and the boundary conditions can be mathematically formalised as follows:

$$\begin{cases} U_x(x = 0, y = 0) = 0, \\ U_y(y = 0) = 0, \\ U_y(y = L) = U. \end{cases} \quad (4.31)$$

Also in this case, the scale effect was analysed by performing homothety operations on the RVE. First, the particle with a 0° orientation is studied. The critical remote

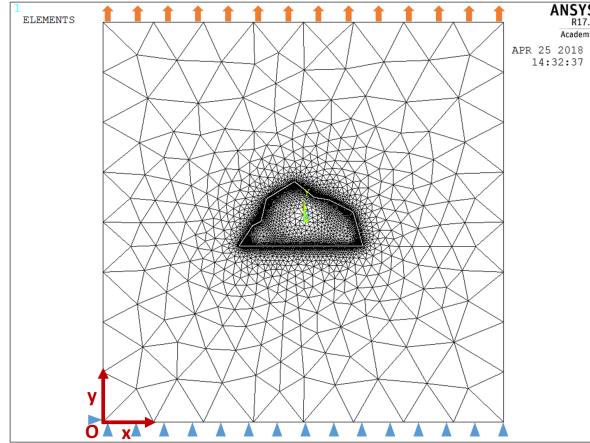


Figure 4.17: Geometry, mesh and loading conditions of the angular particle debonding study with the CZM.

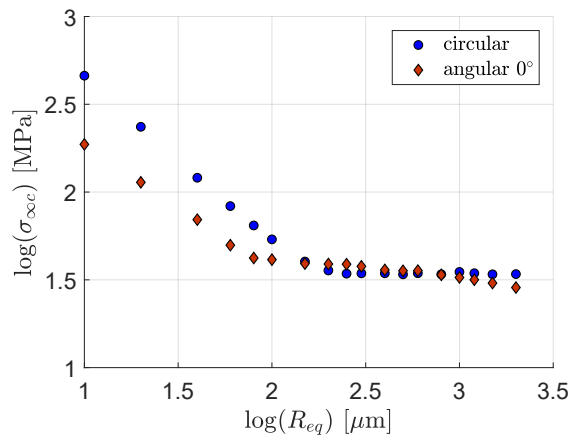


Figure 4.18: Critical remote stress against particle (equivalent) radius for the circular and angular (0° rotation) particles.

stress responsible for the debonding onset is determined and plotted against the size of the particle (expressed through the equivalent radius R_{eq}) in Fig. 4.18. The results are compared to the one obtained with the circular inclusion. It can be observed that the size effect remains very significant and small particles tends to debond at higher remote stresses than larger ones whether they are cylindrical or they exhibit polyhedral nature. As observed for the spherical particle, the critical remote stress reaches a stable value for large particles when we consider a circular inclusion. However, for the angular inclusion, the critical remote stress for large particles slightly decreases with the increase in particle size.

Figs. 4.19 and 4.20 report the critical remote onset stresses for the angular particle as a function of particle size and angular position. A similar large/small particle transition regime is observed whatever the orientation of the particle. However, while stationary

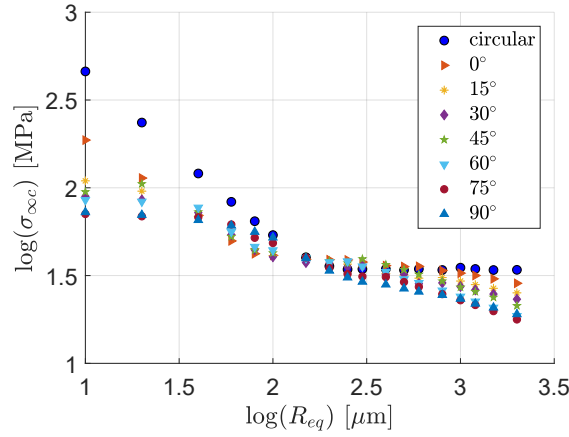


Figure 4.19: Critical remote stress against particle (equivalent) radius for the circular and all the angular (0° to 90° rotation) particles.

critical remote stress is observed at orientation 0° for large particle, a significant decrease is observed for other angular position, the most severe configuration being 90° . For this configuration, almost constant decrease of the remote critical stress is observed. This clearly indicates that the crack onset is not only controlled here by the dimension of the particle but the small curvature radius at the tip of the stress raisers. As a consequence, the crack onset is controlled by energy criteria rather than the stress one. The slope characterising the scaling law depends upon the orientation, since the development of the process zone not only depends upon both the overall particle geometry and size but also on the local particle geometry near the stress raiser at which the decohesion is observed.

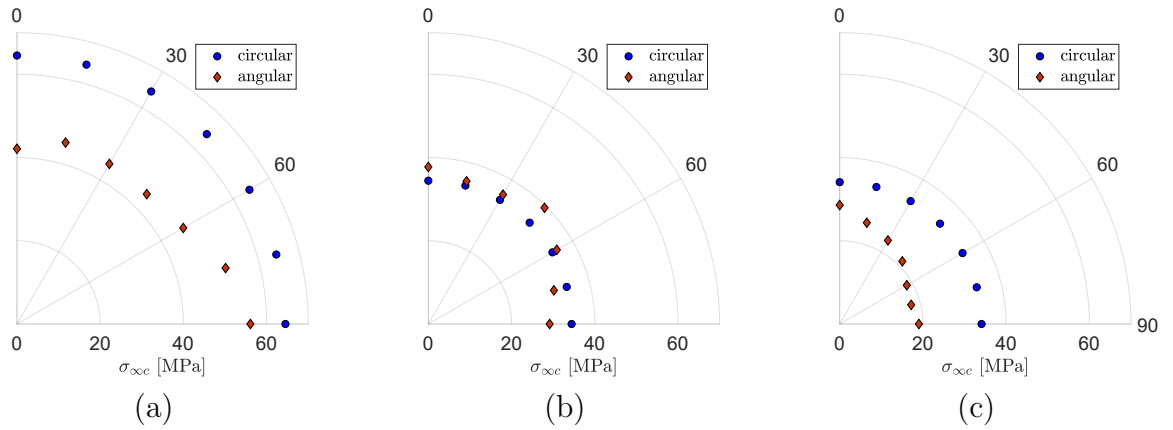


Figure 4.20: Critical remote stress against rotation angle for angular particles ((a) $R_{eq} = 80\mu m$, (b) $R_{eq} = 300\mu m$, (c) $R_{eq} = 2000\mu m$)

4.3 Conclusions

The effect of particle size on particle/matrix debonding has been studied using two different models: an analytical one (FFM) and a numerical one (CZM). First a spherical particle has been considered and two types of loading conditions have been applied: hydrostatic and uniaxial tension respectively. A clear particle size effect has been observed:

- For both models, the larger the particle, the smaller the critical load required to initiate particle debonding. This is in good accordance with experimental observations from the literature.
- Both models are based on two parameters: the critical energy release rate G_c and the strength σ_{max} . For both models two asymptotic behaviours are observed depending on the two parameters introduced:
 - For large particles, both models give a plateau value of the critical stress for debond onset. This value is reached when the stress at the interface exceeds its strength. This means that for large particles, the debonding process is governed by a stress criterion.
 - For small particles, different asymptotic behaviours are observed for the two models. The evolution of the critical stress that triggers debonding is proportional to $1/\sqrt{R}$ for the FFM-based model and proportional to $1/R$ for the CZM. For these small particles, the debonding process is governed by an energy criterion. The value $1/\sqrt{R}$ of the FFM is also in accordance to analytical energetic considerations previously made in the literature.
- The difference between FFM and CZM scaling law is attributed to the presence of large process zone prior to full debond, which is not taken into account with FFM analysis. Such mechanisms enhance the energy dissipation as well as the interface stiffness introduced in the CZM, which modifies the whole RVE behaviour for small particles.
- Both models show an intermediate behaviour for particles in the transition zone between the two asymptotic behaviours. The transition from one behaviour to the other can be estimated using a characteristic length l_{ch} , whatever the interface and materials properties of the model.

Those two models have then been applied to an angular particle situation, this geometry being more representative of the ones observed when ceramics (boron carbide, alumina, etc.) are used as reinforcements. The sharp corners have been smoothed with fillets in order to overcome stress singularity effects, whilst keeping large stress concentration values.

A size effect similar to the one for spherical particles has been observed as large particles tend to debond prior to smaller ones. A scaling law different from that of circular particle is found, and several transition regimes are observed depending on particle orientation: the crack onset is either triggered by the overall geometry or by the influence of local stress raisers around the particle. Individual treatment of the corner/sharp geometry should be undertaken when comparing the FFM approach with the CZM approach for a more precise evaluation of the influence of process zone development on particle/matrix decohesion and critical remote stress value.

Chapter 5

Perforation at slow loading rate: Indentation tests

Ballistic armours are generally composite systems where each layer is added to fulfil part of the functions needed to block or at least drastically hinder the progression of a threat/bullet. Amongst these functions, a hard phase is required to break the tip of the bullet, making its penetration more difficult. In the present study, instrumented macro-indentation tests have been implemented to evaluate the particle reinforced polymer mechanical behaviour under loading conditions, which are more representative of real application (viz. compressive highly hydrostatic - high speed). Indeed, hardness is a prerequisite for ballistic protective materials, enabling the fragmentation and erosion of the projectile. Furthermore, particle percolation and resulting fragmentation are expected to influence the final failure mechanism. This experimental campaign has been developed to observe the behaviour of such a material under a localised compressive loading and to evaluate its hardness. The effects of the nature of the reinforcements, the particle volume fraction or the particle size under quasi-static loading are evaluated.

5.1 Instrumented indentation tests setup

Indentation tests are now routine procedures for rapid evaluations of material mechanical properties. Not only can the hardness be determined but refined analyses could be used for the determination of brittle materials toughness, yield stress of metals, etc, from experimental results. The loads and deformations are very localised so that the material is affected only locally. Also the indenter size and experiment can be miniaturised to probe microscopic material volumes. The material property commonly extracted from indentation tests is the hardness. This is generally defined as the “resistance to permanent deformation” [69] or “the intensity of the maximum pressure which just produces yielding”

[118].

Various types of hardness are described in the literature, as there are multiple definition and test setups. Meyer's hardness is defined as the load applied divided by the projected contact area when indented by a spherical indenter. Brinell hardness is defined as the load applied (expressed in kilogram-force, kgf) divided by the contact area of a spherical indenter. Vickers hardness number is determined by the load over the surface area of the indentation using a four-sided pyramidal indenter. The Berkovich test is similar to that of Vickers' but using a three-sided pyramid. The hardness values obtained with the different tests setup are not absolute but test-dependent. Similarly the size of the indenter and indentation depth has to be chosen so that the material could be considered as homogeneous.

Load-penetration curves are commonly employed to determine mechanical properties using indentation tests. Numerous methods have been developed to extract uniaxial mechanical properties such as elastic moduli, or even stress-strain curves [37]. According to [118], the ability to produce indentation stress-strain curves has generally been more successful with spherical indenters [43], leading to smoother stress fields and larger initial elastic segments (compared to sharper indenters). It is then more simple to follow the evolution of the mechanical response of the material from initial elasticity to large plastic deformations. Spherical indenters also generate a larger contact surface, that is preferable to determine the homogenised mechanical properties of the particle reinforced composite studied here.

5.1.1 Specimen manufacturing and geometry

The samples are cylinders with a 25mm diameter and 8mm height (Fig. 5.1). Various particle volume fractions, particle sizes and mixtures have been used for these series of tests. Unless other reference is mentioned, the default resin used for the matrix is RenLam and no silane treatment is applied to the particles.

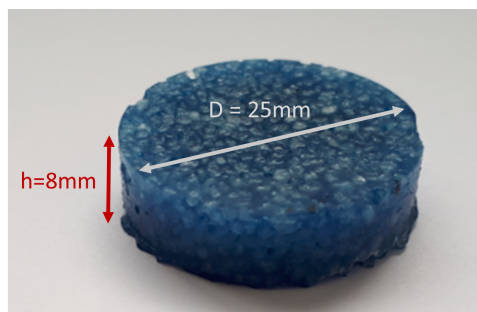


Figure 5.1: Indentation sample (Al_2O_3 F20 $\phi = 50\%$).

To manufacture these samples, a mould based on the same principle as for tensile or

Iosipescu specimens are used (see Fig. 5.2). The mould is divided into 3 parts. The top and bottom parts are steel plates used to apply pressure and confine the specimens. The central part is made of silicone (to be easily manufactured and to ensure simple release of the specimens). This middle part is filled with material before curing, and pressure is applied on the system during the whole curing cycle. Metallic rectangles are inserted at the corners of the central part to prevent excessive deformation when pressure is applied.

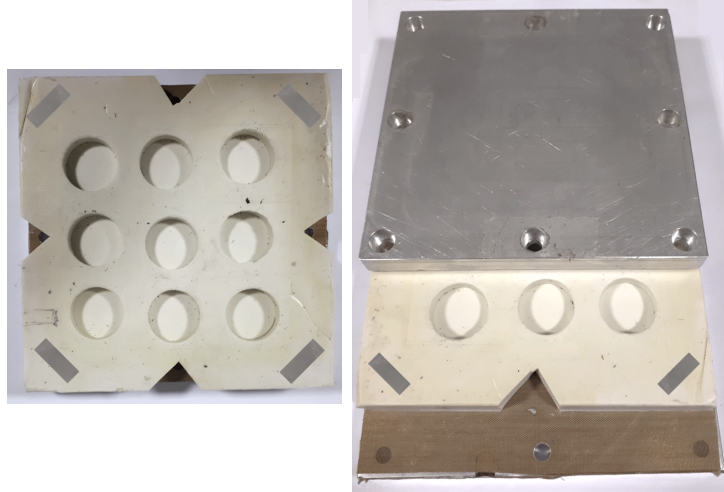


Figure 5.2: 3-part mould for indentation samples.

5.1.2 Experiment protocol

The experimental configuration used for the quasi-static indentation tests are presented in Fig. 5.3. The indenter consists of a 4.38 mm diameter steel ball extracted from a roller bearing and thus ensuring high yield limit. This ball is placed on a conical holder attached to the load cell of an electromechanical tensile testing machine. The load cell capacity is 10 kN. The tests are performed under 0.2 mm/min constant crossbar displacement rate. The crossbar displacement is not a valid quantity to analyse the test since it is affected by the whole machine deformation. The penetration h of the indenter is defined as the displacement of the indenter relative to the initial undeformed surface [114].

In the present configuration, a digital image correlation technique was used to measure both the indenter displacement and the specimen surface displacement. A digital camera can acquire a series of images over the test duration. Black and white random pattern is produced on the specimen by spraying acrylic paint on each specimen and ball. A single camera is used to collate a 3D displacement field, taking advantage of the axisymmetric nature of the test setup. The experimental setup and DIC acquisition results are presented in Fig. 5.3.

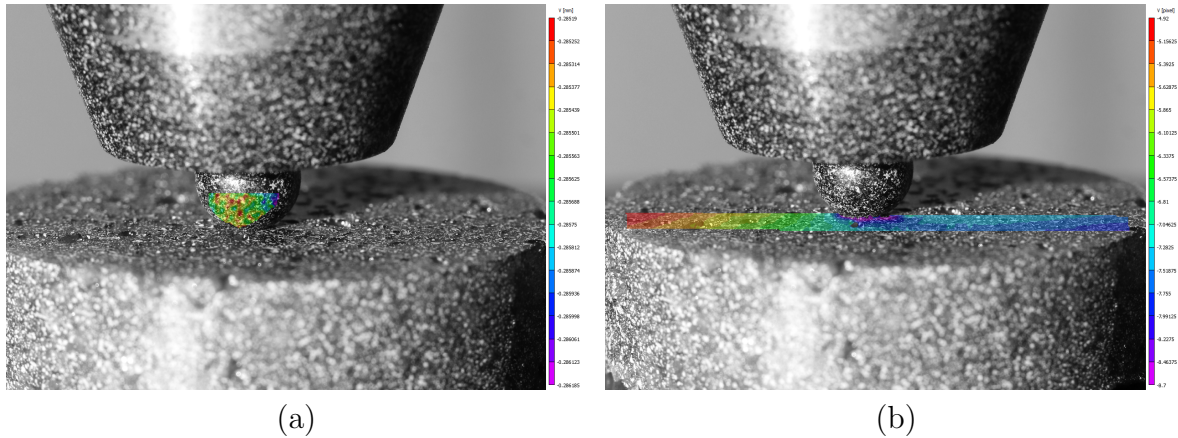


Figure 5.3: Digital image correlation for the indentation tests: vertical displacements of the indenter (a) and of the sample (b).

5.2 Monotonic loading until failure

At first, the specimen were loaded monotonically until failure was observed.. The specimen ultimate load and resistance to penetration were then obtained for various material compositions under the same experimental conditions.

5.2.1 Failure of the particle reinforced composite under indentation loading

Typical load versus penetration depth evolutions are represented in Fig. 5.5 for specimens with various particle contents. Such experiments are little documented in the literature for particle reinforced polymers or granular materials. During the whole experiment, the indenter smoothly penetrates the samples without experiencing any jumps in displacement values. A slight pile-up phenomenon [114] was observed on some samples but this could not be confirmed with DIC (Fig. 5.3 (b)). It was then estimated that this phenomenon did not have an important effect on the contact radius determination. Even for low indentation loads, a significant irreversible behaviour is observed below the indenter and the behaviour of the material quickly deviates from Hertz theory of elastic contact [62].

After the material was permanently indented and compacted in the area below the indenter, a sudden failure of the specimen was observed, and the disk split into three equal sectors. Indeed, three radial cracks, separated by an angle of 60° , were consistently observed at failure. When the composite contains large particles, the radial crack surfaces were very rough (Fig. 5.4 (a)), whereas for fine particles, the crack surfaces were significantly smoother (Fig. 5.4 (b)). This is a clear indication that the cracks propagated between the particles due to the circumferential tensile stress that develops in the disk. The particle strength being much higher than that of the matrix, particle cracking was

obviously not expected. Fracture surfaces of these samples are represented in Appendix D.

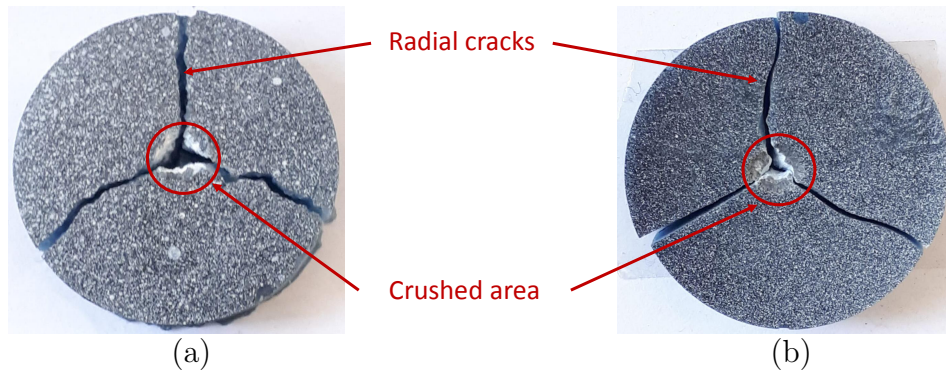


Figure 5.4: Fractured samples under monotonic indentation, with mixed alumina particle sizes (70% F20, 30% F360) (a) and F360 alumina particles (b).

5.2.2 Effect of the design parameters on the indentation behaviour

Several specimens containing various particle volume fractions and size distributions were manufactured. Also the type of matrix was modified. The main objective here was to evaluate how these microstructural parameters could influence the penetration resistance of the specimen through better stress/force transfer through grain chains.

Particle volume fraction effect

The effect of particle volume fraction on the indentation behaviour of the material was evaluated using specimens manufactured with both monodisperse and polydispersed particle sizes. The ones having monodisperse particles were made with F60 alumina particles considering 30% and 50% particle volume fractions. The load-displacement curves recorded during indentation test for these two materials are represented in Fig. 5.5 (a). The results are also compared to bulk resin samples. There is a clear stiffening effect with the introduction of higher particle volume fractions. Moreover, the correlation between the failure load and the particles volume fraction is not monotonic as the highest load to failure is obtained for a volume fraction equal to 30%. This could be explained by the fact that the introduction of more particles could be detrimental as it induces higher stress concentrations.

Secondly, polydispersed particle sizes samples were tested considering 70% of F20 (large particles) and 30% F360 (fine particles) proportions. With such particle mixture, volume fractions up to 60% can be reached. Specimens having 30%, 40%, 50%, and 60% particle volume fractions were manufactured. The load-displacement curves recorded

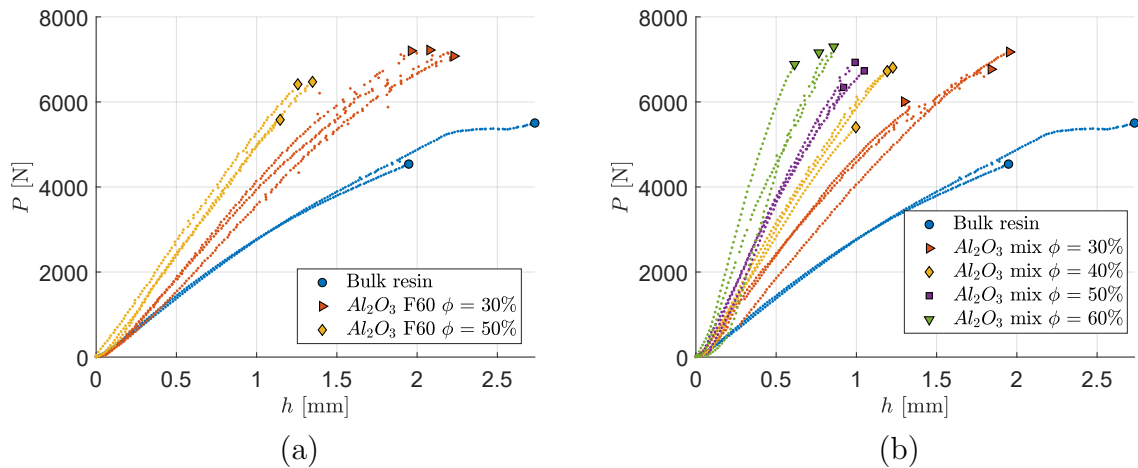


Figure 5.5: Load-displacement curves for monotonic indentation. Effect of particle volume fraction for (a) monodisperse particle size F60 and (b) polydisperse particle sizes.

when performing indentation tests on these specimens are represented in Fig. 5.5 (b). The stiffening effect of the alumina particles is confirmed here as the slope of the force-displacement curves increases with increasing particle content. The ultimate load seems to be stable with respect to particle volume fraction, which also means that the maximum penetration of the indenter is drastically reduced in the case of high particle contents.

Particle size effect

The effect of particle sizes was first evaluated for alumina particles. A first series of specimens having monodisperse particle sizes (F20, F60, and F360) and same particle volume fraction of $\phi=30\%$ were produced. The monotonic indentation curves measured on these samples are plotted in Fig. 5.6 (a). The three types of samples showed roughly the same indentation stiffness. A slight increase of the ultimate load could be observed with decreasing particle size. However, because the experimental scatter was high the ultimate load was considered to be constant.

Similar analysis was undertaken with boron carbide particles (F60, F360, and F1200), the results are represented in Fig. 5.6 (b). Again, the indentation stiffness was unaffected by the particle size (except that the scatter is higher for larger particles) and the ultimate load remained relatively constant.

Effect of the matrix material

Two types of matrices were also tested, a brittle one (RenLam) and a very ductile one (SW2216). The two matrices were tested considering a 60% alumina particle content.

The resulting monotonic indentation curves for the two different epoxy matrices are

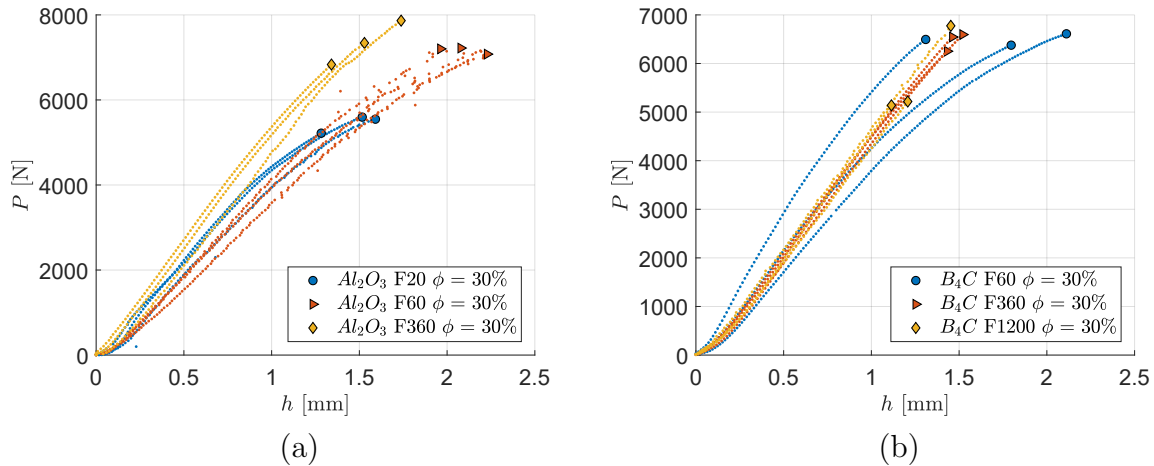


Figure 5.6: Load-displacement curves for monotonic indentation. Effect of particle size for (a) alumina particles and (b) boron carbide particles.

reported in Fig. 5.7 (a). The indentation stiffness of the specimens was remarkably higher when Renlam resin was used compared to SW2216. This observation is consistent with individual properties of the matrices. The natures of failure was also very different for the two types of specimens. The Renlam resin produced a brittle fracture, whilst the SW2216 produced a much more ductile behaviour represented by a stable crack propagation through the composite. This is also confirmed when observing the failed specimens (Fig. 5.7 (b) and (c)). As explained previously, with RenLam, the samples catastrophically failed as three radial cracks develop. However, with SW2216, the failure is more progressive and only one crack developed.

Effect of the reinforcement material

The influence of the particle nature was also evaluated. Two types of particles were considered: alumina and boron carbide. Boron carbide exhibits higher Young's modulus and strength than alumina. First, the samples tested were composed of monodisperse particles (F60 with a volume fraction equal to 50%). The results of monotonic indentation are plotted in Fig. 5.8 (a). For both types of particles, the stiffness and the load to failure were equivalent, and no effect of the particle type was detected.

Secondly, samples with mixed particle sizes were tested to reach particle volume fractions up to 60%. Even if the samples had the same particle volume fractions, different particle size distributions were employed. The samples with alumina particles were mainly composed of large particles (70% F20, 30% F360), whereas the samples with boron carbide particles were mainly composed of small particles (50% F1200, 25% F360, 25% F60). The results of these indentation tests are represented in Fig. 5.8 (b). Again, indentation stiffness are roughly the same, but an increase of failure load was observed for B4C (ϕ

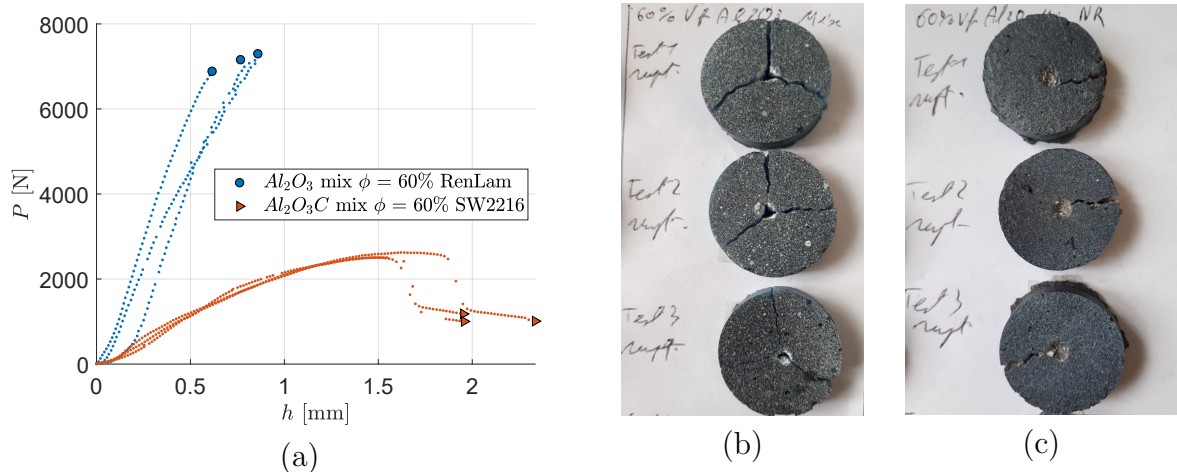


Figure 5.7: Effect of matrix material:
 (a) Load-displacement curves for monotonic indentation;
 (b) Fractured samples with the RenLam matrix;
 (c) Fractured samples with the SW 2216 matrix.

= 60%) mix.

Effect of silane particle treatment

In Chapter 3, silane treatment has proved to significantly improve the composite strength by enhancing the particle/matrix adhesion. The effect of silane treatment on the indentation behaviour was then also evaluated. A series of specimens were manufactured using polydisperse boron carbide particles (50% F1200, 25% F360, 25% F60) up to a 60% particle volume fraction. The results of the indentation of the composite with and without silane treatment are plotted Fig. 5.9 (a).

Unfortunately, the silane did not seem to have any effect on the indentation stiffness of the material nor on the ultimate load. Amongst the various tests performed, one can notice that one specimen stands out from the others as it showed a very low failure load. The crack pattern in this case was also quite different (see Fig. 5.9 (a) Test 2) since the specimen was split into two parts only. The fracture surfaces of these samples are represented in Appendix D.

5.3 Cyclic loading

From the monotonic indentation tests, little conclusion could be drawn: the indentation stiffness increased with particle volume fraction and matrix Young's modulus. However, the ultimate load remained roughly constant whatever the particle mixture is used. For refined evaluation of material properties and damage sequence, a cyclic indentation load-

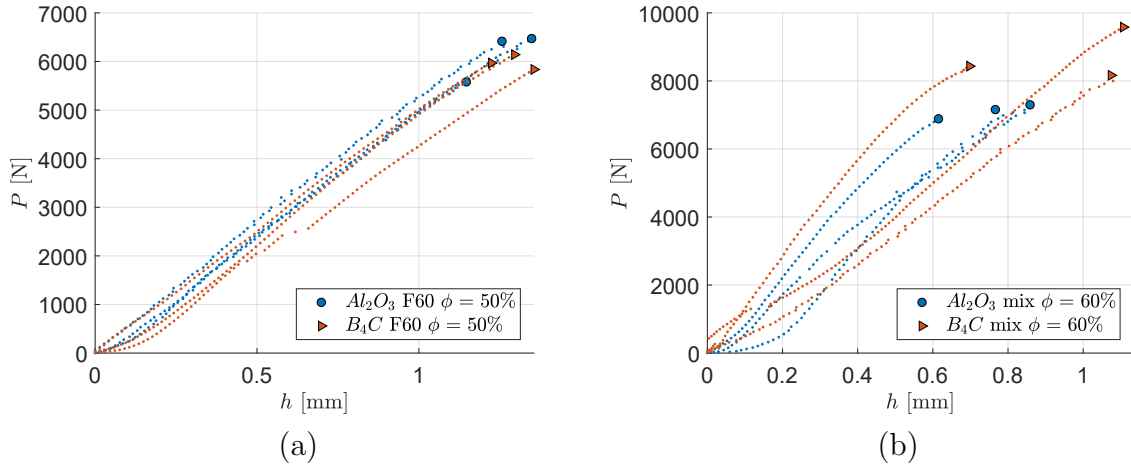


Figure 5.8: Load-displacement curves for monotonic indentation. Effect of particle material for (a) monodisperse particle size and (b) polydisperse particle size.

ing test was then employed to determine the hardness and indentation elastic properties of the material, as each unloading is supposed to be elastic. A method based on that of Oliver-Pharr [113] and [114] was applied for this study. This method was originally developed for instrumented nano-indentation, but no size limitation was introduced in the methodology. The data reduction procedure implemented to extract mechanical properties from load-displacement curves is described in the following section.

5.3.1 Penetration of a spherical indenter during cyclic indentation

A typical compression force versus penetration depth during a loading and unloading cycle is represented in Fig. 5.10. The indenter penetrates the sample until a given maximum load value P_t is reached. A total indentation displacement of the metallic ball h_t is reached at this point. Then, the sample is unloaded and a residual penetration h_r is observed. The indentation stiffness S is determined as the slope of the upper portion of the unloading curve during the initial stages of unloading phase (also called the contact stiffness) [114].

Fig. 5.11 depicts the indentation of a flat surface by a spherical indenter, at both maximum load and unloaded stages. The displacements defined previously are represented: h_t the total displacement of the indenter and h_r the residual displacement after unloading. Assuming the unloading is elastic, the difference between these two values is then the elastic displacement:

$$h_e = h_t - h_r. \quad (5.1)$$

The projected area of contact is circular and its radius is denoted as a . As the hardness and indentation Young's modulus are calculated using the contact radius, it is crucial

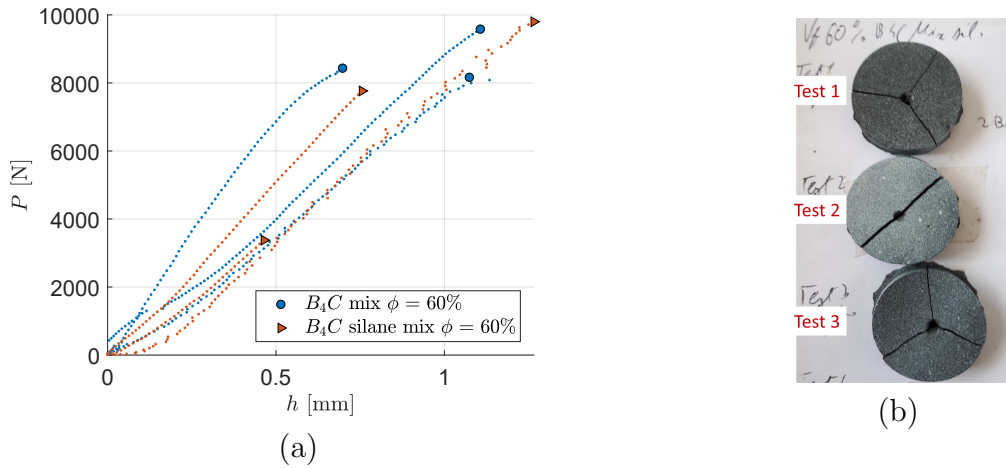


Figure 5.9: Effect of particle treatment with silane:
 (a) Load-displacement curves for monotonic indentation;
 (b) Fractured samples with silane treatment.

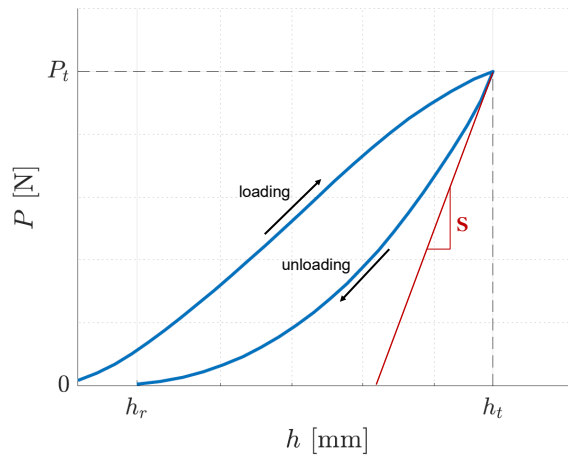


Figure 5.10: One cycle of indentation, complete load and unload.

to be able to determine this value from load-displacement curves. According to Hertz theory [62] for frictionless contact between two isotropic elastic solids, the contact radius is calculated as:

$$a = \sqrt{R_{eff}h_c}, \quad (5.2)$$

where h_c is then the contact depth (see Fig. 5.11) and R_{eff} the effective indentation radius, calculated as the harmonic mean of the indenter and sample's radii R and R_s :

$$\frac{1}{R_{eff}} = \frac{1}{R} + \frac{1}{R_s}. \quad (5.3)$$

The contact radius a is however commonly estimated for a spherical indenter as ([113]

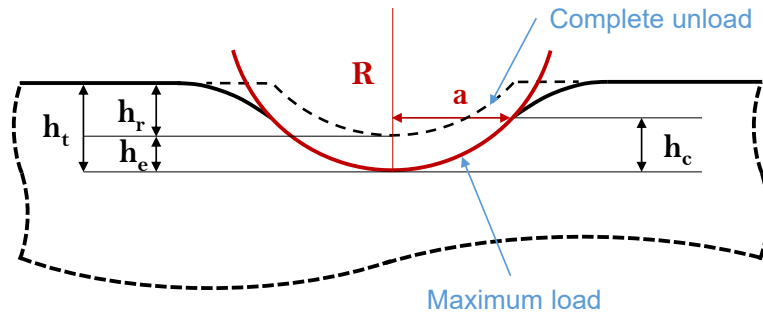


Figure 5.11: Schematic representation of the cyclic indentation with a spherical indenter.

and [43]):

$$a = \sqrt{2h_c R - h_c^2}. \quad (5.4)$$

Note that the two definitions of the contact radius in Eqs. 5.2 and 5.4 may not provide consistent results. According to [37], Eq. 5.2 provides an estimate of the contact radius in the equivalent elastic indentation of a sample with a flat surface with an indenter of radius R_{eff} , while Eq. 5.4 provides an estimate of the contact radius based on the actual geometry of contact between the indenter and the sample. Only Eq. 5.2 is consistent with Hertz theory although it does not reflect the actual contact radius during elastic-plastic indentation experiments [37]. Indeed, both approaches gives consistent values at the first stages of the loading phase, then deviate experimentally as inelastic deformations appear. Another advantage of Eq. 5.4 is that a depends only on the contact depth h_c and the radius of the indenter, which does not change as loading evolves.

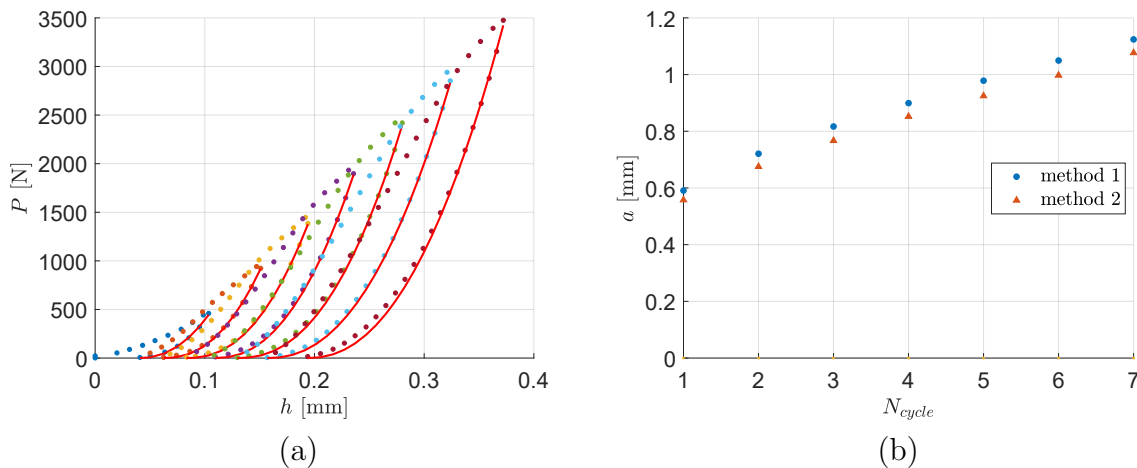


Figure 5.12: (a) Cyclic indentation force-displacement curve with unload fits; (b) Contact radius determination at each cycle.

According to the Oliver-Pharr methodology, the contact depth is calculated as:

$$h_c = h_t - \epsilon \frac{P_t}{S}, \quad (5.5)$$

where ϵ is a constant that depends on the geometry of the indenter: $\epsilon = 0.72$ for a conical punch, $\epsilon = 0.75$ for a paraboloid of revolution (which approximates to a sphere at small depths), and $\epsilon = 1.00$ for a flat punch [114]. For the present study, a value of $\epsilon = 0.75$ is then selected. Once more according to the Oliver-Pharr method, each unloading is fitted with a power law, as represented in Fig. 5.12 (a):

$$P = \alpha(h - h_r)^m. \quad (5.6)$$

S , being the slope of the initial unloading curve, is then calculated as the derivative of this fit at the beginning of the unloading:

$$S = m\alpha(h_t - h_r)^{m-1}. \quad (5.7)$$

It is then possible to calculate a value of the contact depth h_c at each cycle using equation 5.5. This method will then be referred to as “method 1”.

Taking into account the spherical geometry of the indenter, and based on the Hertzian theory, [43] developed an analytical expression of the contact depth h_c . Indeed, according to Hertz elastic contact assumption:

$$P = \frac{4}{3}\sqrt{R_{eff}}E_{eff}(h - h_r)^{3/2}, \quad (5.8)$$

where, E_{eff} is the effective indentation elastic modulus defined as:

$$\frac{1}{E_{eff}} = \frac{1 - \nu_s^2}{E_s} + \frac{1 - \nu_i^2}{E_i}. \quad (5.9)$$

The effective elastic modulus takes into account the fact that elastic displacements occur in both the specimen (with Young’s modulus E_s and Poisson’s ratio ν_s) and the indenter (with elastic constants E_i and ν_i). Then, the elastic unloading stiffness can be expressed as:

$$S = \frac{dP}{dh} = 2\sqrt{R_{eff}}E_{eff}(h - h_r)^{1/2}. \quad (5.10)$$

Using Eq.5.5 combined with Eqs.5.8 and 5.10, one obtains the following expression for the contact depth:

$$h_c = (h_t + h_r)/2. \quad (5.11)$$

This expression is then referred to as “method 2”. The methods 1 and 2 for the evaluation

of h_c have been compared through multiple cyclic loadings for the experimental setup developed in this study and both methods give similar results (see Fig. 5.12 (b)). For the sake of simplicity, the expression based on the method 2 will be employed in the next section for further observations.

5.3.2 Evaluation of hardness and elastic properties with cyclic indentation

In this subsection, the definitions and methodologies employed to determine the hardness and elastic properties from force-displacement curves are first described. The results obtained as functions of the microstructural parameters studied are then developed subsequently.

Hardness

In instrumented indentation, hardness H is defined as the mean contact pressure p_m under the loaded indenter, and is calculated as the indenter load P divided by the projected contact area A , which corresponds to the definition of Meyer's hardness:

$$H = p_m = \frac{P}{A} = \frac{P}{\pi a^2}. \quad (5.12)$$

Generally, the hardness measured with a spherical indenter is Brinell hardness. This hardness value is calculated as a function of the load applied P , the diameter of the indenter D , and the impression diameter d after complete unload:

$$HB = \frac{2F}{g\pi D (D - \sqrt{D^2 - d^2})}, \quad (5.13)$$

where g is the gravitational acceleration.

Elastic modulus

From the indentation data, it is possible to determine the indentation modulus E_{eff} from the unloading contact stiffness S and the contact area A using Sneddon's analysis of penetration of various indenters into elastic half-space [138]:

$$E_{eff} = \frac{\sqrt{\pi}}{2\beta} \frac{S}{\sqrt{A}}, \quad (5.14)$$

where β is the correction factor for the indenter shape. This relationship is then applicable for all types of axisymmetric indenters. It was also demonstrated that although the

relationship was developed for elastic contact, it is also applicable for elastic-plastic ones [114]. A value $\beta = 1$ is selected for the spherical indenter [114]. Indentation Young's modulus of the sample is then calculated as:

$$E = (1 - \nu^2) \left(\frac{1}{E_{eff}} - \frac{1 - \nu_i^2}{E_i} \right)^{-1}. \quad (5.15)$$

This approach is the one adopted for the determination of the indentation elastic properties.

Stress-strain curves

Several authors tried to find equivalence between indentation and uniaxial tensile behaviour [142], [44], or [71]. Tabor [142] first introduced the concept of stress-strain indentation curves. The indentation stress was defined as the mean contact pressure (Meyer's hardness Eq. 5.12), while the indentation strain was invoked to be $0.2a/R$. In Tabor's approach, the contact radius was measured directly from the residual indentation in the sample. Therefore, one complete indentation test was required to get one point of the indentation stress-strain curve. Field and Swain [43] developed Tabor's approach using cyclic loadings to obtain multiple points on the indentation stress-strain curves, as described previously. However, the validity of such approach is only limited to ductile materials [43].

Then based on Hertz theory, Field and Swain proposed a further definition of the indentation stress-strain curves. Eq. 5.8 was recast as:

$$\sigma_{ind} = \frac{4E_{eff}}{3\pi} \epsilon_{ind}, \quad \sigma_{ind} = \frac{P}{\pi a^2}, \quad \epsilon_{ind} = \frac{a}{R_{eff}}. \quad (5.16)$$

a/R_{eff} is commonly employed in the literature as the indentation strain but, according to [71] this definition lacks of any physical interpretation. Moreover, due to the difficulty to estimate R_{eff} , the radius of the indenter R is often used instead. However, the approximation $R_{eff} = R$ only holds for loads in the elastic regime. Moreover, R_{eff} does not even reflect a relevant length scale in characterising the deformation experienced by the sample. In fact, the contact radius a is a better descriptor of the length scale of the indented region [71], [118]. The authors of [71] proposed to recast the elastic indentation relationship and the indentation stress-strains as:

$$\sigma_{ind} = E_{eff} \epsilon_{ind}, \quad \sigma_{ind} = \frac{P}{\pi a^2}, \quad \epsilon_{ind} = \frac{4}{3\pi} \frac{h_e}{a} \approx \frac{h_e}{2.4a}. \quad (5.17)$$

In their review, [37] stated that these new definitions provide much more meaningful

indentation stress-strain curves, as the hardening of the material is better described with this new definition of the indentation strain. These definitions of the indentation stress and strains were adopted for the present study. However, they were developed for nano-indentation, and very low displacements were imposed to catch the elastic behaviour of the material during loading. Macro-indentation was used for the present work, and plastic behaviour was already observed from the first cycle.

5.3.3 Description of cyclic indentation test protocol

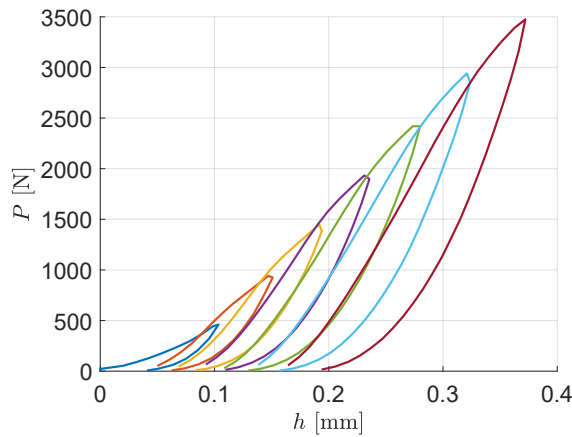


Figure 5.13: Cyclic indentation force-displacement curve.

A typical cyclic loading used for the present study is depicted in Fig. 5.13. Each cycle was load controlled and the maximum force applied at each cycle is incrementally increased by 500 N. Once this maximum value was reached, the sample was unloaded until the applied force became null. The load rate was 0.2 mm/min for loading and unloading phases. A picture was taken every 5 seconds for the evaluation of penetration depth using the DIC.

For each specimen type, the mean load to failure has been determined with the monotonic indentation tests. The cyclic test conditions were determined so that the tests were interrupted at :

- 80% of the mean load to failure,
- 65% of the mean load to failure,
- 50% of the mean load to failure,
- 40% of the mean load to failure.

Each unloading sequence was fitted with a power law described by Eq. 5.6 using the least squared method and the parameters m and S were determined. The contact depth

h_c was then estimated for each cycle peak force with Eq. 5.11. The contact radius a was then deduced from h_c with Eq. 5.4. Meyer's hardness, Brinell hardness, and elastic modulus were then calculated based on these values.

5.3.4 Effect material parameters on composite hardness and indentation stiffness

As for the monotonic indentation, the effect of multiple material characteristics on the indentation behaviour of the material were tested.

Particle volume fraction effect

First, the effect of particle volume fraction was observed. To do so, samples with particle volume fractions ranging from 0% (bulk adhesive) to 60% were tested. The particles used were polydisperse alumina particles (70% F20 and 30% F60).

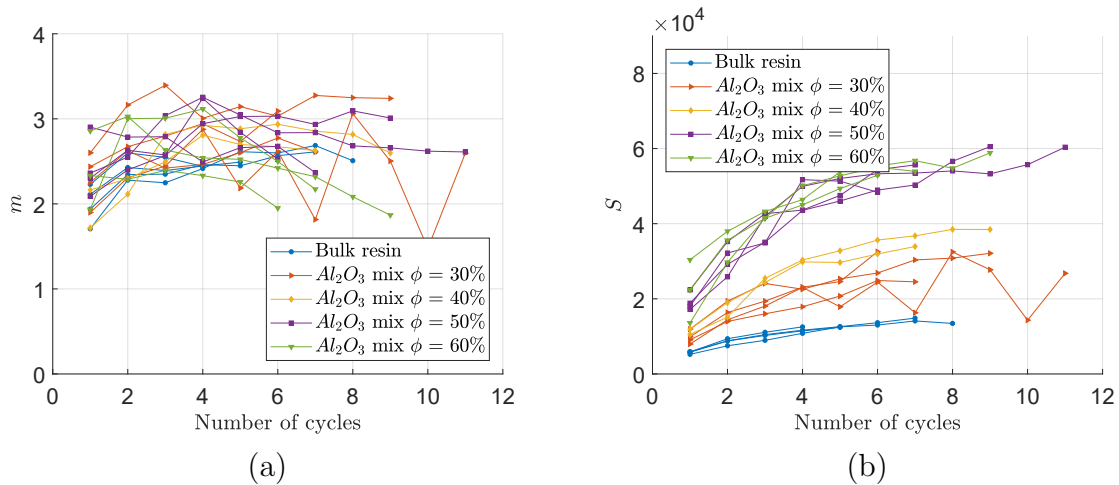


Figure 5.14: Fitting parameters of the unloading phases: exponent m (a) and unloading stiffness S (b) against cycles

Each unload was fitted and the parameters m and S were determined (Fig. 5.14 (a) and (b)). The exponent m was consistently evaluated between 2 and 3 and no effect of particle volume fraction was observed. This observation generally held true for all the microstructural parameters considered. The unloading stiffness S was found to be increasing with particle volume fraction. It also seemed to increase at each cycle (with increasing loads).

Young's modulus and Brinell hardness were determined for each specimen as a function of the number of cycles (Fig. 5.15 (a) and (b) respectively). According to literature and results presented in Chapter 2, the value of Young's modulus increases with particle volume fraction. It also seems to be independent of the number of cycles (and hence the

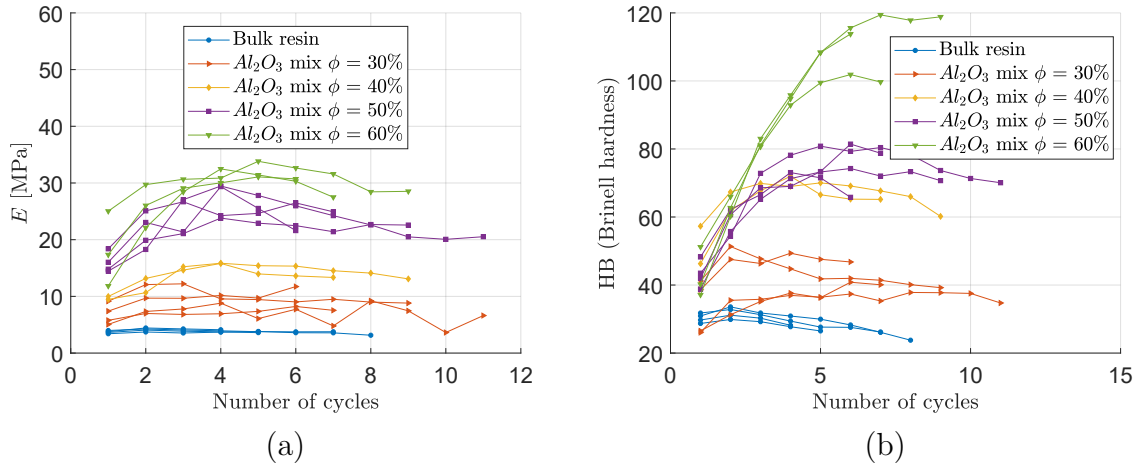


Figure 5.15: (a) Indentation Young's modulus against the cycle number; (b) Brinell hardness against the cycle number.

load applied). Any small increases were attributed to lower particle volume fractions in the near-surface region of the specimens. An increase in hardness was also observed with increasing particle volume fraction. However, for high volume fractions (above 40%), the hardness value increased with the number of cycles, and this evolution was stronger as the particle content increases. This might be a result of the compaction of the samples that leads particle percolation, and hence when particles are in contact the load is re-distributed between them. This effect has already been observed in the literature for various types of particulate composites ([130], [58], or [152]) and has been named the “crowding effect”.

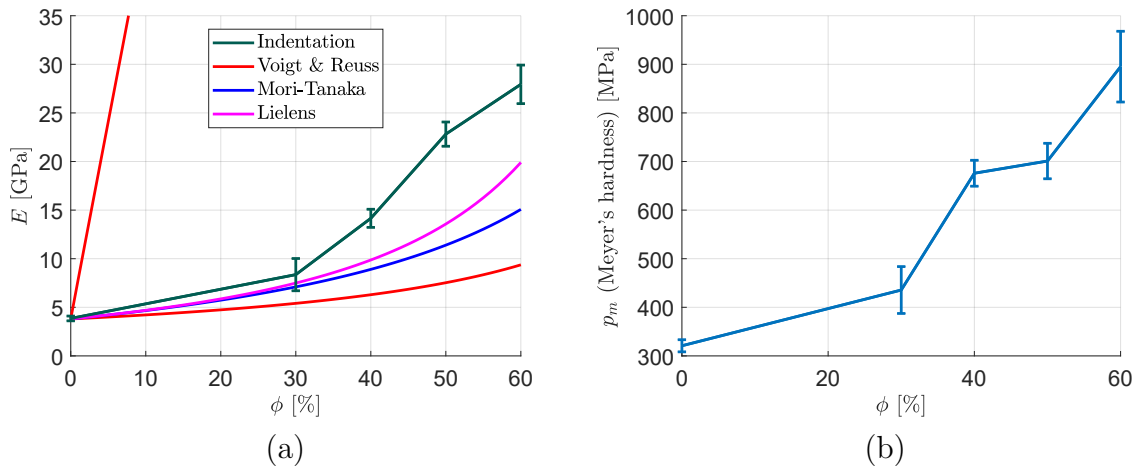


Figure 5.16: Effect of particle volume fraction on (a) indentation Young's modulus, (b) Meyer's hardness, for samples with polydisperse alumina particles.

All the results were averaged for each cycle and particle volume fraction. The indentation Young's modulus is finally plotted against the particle volume fraction in Fig. 5.16 (a).

A clear increase of indentation Young's modulus was visible with increasing particle content. The bounds of Reuss and Voigt are also represented, and the values determined experimentally fall within these bounds. The estimations of the homogenisation schemes of Mori-Tanaka and Lielens are also plotted. The experimental values are above those of the two models.

Averaged values of Meyer's hardness were also plotted against particle volume fraction in Fig. 5.16 (b). Meyer's hardness clearly increases with particle volume fraction, and the samples with $\phi = 60\%$ have a hardness almost three times higher than that of the bulk epoxy resin.

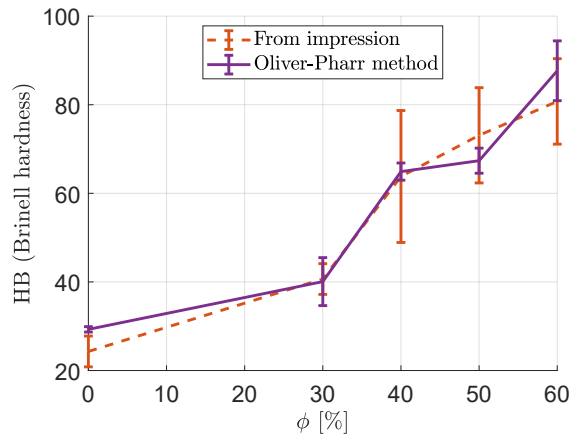


Figure 5.17: Effect of particle volume fraction on Brinell hardness for samples with poly-disperse alumina particles.

Brinell hardness was then calculated with two different methods. The formula employed was always the same (Eq. 5.13) but the value of d was determined, on one hand, from the impression left by the indenter on the sample completely unloaded and, on the other hand, as twice the contact radius a determined with the Oliver-Pharr method. Results from both methods are represented in Fig. 5.17. They are quite close (in the error bars) and the same evolution with particle volume fraction as Meyer's hardness one is observed.

Particle size effect

The effect of the particle size on the indentation behaviour was then studied. Young's modulus, Meyer's hardness and Brinell hardness were determined for samples with a 30% volume fraction of alumina particles (F20, F60, F360, and mixed sizes). The results are plotted in Fig. 5.18. From now on, the results will directly be represented as averaged on the number of cycles and on the sample types. There is no clear trend with regard to mechanical properties and the evolution of particle size; all the material properties were

found to be within the error bars.

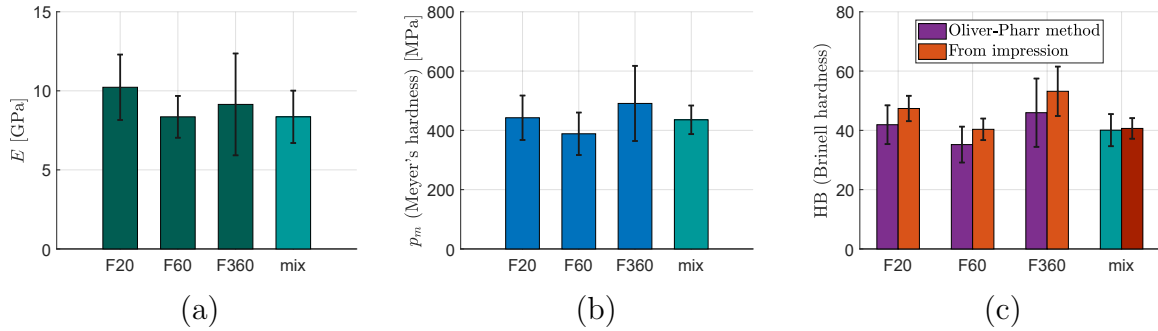


Figure 5.18: Effect of particle size on (a) indentation Young's modulus, (b) Meyer's hardness, and (c) Brinell hardness, for samples with $\phi=30\%$ of alumina particles.

The same study was also carried out on boron carbide particles (F60, F360, and F1200). Fig. 5.19 depicts the evolution of Young's modulus (a), Meyer's hardness (b), and Brinell hardness (c) with particle size. A small Young's modulus reduction was observed with decreasing particle sizes, while a small hardness (for both Meyer's one or Brinell) increase is visible.

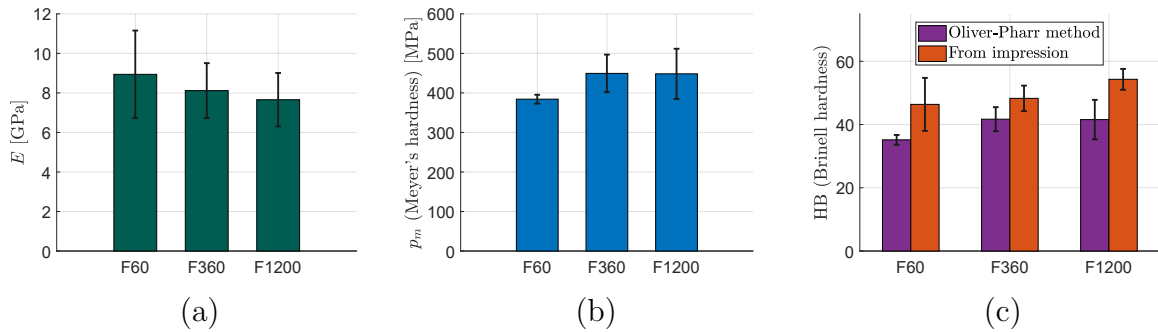


Figure 5.19: Effect of particle size on (a) indentation Young's modulus, (b) Meyer's hardness, and (c) Brinell hardness, for samples with $\phi=30\%$ of boron carbide particles.

Finally, there might be an effect of particle size on the indentation properties of the particle reinforced material, however, it seems that the variations induced by this parameter is quite small and experimental uncertainties hide any fluctuations.

Effect of the matrix material

From monotonic indentation tests, a very strong effect of matrix material choice was visible. As for previous design parameters, Young's modulus (a), Meyer's hardness (b) and Brinell hardness (c) were determined and represented in Fig. 5.20. The samples were prepared with the two types of matrices (RenLam and SW2216) and with polydisperse alumina particles with a volume fraction of $\phi=60\%$.

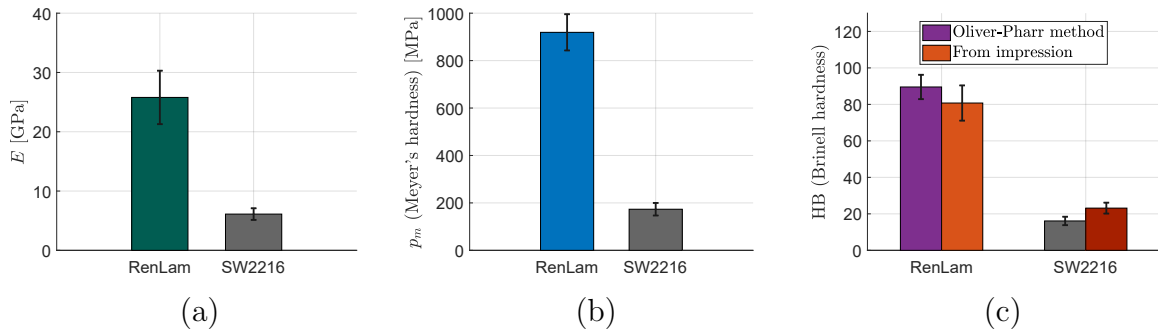


Figure 5.20: Effect of the type of matrix material on (a) indentation Young's modulus, (b) Meyer's hardness, and (c) Brinell hardness (samples with $\phi=60\%$ of polydisperse alumina particles).

The SW2216 resin being very soft and compliant compared to the RenLam, the Young's modulus and hardness values obtained with this matrix are very low compared to those obtained with the RenLam resin.

Effect of the reinforcement material

For monotonic indentation, it was difficult to observe differences in the behaviour of the composite material reinforced by alumina or boron carbide particles. Cyclic indentation tests were then performed to determine the indentation Young's modulus and the hardness of the material with different ceramic materials as reinforcement. The samples were made with a fixed value of $\phi=50\%$ of F60 alumina or boron carbide particles. The averaged results are plotted in Fig. 5.21.

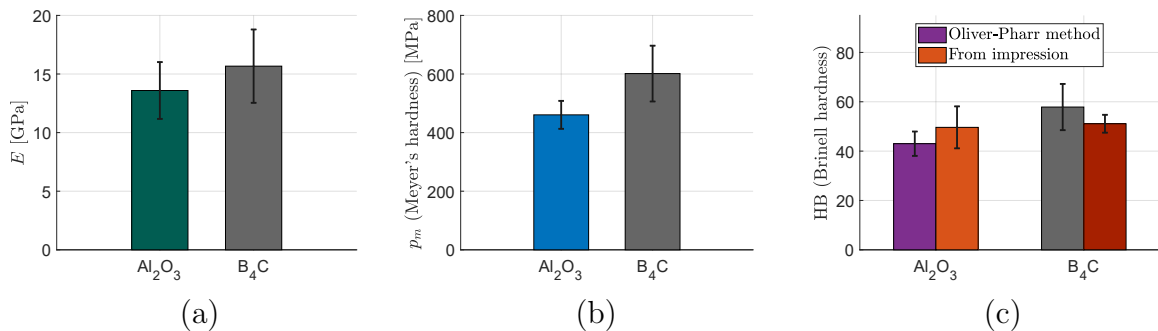


Figure 5.21: Effect of the type of particle material on (a) indentation Young's modulus, (b) Meyer's hardness, and (c) Brinell hardness (samples with $\phi=50\%$ of monodisperse F60 particles).

This time, a higher Young's modulus and hardness (both Meyer's and Brinell) were observed with the use of boron carbide particles instead of alumina ones. This is in accordance with the fact that boron carbide is stiffer and harder than alumina.

Effect of particle/matrix adhesion enhancement

The effect of particle treatment with silane was then tested with samples made of 60% of mixed sizes boron carbide particles (25% F60, 25% F360, 50% F1200). The mechanical properties of samples with and without particle treatment with silane were determined (Fig. 5.22).

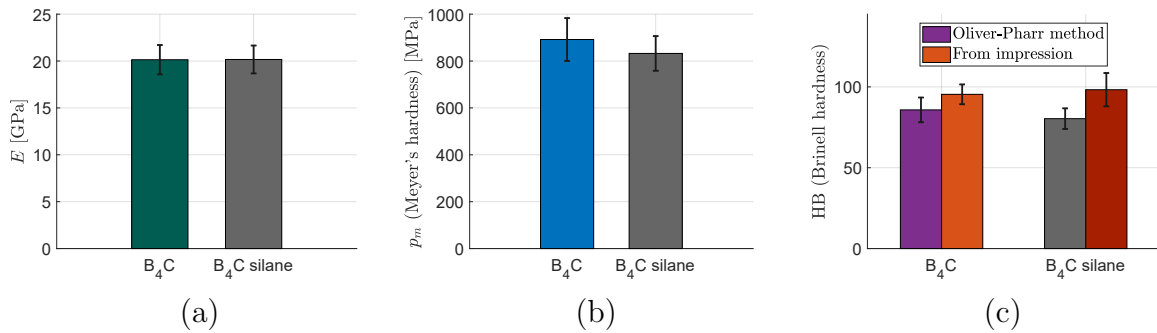


Figure 5.22: Effect of particle silane treatment on (a) indentation Young's modulus, (b) Meyer's hardness, and (c) Brinell hardness (samples with $\phi=60\%$ of polydisperse boron carbide particles).

The indentation Young's modulus and hardness values seem to be constant whether the silane treatment has been applied or not. The silane does not seem to have any effect on hardness or the stiffness of the particle reinforced material.

5.4 Conclusions

This chapter was dedicated to the observation of the resistance to quasi-static indentation of the ceramic particle reinforced polymer. Monotonic and cyclic indentation tests were implemented to evaluate the role of material composition on the behaviour of such a material under a concentrated compressive load. Monotonic indentation tests were used to determine the failure of the specimens. Instrumented cyclic indentation tests were developed to determine material properties such as indentation Young's modulus and the hardness of the composite. Several conclusions can be drawn from this series of tests:

- The introduction of ceramic particles clearly increases the resistance to quasi-static indentation (stiffness and hardness). These properties increase with particle volume fraction content. No effect was observed for all tested configurations on the failure load, with the exception of the tests comparing the ductile and brittle resins. Indeed, while particle type and size do not significantly change indentation resistance, the volume fraction of particle and matrix Young's modulus do.

- The individual mechanical properties of both components influence the behaviour of the composite under indentation. To get materials as stiff and as hard as possible, it is important to use matrices and reinforcements that are also stiff and hard. The mechanical properties of the matrix were observed to greatly influence the behaviour of the composite even at high particle volume fraction. This means that even if a very high content of ceramic particles is introduced into the material, the matrix material plays a very significant role in the indentation behaviour of the material. A possible outlook of this analysis could consist in numerical simulations of indentation tests. A microstructured material could be generated with the algorithms presented previously to test the influence of the various microstructural parameters. This study could represent an interesting link between the tensile and compressive behaviour of the material.
- No effect of the silane treatment to enhance the particle/matrix adhesion was detected on the stiffness or the hardness of the material. More surprisingly, the load to failure was also observed to be unaffected by the silane treatment even though it was expected to reinforce the particle/matrix interfaces.
- Concerning the damage scenario, we suspect, that the crushing/compaction of the material below the indenter mostly controls the shape of the cyclic response. The specimen failure may be attributed to the development of circumferential tensile stresses produced by the expansion of the area below the indenter. Thus, this failure load is not indicative of material performance alone but characteristic of the specimen itself and is probably more related to mode I toughness than compressive strength. In the following chapter, similar perforation experiments are conducted in the ballistic regime so that much higher loading rates will limit finite size effect due to the dynamic confinement effect.

Chapter 6

Perforation at high loading rate: Development of impact tests

The resistance to perforation of the ceramic particle reinforced material has been evaluated using quasi-static indentation tests. However, the ballistic regime might exhibit totally different features since material behaviours are generally strain rate dependent and also because shock wave propagation results in a very different loading path compared to quasi-static indentation. Therefore the mechanical behaviour and damage mechanisms of most materials are different under ballistic loading. For example, at low strain rates, brittle materials (such as ceramics or concrete) undergo a single crack propagation predicted with the weakest link theory [34]. Their behaviour under these types of loadings is probabilistic and can be described by a Weibull-type approach [153]. Under high strain rate conditions, a multiple fragmentation is observed. The more severe the loading rate is, the more important the fragmentation. With the drastic loading rate increase, a transition from probabilistic to deterministic failure is observed [35]. The loading rate then plays a critical role in the failure of brittle materials, and the multiple fragmentation of such materials can only be observed under severe loading conditions.

To observe the resistance to penetration of the particle reinforced composite used for the present study, a ballistic impact test setup has been developed based on that of Simon Dousset's PhD aiming at measuring the force produced by the impacts of hailstones. This system was adapted for our specific needs. A compressed air gun was used to fire steel balls at a composite cylindrical target up to several hundreds of meters per second. The intensity of the shock transmitted through the target is measured using a Hopkinson bar. This chapter aims at describing the developments made for evaluating the resistance of the particle reinforced composite to ballistic threats. The experimental setup is detailed in the first section, and the results are presented in the second one.

6.1 Ballistic impact test set up

An important part of the work on impact testing was devoted to the development of a reliable test setup. Two conditions must be fulfilled in order to get interesting ballistic impacts. On the first hand, a very high impactor velocity must be reached (up to several hundreds of meters per seconds) to be representative of ballistic impacts. On the other hand, the guidance of the impactor must be precise enough to reach the target. The method employed here is developed in the next paragraphs.

6.1.1 Compressed gas gun

The general design of the test setup was developed by Simon Dousset for projecting hailstones on a target with high impact velocities. Several modifications were proposed for projecting small steel balls on composite targets.

A schematic description of the compressed air gun is presented in Fig. 6.1. A 5 meter long gun barrel having a 30 mm inner diameter is fixed to the pressurised tank to guide the projectile during its acceleration phase. Roller bearing steel balls having a 6.2 mm radius were used as impactors. Therefore, in order to have an accurate guidance of the projectiles, the latter were mounted on sabots, whose diameters were adjusted to that of the barrel.

To reach high velocities representative of ballistic impacts, a considerable air flux must be released in a very short period of time. A pressure vessel is pressurised by a pump and the pressure is gradually increased. Fuse-membranes of variable thickness, trapped between the larger part of the pressure vessel and the flange, allow a rapid release of the air flux by exploding when the pressure becomes high enough in the pressure vessel. The air flux penetrates in the gun barrel and propels the sabot and the spherical impactor. The sabot is then stopped after it has exited the gun barrel and the impactor is released to hit the sample.

To assemble all the pieces of the canon (see Fig. 6.1), different techniques were employed. The diameter of the gun barrel was selected so as to produce the required impact velocity. An adapter component was then required to assemble the gun barrel to the flange. The gun barrel was shrink fitted to the adapter. Particular care was given to the dimensions of the inner diameter of the adaptation so that the coupling between the gun barrel and the adapter could withstand the forces. The adapter is screwed into the flange (4 screws). The flange and the pressure vessel are screwed together tightening the membrane between them (8 large screws).

The canon is assembled on rails and all the parts were carefully aligned using a laser, travelling through the flange, gun barrel, sabot catcher and then appearing at the center

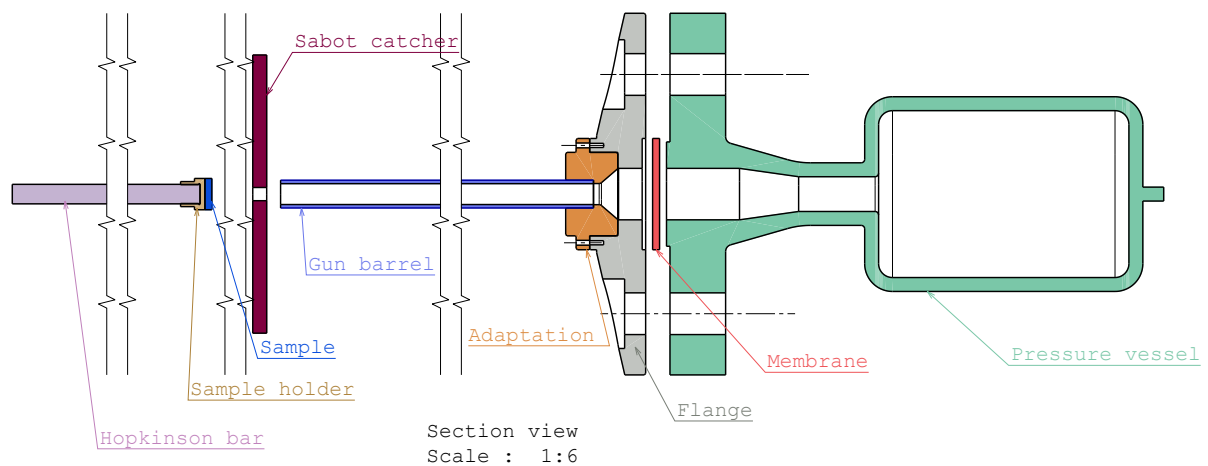


Figure 6.1: Section view of the impact test setup.

of the target. This alignment method was necessary to ensure the sabot was captured, releasing the impactor, the latter then hitting the sample.

6.1.2 Sabot design

A sabot is required to carry the impactor as the diameter of the latter is smaller than the inner diameter of the gun barrel. The geometry of the sabot (see Fig. 6.2) was chosen to be a cylinder of larger diameter equal to $29.9^{+0}_{-0.1}$ to ensure an accurate guidance in the barrel without creating too much friction. Two annular grooves were machined to create pressure losses to ensure a perfect stabilisation of the sabot.

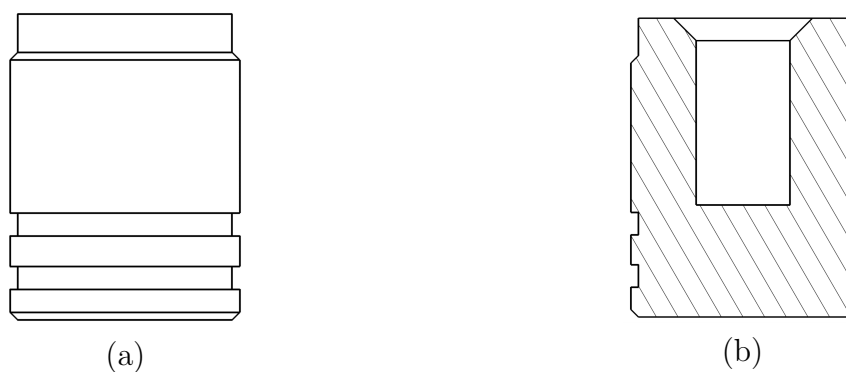


Figure 6.2: Sabot drawing (a) and cut view (b).

The weight of the sabot must be minimal so that maximum kinetic energy is transmitted to the projectile after separation. Sabots are then generally made of plastic materials [141]. Three variations of sabots were made using polyvinyl chloride (PVC), poly(methyl methacrylate) (PMMA), and polycarbonate (PC) (see Fig. 6.3).

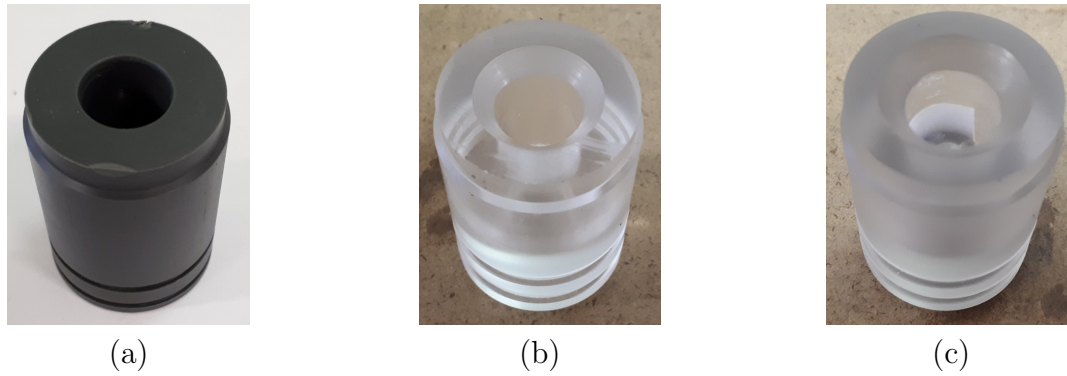


Figure 6.3: Sabots made from (a) PVC, (b) PMMA, and (c) PC.

Another main requirement the sabot has to fulfil, is the complete separation from the projectile before the latter reaches the target. To do so, a thick steel plate (called sabot catcher) is positioned between the exit of the barrel and the target. A circular hole with a 19 mm diameter between that of the projectile (12.4 mm) and the exterior diameter of the sabot (29.9 mm) is machined. When the sabot hits the steel plate, it is abruptly stopped, releasing the projectile. The sabots made of PVC and PMMA were found to be very brittle and fragmented on impact. These fragments were then hitting the target along with the projectile, and were deemed inappropriate for the test (see Fig. 6.4 (a) and (b)). The PC shot was much more satisfactory, only deforming, which meant it was properly stopped by the sabot catcher (see Fig. 6.4 (b)).

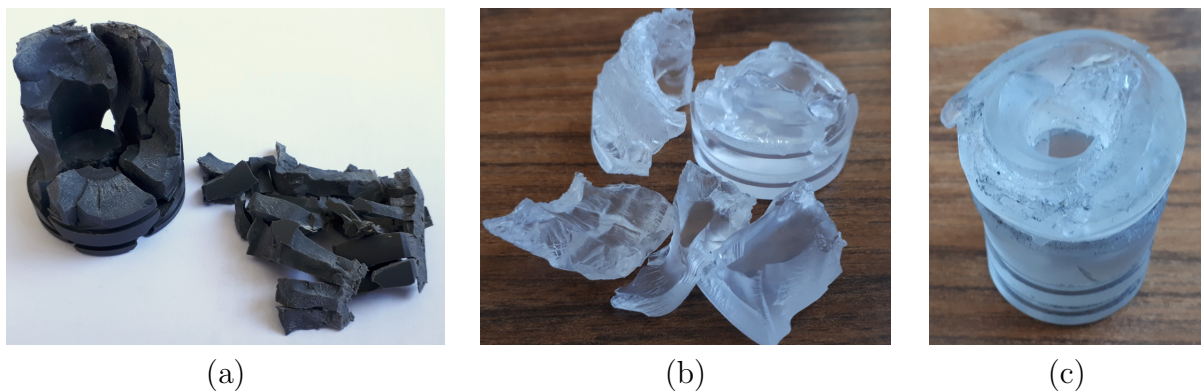


Figure 6.4: Sabots made from (a) PVC, (b) PMMA, and (c) PC after impact.

6.1.3 Samples/Targets

The samples/targets developed for the ballistic impact study were similar to the ones used for indentation tests, but a larger diameter of 45 mm is used to match that of the Hopkinson bar. A typical impact sample is shown in Fig. 6.5, with a height of 10mm. The influence of all the design parameters previously investigated could again be determined.

To do so, samples with varying particle and matrix types, reinforcement volume fractions and sizes were manufactured. The samples were glued onto the Hopkinson bar, which is used as a dynamic load cell. This device will be described in the next subsection.

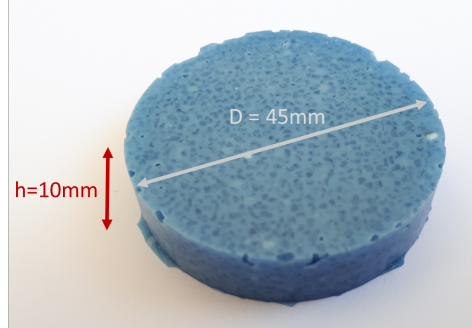


Figure 6.5: Impact sample (Al_2O_3 mix $\phi = 60\%$).

6.1.4 Instrumentation of the impact test

A high speed camera was used to record the impact of the ball on the target. It allows for the determination of the velocity of the impactor just prior to the impact and hence the impactor kinetic energy:

$$E_{impactor} = \frac{1}{2}mv^2 \quad (6.1)$$

It also provides a means by which to observe any fragmentation and failure of the particle reinforced material during impact. The Hopkinson bar was instrumented with two diametrically opposed strain gauges (in order to account for any potential bending effects) for measuring the force transmitted through the bar: the tension from the strain gauge bridge (U) is transformed into strain (ϵ) via a calibration constant k . Knowing the elastic behaviour (Young's modulus E) and the dimensions (cross section A) of the bar, and assuming a uniaxial stress wave propagation, it is possible to get the stress σ and then the force F applied to the bar:

$$U \text{ [V]} \xrightarrow{\epsilon = k * U} \epsilon \xrightarrow{\sigma = E * \epsilon} \sigma \text{ [MPa]} \xrightarrow{F = \sigma * A} F \text{ [kN]}$$

The signal given by the gauge bridge during an impact on the bar is plotted in Fig. 6.6. The incident wave and the successive reflections in the bar are also represented in the figure. The incident compressive wave travels up to the end of the bar and is reflected as a tensile wave. This tensile wave is then re-reflected as a compressive wave when it returns back to the beginning of the bar and so on. This observation allows to assess that the incident signal is not perturbed by reflections in the bar.

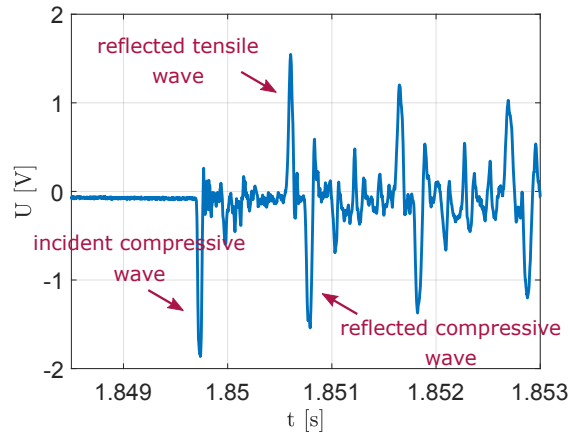


Figure 6.6: Tension signal given by the gauge bridge during impact.

The force-time history of the impact event was then recorded. Assuming a one dimensional wave propagation in the bar, the energy transmitted to the bar during the impact is then [146]

$$E_{bar} = \frac{1}{\rho A c} \int_0^{t_f} F^2(t) dt, \quad (6.2)$$

where ρ is the density of the bar, A its cross section, c its wave velocity, F the force recorded and t_f the final time of contact.

The energy dissipated by the target can be determined using an energy balance of the system [146]:

$$E_{dissipated} = E_{impactor} - E_{bar} \quad (6.3)$$

Other types of energies (such as the residual kinetic energy of the impactor with its possible rebound) are neglected.

6.2 Validation of the test setup and preliminary results

Three shots were carried out to validate the experimental setup. Three different specimens were used as targets and the velocities of the impactors were measured (see Table 6.1). Shot 1 was performed using a PC sabot whereas shots 2 and 3 were undertaken using PMMA sabots. Membranes of the same thickness were used for all the tests and hence the same pressure was supposed to be released when the membranes failed. However different projectile velocities were measured.

The velocity of shot 1 was significantly higher than that of shots 2 and 3. However no generalisation can be made as too few tests were carried out. Moreover, PC and PMMA have similar densities and are therefore supposed to have the same kinetic energy. Possible

| | Sample | sabot | $v_{impactor}$ [m/s] | $E_{impactor}$ [J] | E_{bar} [J] |
|--------|-----------------------------|-------|----------------------|--------------------|---------------|
| Shot 1 | Al_2O_3 mix $\phi = 60\%$ | PC | 145 | 78 | 6.0 |
| Shot 2 | Al_2O_3 mix $\phi = 50\%$ | PMMA | 86 | 28 | 3.1 |
| Shot 3 | Al_2O_3 mix $\phi = 30\%$ | PMMA | 95 | 34 | 2.1 |

Table 6.1: Summary of impact tests

explanations are that the geometry of the PC sabot was more precise - limiting energy losses (e.g. friction), that the membrane was tougher - releasing more pressure, or that the brittle failure of the PMMA influenced the release of the projectile.

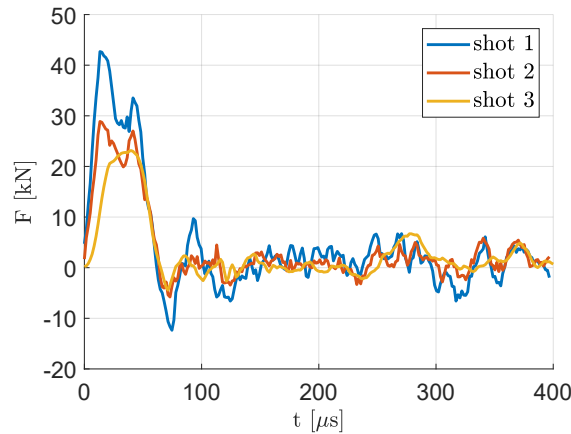


Figure 6.7: Impact force-time curves.

The force against time evolutions for the three shots are represented in Fig. 6.7. For the three shots, the force rapidly increased up to a maximum value. The force decreased and vanished between 60 and 70 μs . Then, small erratic oscillations were visible. They might have been caused by noise, small wave reflections, or by the fact that the incident wave is not perfectly uniaxial. They were however small compared to the peaks and oscillated around 0 and therefore were assumed to have no influence on the extraction of results. As expected with the measurements of the impactor velocities, the highest peak was observed for shot 1. Both shot 1 and shot 2 showed two successive peaks.

The energy transmitted to the bar was calculated using Eq. 6.2 (the integral is performed numerically) and the results are represented in Fig. 6.8. Transmitted energies of 6.0, 3.1 and 2.1 J were obtained for shot 1, 2, and 3 respectively. The energy dissipated by the particle reinforced material was then calculated with Eq. 6.3 and the “efficiency” e of the armouring was determined as the relative quantity of energy dissipated by it:

$$e = \frac{E_{dissipated}}{E_{impactor}} * 100. \quad (6.4)$$

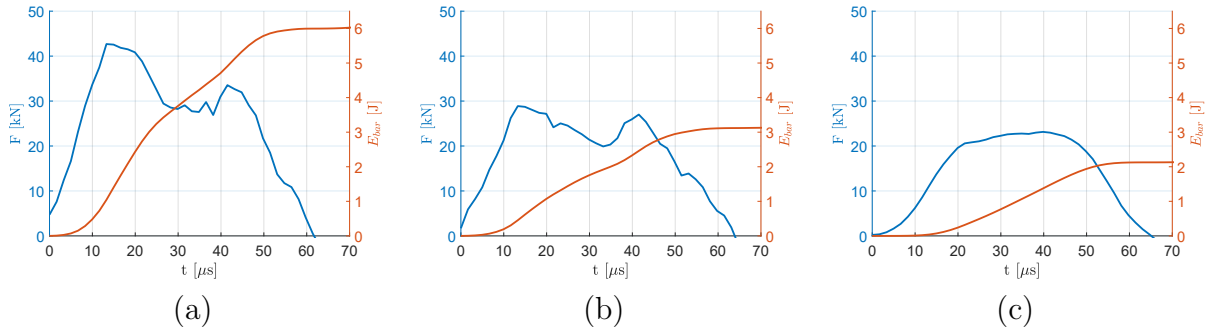


Figure 6.8: Force and energy transmitted to the bar against time for shot 1 (a), shot 2 (b), and shot 3 (c).

The efficiency factors obtained for the materials were equal to 92.3% for shot 1, 88.9% for shot 2, and 93.8% for shot 3. More tests are required to really make quantitative comparisons between the different grades of materials.

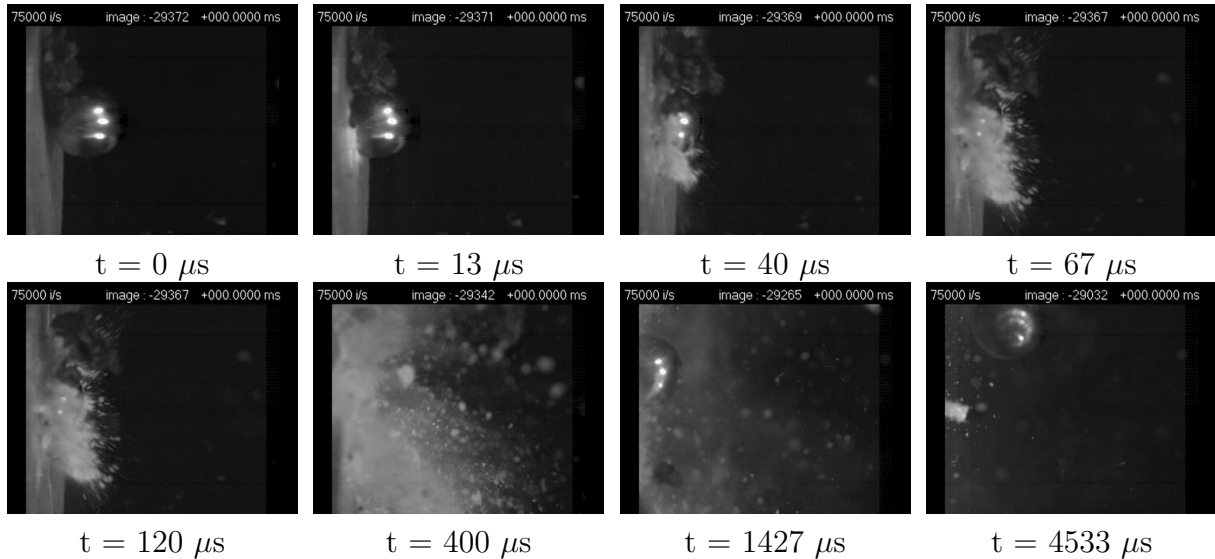


Figure 6.9: Pictures of the penetration process for shot 1.

The use of the high speed camera provided images of the impact event and the evolution of damage in the target. The impact from shot 1 is represented in Fig. 6.9. The reference time $t = 0 \mu s$ is selected as the moment of impact. During the first microseconds, the projectile penetrates into the sample and a very intense fragmentation just under the impact location is visible. After around $100 \mu s$, long radial cracks appear and propagate to the external boundary of the sample. After circa few hundreds microseconds, the heavily fragmented parts of the sample are ejected. After 1 ms, a rebound of the impactor is observed.

Similar observations are made for shot 2 (Fig. 6.10). The penetration into the target is slower than the one observed for the shot 1 as the impactor velocity was measured to be

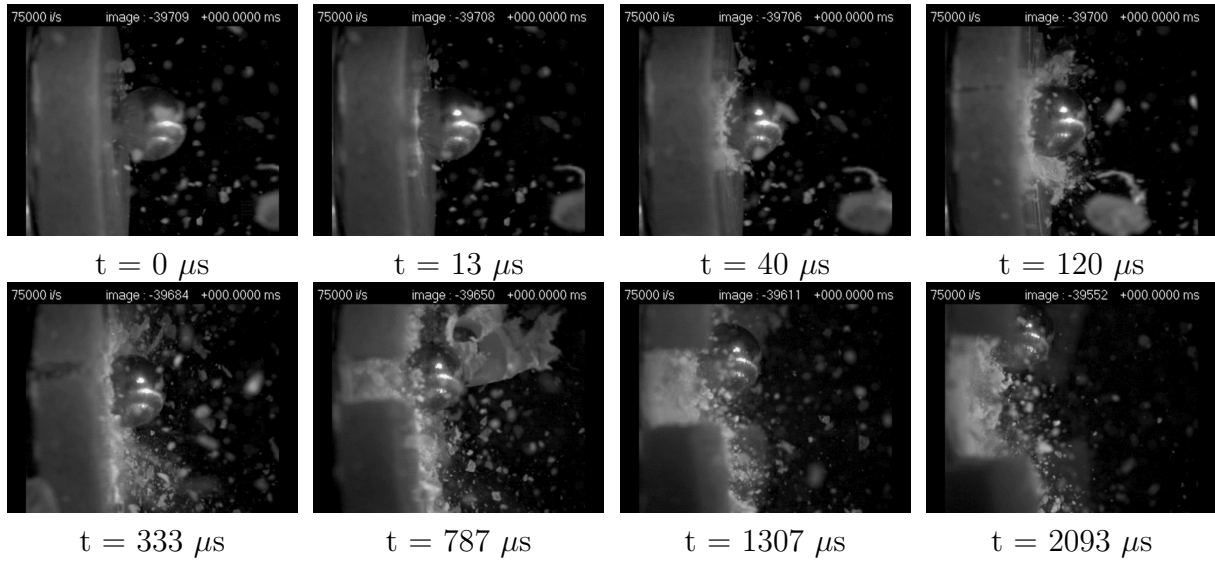


Figure 6.10: Pictures of the penetration process for shot 2.

lower. One can also see long radial cracks propagating between $30 \mu\text{s}$ and $300 \mu\text{s}$. After this time, the large fragments of the sample are ejected from the bar.

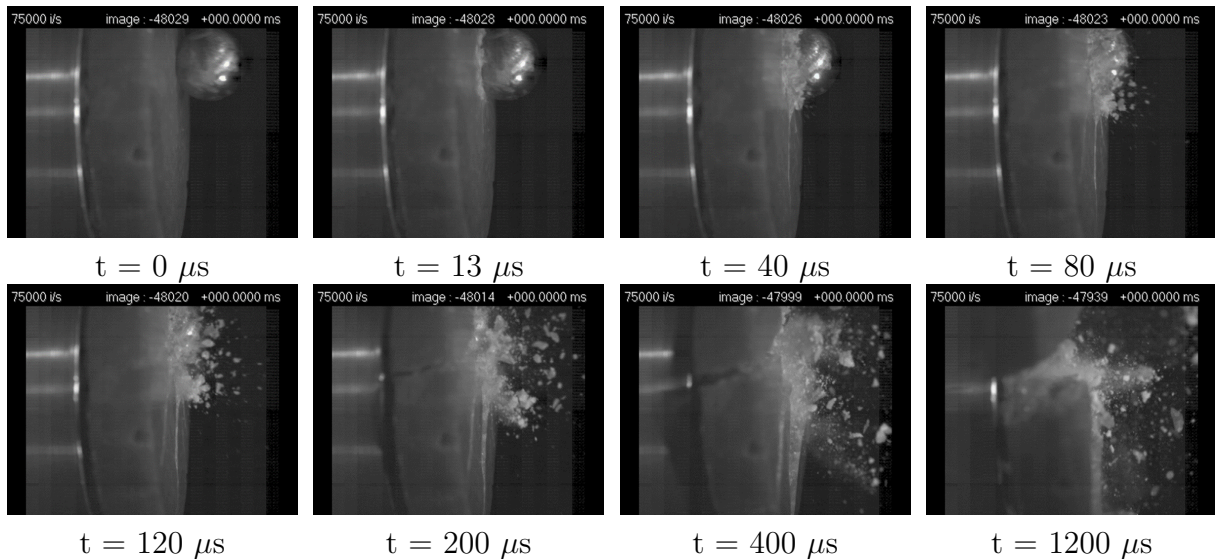


Figure 6.11: Pictures of the penetration process for shot 3.

Shot 3 (Fig. 6.11) was slightly off centred. The fracture events observed for the previous shot are still visible here: intense fragmentation under the impact location, then long radial cracks propagation, and successive ejection of the small and large fragments of material.

The large fragments of samples were reassembled after impact and the front and back faces were observed. The sample from shot 1 is represented in Fig. 6.12. The central part where the sample has been impacted is completely crushed. Numerous long radial

cracks are visible. During indentation tests, the quasi-static penetration of the sample consistently led to 3 radial cracks, whereas, here, at least ten or more are present. A lot of small fragments have also been gathered.

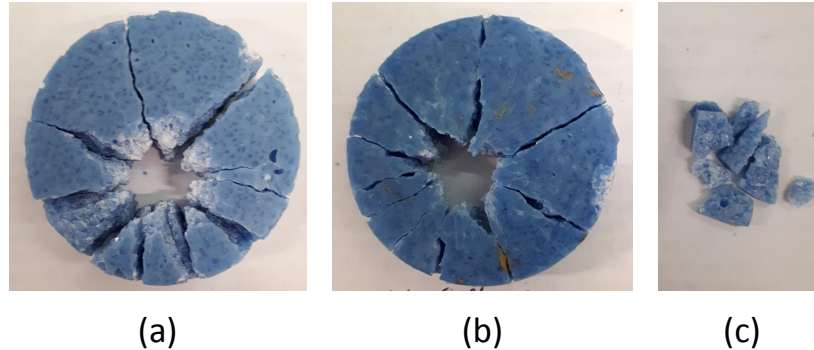


Figure 6.12: Post failure pictures of sample (Al_2O_3 mix $\phi = 60\%$) shot 1, (a) front, (b) back, (c) fragments.

Fig. 6.13 represents the sample from shot 2. The central crushed part seems to be smaller (especially on the back face of the sample). The hole observed on the backside face is much smaller than the ball diameter, which certainly indicates that the impactor rebounded on the target instead of passing through. This can be correlated with the smaller impactor velocity of this shot. However, more radial cracks are present.

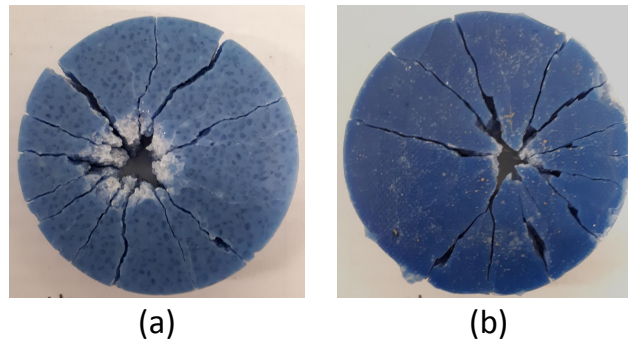


Figure 6.13: Post failure pictures of sample (Al_2O_3 mix $\phi = 50\%$) shot 2, (a) front, (b) back.

Fig. 6.13 represents the sample from shot 3. As the impact was off-centred, a part of the sample is fragmented into small pieces whereas the other one contains large fragments. The part crushed by the impactor also seems to be smaller than for shot 1.

Even though the tested samples were different (different volume fractions of alumina particles were used), the fact that the impactors energies were different makes comparisons between the samples difficult. At this stage of the project, a full validation of the test setup and protocol is achieved. Preliminary dynamic impact tests were performed showing a very different behaviour compared to the one obtained under quasi-static conditions. More

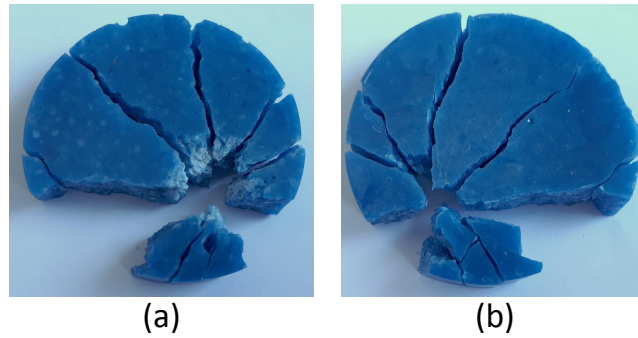


Figure 6.14: Post failure pictures of sample (Al_2O_3 mix $\phi = 30\%$) shot 3, (a) front, (b) back.

impact tests are required to evaluate the behaviour of each particle reinforced composite grade to obtain comparable and repeatable data and draw conclusions.

6.3 Conclusions

A ballistic impact test setup has been developed to observe the dynamic behaviour of the particle reinforced composite. Impactors are projected at velocities up several meters per second which are representative of the ballistic regime. The kinematics of the material failure under impact can be observed using a high speed camera. A Hopkinson bar is employed as a dynamic load cell and allow to determine the load-time curve generated by the impact. It is especially possible to observe the fragmentation of the material with the use of a high speed camera, and to determine the energy absorbed by the material based on the dynamic load cell employed here. A post-failure observation of the samples has been carried out and it showed its usefulness to understand the impact behaviour of the different grades of material. However, these results are only preliminary since very few material grades were tested and tests were not repeated to check for reproducibility. In order to get a more complete comprehension of the behaviour of the particle reinforced composite under impact, the following actions could be undertaken:

- A more exhaustive test plan is in progress on different grades of the material to study the effect of the microstructural parameters (particle volume fraction, size, types of reinforcements) on its ballistic behaviour.
- It would also be interesting to study the behaviour of the confined material for multiple reasons. First, it would maintain all the fragments together to observe the failure of the material. Then, it could also have an impact on the mechanical response of the material.

General conclusion and outlook

Understanding the behaviour of a ceramic particle reinforced polymer

The objective of the present study was to evaluate the behaviour of a polymer filled with a high content of ceramic particles and to establish its ability to replace traditional monolithic ceramic tiles for ballistic applications. Indeed, the particle reinforced polymer is a material that can be moulded and therefore allows larger and more complex geometries compared to classical monolithic ceramic rectangular plates. The first chapter was devoted to a bibliographic study on the behaviour of materials under ballistic impacts and to understand what mechanical properties are required to obtain an interesting material for ballistic protection. Nowadays, the main solutions are monolithic ceramic tiles and much of the published literature is focused on this class of materials. A few studies have however introduced ceramic particle reinforced materials for armouring. For both types of materials, it has been observed that the loading during impact is very complex and therefore the capacity of a material to be an efficient armour relies on multiple relevant mechanical parameters. The mechanical properties of a polymer reinforced with a high content of ceramic particles are quite unknown and the present thesis was then dedicated to the comprehension and evaluation of the mechanical behaviour and damage mechanisms of such a material.

The second chapter first focused on the manufacturing process of a polymer filled with a high volume fraction of particles. The second part of the chapter was devoted to the determination of elastic properties of such a material as function of the various design parameters such as the individual material properties of the components, the particle size, shape, distribution, and volume fraction. The overall elastic properties were determined first experimentally and then using a numerical homogenisation procedure. As a general result and according to literature, to obtain a stiff composite material, a very high volume fraction of particles needs to be incorporated. Multiple particle sizes distributions are required to obtain high particle volume fractions. A maximum value of the volume fraction of particles was obtained corresponding to 65%. However, even with this high reinforce-

ment content, the composite Young's modulus is still very low compared to monolithic ceramics.

The third chapter was dedicated to the observation and the description of the failure of the particle reinforced polymer under tensile loading. First, an experimental campaign was carried out in order to determine the damage mechanisms and the effect of various design parameters on the failure of such a material. Debonding was found to be a very important damage mechanism and the adhesion between the components plays a significant role in the composite failure. Moreover, it has been proven that the interfaces between the particles and the matrix can be enhanced using a silane treatment that creates chemical bonds between the organic and inorganic components. This way, the strength of the material is considerably increased. The experimental campaign has been followed by a theoretical one. First a FE-based model has been developed by using CZM to model the imperfect interfaces between the matrix and the particles. Secondly a semi-analytical model based on a modified version of Eshelby approach for homogenisation has been used. From both approaches, the particle size was observed to strongly impact the results and especially on the debonding phenomenon. Such an observation was then the starting point of the next chapter.

This noticeable particle size effect was then developed and observed by the mean of two distinct models through the fourth chapter. On the one hand, the particle size effect was described in a numerical framework using a Cohesive Zone Model and on the other hand, it was described using Finite Fracture Mechanics in an analytical framework. The Finite Fracture Mechanics is based on coupled energetic and stress criteria and a crack of a finite length is created when both criteria are simultaneously fulfilled. The case study of a single spherical particle was first addressed by determining the critical remote stress responsible for the debonding onset. Both models gave a clear size effect as large particles tend to be debonded prior to smaller ones. Two asymptotic regimes are observed for the critical remote stress and the parameters governing the debonding phenomenon are identified. For large particles, the strength of the interface is the governing parameter and the critical remote stress reaches a plateau value. For small particles, this critical remote stress is proportional to $1/R$ for the Cohesive Zone Model and to $1/\sqrt{R}$ for the Finite Fracture Mechanics. The governing parameter is then the critical displacement for the Cohesive Zone Model and the fracture energy for the Finite Fracture Mechanics.

Towards ballistic performances of the material

The resistance to perforation was then addressed in Chapter 5 where the problem is experimentally analysed by using indentation tests. These tests correspond to perforation

at very low loading rates and allow to determine the hardness of the material. In order to obtain meaningful results, a special procedure of instrumented indentation tests based on the Oliver-Pharr method was developed. Load-displacement curves were obtained using Digital Image Correlation. Monotonic and cyclic indentation tests were performed to obtain hardness, elastic properties and information on the failure under localised compressive loading of the particle reinforced material. The hardness and the stiffness of the material were observed to be increasing with increasing particle content. The matrix behaviour still had an important impact on the properties of the composite reinforced with high volume fractions of particles, as a brittle matrix lead to brittle failure and a ductile one to a ductile failure. The composite behaviour under this kind of loading is, however, still very low compared to the one of monolithic ceramics in terms of stiffness and hardness.

Finally, a ballistic test setup was developed to determine the behaviour of the particle reinforced material under ballistic impacts. The test system is composed of a compressed gas canon able to project impactors up to several hundreds of meters per second. The velocity of the impactor (hence its energy) can be measured using a high speed camera. This device also allowed the penetration of the impactor into the target and the failure of the latter to be observed. A dynamic load cell composed of a Hopkinson bar instrumented with strain gauges allowed the force-time history of the bar and hence the energy transmitted to the bar to be determined.

Contributions of the study

Numerical simulations based on FE-calculations were developed to determine the homogenised mechanical properties of the particle reinforced composite. More precisely, different algorithms have been introduced and implemented to generate representative synthetic of 2D microstructures. They were especially designed to obtain a rapid generation of a microstructure characterised by a high volume fraction of inclusions. Another important point is the introduction of various morphological properties: circular and polygonal particles, distribution of sizes and spatial positions of particles.

A particular attention was paid to the determination of the effect of various microstructural parameters on the mechanical behaviour of the material: particle volume fraction, particle size, shape, particle/matrix adhesion. It was experimentally demonstrated that the introduction of silane has a significant effect on the strength of the material. Various homogenisation methods were employed through this study based on analytical, numerical and experimental developments. Rigorous extensions of the analytical and numerical models were introduced in order to take into account particle debonding, that was ob-

served to be a crucial phenomenon for this class of material.

Experimental methods were adapted in order to observe the resistance to penetration of the particle reinforced composite. Instrumented macro-indentation tests were used to determine multiple mechanical parameters while a ballistic test setup was developed to observe the failure of the material under impact. This test setup could be used for to evaluate the impact behaviour of other materials, such as various types of fibrous or woven composites, metals, or to observe the impact of hailstones (as it was originally developed for).

Limitations and outlook

From this study multiple potential outcomes arise. From the theoretical point of view, only the elastic behaviour and the particle/matrix debonding phenomenon were taken into account. A significant improvement would be to implement a relevant nonlinear behaviour for the matrix representative of the damage mechanisms of brittle epoxies like the one used for this study. The compressive behaviour of the particle reinforced material can also be studied. The determination of the possible percolation of particles, and the resulting chain forces could be of significant interest.

Studying the effect of the loading rate on the different components of the material (particles and matrix) and on the interfaces between them could also consist in a step towards the comprehension of the material behaviour under severe dynamic loading observed during impact. Correlations between the quasi-static behaviour of the material and the one under impact remains an important outcome for this study.

From the experimental point of view, even though the ballistic impact test system was installed, very few tests were carried out so that quantitative data on the behaviour under impact of the material could not be extracted for the moment. An experimental campaign to determine the effect of microstructural parameters (particle volume fraction, size, adhesion between the phases, types of reinforcements) on the ballistic behaviour of the material could be carried out using the ballistic test setup developed for the present study.

Bibliography

- [1] ML Abel, RD Allington, RP Digby, N Porritt, SJ Shaw, and JF Watts. Understanding the relationship between silane application conditions, bond durability and locus of failure. *International Journal of Adhesion and Adhesives*, 26(1-2):2–15, 2006. [↑p. 42](#)
- [2] S Abrate. *Impact engineering of composite structures*, volume 526. Springer Science & Business Media, 2011. [↑p. 6](#), [↑p. 9](#), [↑p. 10](#), [↑p. 11](#)
- [3] R Affes, JY Delenne, Y Monerie, F Radjaï, and V Topin. Tensile strength and fracture of cemented granular aggregates. *The European Physical Journal E*, 35(11):117, 2012. [↑p. 34](#), [↑p. 35](#)
- [4] R Affes, V Topin, JY Delenne, Y Monerie, and F Radjai. Fissuration des matériaux à inclusions granulaires: effet de la microstructure. *20ème Congrès Français de Mécanique, 28 août/2 sept. 2011-25044 Besançon, France (FR)*, 2011. [↑p. 35](#)
- [5] S Ahmed and FR Jones. A review of particulate reinforcement theories for polymer composites. *Journal of Materials Science*, 25(12):4933–4942, 1990. [↑p. 20](#)
- [6] G Alfano and MA Crisfield. Finite element interface models for the delamination analysis of laminated composites: mechanical and computational issues. *International journal for numerical methods in engineering*, 50(7):1701–1736, 2001. [↑p. 96](#)
- [7] A Alizadeh, E Taheri-Nassaj, and N Ehsani. Synthesis of boron carbide powder by a carbothermic reduction method. *Journal of the European Ceramic Society*, 24(10-11):3227–3234, 2004. [↑p. 38](#)
- [8] A Arias, P Forquin, and R Zaera. Impact damage in concrete targets subjected to perforation of high velocity metallic fragment. In *DYMAT-International Conference on the Mechanical and Physical Behaviour of Materials under Dynamic Loading*, volume 2, pages 1215–1221. EDP Sciences, 2009. [↑p. 15](#), [↑p. 16](#), [↑p. 17](#)

- [9] A Arias, P Forquin, R Zaera, and C Navarro. Relationship between static bending and compressive behaviour of particle-reinforced cement composites. *Composites Part B: Engineering*, 39(7-8):1205–1215, 2008. [↑p. 16](#)
- [10] A Arias, R Zaera, J López-Puente, and C Navarro. Numerical modeling of the impact behavior of new particulate-loaded composite materials. *Composite Structures*, 61(1-2):151–159, 2003. [↑p. 9](#), [↑p. 37](#)
- [11] S Asenov, L Lakov, and K Toncheva. Promising ceramic materials for ballistic protection. *Journal of Chemical Technology and Metallurgy*, 48(2):190–195, 2013. [↑p. 8](#), [↑p. 15](#)
- [12] GI Barenblatt. The formation of equilibrium cracks during brittle fracture. general ideas and hydrotheses: Axially-symmetric cracks. *J. Appl. Math. Mech.*, 23:622–636, 1959. [↑p. 31](#)
- [13] Y Benveniste. A new approach to the application of mori-tanaka’s theory in composite materials. *Mechanics of Materials*, 6:147–157, 1987. [↑p. 25](#), [↑p. 67](#), [↑p. 68](#)
- [14] B Budiansky. On the elastic moduli of some heterogeneous materials. *Journal of the Mechanics and Physics of Solids*, 13(4):223–227, 1965. [↑p. 25](#)
- [15] GT Camacho and M Ortiz. Computational modelling of impact damage in brittle materials. *International Journal of solids and structures*, 33(20-22):2899–2938, 1996. [↑p. 31](#)
- [16] A Catapano and J Jumel. A numerical approach for determining the effective elastic symmetries of particulate-polymer composites. *Composites Part B: Engineering*, 78:227–243, 2015. [↑p. 64](#)
- [17] KW Chan and AKH Kwan. Evaluation of particle packing models by comparing with published test results. *particuology*, 16:108–115, 2014. [↑p. 43](#)
- [18] JK Chen, ZP Huang, and J Zhu. Size effect of particles on the damage dissipation in nanocomposites. *Composites Science and Technology*, 67(14):2990–2996, 2007. [↑p. 111](#)
- [19] JK Chen and M Yuan. Decoupling of viscous dissipation and damage dissipation in particulate-reinforced polymeric materials. *Computational materials science*, 40(2):267–274, 2007. [↑p. 109](#)
- [20] ESC Chin. Army focused research team on functionally graded armor composites. *Materials Science and Engineering: A*, 259(2):155–161, 1999. [↑p. 7](#), [↑p. 14](#)
-

- [21] J Cho, MS Joshi, and CT Sun. Effect of inclusion size on mechanical properties of polymeric composites with micro and nano particles. *Composites Science and Technology*, 66(13):1941–1952, 2006. [↑p. 115](#)
- [22] RM Christensen and KH Lo. Solutions for effective shear properties in three phase sphere and cylinder models. *Journal of the Mechanics and Physics of Solids*, 27(4):315–330, 1979. [↑p. 27](#)
- [23] J Christoffersen. Bonded granulates. *Journal of the Mechanics and Physics of Solids*, 31(1):55–83, 1983. [↑p. 29](#)
- [24] AL Collins, JW Addiss, SM Walley, K Promratana, F Bobaru, WG Proud, and DM Williamson. The effect of rod nose shape on the internal flow fields during the ballistic penetration of sand. *International Journal of Impact Engineering*, 38(12):951–963, 2011. [↑p. 34](#)
- [25] RL Cook, WJ Hampshire, and RV Kolarik. Ballistic armor system, December 25 1979. US Patent 4,179,979. [↑p. 10](#)
- [26] P Cornetti, N Pugno, A Carpinteri, and D Taylor. Finite fracture mechanics: a coupled stress and energy failure criterion. *Engineering Fracture Mechanics*, 73(14):2021–2033, 2006. [↑p. 115](#)
- [27] JRM d’Almeida and SN Monteiro. The iosipescu test method as a method to evaluate the tensile strength of brittle materials. *Polymer Testing*, 18(6):407–414, 1999. [↑p. 78](#)
- [28] S Dartois. *Prise en compte de l’évolution de l’endommagement anisotrope dans une modélisation par transition d’échelle pour des composites particulaires fortement chargés*. PhD thesis, Poitiers, 2008. [↑p. 30](#)
- [29] S Dartois, D Halm, C Nadot, A Dragon, and A Fanget. Introduction of damage evolution in a scale transition approach for highly-filled particulate composites. *Engineering Fracture Mechanics*, 75(11):3428–3445, 2008. [↑p. 29](#), [↑p. 30](#)
- [30] F de Larrard. Concrete mixture-proportioning - a scientific approach. *Modern Concrete Technology*, 7:314, 1999. [↑p. 44](#)
- [31] C Denoual. *Approche probabiliste du comportement à l’impact du carbure de silicium: application aux blindages moyens*. PhD thesis, 1998. [↑p. 13](#)
- [32] C Denoual, CE Cottenot, et al. Visualization of the damage evolution in impacted silicon carbide ceramics. *International Journal of Impact Engineering*, 21(4):225–235, 1998. [↑p. 12](#)

- [33] C Denoual, CE Cottenot, and F Hild. On the identification of damage during impact of a ceramic by a hard projectile. In *Proceedings 16th International Conference on BALLISTICS,(APDS, Arlington (USA), 1996)*, pages 541–550, 1996. [↑p. 13](#)
- [34] C Denoual and F Hild. A damage model for the dynamic fragmentation of brittle solids. *Computer methods in applied mechanics and engineering*, 183(3-4):247–258, 2000. [↑p. 155](#)
- [35] C Denoual and F Hild. Dynamic fragmentation of brittle solids: a multi-scale model. *European Journal of Mechanics-A/Solids*, 21(1):105–120, 2002. [↑p. 155](#)
- [36] F Dinzart and H Sabar. New micromechanical modeling of the elastic behavior of composite materials with ellipsoidal reinforcements and imperfect interfaces. *International Journal of Solids and Structures*, 108:254–262, 2017. [↑p. 92](#)
- [37] BR Donohue, A Ambrus, and SR Kalidindi. Critical evaluation of the indentation data analyses methods for the extraction of isotropic uniaxial mechanical properties using finite element models. *Acta Materialia*, 60(9):3943–3952, 2012. [↑p. 134](#), [↑p. 143](#), [↑p. 146](#)
- [38] DS Dugdale. Yielding of steel sheets containing slits. *Journal of the Mechanics and Physics of Solids*, 8(2):100–104, 1960. [↑p. 31](#)
- [39] MGGV Elices, GV Guinea, J Gomez, and J Planas. The cohesive zone model: advantages, limitations and challenges. *Engineering fracture mechanics*, 69(2):137–163, 2002. [↑p. 97](#), [↑p. 98](#)
- [40] B Erzar, P Forquin, C Pontiroli, and E Buzaud. Influence of aggregate size and free water on the dynamic behaviour of concrete subjected to impact loading. In *EPJ Web of Conferences*, volume 6, page 39007. EDP Sciences, 2010. [↑p. 17](#)
- [41] JD Eshelby. The determination of the elastic field of an ellipsoidal inclusion, and related problems. *Proc Roy. Soc. London*, A241:376, 1957. [↑p. 25](#), [↑p. 66](#)
- [42] M Esteva and P Spanos. Effective elastic properties of nanotube reinforced composites with slightly weakened interfaces. *Journal of Mechanics of Materials and Structures*, 4(5):887–900, 2009. [↑p. 93](#)
- [43] JS Field and MV Swain. A simple predictive model for spherical indentation. *Journal of Materials Research*, 8(2):297–306, 1993. [↑p. 134](#), [↑p. 143](#), [↑p. 144](#), [↑p. 146](#)
- [44] JS Field and MV Swain. Determining the mechanical properties of small volumes of material from submicrometer spherical indentations. *Journal of Materials Research*, 10(1):101–112, 1995. [↑p. 146](#)

- [45] P Forquin, A Arias, and R Zaera. An experimental method of measuring the confined compression strength of geomaterials. *International Journal of Solids and Structures*, 44(13):4291–4317, 2007. [↑p. 16](#)
- [46] P Forquin, A Arias, and R Zaera. Role of porosity in controlling the mechanical and impact behaviours of cement-based materials. *International Journal of Impact Engineering*, 35(3):133–146, 2008. [↑p. 16](#)
- [47] P Forquin, A Arias, and R Zaera. Relationship between mesostructure, mechanical behaviour and damage of cement composites under high-pressure confinement. *Experimental mechanics*, 49(5):613–625, 2009. [↑p. 16](#)
- [48] MJ Forrestal and VK Luk. Penetration into soil targets. *International Journal of Impact Engineering*, 12(3):427–444, 1992. [↑p. 32](#)
- [49] GA Francfort and JJ Marigo. Revisiting brittle fracture as an energy minimization problem. *Journal of the Mechanics and Physics of Solids*, 46(8):1319–1342, 1998. [↑p. 32](#)
- [50] S Fu, X Feng, B Lauke, and Y Mai. Effects of particle size, particle/matrix interface adhesion and particle loading on mechanical properties of particulate–polymer composites. *Composites Part B: Engineering*, 39(6):933–961, 2008. [↑p. 17](#), [↑p. 18](#), [↑p. 19](#), [↑p. 20](#), [↑p. 21](#), [↑p. 24](#)
- [51] IG García, V Mantič, and E Graciani. Debonding at the fibre–matrix interface under remote transverse tension. one debond or two symmetric debonds? *European Journal of Mechanics-A/Solids*, 53:75–88, 2015. [↑p. 120](#), [↑p. 125](#)
- [52] IG García, V Mantič, and E Graciani. A model for the prediction of debond onset in spherical-particle-reinforced composites under tension. application of a coupled stress and energy criterion. *Composites Science and Technology*, 106:60–67, 2015. [↑p. 114](#), [↑p. 115](#)
- [53] AC Garg and YW Mai. Failure mechanisms in toughened epoxy resins—a review. *Composites Science and Technology*, 31(3):179–223, 1988. [↑p. 17](#), [↑p. 23](#)
- [54] AN Gent. Detachment of an elastic matrix from a rigid spherical inclusion. *Journal of Materials Science*, 15(11):2884–2888, 1980. [↑p. 110](#)
- [55] E Ghossein and M Lévesque. A fully automated numerical tool for a comprehensive validation of homogenization models and its application to spherical particles reinforced composites. *International Journal of Solids and structures*, 49(11):1387–1398, 2012. [↑p. 31](#), [↑p. 47](#), [↑p. 71](#)

- [56] E Ghossein and M Lévesque. A comprehensive validation of analytical homogenization models: The case of ellipsoidal particles reinforced composites. *Mechanics of Materials*, 75:135–150, 2014. [↑p. 27](#)
- [57] JN Goodier. Concentration of stress around spherical and cylindrical inclusions and flaws. *J. appl. Mech*, 1(1):39–44, 1933. [↑p. 110](#)
- [58] A Gouldstone, N Chollacoop, M Dao, J Li, AM Minor, and YL Shen. Indentation across size scales and disciplines: Recent developments in experimentation and modeling. *Acta Materialia*, 55(12):4015–4039, 2007. [↑p. 149](#)
- [59] B Guiot, C Nadot-Martin, and A Dragon. Towards a non-linear micromechanics-based analysis for particulate composites. *Composites Science and Technology*, 66(15):2726–2735, 2006. [↑p. 29](#)
- [60] Z Hashin and S Shtrikman. A variational approach to the theory of the elastic behaviour of multiphase materials. *J. Mech. Phys Solids*, 11:127–140, 1963. [↑p. 25](#)
- [61] PJ Hazell, CJ Roberson, and M Moutinho. The design of mosaic armour: The influence of tile size on ballistic performance. *Materials & Design*, 29(8):1497–1503, 2008. [↑p. 9](#)
- [62] H Hertz, DE Jones, and GA Schott. *Miscellaneous papers*. Macmillan and Company, 1896. [↑p. 136](#), [↑p. 142](#)
- [63] E Herve and A Zaoui. N-layered inclusion-based micromechanical modelling. *International Journal of Engineering Science*, 31(1):1–10, 1993. [↑p. 27](#)
- [64] R Hill. A self-consistent mechanics of composite materials. *Journal of the Mechanics and Physics of Solids*, 13(4):213–222, 1965. [↑p. 25](#)
- [65] HM Inglis. *Modeling the effect of debonding on the constitutive response of heterogeneous materials*. PhD thesis, University of Illinois at Urbana-Champaign, 2014. [↑p. 29](#)
- [66] HM Inglis, PH Geubelle, K Matouš, H Tan, and Y Huang. Cohesive modeling of dewetting in particulate composites: micromechanics vs. multiscale finite element analysis. *Mechanics of materials*, 39(6):580–595, 2007. [↑p. 28](#)
- [67] Oe Ishai and LJ Cohen. Elastic properties of filled and porous epoxy composites. *International Journal of Mechanical Sciences*, 9(8):539–546, 1967. [↑p. 19](#)

- [68] KC Jajam and HV Tippur. Quasi-static and dynamic fracture behavior of particulate polymer composites: a study of nano-vs. micro-size filler and loading-rate effects. *Composites Part B: Engineering*, 43(8):3467–3481, 2012. [↑p. 19](#), [↑p. 20](#)
- [69] Z Jeffries and RS Archer. *The science of metals*. McGraw-Hill, 1924. [↑p. 133](#)
- [70] J Jovicic, A Zavaliangos, and F Ko. Modeling of the ballistic behavior of gradient design composite armors. *Composites Part A: Applied Science and Manufacturing*, 31(8):773–784, 2000. [↑p. 9](#)
- [71] SR Kalidindi and S Pathak. Determination of the effective zero-point and the extraction of spherical nanoindentation stress–strain curves. *Acta Materialia*, 56(14):3523–3532, 2008. [↑p. 146](#)
- [72] T Kanit, S Forest, I Galliet, V Mounoury, and D Jeulin. Determination of the size of the representative volume element for random composites: statistical and numerical approach. *International Journal of solids and structures*, 40(13):3647–3679, 2003. [↑p. 31](#)
- [73] P Kanouté, DP Boso, JL Chaboche, and BA Schrefler. Multiscale methods for composites: a review. *Archives of Computational Methods in Engineering*, 16(1):31–75, 2009. [↑p. 27](#)
- [74] S Kari, H Berger, R Rodriguez-Ramos, and U Gabbert. Computational evaluation of effective material properties of composites reinforced by randomly distributed spherical particles. *Composite Structures*, 77(2):223–231, 2007. [↑p. 31](#), [↑p. 47](#)
- [75] C Kaufmann, D Cronin, M Worswick, G Pageau, and A Beth. Influence of material properties on the ballistic performance of ceramics for personal body armour. *Shock and Vibration*, 10(1):51–58, 2003. [↑p. 7](#), [↑p. 14](#)
- [76] T Kawaguchi and RA Pearson. The effect of particle–matrix adhesion on the mechanical behavior of glass filled epoxies. part 2. a study on fracture toughness. *Polymer*, 44(15):4239–4247, 2003. [↑p. 21](#)
- [77] AJ Kinloch, DL Maxwell, and RJ Young. The fracture of hybrid-particulate composites. *Journal of materials science*, 20(11):4169–4184, 1985. [↑p. 19](#)
- [78] R Kitey and HV Tippur. Role of particle size and filler–matrix adhesion on dynamic fracture of glass-filled epoxy. i. macromerements. *Acta Materialia*, 53(4):1153–1165, 2005. [↑p. 19](#), [↑p. 21](#)

- [79] R Kitey and HV Tippur. Role of particle size and filler–matrix adhesion on dynamic fracture of glass-filled epoxy. ii. linkage between macro-and micro-measurements. *Acta Materialia*, 53(4):1167–1178, 2005. [↑p. 19](#), [↑p. 21](#)
- [80] B Klusemann and B Svendsen. Homogenization methods for multi-phase elastic composites: Comparisons and benchmarks. *Technische Mechanik*, 30(4):374–386, 2010. [↑p. 27](#), [↑p. 71](#)
- [81] DB Knorr, HY Jian, AD Richardson, MD Hindenlang, IM McAninch, JJ La Scala, and JL Lenhart. Glass transition dependence of ultrahigh strain rate response in amine cured epoxy resins. *Polymer*, 53(25):5917–5923, 2012. [↑p. 21](#)
- [82] FK Ko, AJ Geshury, and JW Song. Behavior of gradient designed composite under ballistic impact. In *Proc. 11th Int. Conf. on Composite Materials*, volume 2, pages 464–473, 1997. [↑p. 9](#)
- [83] SG Kulkarni, XL Gao, SE Horner, JQ Zheng, and NV David. Ballistic helmets—their design, materials, and performance against traumatic brain injury. *Composite Structures*, 101:313–331, 2013. [↑p. 2](#)
- [84] V Kushvaha and H Tippur. Effect of filler shape, volume fraction and loading rate on dynamic fracture behavior of glass-filled epoxy. *Composites Part B: Engineering*, 64:126–137, 2014. [↑p. 20](#)
- [85] AKH Kwan, KW Chan, and V Wong. A 3-parameter particle packing model incorporating the wedging effect. *Powder technology*, 237:172–179, 2013. [↑p. 44](#)
- [86] AKH Kwan, V Wong, and WWS Fung. A 3-parameter packing density model for angular rock aggregate particles. *Powder Technology*, 274:154–162, 2015. [↑p. 44](#), [↑p. 45](#)
- [87] SC Kwon, T Adachi, W Araki, and A Yamaji. Effect of composing particles of two sizes on mechanical properties of spherical silica-particulate-reinforced epoxy composites. *Composites Part B: Engineering*, 39(4):740–746, 2008. [↑p. 19](#)
- [88] B Lauke. Effect of particle size distribution on debonding energy and crack resistance of polymer composites. *Computational Materials Science*, 77:53–60, 2013. [↑p. 110](#), [↑p. 111](#)
- [89] HK Lee and SH Pyo. Micromechanics-based elastic damage modeling of particulate composites with weakened interfaces. *Int. J. Solids Struct.*, 44:8390–8406, 2007. [↑p. 93](#)

- [90] HK Lee and SH Pyo. Multi-level modeling of effective elastic behavior and progressive weakened interface in particulate composites. *Composites Science and Technology*, 68:387–397, 2008. [↑p. 94](#)
- [91] D Leguillon. Strength or toughness? a criterion for crack onset at a notch. *European Journal of Mechanics-A/Solids*, 21(1):61–72, 2002. [↑p. 113](#), [↑p. 114](#)
- [92] S Li, MD Thouless, AM Waas, JA Schroeder, and PD Zavattieri. Use of a cohesive-zone model to analyze the fracture of a fiber-reinforced polymer–matrix composite. *Composites Science and Technology*, 65(3):537–549, 2005. [↑p. 98](#)
- [93] G Lielens, P Pirotte, A Couniot, F Dupret, and R Keunings. Prediction of thermo-mechanical properties for compression moulded composites. *Composites Part A: Applied Science and Manufacturing*, 29(1):63–70, 1998. [↑p. 26](#), [↑p. 68](#), [↑p. 69](#)
- [94] HT Liu, LZ Sun, and JW Ju. An interfacial debonding model for particle-reinforced composites. *International Journal of Damage Mechanics*, 13(2):163–185, 2004. [↑p. 28](#)
- [95] BD Lubachevsky and FH Stillinger. Geometric properties of random disk packings. *Journal of statistical Physics*, 60(5-6):561–583, 1990. [↑p. 47](#)
- [96] BD Lubachevsky, FH Stillinger, and EN Pinson. Disks vs. spheres: Contrasting properties of random packings. *Journal of Statistical Physics*, 64(3-4):501–524, 1991. [↑p. 47](#)
- [97] LM McGrath, RS Parnas, SH King, JL Schroeder, DA Fischer, and JL Lenhart. Investigation of the thermal, mechanical, and fracture properties of alumina–epoxy composites. *Polymer*, 49(4):999–1014, 2008. [↑p. 20](#), [↑p. 22](#)
- [98] C Miehe, M Hofacker, and F Welschinger. A phase field model for rate-independent crack propagation: Robust algorithmic implementation based on operator splits. *Computer Methods in Applied Mechanics and Engineering*, 199(45-48):2765–2778, 2010. [↑p. 32](#)
- [99] N Moës, J Dolbow, and T Belytschko. A finite element method for crack growth without remeshing. *International journal for numerical methods in engineering*, 46(1):131–150, 1999. [↑p. 32](#)
- [100] AC Moloney, HH Kausch, T Kaiser, and HR Beer. Parameters determining the strength and toughness of particulate filled epoxide resins. *Journal of materials science*, 22(2):381–393, 1987. [↑p. 18](#), [↑p. 20](#), [↑p. 21](#)

- [101] T Mori and K Tanaka. Average stress in matrix and average elastic energy of materials with misfitting inclusions. *Acta Metal*, 21:571, 1973. [↑p. 25](#), [↑p. 67](#)
- [102] T Mura. *Micromechanics of defects in solids*. Springer, 1987. [↑p. 66](#), [↑p. 96](#)
- [103] C Nadot, A Dragon, H Trumel, and A Fanget. Damage modelling framework for viscoelastic particulate composites via a scale transition approach. *Journal of Theoretical and Applied Mechanics*, 44(3):553–583, 2006. [↑p. 29](#)
- [104] C Nadot-Martin, M Touboul, A Dragon, and A Fanget. Direct scale transition approach for highly-filled viscohyperelastic particulate composites: Computational study. *Multiscale Modeling of Heterogenous Materials: From Microstructure to Macro-scale Properties*, pages 215–235, 2008. [↑p. 29](#)
- [105] C Nadot-Martin, H Trumel, and A Dragon. Morphology-based homogenization for viscoelastic particulate composites: Part i: Viscoelasticity sole. *European Journal of Mechanics-A/Solids*, 22(1):89–106, 2003. [↑p. 29](#)
- [106] M Naebe, J Sandlin, I Crouch, and B Fox. Novel polymer-ceramic composites for protection against ballistic fragments. *Polymer composites*, 34(2):180–186, 2013. [↑p. 9](#)
- [107] Y Nakamura, M Yamaguchi, A Kitayama, M Okubo, and T Matsumoto. Effect of particle size on fracture toughness of epoxy resin filled with angular-shaped silica. *Polymer*, 32(12):2221–2229, 1991. [↑p. 19](#)
- [108] Y Nakamura, M Yamaguchi, M Okubo, and T Matsumoto. Effect of particle size on impact properties of epoxy resin filled with angular shaped silica particles. *Polymer*, 32(16):2976–2979, 1991. [↑p. 19](#)
- [109] Y Nakamura, M Yamaguchi, M Okubo, and T Matsumoto. Effects of particle size on mechanical and impact properties of epoxy resin filled with spherical silica. *Journal of applied polymer science*, 45(7):1281–1289, 1992. [↑p. 19](#)
- [110] S Nemat-Nasser and M Hori. *Micromechanics: overall properties of heterogeneous materials*, volume 37. Elsevier, 2013. [↑p. 17](#)
- [111] TT Nguyen, J Yvonnet, QZ Zhu, M Bornert, and C Chateau. A phase-field method for computational modeling of interfacial damage interacting with crack propagation in realistic microstructures obtained by microtomography. *Computer Methods in Applied Mechanics and Engineering*, 312:567–595, 2016. [↑p. 32](#)

- [112] AN Norris. A differential scheme for the effective moduli of composites. *Mechanics of materials*, 4(1):1–16, 1985. [↑p. 26](#)
- [113] WCl Oliver and GM Pharr. An improved technique for determining hardness and elastic modulus using load and displacement sensing indentation experiments. *Journal of materials research*, 7(6):1564–1583, 1992. [↑p. 141](#), [↑p. 142](#)
- [114] WCl Oliver and GM Pharr. Measurement of hardness and elastic modulus by instrumented indentation: Advances in understanding and refinements to methodology. *Journal of materials research*, 19(1):3–20, 2004. [↑p. 135](#), [↑p. 136](#), [↑p. 141](#), [↑p. 144](#), [↑p. 146](#)
- [115] M Omidvar, M Iskander, and S Bless. Response of granular media to rapid penetration. *International Journal of Impact Engineering*, 66:60–82, 2014. [↑p. 32](#), [↑p. 33](#)
- [116] E Onate and J Rojek. Combination of discrete element and finite element methods for dynamic analysis of geomechanics problems. *Computer methods in applied mechanics and engineering*, 193(27-29):3087–3128, 2004. [↑p. 33](#)
- [117] Y Othmani, L Delannay, and I Doghri. Equivalent inclusion solution adapted to particle debonding with a non-linear cohesive law. *International Journal of Solids and Structures*, 48(24):3326–3335, 2011. [↑p. 28](#), [↑p. 91](#), [↑p. 92](#)
- [118] S Pathak and SR Kalidindi. Spherical nanoindentation stress–strain curves. *Materials Science and Engineering: R: Reports*, 91:1–36, 2015. [↑p. 134](#), [↑p. 146](#)
- [119] J Qu. The effect of slightly weakened interfaces on the overall elastic properties of composite materials. *Mechanics of Materials*, 14(4):269–281, 1993. [↑p. 28](#), [↑p. 90](#), [↑p. 91](#), [↑p. 92](#), [↑p. 93](#)
- [120] J Qu. Eshelby tensor for an elastic inclusion with slightly weakened interface. *Journal of applied mechanics*, 60(4):1048–1050, 1993. [↑p. 28](#), [↑p. 90](#)
- [121] PJ Rae, HT Goldrein, SJP Palmer, JE Field, and AL Lewis. Quasi–static studies of the deformation and failure of β -hmx based polymer bonded explosives. In *Proceedings of the Royal Society of London A: Mathematical, Physical and Engineering Sciences*, volume 458, pages 743–762. The Royal Society, 2002. [↑p. 29](#)
- [122] PC den Reijer. *Impact on ceramic faced armour*. PhD thesis, Technische Universiteit Delft, 1992. [↑p. 6](#), [↑p. 8](#), [↑p. 14](#)

- [123] DD Rodrigues and JG Broughton. Silane surface modification of boron carbide in epoxy composites. *International Journal of Adhesion and Adhesives*, 46:62–73, 2013. [↑p. 9](#), [↑p. 10](#), [↑p. 42](#), [↑p. 58](#)
- [124] Z Rosenberg, Y Yeshurun, and DG Brandon. Dynamic response and microstructure of commercial alumina. *Le Journal de Physique Colloques*, 46(C5):C5–331, 1985. [↑p. 11](#)
- [125] EF Rybicki and MF Kanninen. A finite element calculation of stress intensity factors by a modified crack closure integral. *Engineering Fracture Mechanics*, 9(4):931–938, 1977. [↑p. 115](#)
- [126] M Salviato, M Zappalorto, and M Quaresimin. Nanoparticle debonding strength: A comprehensive study on interfacial effects. *International Journal of Solids and Structures*, 50(20):3225–3232, 2013. [↑p. 111](#)
- [127] DJ Sandstrom, NC Calkins, and FD Gac. Constrained ceramic-filled polymer armor, November 13 1990. US Patent 4,969,386. [↑p. 10](#)
- [128] J Segurado and J LLorca. A numerical approximation to the elastic properties of sphere-reinforced composites. *Journal of the Mechanics and Physics of Solids*, 50(10):2107–2121, 2002. [↑p. 31](#), [↑p. 47](#)
- [129] Q Shang and GPAG Van Zijl. Characterising the shear behaviour of strainhardening fibre-reinforced cement-based composites. *Journal of the South African Institution of Civil Engineering= Joernaal van die Suid-Afrikaanse Instituut van Siviele Ingenieurswese*, 49(2):16–23, 2007. [↑p. 80](#)
- [130] YL Shen, JJ Williams, G Piotrowski, N Chawla, and YL Guo. Correlation between tensile and indentation behavior of particle-reinforced metal matrix composites: an experimental and numerical study. *Acta materialia*, 49(16):3219–3229, 2001. [↑p. 149](#)
- [131] Yu Shi and Yuwen Zhang. Simulation of random packing of spherical particles with different size distributions. In *ASME 2006 International Mechanical Engineering Congress and Exposition*, pages 539–544. American Society of Mechanical Engineers, 2006. [↑p. 47](#)
- [132] W Shiu, FV Donze, and L Daudeville. Discrete element modelling of missile impacts on a reinforced concrete target. *International Journal of Computer Applications in Technology*, 34(1):33, 2009. [↑p. 33](#)

- [133] DA Shockey, AH Marchand, SR Skaggs, GE Cort, MW Burkett, and R Parker. Failure phenomenology of confined ceramic targets and impacting rods. *International Journal of Impact Engineering*, 9(3):263–275, 1990. [↑p. 14](#)
- [134] RB Sills and MD Thouless. The effect of cohesive-law parameters on mixed-mode fracture. *Engineering Fracture Mechanics*, 109:353–368, 2013. [↑p. 98](#)
- [135] IV Singh, AS Shedbale, and BK Mishra. Material property evaluation of particle reinforced composites using finite element approach. *Journal of Composite Materials*, page 0021998315612539, 2015. [↑p. 31](#), [↑p. 47](#)
- [136] RP Singh, M Zhang, and D Chan. Toughening of a brittle thermosetting polymer: effects of reinforcement particle size and volume fraction. *Journal of Materials Science*, 37(4):781–788, 2002. [↑p. 19](#)
- [137] TW Sirk, KS Khare, M Karim, JL Lenhart, JW Andzelm, GB McKenna, and R Khare. High strain rate mechanical properties of a cross-linked epoxy across the glass transition. *Polymer*, 54(26):7048–7057, 2013. [↑p. 21](#)
- [138] IN Sneddon. The relation between load and penetration in the axisymmetric boussinesq problem for a punch of arbitrary profile. *International journal of engineering science*, 3(1):47–57, 1965. [↑p. 145](#)
- [139] J Spanoudakis and RJ Young. Crack propagation in a glass particle-filled epoxy resin - part 1 effect of particle volume fraction and size. *Journal of Materials Science*, 19(2):473–486, 1984. [↑p. 19](#)
- [140] J Spanoudakis and RJ Young. Crack propagation in a glass particle-filled epoxy resin - part 2 effect of particle-matrix adhesion. *Journal of Materials Science*, 19(2):473–486, 1984. [↑p. 18](#), [↑p. 19](#), [↑p. 21](#)
- [141] AJ Stilp. Sabot designs for launching penetrators and projectiles. In *High-pressure shock compression of solids VIII*, pages 201–225. Springer, 2005. [↑p. 157](#)
- [142] D Tabor. *The hardness of metals*. Oxford university press, 1951. [↑p. 146](#)
- [143] H Tan, Y Huang, C Liu, and PH Geubelle. The mori–tanaka method for composite materials with nonlinear interface debonding. *International Journal of Plasticity*, 21(10):1890–1918, 2005. [↑p. 28](#)
- [144] H Tan, Y Huang, C Liu, G Ravichandran, and GH Paulino. Constitutive behaviors of composites with interface debonding: the extended mori–tanaka method for uniaxial tension. *International Journal of Fracture*, 146(3):139–148, 2007. [↑p. 28](#)

- [145] H Tan, C Liu, Y Huang, and PH Geubelle. The cohesive law for the particle/matrix interfaces in high explosives. *Journal of the Mechanics and Physics of Solids*, 53(8):1892–1917, 2005. [↑p. 28](#)
- [146] LM Tavares. Energy absorbed in breakage of single particles in drop weight testing. *Minerals Engineering*, 12(1):43–50, 1999. [↑p. 160](#)
- [147] JA Tjernlund, EK Gamstedt, and P Gudmundson. Length-scale effects on damage development in tensile loading of glass-sphere filled epoxy. *International journal of solids and structures*, 43(24):7337–7357, 2006. [↑p. 110](#)
- [148] V Topin, JY Delenne, F Radjai, L Brendel, and F Mabilbe. Strength and failure of cemented granular matter. *The European Physical Journal E*, 23(4):413–429, 2007. [↑p. 34](#)
- [149] S Torquato. Random heterogeneous media: microstructure and improved bounds on effective properties. *Applied mechanics reviews*, 44(2):37–76, 1991. [↑p. 25](#), [↑p. 47](#)
- [150] A Turon, CG Davila, PP Camanho, and J Costa. An engineering solution for mesh size effects in the simulation of delamination using cohesive zone models. *Engineering fracture mechanics*, 74(10):1665–1682, 2007. [↑p. 97](#), [↑p. 98](#)
- [151] WM Visscher and M Bolsterli. Random packing of equal and unequal spheres in two and three dimensions. *Nature*, 239:504–507, 1972. [↑p. 47](#)
- [152] Zi Wang, P Gu, H Zhang, Z Zhang, and X Wu. Finite element modeling of the indentation and scratch response of epoxy/silica nanocomposites. *Mechanics of Advanced Materials and Structures*, 21(10):802–809, 2014. [↑p. 149](#)
- [153] W Weibull. A statistical theory of strength of materials. *IVB-Handl.*, 1939. [↑p. 82](#), [↑p. 155](#)
- [154] P Weißgraeber, D Leguillon, and W Becker. A review of finite fracture mechanics: crack initiation at singular and non-singular stress raisers. *Archive of Applied Mechanics*, 86, 2016. [↑p. 114](#), [↑p. 115](#)
- [155] ML Wilkins. Mechanics of penetration and perforation. *International Journal of Engineering Science*, 16(11):793–807, 1978. [↑p. 14](#)
- [156] JG Williams. Particle toughening of polymers by plastic void growth. *Composites science and technology*, 70(6):885–891, 2010. [↑p. 111](#)

- [157] XP Xu and A Needleman. Numerical simulations of fast crack growth in brittle solids. *Journal of the Mechanics and Physics of Solids*, 42(9):1397–1434, 1994. [↑p. 31](#), [↑p. 32](#)
- [158] AB Yu, J Bridgwater, and A Burbidge. On the modelling of the packing of fine particles. *Powder technology*, 92(3):185–194, 1997. [↑p. 44](#)
- [159] M Zappalorto, M Salviato, and M Quaresimin. Assessment of debonding-induced toughening in nanocomposites. *Procedia Engineering*, 10:2973–2978, 2011. [↑p. 111](#)
- [160] M Zappalorto, M Salviato, and M Quaresimin. Influence of the interphase zone on the nanoparticle debonding stress. *Composites Science and Technology*, 72(1):49–55, 2011. [↑p. 111](#)
- [161] M Zappalorto, M Salviato, and M Quaresimin. Stress distributions around rigid nanoparticles. *International Journal of Fracture*, pages 1–8, 2012. [↑p. 111](#)
- [162] YH Zhao and GJ Weng. The effect of debonding angle on the reduction of effective moduli of particle and fiber-reinforced composites. *Journal of applied mechanics*, 69(3):292–302, 2002. [↑p. 28](#)
- [163] JL Zinszner. *Identification des paramètres matériau gouvernant les performances de céramiques à blindage*. PhD thesis, Université de Lorraine, 2014. [↑p. 7](#), [↑p. 8](#), [↑p. 11](#), [↑p. 14](#), [↑p. 15](#)

Appendix A

Density measurements for effective volume fraction determination

To determine the effective particle volume fraction, the real density of the samples is measured. As the samples do not show a simple geometric shape, a precise density measurement method is employed.

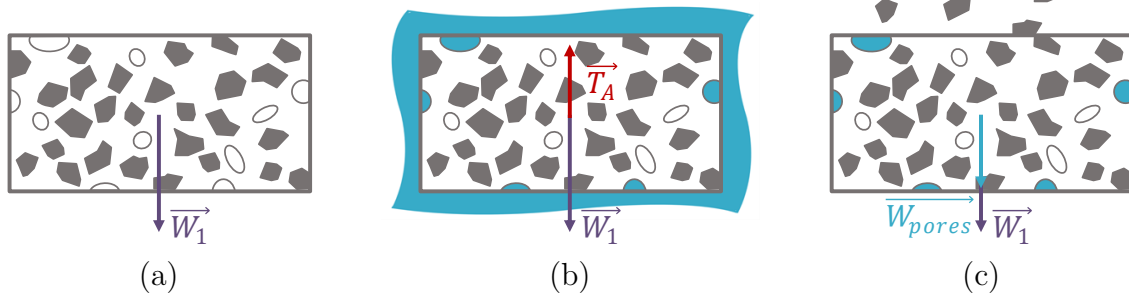


Figure A.1: (a) Forces acting on the dry sample;
(b) Forces acting on the immersed sample;
(c) Forces acting on the soaked sample.

It can be summarised as: first, the mass m_1 of the dry sample (Fig. A.1 (a), W_1 being the weight associated to the mass m_1) is measured. Then, the apparent mass m_2 (weight W_1 of the soaked sample minus the effect of Archimedes thrust T_A) of the immersed sample (Fig. A.1 (b)) is determined. And finally, the weight m_3 of the soaked sample (Fig. A.1 (c), W_{pores} being the mass of the water trapped in the open pores) is evaluated. The density of the composite (ρ_b) and the open porosity (π_a) are then calculated as:

$$\rho_b = \frac{m_1}{m_3 - m_2}, \quad (\text{A.1})$$

$$\pi_a = \frac{m_3 - m_1}{m_3 - m_2} * 100. \quad (\text{A.2})$$

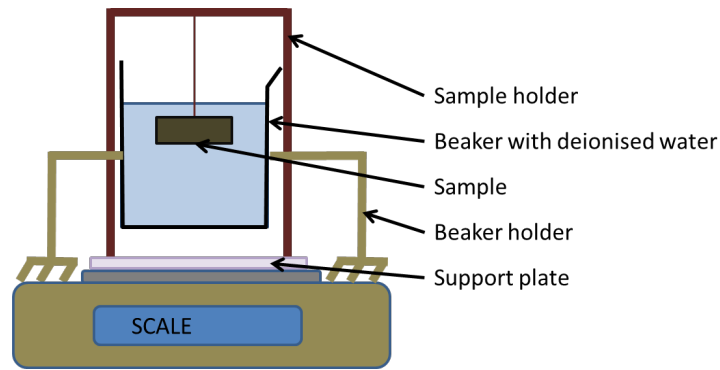


Figure A.2: Mass determination of the immersed sample.

The weighing procedure is summed up hereafter (according to the standard BS EN 1389:2003):

1. The mass of the test specimen is determined by weighing the dry test specimen in air.
2. The test specimen is impregnated under vacuum. Then the mass of the test specimen is determined by weighing the test specimen immersed in the impregnated liquid (see Fig. A.2 for a schematic drawing set up.)
3. The mass of the test specimen is determined by weighing test specimen in air while still impregnated with the liquid.

Appendix B

Study on the size of the process zone for particle debonding

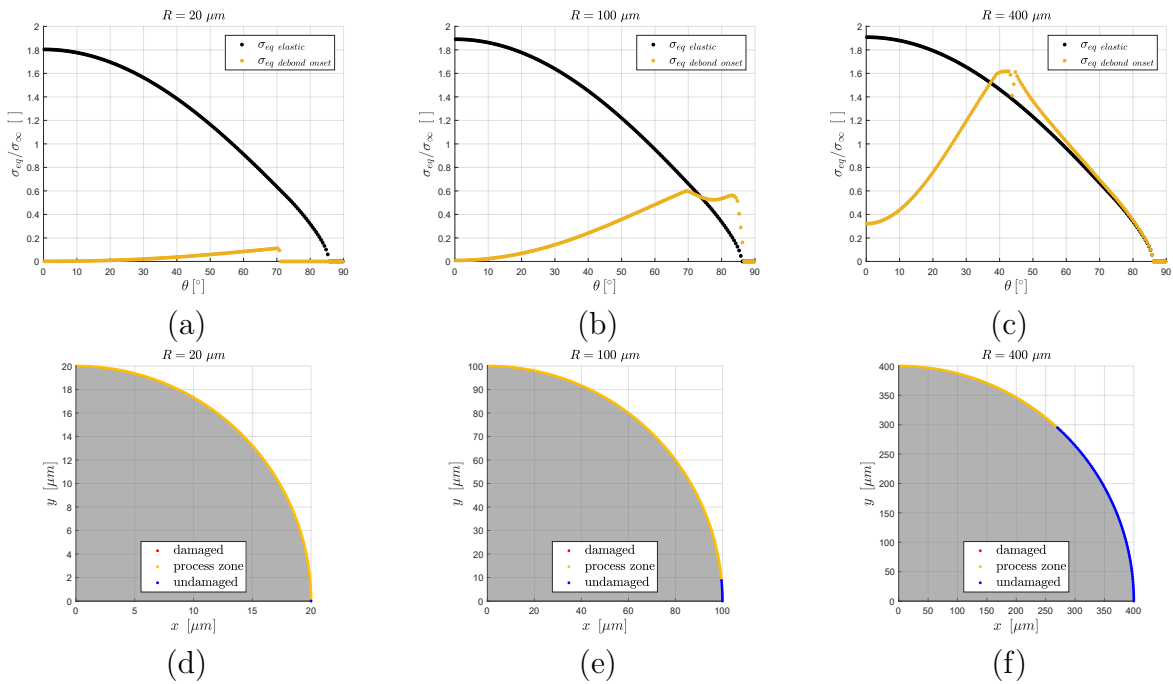


Figure B.1: Equivalent stress concentration around the particle for (a) $R = 20 \mu\text{m}$, (b) $R = 100 \mu\text{m}$, and (c) $R = 400 \mu\text{m}$, and size of the process zone for (d) $R = 20 \mu\text{m}$, (e) $R = 100 \mu\text{m}$, and (f) $R = 400 \mu\text{m}$, the time step before debonding onset.

To investigate/illustrate the effect of process zone development during the debonding nucleation and onset process, the stress concentrations around the particle at the time step just before the debonding onset are represented in Fig. 4.13 together with the the size of the process zone obtained from the numerical simulations. The Figs. 4.13 (d), (e), and (f) represent the quarter of the particle modelled (gray area) and the process zone is

represented in yellow. Three particle sizes are considered ($R = 20 \mu\text{m}$, $R = 100 \mu\text{m}$, $R = 400 \mu\text{m}$). Clearly the situation appears different. For large particles, a small process zone is observed ahead of the crack tip prior to unstable crack propagation, whereas a large process zone is observed for small particles.

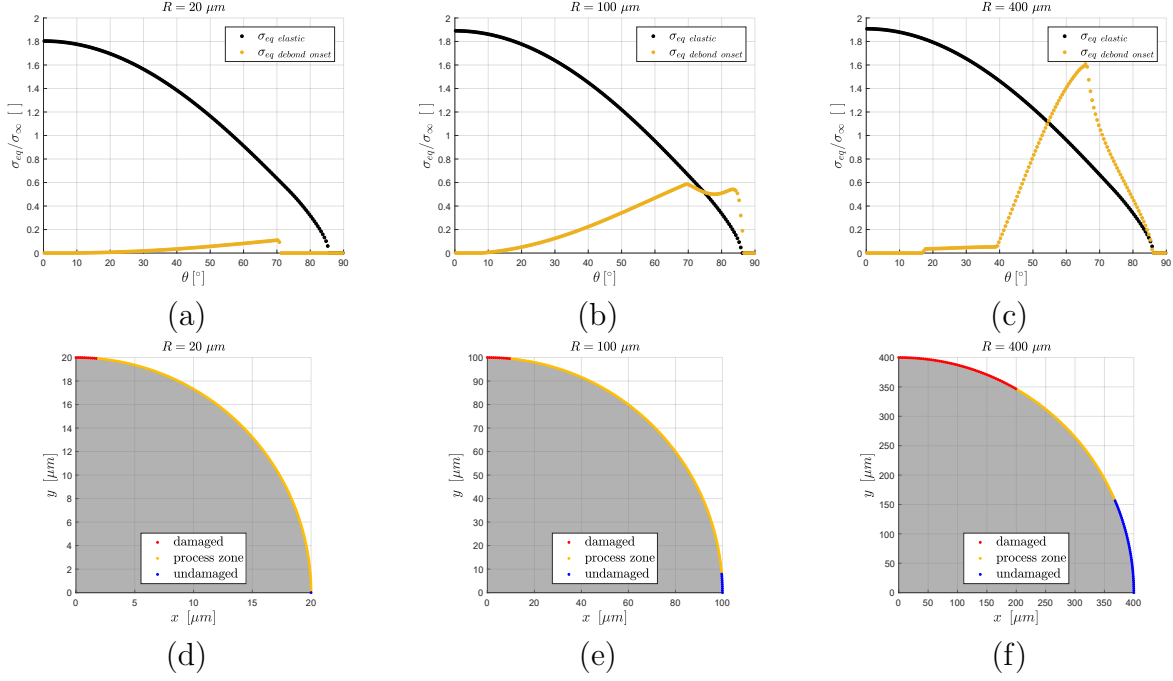


Figure B.2: Equivalent stress concentration around the particle for (a) $R = 20 \mu\text{m}$, (b) $R = 100 \mu\text{m}$, and (c) $R = 400 \mu\text{m}$, and size of the process zone and debonded zone for (d) $R = 20 \mu\text{m}$, (e) $R = 100 \mu\text{m}$, and (f) $R = 400 \mu\text{m}$, the time step after debonding onset.

The same analysis is carried out just after the first debond has occurred (see Fig. B.2). While the size of the process zone is smaller as the particle size increases, the size of the damaged zone increases with increasing particle size. This correlates the fact that, for small particles, the interface failure is ductile and progressive, while for large particles, it is brittle and sudden.

The sizes of the process and damaged zones are represented on top of the plot of the critical remote stress against particle radius in Fig. B.3 for a better visualisation of the results. This also confirms the fact that the characteristic length l_{ch} seems to be a good descriptor of the brittleness of the interface as it separates the zones where the interface failure is ductile and where it is brittle.

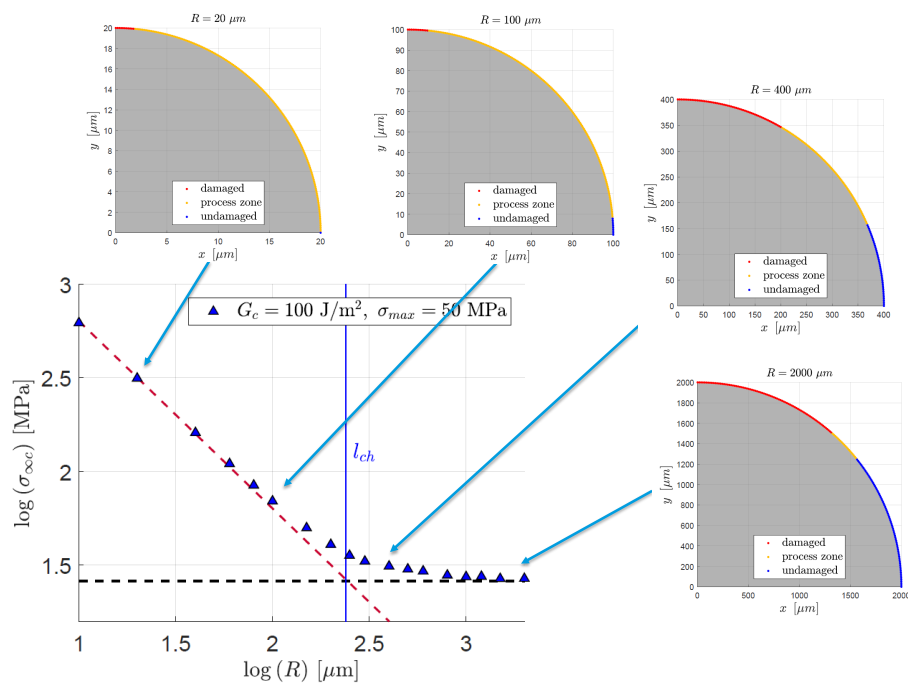


Figure B.3: Size of the process and damaged zones for different particle sizes.

Appendix C

Parametric study for particle debonding with CZM

Effect of interface strength and fracture energy on debonding with CZM

The influence of all three CZM law parameters (fracture energy G_c , strength of the interface σ_{max} , and critical displacement u_c) on master curves is evaluated. Four CZM are employed and their properties are expressed in Table C.1.

| | G_c [$J.m^{-2}$] | σ_{max} [MPa] | u_c [mm] | l_{ch} [mm] |
|-------|----------------------|--------------------------|----------------|-------------------|
| CZM 1 | 100 | 50 | 0.004 | 238.4 |
| CZM 2 | 50 | 50 | 0.002 | 119.2 |
| CZM 3 | 200 | 100 | 0.004 | 119.2 |
| CZM 4 | 100 | 100 | 0.002 | 59.6 |

Table C.1: CZM properties

The CZM 1 and 2 share the same strengths σ_{max} . The CZM 1 and 3 share the same critical displacements u_c . The CZM 1 and 4 share the same critical energies G_c . The uniaxial tensile loading defined in Chapter 4 is used here. The results for the critical remote stress against the particle radius are plotted in Fig. C.1 a. for the 4 different CZM. Fig. C.1 b. represents the same plot in a log-log scale.

As previously observed, two asymptotic regimes are visible for small and large particles. The characteristic length l_{ch} seems to be a very good descriptor of the transition between the two regimes as it corresponds to the intersection of the asymptotes for all the CZM. For small particles, the critical remote stresses obtained using the CZM 1 and 3 are the same. This result seems to imply that the predominant CZM parameter for small particle

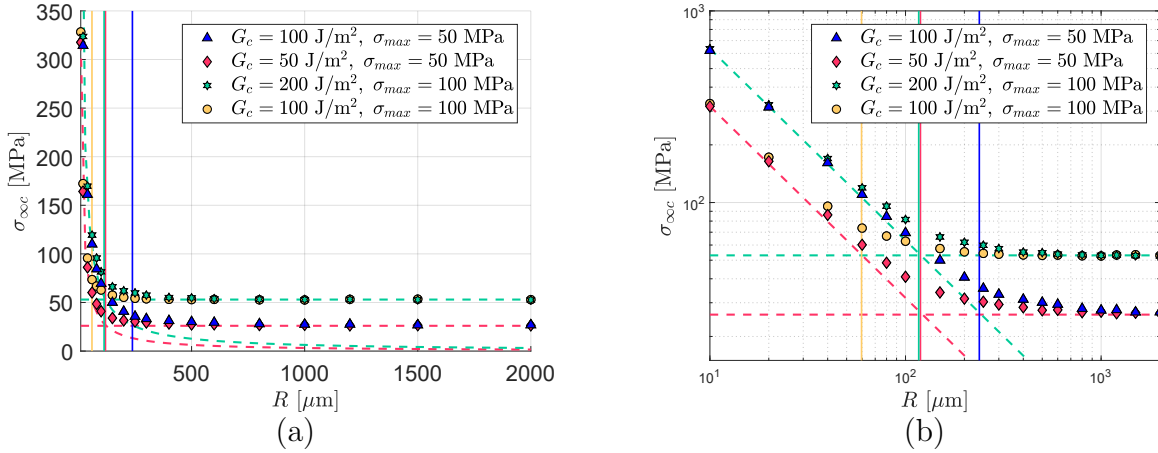


Figure C.1: (a) Critical remote stress against particle radius for different CZM; (b) Same plot in log-log scale.

debonding is the critical length u_c . For large particles, the plateau values of $\sigma_{\infty c}$ when using CZM 1 and 2 are the same. This last result confirms that the strength σ_{max} of the CZM governs the debonding for large particle sizes. A final remark concerns the results related to the CZM 1 and 4 which share the same fracture energy: the respective remote stresses don't have any asymptote in common.

Effect of interface stiffness on debonding with CZM

The effect of the interface stiffness is also observed. Three different traction-separation laws are introduced. They are characterised by the same fracture energy G_c and strength σ_{max} . They however show different initial stiffness. The only difference is then the position of the peak of the traction-separation laws. The stiffness of the interface is defined by the ratio of the displacement when the strength is reached \bar{u} over the critical displacement u_c . Three values of this ratios are selected: $1/200$, $1/2$, and $4/5$. The first one is the one used for all the calculations of Chapter 4 and corresponds to an initially very stiff interface that is progressively degraded. The last one corresponds to a very compliant interface that brutally fails. The three traction-separation laws are represented in Fig. C.2.

Fig. C.3 represents the critical remote stress for particle debonding onset against the particle size for the three traction-separation laws previously introduced. For small particles, no differences in critical remote stress can be observed. As stated with the parametric study, for small particles with CZM the critical remote stress is governed by the critical displacement u_c . The opening of the interface is unaffected by the shape of the CZM and thus we obtain the same critical remote stress.

For large particles, however, the debonding is governed by the stress of the interface.

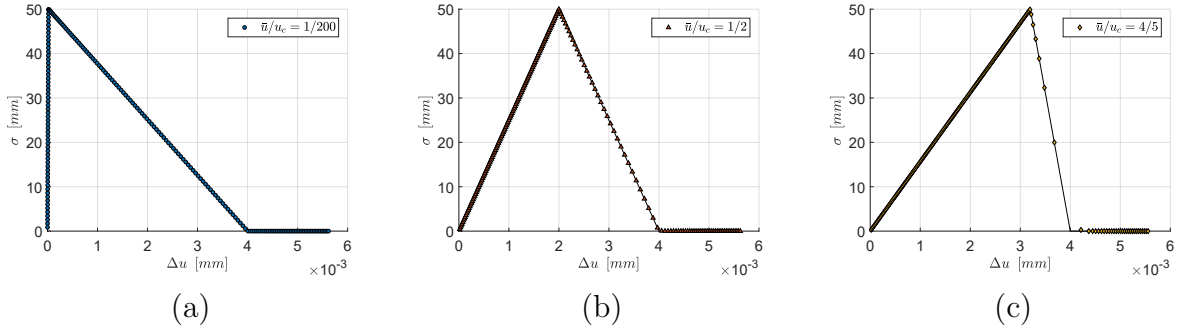


Figure C.2: Traction-separation laws for different interface stiffness (a) $\bar{u}/u_c = 1/200$, (b) $\bar{u}/u_c = 1/2$, (c) $\bar{u}/u_c = 4/5$, for particle size $R = 100 \mu\text{m}$.

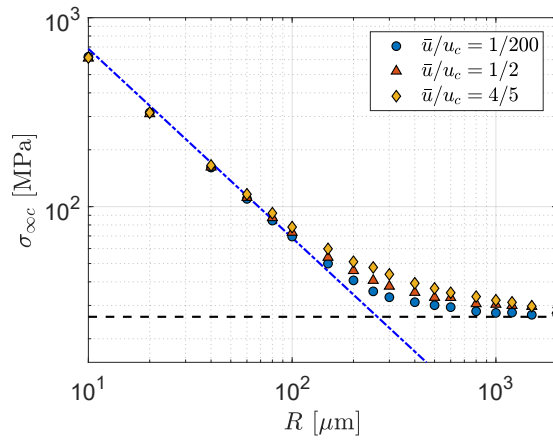


Figure C.3: Effect of the interface stiffness on the debonding onset of a spherical particle.

The global compliance of the system is modified by the presence of a compliant interface, and the stress distribution in the material is affected. A higher remote stress is required to debond the particle. However, for very large particles, the critical remote stress tends to the same asymptotic value regardless of the stiffness of the interface.

Effect of interface strength and fracture energy on debonding: Asymptotic behaviours with CZM and FFM

The parametric study is also carried out for the FFM-based model and comparisons are drawn between the CZM and FFM. Fig. C.4 represents the critical remote stress against particle radius for 4 different configurations of the interface parameters. Fig. C.4 (a) shows the curves for the parameters used for this study in Chapter 4. The horizontal asymptote describes the strength criterion. Indeed the equation of the asymptote can be

calculated as:

$$\sigma_{\infty c} = \frac{\sigma_{max}}{K_t}, \quad (C.1)$$

with K_t being the stress concentration factor at the pole of the particle expressed as: $\sigma_n(\theta = 0) = K_t \sigma_{\infty}$.

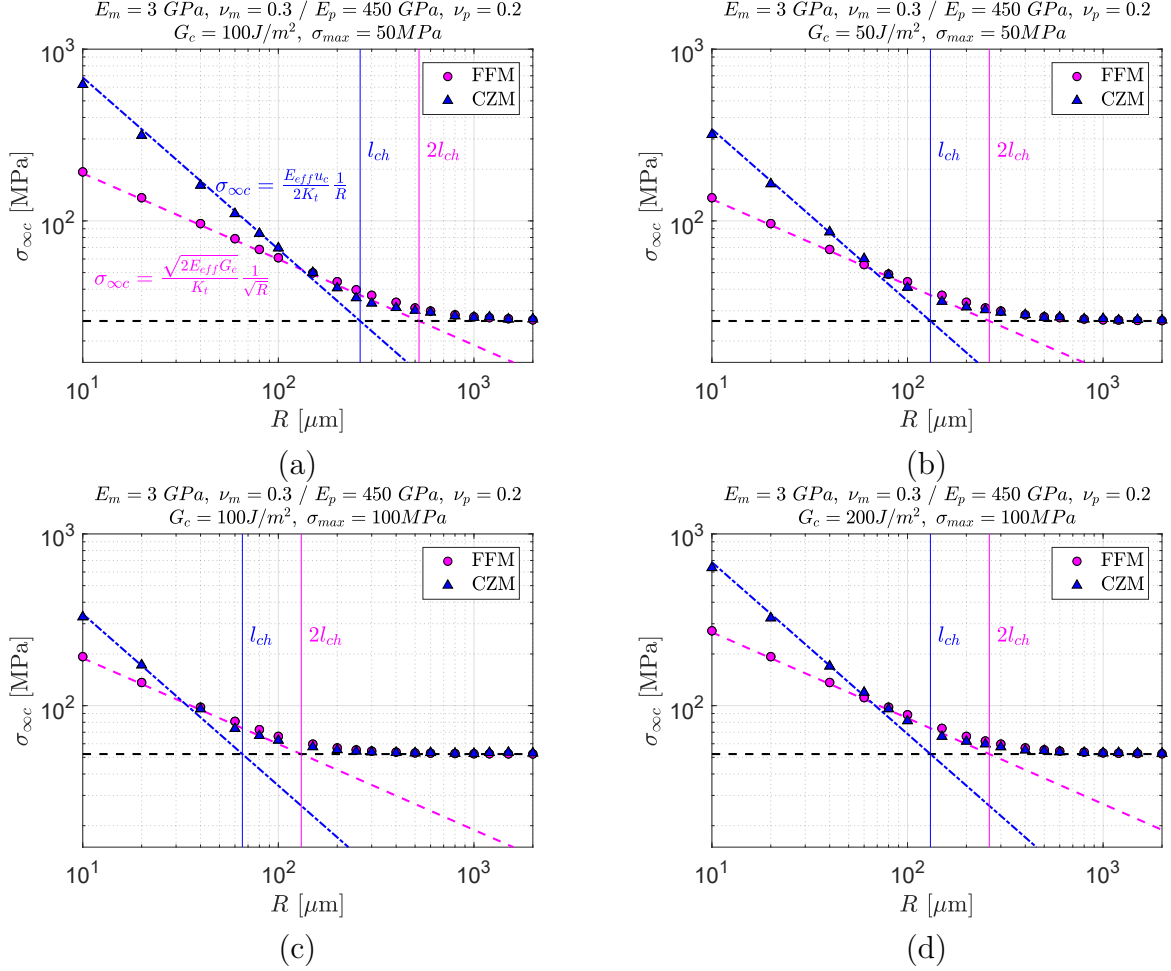


Figure C.4: Effect of interface strength and fracture energy on debonding (a) $G_c = 100 \text{ J/m}^2$ and $\sigma_{max} = 50 \text{ MPa}$, (b) $G_c = 50 \text{ J/m}^2$ and $\sigma_{max} = 50 \text{ MPa}$, (c) $G_c = 100 \text{ J/m}^2$ and $\sigma_{max} = 100 \text{ MPa}$, (d) $G_c = 200 \text{ J/m}^2$ and $\sigma_{max} = 100 \text{ MPa}$.

It is also possible to determine asymptotes for the energy criterion for both the CZM and the FFM. Based on a dimensional analysis of the parameters involved the debonding onset for both models, we obtained an accurate fit with:

$$\sigma_{\infty c} = \frac{E_{eff} u_c}{2K_t} \frac{1}{R}, \quad \text{for the CZM and} \quad (C.2)$$

$$\sigma_{\infty c} = \frac{\sqrt{2E_{eff} G_c}}{K_t} \frac{1}{R}, \quad \text{for the FFM} \quad (C.3)$$

This analysis is reproduced for the other interface parameters and the results are

visible in Fig. C.4 (b), (c) and (d). With the exact same expressions for the asymptotes, the fit for the energy criterion is very good as well, whatever the interface parameters are.

Effect of particle and matrix elastic moduli on debonding: Asymptotic behaviours with CZM and FFM

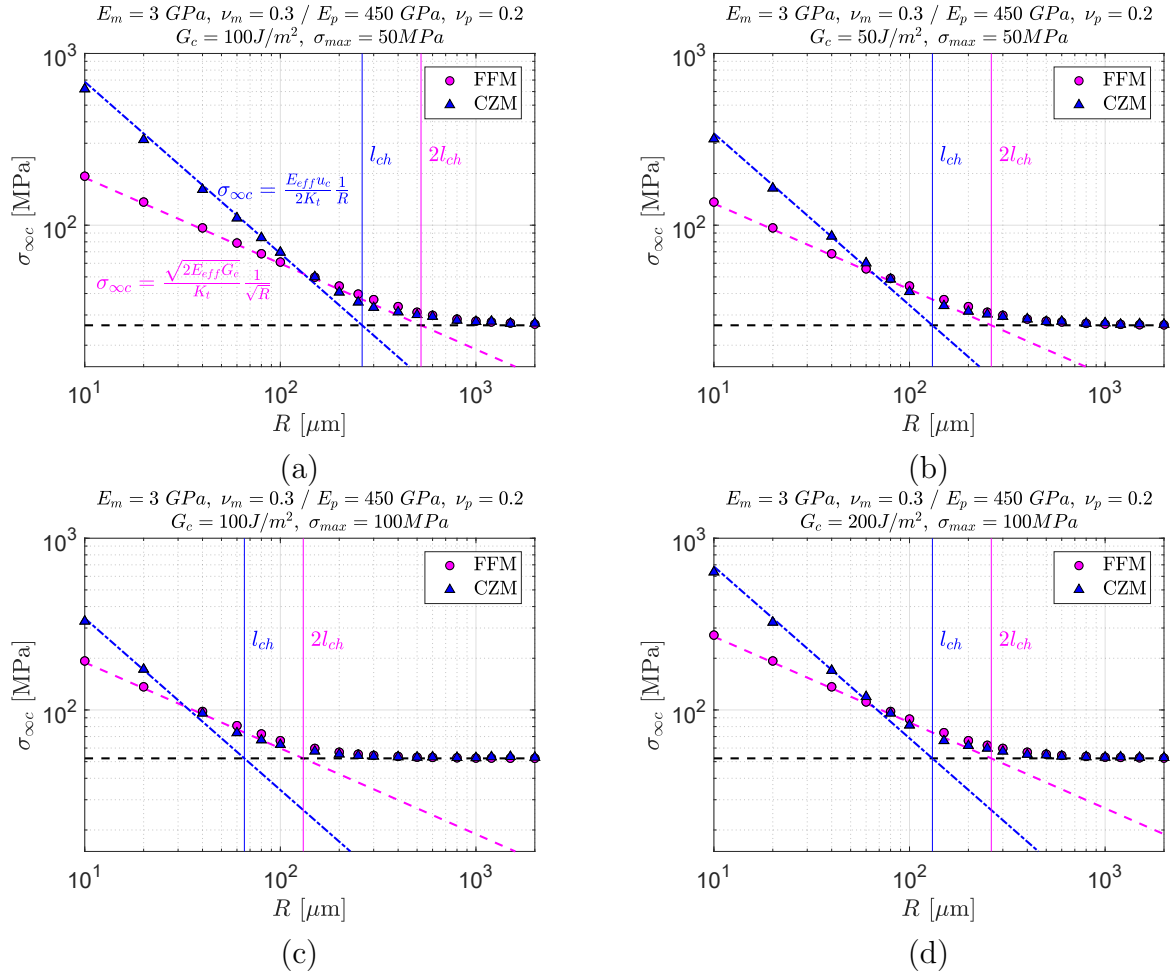


Figure C.5: Effect of elastic moduli of the phases on debonding (a) $E_m = 3 \text{ GPa}$ and $E_p = 450 \text{ GPa}$, (b) $E_m = 3 \text{ GPa}$ and $E_p = 8 \text{ GPa}$, (c) $E_m = 10 \text{ GPa}$ and $E_p = 20 \text{ GPa}$, (a) $E_m = 3 \text{ GPa}$ and $E_p = 8 \text{ GPa}$, $G_c = 100 \text{ J/m}^2$ and $\sigma_{max} = 100 \text{ MPa}$.

The expressions found for the asymptotes are checked by changing the particle and matrix Young's modulus. Figs. C.5 (a), (b) and (c) represent the results of the CZM and the FFM with three sets of Young's moduli (high and low contrasts between the phases are tested as it severely impacts Dundurs' coefficients that are descriptors of the differences in mechanical behaviour of two adjacent materials). The interface parameters are fixed for these three figures. It can be seen that the expressions given for the asymptotes give a very

precise fit of the critical remote stress for both small and large particles. In Fig. C.5 (d), both the properties of the phases and the interface parameters have been modified and the expressions of the asymptotes are still correct.

Appendix D

Fracture surfaces after monotonic indentation tests

The fracture surfaces were observed after monotonic indentation tests. Fig. D.1 represents the fracture surfaces of two different specimens composed of alumina particles: one with mostly large particles (a) (70% F20, 30% F360) and the other with only fine particles (b) (F360). An important roughness difference was observed between the two samples because of the size of the particles introduced.

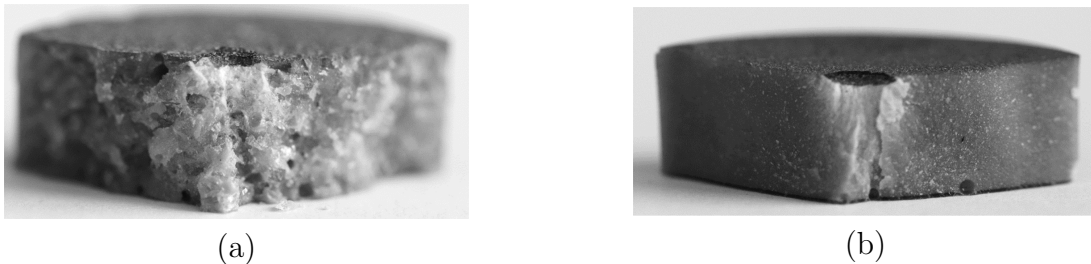


Figure D.1: Fracture surfaces of specimens with (a) mixed Al_2O_3 particle sizes (70% F20, 30% F360) and (b) F360 Al_2O_3 particles (camera).

Two different failure zones were visible for each sample. The first zone is the one directly under the indenter, where the particles and the matrix were compacted and crushed. This zone was also characterised by a white color probably coming from the plasticised resin. Fig. D.2 shows a higher magnification of this zone.

Then, away from the contact point, the material was not whitened. A sudden failure was observed when the material was split in 3 parts. No particle failure could be observed.

The same type of observations were undertaken with samples made of boron carbide particles. The fracture surfaces were especially observed to understand the effect of the silane and why some specimens were split in 2 pieces instead of 3. Fig. D.3 shows the fracture surfaces of specimens with $\phi = 60\%$ of mixed B_4C particles without silane (a), with silane split in 2 (b) and without silane split in 3 (c).

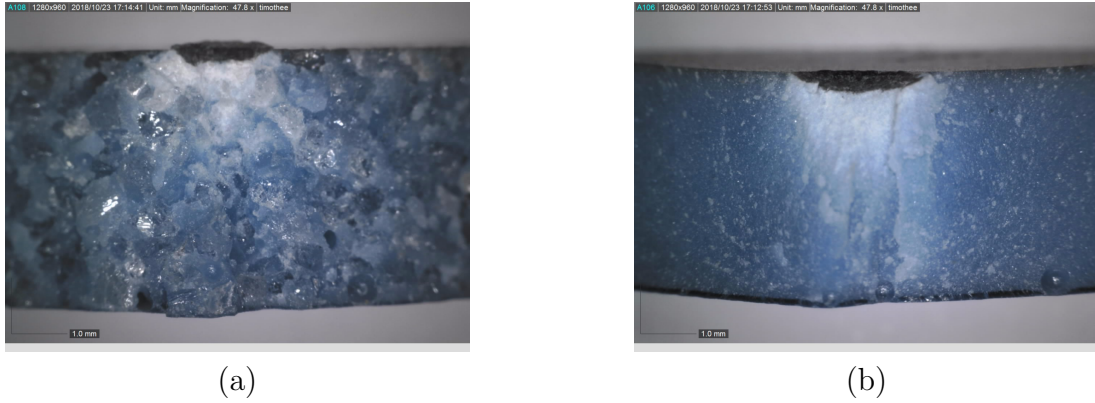


Figure D.2: Fracture surfaces of specimens with (a) mixed Al_2O_3 particle sizes (70% F20, 30% F360) and (b) F360 Al_2O_3 particles (optical microscope).

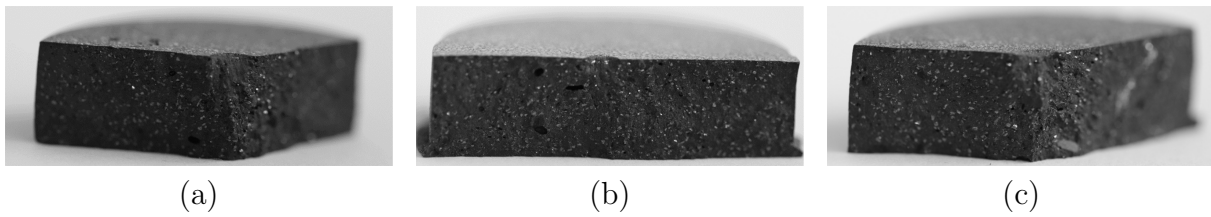


Figure D.3: Fracture surfaces of specimens with $\phi = 60\%$ of mixed B_4C particles, (a) no silane, (b) with silane split in 2, (c) with silane split in 3 (camera).

Generally speaking, the same types of observations as for the alumina particles can be made (two different zones of failure). The crushed zone was smaller with the sample split in 2 parts, as it failed prematurely. Some porosities can be also be observed in this sample.

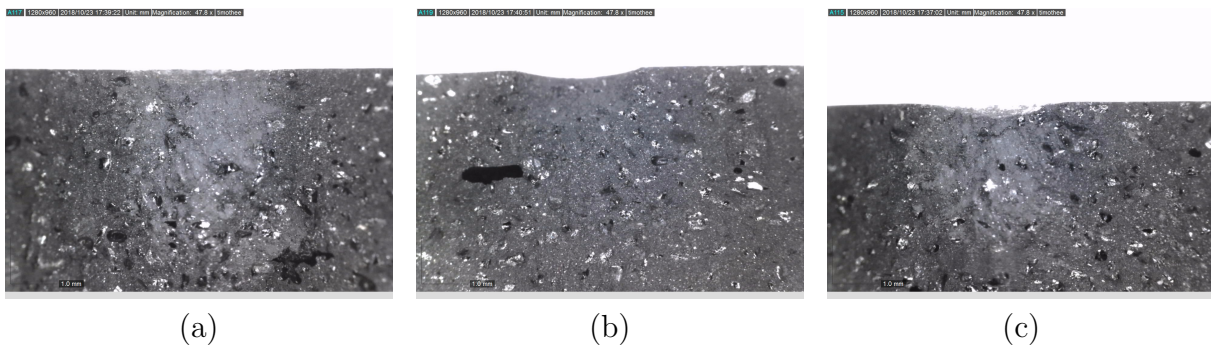


Figure D.4: Fracture surfaces of specimens with $\phi = 60\%$ of mixed B_4C particles, (a) no silane, (b) with silane split in 2, (c) with silane split in 3 (optical microscope).

Appendix E

Publications and communications

Journal articles

- T Gentieu, A Catapano, J Jumel, and J Broughton. Computational modelling of particulate-reinforced materials up to high volume fractions: Linear elastic homogenisation. Proceedings of the Institution of Mechanical Engineers, Part L: Journal of Materials: Design and Applications, 1464420717707227, 2017.
- T Gentieu, A Catapano, J Jumel, and J Broughton. Size effect in particle debonding: Comparisons between finite fracture mechanics and the cohesive zone model. In progress, 2018.

Conference articles

- T Gentieu, A Catapano, J Jumel, and J Broughton. Computational modelling of the progressive failure in carbon composites. 5th International Carbon Composite Conference (IC3), 2016
- T Gentieu, A Catapano, J Jumel, and J Broughton. Simulation of particle size effect on particle/matrix debonding. 6th European Conference on Computational Mechanics (ECCM6), 2018

Conference presentations and posters

- 5th International Carbon Composite Conference (IC3), 9-11/05/2016: Computational modelling of the progressive failure in carbon composites (Presentation)
- 5th International Conference on Material Modeling (ICMM5), 14-16/06/2017: Influence of cohesive zone parameters on the failure of particle reinforced composite materials (Presentation)

- UK-French PhD Scheme Conference 2017, 6/07/2017: Development of filled polymers for the replacements of ceramics used as ballistic protection layer (Presentation + Poster)
- Aussois 2018 - Colloque National Mécamat Matériaux Numériques, 22-26/01/2018: Microstructures et comportements thermomécaniques: Simulation de l'effet de taille des particules dans la décohésion particule/matrice (Poster)
- 6th European Conference on Computational Mechanics (ECCM6), 22-26/01/2018: Simulation of particle size effect on particle/matrix debonding (Presentation)
- UK-French PhD Scheme Conference 2018, 2/07/2018: Development of filled polymers for the replacements of ceramics used as ballistic protection layer (Presentation + Poster)

Abstract

Ceramics have extensively been used for ballistic protection in the last decades. The combination of their mechanical properties makes them very interesting for armouring. Indeed, they exhibit a high hardness, large compression strength, high stiffness and low density. Ceramic armouring plates are commonly manufactured through a sintering process, where ceramic powders are pressed at high temperatures. This manufacturing process tends to limit the size and shape of components and imparts high costs. On the other hand, moulding using a polymer matrix composite provides an alternative process for developing lower cost parts whilst accommodating increased complexity of geometry and size.

However, the mechanical behaviour of such a material is not completely known and depends on multiple design parameters: the mechanical properties of the phases, their volume fraction, the size and spatial distributions of the particles, and the adhesion between the components. The aim of this thesis is to evaluate the primary morphological parameters that affect the overall mechanical properties, emphasising the influence of the particle/matrix adhesion. To do so, both numerical and experimental multiscale analyses of the material under quasi-static and dynamic loadings were carried out.

More precisely, static and dynamic properties of the particle-reinforced composite have been determined for different constituent material combinations. In particular, attention has been dedicated to the particle/matrix debonding mechanism. Cohesive zone models (CZM) and Finite Fracture Mechanics (FFM) approaches were used to model this phenomenon and a strong effect of the particle size on decohesion was observed.

Résumé

Les matériaux céramiques présentent généralement des propriétés mécaniques très intéressantes pour la réalisation de blindages. Ce sont des matériaux très durs et pourtant légers. Les plaques de blindages en céramique sont classiquement mises en forme par pressage à haute température de poudres, ce qui limite la taille et la forme des réalisations tout en impliquant un coût élevé. Une alternative pour produire ces pièces est le moulage d'un composite constitué de particules de céramiques dans une matrice époxy. Ce procédé permet de réduire le coût des pièces tout en autorisant des géométries plus complexes et des dimensions plus importantes.

Le comportement mécanique de ce type de matériau dépend de multiples paramètres de conception : propriétés mécaniques des constituants (matrice polymère et particules céramiques), proportion volumique des deux phases, taille et distribution spatiale des particules ou encore l'adhésion entre les constituants. L'objectif de la thèse est d'évaluer l'influence de ces paramètres sur les propriétés d'usage du matériau. Pour ce faire, une analyse multi-échelle du matériau sous sollicitations quasi-statique et dynamique est réalisée.

Plus précisément, les propriétés statiques et dynamiques du composite à renforts particuliers ont été déterminées pour différentes combinaisons de ces paramètres de conception. En particulier, le mécanisme de décohesion particule/matrice a été spécifiquement étudié. Les approches de Modèles de Zone Cohésive (CZM) et de Mécanique de la Rupture Finie (FFM) ont été utilisées pour modéliser ce phénomène et un fort effet de taille des particules a été observé.